UNIVERSIDAD COMPLUTENSE DE MADRID

FACULTAD DE CIENCIAS FÍSICAS
Departamento de Física Atómica, Molecular y Nuclear

STUDY OF THE (e,e'p) QUASIELASTIC REACTION IN COMPLEX NUCLEI: THEORY AND EXPERIMENT.

MEMORIA PARA OPTAR AL GRADO DE DOCTOR

PRESENTADA POR

Joaquín López Herraiz

Bajo la dirección del doctor

José Manuel Udías Moinelo

Madrid, 2010

ISBN: 978-84-693-8348-3

Universidad Complutense de Madrid
Facultad de Ciencias Físicas
Dpto. de Física Atómica, Molecular y Nuclear

STUDY OF THE (e,e'p) QUASIELASTIC REACTION IN COMPLEX NUCLEI: THEORY AND EXPERIMENT

JOAQUÍN LÓPEZ HERRAIZ

Tesis dirigida por el profesor
Dr. José Manuel Udías Moinelo

Madrid, March 2010

Abstract
Study of the (e,e'p) Quasielastic Reaction in Complex Nuclei: Theory and Experiment

Joaquín López Herraiz

Experimental coincidence cross section and transverse-longitudinal asymmetry A_{TL} have been obtained for the quasielastic (e,e'p) reaction in ^{16}O, ^{12}C, and ^{208}Pb in constant q-ω kinematics in the missing momentum range -350 < p_{miss} < 350 MeV/c. In these experiments, performed in experimental Hall A of the Thomas Jefferson National Accelerator Facility (JLAB), the beam energy and the momentum and angle of the scattered electrons were kept fixed, while the angle between the proton momentum and the momentum transfer q was varied in order to map out the missing momentum distribution.

The experimental cross section and A_{TL} asymmetry have been compared with Monte Carlo simulations based on Distorted Wave Impulse Approximation (DWIA) calculations with both relativistic and non-relativistic spinor structure. The spectroscopic factors obtained for both models are in agreement with previous experimental values, while A_{TL} measurements favor the relativistic DWIA calculation.

This thesis describes the details of the experimental setup, the calibration of the spectrometers, the techniques used in the data analysis to derive the final cross sections and the A_{TL}, the ingredients of the theoretical calculations employed and the comparison of the results with the simulations based on these theoretical models.

Thesis Supervisor: José Manuel Udías Moinelo

Contents

AGRADECIMIENTOS

Esta tesis no podría haber sido realizada sin la ayuda de toda esa gente que ha estado apoyándome a lo largo de todos estos años. Para evitar el imperdonable pecado de olvidarme de alguno de vosotros, quiero daros las gracias ya desde el principio: vosotros sabéis quienes sois.

En esta larga aventura han sido muchas las personas que han contribuido de una u otra forma a que pueda sacar adelante este trabajo. Sobre todo, quisiera agradecer a mi director de tesis, José Manuel Udías, por haberme ofrecido la posibilidad de trabajar con él, por haberme enseñado no sólo física nuclear sino también cómo investigar y buscar soluciones a todos los problemas que hemos ido encontrando, por haber dedicado tanto tiempo a debatir frente a la pizarra o el ordenador, y como no, por los innumerables emails que hemos intercambiado a cualquier hora del día. No importaba en qué país nos encontrásemos, siempre sabía que podía contar con él.

Samuel España, con quién comencé esta andadura, ha sido un inmejorable compañero de viaje. Hemos compartido no sólo despacho, sino también charlas, viajes y mil batallas. El Grupo de Física Nuclear se ha ido convirtiendo, poco a poco, en una gran familia, de la que forman parte tan buenos amigos, y que está llena de anécdotas, risas, congresos, comidas de grupo y buen ambiente. Gracias por vuestro apoyo, en especial a los que habéis compartido despacho conmigo, día tras día. Ha sido un placer pasar estos años con vosotros; esperemos que pronto vengan muchas más tesis y plazas para todos.

No puedo seguir sin dar mil gracias a Rosa por lo que ha hecho para que logre terminar esta tesis. No sólo por el gran apoyo y ayuda en los meses de redacción, sino sobre todo por los ánimos y la confianza que siempre me ha dado para lograr aquello que tuviese en mente. Esta tesis te debe mucho.

Quiero agradecer a los miembros de la Colaboración del Hall A del JLAB, que siempre han mostrado su disposición a ayudarme y responder mis preguntas. En el tiempo que he pasado en el JLAB, he podido aprender mucho de todos ellos.

Merecen un agradecimiento especial los portavoces de los dos experimentos de esta tesis. Por un lado, Larry Weinstein y Kevin Fissum del experimento (e,e'p) en oxígeno, que siempre me han ofrecido sus conocimientos y ayuda. Han sido muchas las reuniones que hemos mantenido respecto al análisis de los datos y sus sugerencias siempre han sido acertadas. Gracias también por revisar una versión preliminar de esta tesis ya que los comentarios han permitido mejorar mucho este trabajo. Por otro lado, Guido Urciuoli, Arun Saha y Konrad Aniol del experimento (e,e'p) en plomo y carbono, por haber hecho posible el experimento y por las numerosas conferencias telefónicas que hemos mantenido. Un especial agradecimiento al incansable Alexandre Camsonne, por venir a Madrid a enseñarme a realizar el análisis de los datos y el manejo de los distintos códigos del JLAB, así como por resolverme dudas a lo largo de estos años.

Aunque quizá no lo sepáis, vosotros, los amigos y amigas que siempre estáis ahí, habéis sido un pilar fundamental para continuar adelante, aunque os seguían sorprendiendo los numerosos viajes que iba realizando, y los temas "tan raros" en los que estaba investigando. He tenido la suerte de encontrarme excelentes amigos ya desde primero de carrera, que han sabido aguantarme todos estos años. Mis amigos conquenses, a los que conozco de toda la vida y con los que siempre he podido compartir una cerveza. Y todos los que he encontrado en Madrid y con los que he realizado viajes inolvidables y compartido vida nocturna. Gracias a todos vosotros.

Y por último, pero no menos importante, quiero agradecer a mi familia por haberme apoyado siempre en las decisiones que he tomado y por animarme a seguir. Y como no, gracias también a mi hermana por el diseño original de la portada.

Sin todos los que estáis aquí, esta tesis no habría sido posible. Gracias.

e	e	s	t	a	t	e	s	i	s	j	n	i	u	q	a	o	j	n	a	o	y
o	r	a	l	e	u	b	a	p	o	d	a	m	r	e	l	r	l	n	i	a	r
s	d	i	v	a	n	h	a	b	e	r	r	v	s	i	d	m	e	o	l	r	r
c	n	i	o	l	a	z	n	o	g	e	a	a	i	l	a	l	a	m	a	i	a
a	a	z	s	a	n	e	d	u	m	l	a	a	f	r	e	n	d	a	u	a	l
r	x	s	i	m	n	i	a	h	i	m	v	u	i	a	i	e	s	r	r	t	s
f	e	r	a	n	a	b	e	t	s	e	a	o	b	t	e	y	u	i	a	a	n
e	l	m	i	g	u	e	l	s	a	i	d	u	s	r	d	l	a	a	m	j	a
r	a	o	a	r	u	n	a	d	e	l	a	i	o	o	u	s	a	u	l	r	d
n	m	v	t	u	c	h	i	m	s	i	r	s	m	b	a	n	e	s	e	o	i
a	h	j	a	i	t	a	t	i	c	c	a	g	r	o	a	l	o	c	s	b	a
n	u	o	a	n	n	i	a	s	g	a	r	o	t	c	e	h	p	g	t	o	r
d	g	r	e	h	e	a	a	b	u	c	r	e	r	a	e	n	s	u	h	s	p
o	o	d	r	t	e	s	u	a	i	e	d	m	o	j	a	i	l	i	e	u	a
p	o	i	e	v	y	a	s	j	l	s	n	d	e	o	m	v	u	d	r	s	l
e	a	a	n	a	o	l	o	a	l	a	l	a	r	n	g	e	i	o	o	e	o
d	e	e	t	r	o	d	a	a	e	r	o	s	e	s	t	k	s	e	t	j	m
i	i	e	a	m	p	l	o	e	r	s	o	i	n	i	m	r	e	h	t	a	a
b	t	v	a	l	e	t	s	e	m	s	e	s	d	a	m	i	a	n	i	s	v
a	l	d	e	i	n	o	e	d	o	i	i	r	a	q	u	e	l	c	a	d	a
a	a	v	x	o	s	d	e	l	a	h	k	o	t	i	v	o	p	a	b	l	o

1. Introduction

This thesis presents the analysis of data from several (e,e'p) experiments on complex nuclei performed in Hall A at the Thomas Jefferson National Accelerator Facility (JLAB) [JLab].

The first of these experiments [E00-102] [Sah00] was performed in the fall of 2001 using a waterfall (H_20) target for studying the nuclear structure of ^{16}O. The main purpose of this experiment was to study the ^{16}O(e,e'p) reaction in quasielastic kinematics testing the limits of the Single-Particle Model with unprecedented statistical accuracy and spanning one of the largest ranges of missing momentum ever explored.

The second experiment [E06-007] [Ani06] was performed in the spring of 2007 (first run) and in January 2008 (second run) using three-foil C+Pb+C and C+Bi+C targets to study the nuclear structure of ^{208}Pb and ^{206}Bi. Additional measurements of a single carbon target foil were also performed, allowing for the study of the nuclear structure of ^{12}C. The Nuclear Group of UCM took part in the preparation of this proposal, as well as in data taking and analysis.

In this thesis, experimental results from proton knock-out from the $p_{1/2}$ shell of ^{16}O, the $p_{3/2}$ shell of ^{12}C and the valence states of ^{208}Pb in the p_{miss} range [-350,350] MeV/c are shown. They all have been compared with simulations based on relativistic and non-relativistic theoretical calculations.

This thesis is organized in the following manner. The initial part of this Chapter presents the quasi-elastic (e,e'p) reaction formalism, while the subsequent part surveys previous (e,e'p) experiments that motivated the ones presented in this work. In Chapters 2 and 3, the details of the theory and simulations used to compare with the measured data are explained. Chapter 4 contains a detailed description of the experimental setup at JLAB. In Chapters 5 and 6, a discussion of the steps followed in the data analysis is presented. Finally, Chapters 7-8 present and discuss the actual results for each target. Chapters 9 contains the summary and conclusions of this thesis.

1.1. Electron Scattering

Electron scattering is one of the most powerful methods to study nuclear structure and interactions, as it has several advantages over other available nuclear probes [For83, For66, Don86, Fru84, Udi93, Udi95, Bof96]. The electromagnetic interaction is described

by Quantum Electrodynamics (QED). The electromagnetic coupling strength, characterized by the value of the fine structure constant α ~1/137.036, is relatively small and the interaction between the incident electron and the nucleus can be well described by the exchange of one single virtual photon. On the contrary, proton and pion scattering from nuclei are dominated by the strong force, so in order to extract nuclear structure information from reaction data, phenomenological models of the hadron-nucleus interaction must be relied upon. Further, the weakness of the electromagnetic interaction compared to the hadronic interaction means that the resulting virtual photon can probe the entire nuclear volume, in contrast to hadronic probes which interact strongly and thus primarily sample the nuclear surface.

The virtual photon carries energy ω and 3-momentum $\vec{q}$ which can be varied independently (subject to the restriction $Q^2 = q^2 - \omega^2 > 0$). Thus, for example, one could fix the energy transfer ω and, by measuring the nuclear responses at a range of $\vec{q}$ values, map out the spatial distributions of the nuclear charge and current densities. Note that real photon absorption experiments are bound to $q^2 - \omega^2 = 0$.

Virtual photons interact with charge density ρ and electromagnetic currents $\vec{J}$ of the target nucleus, transferring ω and $\vec{q}$. By measuring the cross section for electron scattering at various kinematics (that is, for different initial and final electron energies and scattering angles), one can map out the response of the nucleus to the electromagnetic probe, unveiling the details of the underlying nuclear structure.

However, electron scattering also has drawbacks and difficulties:

- A weakly-interacting probe implies a small cross section. Thus, the count rate for electron scattering experiments (especially for coincidence experiments) is usually low, requiring long beam-times to obtain statistically significant measurements. High intensity electron beams are required to achieve a good signal-to-noise ratio. In this regard, JLAB is unique amongst all facilities that are (or have been) capable of performing (e,e'p) experiments.

- The small mass of the electron complicates the analysis of electron scattering data due to radiative processes, which can result in large corrections.

1.2. Inclusive Electron Scattering - (e,e')

In single-arm electron-scattering experiments, the electron beam is incident on the target and a spectrometer is set at a particular momentum and angle to detect the scattered electron. This kind of experimental setup does not select a particular reaction channel, but rather all processes that can be caused by the interaction with the electron contribute to the measured signal. Therefore, this kind of experiments is termed *inclusive*. A general inclusive (e,e') spectrum showing the cross section $d\sigma/d\Omega_e$ (where $d\Omega_e$ is the solid angle into which the electron scatters) as a function of ω, for a fixed value of $Q^2 = q^2 - \omega^2$, is sketched in Figure 1.1 [For66].

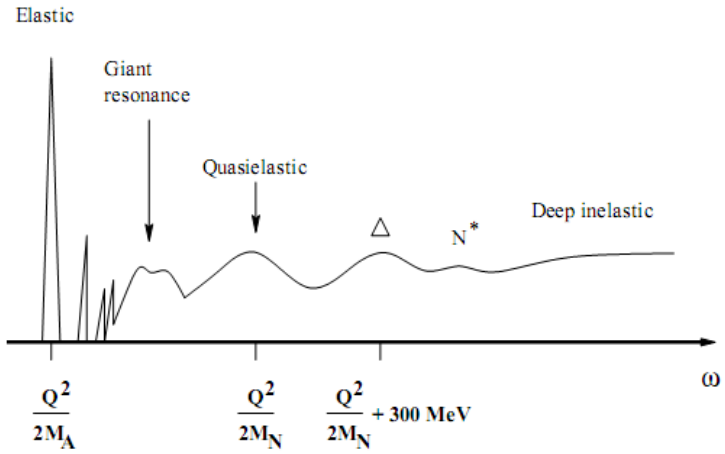

Figure 1.1: Schematic (e,e') spectrum.

The first sharp peak to the left corresponds to elastic electron scattering from the nucleus as a whole, which appears at $\omega = Q^2/(2M_A)$ (where M_A is the mass of the nucleus). The next few sharp peaks at higher ω correspond to nuclear excitations to discrete states. Often, excitations of collective modes such as giant resonances are seen beyond the discrete part of the spectrum. Even higher in energy, the quasielastic peak appears near $\omega = Q^2/(2M_N)$, where M_N is the mass of a nucleon. The position of this peak corresponds approximately to the kinematical condition for elastic scattering off a free single nucleon of mass M_N. Thus, this peak may be attributed to electron scattering from individual constituent nucleons. The Bjorken x scaling variable, defined as $x_B = Q^2/(2M_N\omega)$ is a useful reference value to characterize the (e,e') reaction. Values of x_B close to one, as the ones obtained in the experiments analyzed in this thesis, correspond to quasielastic reactions.

The next few bumps at even higher energy transfer arise from nucleon excitations such as Δ and N^* resonances. The intermediate region between the quasielastic peak and the Δ resonance is often referred to the dip region. Further away from the position of low lying N^*

excitations, lies the so-called deep inelastic scattering region (DIP), where nucleon resonances are broad and overlapping. In this region, electrons may be thought of as scattering quasielastically from individual quarks of the nucleon.

1.3. Exclusive Electron Scattering - (e,e'p)

Since inclusive (e,e') cross section is comprised of data from many possible channels, it is inherently difficult to study and evaluate the individual contributions of the different channels to the observed data. Sum rule approaches [Cab10] or scaling ideas [Don88] may be of use, but in order to study single-nucleon properties it is better to focus on exclusive experiments. For these exclusive experiments, the final state can be selected and fully identified. For instance, the contributions to the electron-nucleus cross section coming from different valence nucleons can be disentangled, allowing for a more detailed study of the reaction mechanism. The theoretical description of the exclusive reaction is relatively simple, as only one channel needs to be taken into account.

To obtain data under exclusive conditions in electron-scattering experiments, the scattered electron is detected and analyzed in one spectrometer and, at the same time, a knocked-out nucleon is detected and analyzed with another spectrometer. If the detected nucleon is a proton, this reaction is called (e,e'p). In this way, if the energy and momentum of the incoming and outgoing electron and the detected nucleon are both measured, four-momentum conservation makes it possible to determine the energy transferred to the nucleus.

It is then possible to set conditions which warrant that the final state corresponds to single-nucleon knockout, simply because not enough energy has been transferred to the nucleus to knock out two nucleons. Coincidence (e,e'p) measurements, under these conditions, which include signals from only one reaction channel, are an example of an exclusive measurement. One must bear in mind that, if the energy transferred to the nucleus is large enough, then more than one nucleon may be knocked out. This type of (e,e'p) measurement is not performed under exclusive conditions, and is the case for most transparency experiments [Lav04]. Quite generally, in existing facilities to date, only valence shells can be studied under exclusive conditions in (e,e'p). It is worth mentioning that electron-ion colliders such as the ELISe facility planned for FAIR [ELISe, ELISeb] may allow for exclusive (e,e'N) measurements for any neutron or proton shell.

The history of quasielastic (e,e'p) experiments began in 1962 when Jacob and Maris

[Jac62] suggested that it could be a powerful experimental technique to study the energy levels and shell structure of light and medium nuclei. To date, many (e,e'p) experiments have been performed under exclusive conditions at accelerator facilities such as Saclay, NIKHEF-K, Mainz, Tokyo, MIT-Bates and JLAB. Results from these experiments prove that the (e,e'p) reaction is an excellent tool for the study of single-particle properties of nucleons in nucleus.

1.4. Kinematics

For light or medium nuclei where $Z\alpha<<1$ (Z is the number of protons inside nucleus and α is the fine-structure constant), it is a good approximation to assume that only one virtual photon is exchanged in the process of electron scattering. This constitutes the first order Born Approximation [Bjo64]. Using standard notation [Udi95], the laboratory coordinate system, four-momenta, total energies and three momenta of the participants in the reaction are presented in Table 1.1:

Incident electron: $k_i^\mu = (E_i, \mathbf{k}_i)$	Detected electron: $k_f^\mu = (E_f, \mathbf{k}_f)$
Target nucleus: $p_A^\mu = (E_A, \mathbf{p}_A)$	Undetected residual system: $p_B^\mu = (E_B, \mathbf{p}_B)$
Energy-momentum transferred: $q^\mu = k_i - k_f = (\omega, \mathbf{q})$	Detected proton: $p_p^\mu = (E_p, \mathbf{p}_p)$

Table 1.1: Four-momentum of the participants in the (e,e'p) reaction.

The reaction A(e,e'p)B in the Born Approximation is illustrated in Figure 1.2. The figure can be divided into two parts: the *electron side* and the *target* or *nuclear side*. On the electron side, the plane defined by the incident and outcoming electron momenta is called the *electron-scattering plane*, or often just the *scattering plane*; the electron-scattering angle is denoted as θ_e. On the target side, the plane defined by the momentum transfer $\vec{q}$ and the knocked-out proton momentum $\vec{p}_p$ is called *ejectile plane*, *nuclear-scattering plane* or, often just *reaction plane*. The angle between the three-momentum transfer $\vec{q}$ and the proton momentum is denoted θ_{pq}. The angle between electron- and nuclear-scattering planes is the out-of-plane angle ϕ.

If the proton is detected at $\phi = 0^o$ or $\phi = 180^o$, the scattering and reaction planes coincide and the measurement is said to be performed *in-plane*. Measurements for which the knocked-out nucleon momentum is along $\vec{q}$ ($\theta_{pq}=0^o$) correspond to "parallel" kinematics, and measurements values of θ_{pq} other than 0^o are said to be made in "quasi-perpendicular" kinematics, of which constant q-ω measurements are most often employed.

Figure 1.3 illustrates these two kinematical conditions.

As has been said, the quantities experimentally measured in (e,e'p) experiments are $\vec{k}_i$, $\vec{k}_i$ and $\vec{p}_p$. The total energy of the detected proton E_p is obtained from $E_p = \sqrt{M_p^{\,2} + \vec{p}_p^{\,2}}$, where M_p is the proton rest mass. In the laboratory reference frame, the target nucleus is at rest so $p_A{}^{\mu} = (M_A, 0)$, where M_A is the rest mass of the nucleus. Most often, electrons are ultrarelativistic and their masses can be neglected so that $E_i \approx |\vec{k}_i|$ and $E_f \approx |\vec{k}_f|$. The transferred four-momentum q^{μ} is found from the energy-momentum conservation relation

$$q^{\mu} = k_i{}^{\mu} - k_f{}^{\mu} = (\omega, \vec{q}) \tag{1.1}$$

It can be shown [For66] that $(q^2 = q^{\mu} q_{\mu}) \le 0$, for ultrarelativistic electrons, $q^2 = -4E_i E_f \sin^2(\theta_e / 2)$. Q^2 is defined as $Q^2 = -q^2 = \vec{q}^2 - \omega^2 \ge 0$.

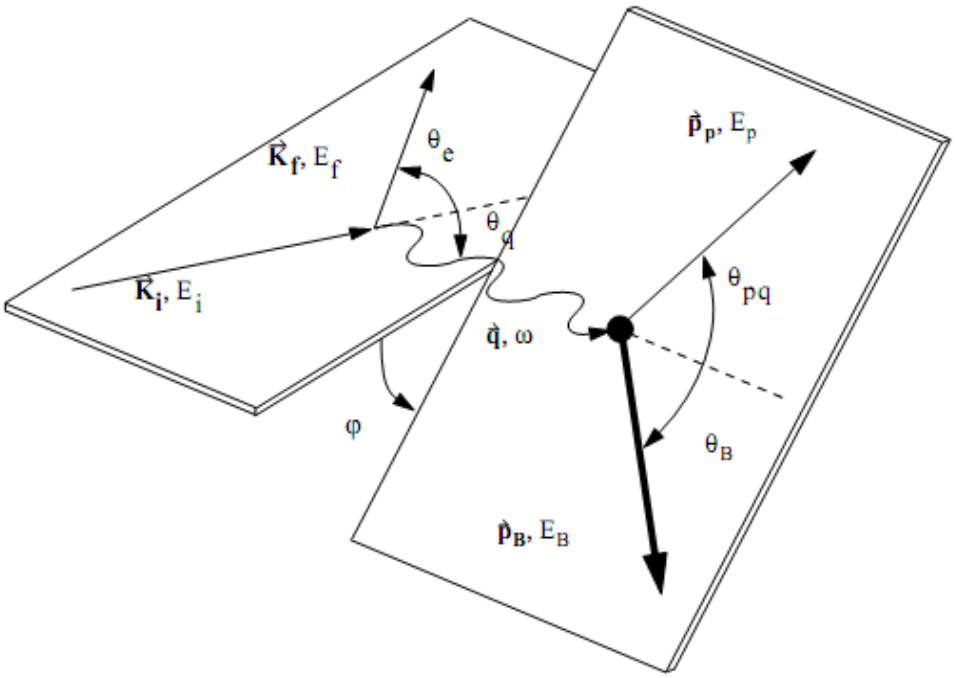

Figure 1.2: Schematic view of the (e,e'p) reaction and definition of kinematical variables.

Two important quantities are the missing momentum $\vec{p}_{miss}$ and the missing energy E_m [Udi93, Udi95, Kel96]. The missing energy is given by

$$E_{miss} \equiv \omega - T_p - T_B \tag{1.2}$$

where T_p and T_B are the kinetic energies of the ejected proton and the recoil nucleus, respectively. Writing down the kinetic-energy terms explicitly yields

$$E_{miss} \equiv \omega - \left(\sqrt{\vec{p}_p^{\,2} + m_p^{\,2}} - m_p\right) - \left(\sqrt{\vec{p}_B^{\,2} + M_B^{\,2}} - M_B\right) \tag{1.3}$$

Conservation of momentum at the reaction vertex leads to

$$\vec{p}_{miss} = \vec{p}_p - \vec{q} = -\vec{p}_B \tag{1.4}$$

Thus, without any approximations, the missing momentum simply represents the

momentum of the recoiling system or residual nucleus. Conservation of energy at the reaction vertex implies that

$$\begin{aligned} E_i + M_A &= E_f + E_p + E_B \\ \omega &= (m_p + T_p) + (M_B + T_B) - M_A \end{aligned} \tag{1.5}$$

Substituting Eq. (1.5) into Eq. (1.2) results in

$$E_{miss} = m_p - M_A + M_B \tag{1.6}$$

Rewriting the residual mass in terms of energy and momentum gives

$$\begin{aligned} E_B &= \omega + M_A - E_p \\ M_B &= \sqrt{{E_B}^2 - {\vec{p}_B}^2} = \sqrt{{E_B}^2 - {\vec{p}_{miss}}^2} \\ M_B &= \sqrt{\left(\omega + M_A - E_p\right)^2 - {\vec{p}_{miss}}^2} \end{aligned} \tag{1.7}$$

Thus, the missing energy can be written as

$$E_{miss} = m_p - M_A + \sqrt{\left(\omega + M_A - E_p\right)^2 - {\vec{p}_{miss}}^2} \tag{1.8}$$

This expression for the missing energy does not require any *a priori* knowledge of the residual system. Eq. (1.6) indicates that the missing energy represents the difference in binding energy between the initial and final nuclear states and, thus, it is the energy not observed (missing) as kinetic energy of the knocked-out particles. If the residual system is in its ground state, E_{miss} represents the separation energy E_s of the ejected proton.

Generally speaking, the residual system may be in an excited state. Conservation of energy has been used to remove M_B from these expressions. This mass of the residual system also includes any excitation energy needed to remove a proton from the target nucleus, but not leaving the residual system in its ground state. So in a more general case

$$\begin{aligned} M_B &= {M_B}^0\left(fundamental\ \ state\right) + E_x(excitation\ \ energy) \\ E_{miss} &= E_s + E_x \end{aligned} \tag{1.9}$$

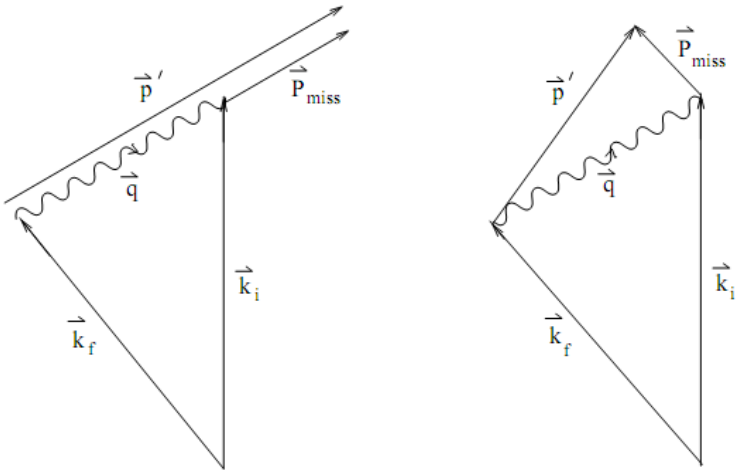

Figure 1.3: Schematic representation of parallel (left) and perpendicular (right) kinematics.

The invariant cross section can be written as [For66, Udi93, Udi95, Kel96]

$$d\sigma = \frac{1}{(2\pi)^3}\frac{E_f}{E_i}\frac{\alpha^2}{Q^4}\eta_{\mu\nu}W_{\mu\nu}dE_f d\Omega_e d^3\vec{p}_p \tag{1.10}$$

where $d\Omega_e$ is the solid angle for the electron momentum in the laboratory and $\eta_{\mu\nu}$ and $W_{\mu\nu}$ are the electron and nuclear response tensors. Using

$$d^3\vec{p} = p^2 \cdot dp \cdot d\Omega_p \tag{1.11}$$

where $d\Omega_p$ is the solid angle for the proton momentum in the laboratory, one can obtain the six-fold differential cross section

$$\frac{d^6\sigma}{dE_f d\Omega_e dE_p d\Omega_p} = \frac{E_p p_p}{(2\pi)^3}\frac{E_f}{E_i}\frac{\alpha^2}{Q^4}\eta_{\mu\nu}W_{\mu\nu} \tag{1.12}$$

For extremely relativistic electrons, the electron mass can be neglected and the electron-response tensor can be written as [For66]

$$\begin{aligned} \eta_{\mu\nu} &= 2\left(k_{i\mu}k_{f\nu} + k_{f\mu}k_{i\nu} - k_i k_f g_{\mu\nu}\right) \\ \rightarrow \eta_{\mu\nu} &= K_\mu K_\nu - q_\mu q_\nu - Q^2 g_{\mu\nu} \end{aligned} \tag{1.13}$$

where $K_\mu \equiv k_{i\mu} + k_{f\mu}$ and $q_\mu \equiv k_{i\mu} - k_{f\mu}$.

Matrix elements of the nuclear response tensor are obtained from bilinear products of the nuclear current matrix elements, appropriately averaged over initial states and summed over final states

$$W_{\mu\nu} = \left\langle J_\mu J_\nu^{+} \right\rangle \tag{1.14}$$

Often, (but not in the theoretical calculations employed in this thesis, that rely on more general expressions as given in [Udi95,Umi95b]) current conservation and the continuity equation are employed to make the following substitutions

$$q_\mu W^{\mu\nu} = W^{\mu\nu} q_\nu = 0 \tag{1.15}$$

$$J_z = \frac{\omega}{|\vec{q}|}\rho \tag{1.16}$$

After some algebra, the contraction of electron and nuclear response tensors reduces to the form

$$\eta_{\mu\nu}W^{\mu\nu} = 4E_i E_f \cos^2\frac{\theta_e}{2}\left[V_L R_L + V_T R_T + V_{LT}R_{LT}\cos\phi + V_{TT}R_{TT}\cos 2\phi\right] \tag{1.17}$$

If $\lambda \equiv Q^2 / \vec{q}^2$ and $\chi \equiv \tan^2(\theta_e / 2)$ are defined, the kinematical factors may be expressed as

$$\begin{aligned} V_L &= \lambda^2 & V_T &= \frac{\lambda}{2} + \chi \\ V_{LT} &= \lambda \cdot \left[\lambda + \chi\right]^{1/2} & V_{TT} &= \frac{\lambda}{2} \end{aligned} \tag{1.18}$$

The response functions can be expressed in terms of the nuclear current tensor

$$\begin{aligned} R_L &= \left\langle W_{00} \right\rangle = \left\langle \rho\rho^+ \right\rangle \\ R_T &= \left\langle W_{xx} + W_{yy} \right\rangle = \left\langle J_\parallel J_\parallel{}^+ + J_\perp J_\perp{}^+ \right\rangle \\ R_{LT}\cos\phi &= -\left\langle W_{0x} + W_{x0} \right\rangle = -\left\langle \rho J_\parallel{}^+ + J_\parallel \rho^+ \right\rangle \\ R_{TT}\cos 2\phi &= \left\langle W_{xx} - W_{yy} \right\rangle = \left\langle J_\parallel J_\parallel{}^+ - J_\perp J_\perp{}^+ \right\rangle \end{aligned} \tag{1.19}$$

where ρ is the charge component of the nuclear current, $J_\parallel$ is the transverse component of the nuclear current in the scattering plane and J± is the transverse component of the nuclear current orthogonal to the scattering plane. Both $J_\parallel$ and $J_\pm$ are orthogonal to $\vec{q}$. The longitudinal response function R_L arises from the charge and the longitudinal component of the nuclear current. The transverse response function R_T is the incoherent sum of the contributions from the two transverse components of the nuclear current. The transverse-longitudinal interference response function R_{TL} is the interference of the transverse current with the longitudinal component of the nuclear current in the scattering plane. The transverse-transverse interference response function R_{TT} is the interference between the two transverse components of the nuclear current.

For (e,e'p) reactions in which only a single discrete state or narrow resonance of the target is excited, one can integrate over the peak in proton energy to obtain a fivefold differential cross section. From Eq. (1.12) we can integrate

$$\begin{aligned} \frac{d^5\sigma}{dE_f d\Omega_e d\Omega_p} &= \int \frac{d^6\sigma}{dE_f d\Omega_e dE_p d\Omega_p} \cdot \frac{1}{\left|\partial E_m / \partial E_p\right|} dE_m \\ \frac{d^5\sigma}{dE_f d\Omega_e d\Omega_p} &= R\frac{E_p p_p}{\left(2\pi\right)^3}\frac{E_f}{E_i}\frac{\alpha^2}{Q^4}\eta_{\mu\nu}W_{\mu\nu} \end{aligned} \tag{1.20}$$

where R represents a recoil factor given by

$$R = \frac{1}{\left|\partial E_m / \partial E_p\right|} = \left|1 - \frac{E_p}{E_B}\frac{\vec{p}_p \cdot \vec{p}_B}{\vec{p}_p \cdot \vec{p}_p}\right|^{-1} = \left|1 - \frac{E_p}{E_B}\left(1 - \frac{q}{p_p}\cos\theta_{pq}\right)\right|^{-1} \tag{1.21}$$

By inserting Eq. (1.17) into Eq. (1.20) and rewriting, the 5-fold differential unpolarized cross section can be expressed in a compact form as

$$\frac{d^5\sigma}{d\omega d\Omega_e d\Omega_p} = R\frac{E_p p_p}{\left(2\pi\right)^3}\sigma_M\left[V_L R_L + V_T R_T + V_{TL} R_{TL}\cos\phi + V_{TT} R_{TT}\cos 2\phi\right] \tag{1.22}$$

where σ_M is the Mott cross section

$$\sigma_M = \frac{E_f}{E_i}\frac{\alpha^2}{Q^4}4E_i E_f \cos^2\left(\frac{\theta_e}{2}\right) \tag{1.23}$$

In general, R_L, R_T, R_{TL} and R_{TT} are functions of the variables ω, Q^2, p_{miss}, E_{miss} and $\left|\vec{p}_p\right|$ and contain all the information that can be extracted from the (e,e'p) reaction with unpolarized electrons and nucleons.

Therefore the cross section expressed in Eq. (1.22) can be separated in two parts: the kinematical factors R, $E_p p_p \Big/ (2\pi)^3$, V_L, V_T, V_{LT}, V_{TT}, and σ_M, independent of the nuclear structure, and the response functions which contain the nuclear structure information and are independent on electron kinematics, meaning that they depend only of the nuclear kinematics.

In parallel kinematics $(\vec{p}_p \parallel \vec{q})$, the orientation of the reaction plane (the azimuthal angle ϕ) becomes undefined. In this special case, only the response functions R_L and R_T contribute to the cross section [For66, Gard94].

1.5. Mechanisms of the (e,e'p) Reaction

In order to understand (e,e'p) scattering experiments, one needs to study the mechanism of the process in detail. A realistic description of the (e,e'p) reaction has to take into account several components. Some of them are not easy to handle and are sometimes neglected, but it is important to address them in order to obtain meaningful conclusions from the results. These include:

-**Energy loss, bremsstrahlung and Coulomb distortion of incident and scattered electrons**. In their path through scattering-chamber windows, the target and the detector, electrons lose part of their energy and change their momentum. This causes the asymptotic values of the energy and momentum of the outcoming particles measured at the spectrometers to be different from the corresponding values at the interaction vertex. Furthermore, the Coulomb potential of the nucleus modifies the electron wave function, and thus the customarily employed plane-wave description of the electrons is only approximately valid. While all of these effects are technically challenging, they are theoretically well described by QED.

-**Electron-proton interaction**. As the protons are embedded in a nuclear medium, the electron-nucleon interaction may be different to the electron interaction with free nucleons. Medium modifications to nucleons are only possible to disentangle within a particular nucleon model.

-**The single-particle structure of the target nucleus**. Within the *Impulse Approximation* that will be employed here, the single-particle structure of the target nucleus is sampled by the (e,e'p) reaction only via the overlap function of the initial and final nuclear systems. This overlap function has a simple interpretation within extreme mean-field models, but it is difficult to compute when correlations are considered.

-**Final state interactions (FSI).** The interaction of the knocked out proton with the residual system must be taken into account for realistic comparison between calculations and data. This complicates the theoretical calculations.

1.5.1. Impulse Approximation

(e,e'p) experiments are analyzed under a common framework known as *Impulse Approximation* (IA) [Fru84, Kel96]. The approximations made in the IA are sound for quasielastic conditions, where it is known that the reaction is dominated by electron scattering by the individual constituent nucleons. IA assumes that the exchanged virtual photon interacts only with one nucleon, precisely the one that is detected.

- **Plane Wave Impulse Approximation**

If aside from IA, the knocked-out proton is further assumed to come out of the nucleus without further interaction with the residual nucleus, then this nucleon can be described by a plane wave (Plane Wave Impulse Approximation or PWIA). Figure 1.4 sketches a diagram of this process.

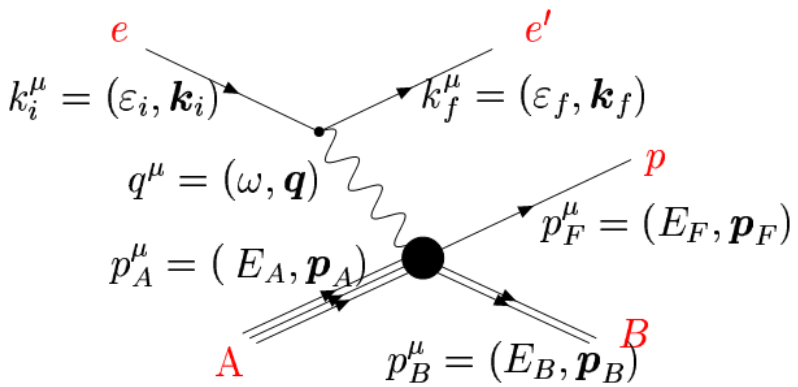

Figure 1.4: Plane Wave Impulse Approximation in (e,e'p).

Under IA, $\vec{p}_{miss}$ represents the momentum that the initial nucleon had inside the target nucleus, while the missing energy allows us to specify its binding energy. This supports the view that with the (e,e'p) reaction, we map out the momentum distributions of individual nucleons coming from a particular single-particle state inside nuclei, selected by adjusting the missing energy.

In non-relativistic PWIA, the cross section can be factorized as [Fru84, Vig04]

$$\frac{d^6\sigma}{dE_f d\Omega_e dE_p d\Omega_p} = R \cdot K \cdot \sigma_{ep} \cdot S\left(E_{miss}, \left|\vec{p}_{miss}\right|\right) \tag{1.24}$$

where $K \equiv E_p p_p$, R is the recoil factor and σ_{ep} is the single nucleon off-shell cross section [For83], and $S(E_{miss}, |\vec{p}_{miss}|)$ is the *spectral function*, which can be written as

$$S(E_{miss},\ |\vec{p}_{miss}|)\ =\ \rho(|\vec{\mathrm{p}}_{\mathrm{miss}}|)\cdot\delta(E_a\ -\ E_{miss}) \qquad (1.25)$$

Here $\rho(|\vec{\mathrm{p}}_{\mathrm{miss}}|)$ is the proton momentum distribution, and E_a is the binding energy for shell "a"; that is, for the single-particle state whose energy is compatible with the missing energy constraints of the experiment. Therefore, the spectral function $S(E_{miss},|\vec{p}_{miss}|)$ can be interpreted as the probability of finding a proton with initial momentum $|\vec{p}_{miss}|$ and binding energy E_{miss} inside the initial nucleus. Within the factorization approach, we can map out the spectral function independently of the electron kinematics, as all direct dependence of the cross section on the electron kinematics appears as simple factors. One must bear in mind that factorization, as expressed in Eq. (1.24), is not fulfilled in Nature. In general, *FSI* introduce a dependency on the electron kinematics beyond the one introduced in Eq. (1.24). General conditions needed to recover factorized result were reviewed in [Vig04]. It should be emphasized that within relativistic approaches, factorization does not hold even in *PWIA*.

If a spectral function is to be derived from experimental cross section data, one needs to compute values for the elementary electron-nucleon cross section. Most often, the σ_{cc1} prescription of DeForest [For83] is used for the single nucleon off-shell cross section. This prescription is a current conserving off-shell extrapolation of the on-shell nucleon current, obtained from the Dirac equation for relativistic scattering interactions. This prescription includes explicitly the four-momentum transfer in the nucleon current calculation; further details are given in [For83]. For quasielastic kinematics, as the ones considered in this work, most prescriptions for the elementary electron-nucleon cross section are within few percent, thus this is not a main source of uncertainty.

- **Distorted Wave Impulse Approximation**

In the *Distorted Wave Impulse Approximation* (DWIA), the IA is assumed, but in contrast to the PWIA, the interaction between the knocked-out proton and the residual nucleus is taken into account. Figure 1.5 presents a diagram for the DWIA.

Due to FSI, a factorization such as the one given in Eq. (1.24) may not be achieved, as FSI are different for nucleons knocked out with large or small momentum, even if the missing momentum and missing energy values are identical.

A *distorted spectral function* or *reduced cross section* is often defined according to

$$\frac{d^5\sigma}{d\omega d\Omega_e d\Omega_p} = R \cdot K \cdot \sigma_{ep} \cdot S^D\left(E_{miss}, \vec{p}_{miss}, \left|\vec{p}_p\right|\right) \tag{1.26}$$

As a definition, Eq. (1.26) is of course always valid, but the distorted spectral function $S^D\left(E_{miss}, \vec{p}_{miss}, \left|\vec{p}_p\right|\right)$ derived from data using Eq. (1.26) will depend upon the proton momentum $\left|\vec{p}_p\right|$ and the angle between the initial and final proton momenta, whereas the (undistorted) spectral function depends only on E_{miss} and $|\vec{p}_{miss}|$.

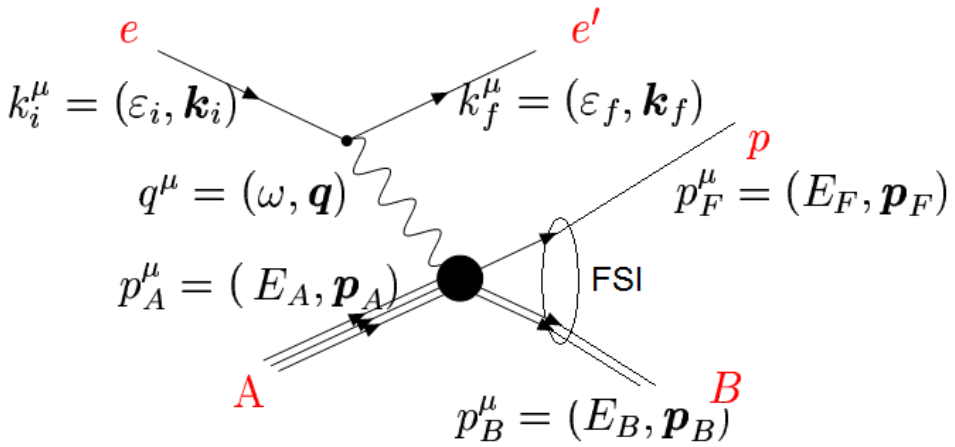

Figure 1.5: Distorted Wave Impulse Approximation in (e,e'p).

1.5.2. Coulomb Distortion

The Coulomb distortion of electron wave functions is sizeable effect for medium and heavy nuclei. Although it involves lengthy calculations, it is in principle under control [Yen65, Jin93, Kim97, Udi93, Kno74] but unfortunately invalidates the electron/nuclear separation and further breaks factorization. However, for large electron energies and especially for reasonably light targets such as carbon and oxygen, the dominant effect of Coulomb distortion upon the electron wave functions can be described using the *Effective Momentum Approximation* (EMA) to the electron Coulomb distortion [Kno74, Tra01, Bof96, Udi93, Kim96, Kim97, Jin93, Qui88, Kel97]. In this approximation, the asymptotic electron momentum $\vec{k}$ is replaced by $\vec{k}_{eff}$ to account for the acceleration of the electron by the mean electrostatic potential. Other than changing the effective momentum, all plane-wave expressions derived for the electrons are valid. The effective momentum can be estimated from expressions such as

$$\vec{k}_{eff} = \vec{k} + \frac{3\alpha Z}{2R_Z}\frac{\vec{k}}{\left|\vec{k}\right|} \tag{1.27}$$

Here, R_Z is the nuclear radius determined by assuming the nucleus as a uniformly charged sphere.

This yields an effective momentum transfer [Jin93] given by.

$$\vec{q}_{eff} = \vec{q} + \frac{3\alpha Z}{2R_Z E_i}\left(\vec{q} - \omega\frac{\vec{k}_f}{\left|\vec{k}_f\right|}\right) \quad (1.28)$$

However, comparisons with positron/electron data and studies of (e,e'p) on heavy nuclei made by several authors [Qui88, Udi93, Udi93b] have shown that this yields too much correction. Indeed, considering the nucleus as a hard sphere yields a Coulomb potential that is too large. Much better agreement with data has been found using full calculations that include the electron Coulomb distortion by substituting the potential of a hard charged sphere by the average value of the Coulomb potential for the nucleus of interest, computed from the experimental charge distribution.

For a light or medium nucleus like ^{208}Pb, Coulomb distortion has a significant effect as shown in [Udi93, Udi93b, Her05, Kim97]. Nevertheless, for the high beam energies considered in this thesis, the effect is small and it has not been considered in the simulations.

1.5.3. Mean Field and Correlations

In a mean field picture, nuclei are described as independent particles interacting only through the average mean field potential created by the other nucleons. In this scheme, nucleons occupy specific states (or orbits), that are bound solutions of the mean field potential. The many body function for the whole system is an (antisymmetrized) product of A of these single-particle states. This somewhat oversimplified picture is, however, quite successful in explaining general properties of A>4 nuclei. This independent-particle shell model (IPSM) describes several basic properties of atomic nuclei. For example, the observed clustering of energy levels for protons (neutrons) in groups of closely-spaced energy levels, the so-called shell structure of the nucleus. Under this approximation, the probability of finding a nucleon in the target system with a given momentum and binding energy will be zero if this binding energy does not coincide with any of the single particle energies occupied in the nucleus. The IPSM is known to be a good approximation to describe closed-shell nuclei, as ^{12}C, ^{16}O and ^{208}Pb studied in this work.

The (e,e'p) cross section, in general, samples the overlap of the initial and final nuclear system, which has a very simple expression in the IPSM. Thus, when the energy sampled in the (e,e'p) experiment coincides with removal of a nucleon in a single-particle state, then the removal probability will be proportional to the number of nucleons in that orbit and to the momentum distribution characteristic of that orbit, that is, in this extreme picture, the

modulus of the wave function in momentum space, $|\Psi(p)|^2$ for the orbit from which the nucleon was removed. Thus, within the mean field approximation, together with the Impulse Approximation, neglecting final state interactions and in a factorized approach, the reduced cross section introduced in Eq. (1.26) is a direct measure of the nucleon wave function corresponding to the adequate orbit, in momentum space. The magnitude of the cross section will also be proportional to the number of nucleons in the selected shell.

However, the IPSM model ignores the residual nucleon-nucleon (N-N) interactions, Although this approach is incomplete, the model produces wave functions for individual protons that reasonably match the momentum distributions derived from (e,e'p) experiments [Lap93].

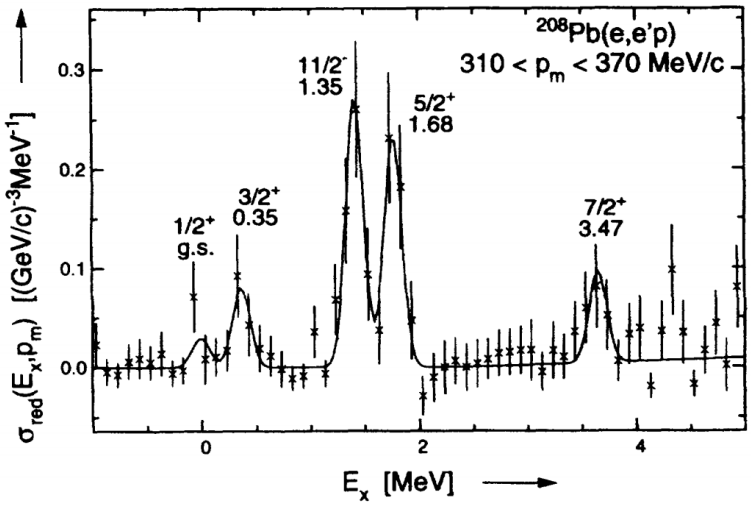

Figure 1.6: Experimental reduced cross sections obtained in a $^{208}Pb(e,e'p)^{207}Tl$ experiment performed at NIKHEF-K [Bob94]. Peaks corresponding to knock out of protons from particular outermost states in ^{208}Pb are clearly seen.

Effects beyond mean field, such as correlations, break the IPSM picture in several ways. In the one side, the nuclear many body wave function would no longer be a simple product of single-particle states and the excitation (or E_{miss}) energy spectrum will not consist of a series of delta functions at the single-particle energies, but rather a series of finite width peaks (at least for the valence shells). Further, the overlap of the initial and final nuclear systems sampled in a narrow excitation energy range by the (e,e'p) experiment, will miss part of the nucleons that would contribute to that overlap. All these effects are explained in more detail in Chapter 2.

1.6. Results from Previous (e,e'p) Experiments on ^{16}O, ^{12}C and ^{208}Pb

1.6.1. Previous $^{16}O(e,e'p)$ experiments

^{16}O is a doubly-magic, closed-shell nucleus. Its bound-state wave function is relatively easy to calculate. As proton elastic scattering from ^{16}O has been studied over a wide range of kinematics, the final-state interaction for $^{16}O(e,e'p)$ reaction is generally well understood. Therefore, one can derive good predictions for both cross sections and response functions. This makes ^{16}O a very good candidate for the study of the reaction mechanism for proton knockout.

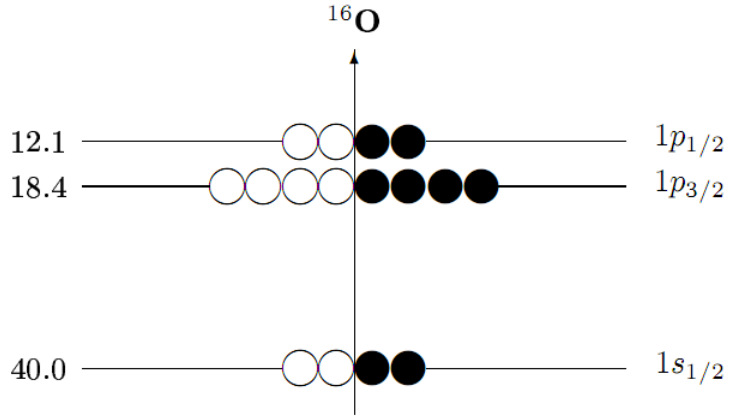

Figure 1.7: Shell model for ^{16}O (energy levels not to scale).The numbers on the left are the separation energies in MeV.

Quasielastic $^{16}O(e,e'p)$ experiments have been previously performed at NIKHEF, Saclay, MAMI and JLAB in various kinematics. A summary of these experiments is presented in

Table 1.2.

SITE	KINEMATICS	Q^2 (GeV/c)^2	T_p (MeV)	REFERENCE
NIKHEF	PARALLEL	0.1-0.4	96	Leuschner, M. et al. [Leu94]
NIKHEF	PERPEND.	0.20	84	Spaltro, C.M. et al. [Spa93]
SACLAY	PERPEND.	0.30	160	Chinitz, L. et al. [Chi91]
SACLAY	PERPEND.	0.19	100	Bernheim, M. et al. [Ber82]
MAMI	PARALLEL	0.08	92	Blomqvist, K.I. et al. [Blo95]
MAMI	VARIED	0.04-0.26	215	Blomqvist, K.I. et al. [Blo95]
JLAB	PERPEND.	0.80	427	Fissum, K.G. et al.[Fis04]

Table 1.2: Summary of previous $^{16}O(e,e'p)$ experiments

Before the E89-003 experiment that was performed in Hall A at JLAB during the summer of 1997, only $^{16}O(e,e'p)$ experiments with low and moderate Q^2 were carried out.

The former low Q^2 experiments provided tests for different optical potentials and helped to understand effects beyond standard non-relativistic DWIA. Some results obtained from these experiments are presented in Figure 1.8.

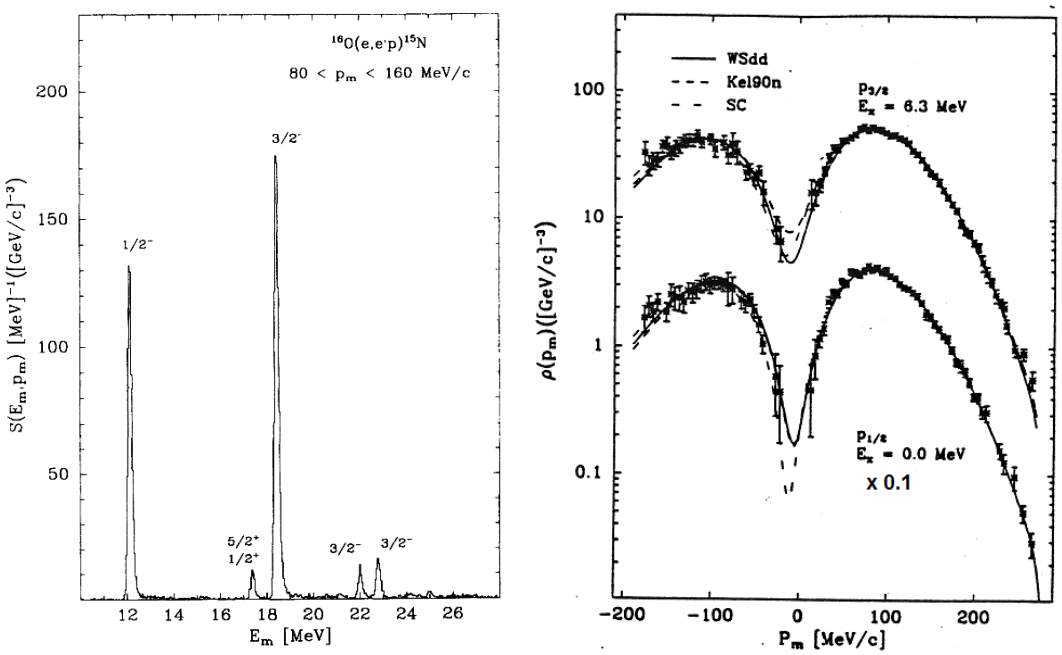

Figure 1.8: Missing-energy distribution (left panel) and missing-momentum distribution (right panel) from the ^{16}O(e,e'p) reaction in parallel kinematics measured at NIKHEF-K [Leu94].

Figure 1.8 (left panel) shows an E_{miss} spectrum measured at NIKHEF-K [Leu94] for p_{miss} in the range [80,160] MeV/c. The spectrum is dominated by the two peaks at 12.1 MeV and 18.4 MeV, corresponding to proton knock-out from the $1p_{1/2}$ and $1p_{3/2}$ states shown in Figure 1.10. Due to the excellent energy resolution at NIKHEF-K the $1d_{5/2}$ and $2s_{1/2}$ doublet at 17.4 MeV, as well as a pair of 3/2- states at 22.0 and 22.8 MeV, were also distinguishable. These states are not explained in the extreme IPSM, but correspond to configuration mixing that fragments the pure mean-field orbits into several states. Prevalence of the IPSM in this nucleus is shown by the fact that 'pure IPSM hole states' have considerably more strength than other types. Figure 1.8 (right panel) shows the momentum distributions for protons in the $1p_{1/2}$ and $1p_{3/2}$ states for -180 < p_{miss} < 270 MeV/c and its comparison with the theoretical prediction. Note that the $1p_{1/2}$ distribution in this figure was multiplied by a 0.1 factor.

Response functions have also been extracted in these low-Q^2 kinematics, and Figure 1.9 shows a comparison of the measured transverse-longitudinal response function R_{TL} with a modern relativistic DWIA calculation [Udi99, Vig04] for 30 < p_{miss} < 190 MeV/c. The agreement between calculations and data improves with increasing Q^2. The top panel

corresponds to the knockout of a proton from the $1p_{1/2}$ state and the bottom panel corresponds to the knockout of a proton from the $1p_{3/2}$ state.

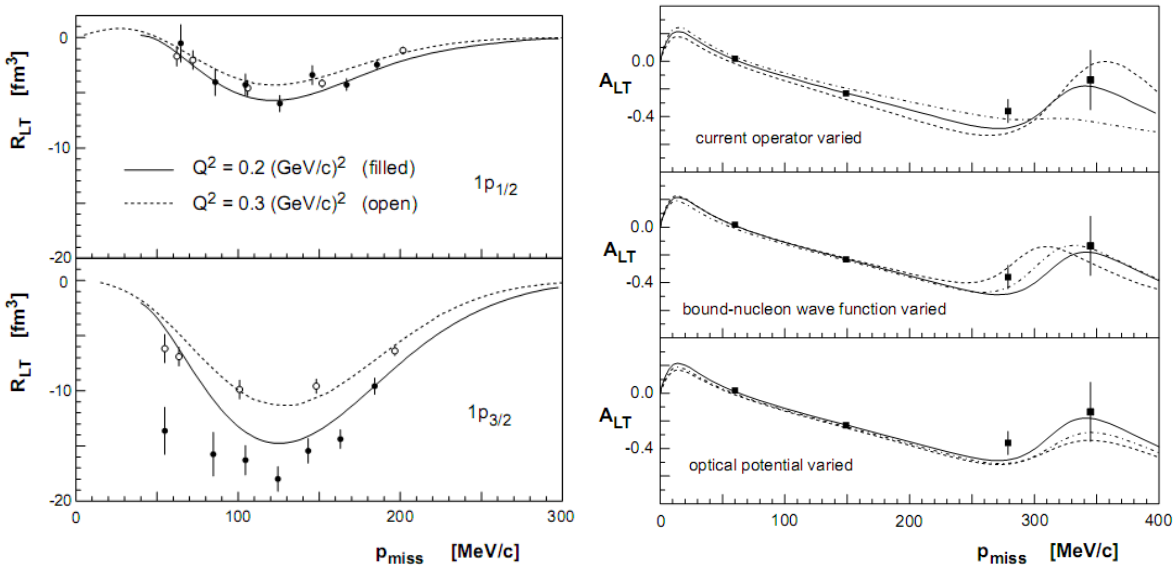

Figure 1.9: (Left panel) R_{TL} of $^{16}O(e,e'p)$ extracted at NIKHEF-K (filled circles)[Spa93] and Saclay (open circles) [Chi91]. The curves are modern relativistic DWIA calculations (presented in [Fis04]). (Right panel) A_{TL} calculations by Udías [Udi99] for the $p_{1/2}$ shell, compared with data from the experiment E89-003 [Gao00, Fis04].

In the summer of 1997, the precursor to the $^{16}O(e,e'p)$ experiment analyzed in this thesis was performed in Hall A at JLAB. As mentioned, it received the name E89-003 [Gao00, Liy01, Fis04]. Quasielastic kinematics were employed at Q^2 = 0.802 (GeV/c)^2, $|q|$ = 1.000 GeV/c and ω = 445 MeV. Data were obtained for the p-shell, the $s_{1/2}$ state and even higher energies for $E_{miss} \leq 120$ MeV and $p_{miss} \leq 375$ MeV/c.

The results for A_{TL} are shown in Figure 1.9 (right panel). The top pad shows the effect of varying the current operator, the middle pad shows the effect of varying the bound-nucleon wave function and the bottom pad shows the effect of varying the optical potential. More data are clearly needed at higher p_{miss} to allow the bound-nucleon wave function, the current operator and the optical potential to be determined independently.

One must keep in mind that the non-relativistic calculation for R_{TL} was ruled out by the experimental data. This can be seen in Figure 1.10, where NIKHEF-K results [Chi91] (set (b)) and Saclay results [Spa93] (set(c)) are compared to the non-relativistic calculation (with dotted red line), showing poor agreement with the data for the $p_{3/2}$ shell. On the other hand, relativistic calculations performed by Udías [Udi01] are in fair agreement for the two shells and experiments. This illustrates the sensitivity of TL observables (response and

asymmetry) to whether or not the calculation is relativistic or non-relativistic.

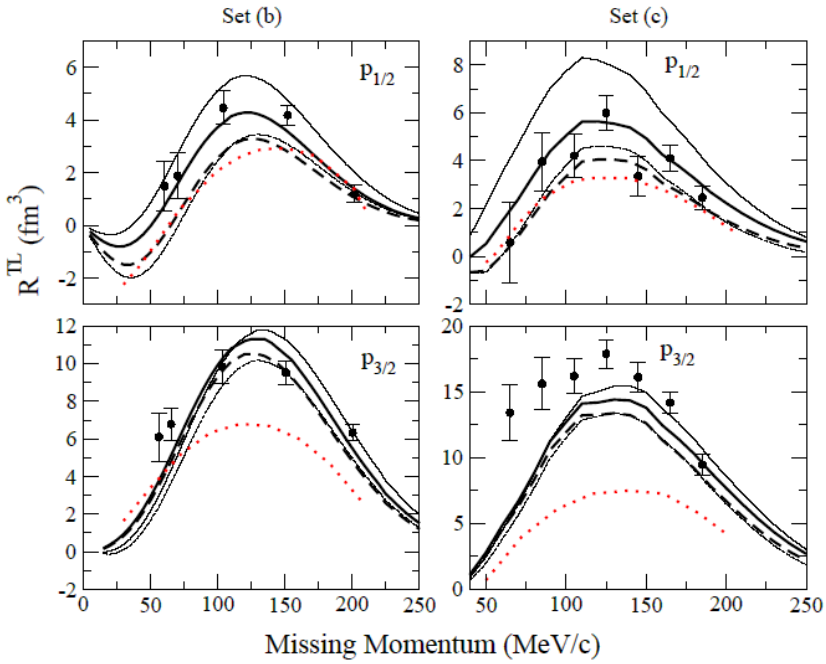

Figure 1.10: R_{TL} for ^{16}O(e,e'p) from Saclay (Set b, [Chi91]) and NIKHEF-K (Set c, [Spa93]) compared to non-relativistic (dotted red line) and relativistic calculations (black lines) [Udi01].

These results motivated the proposal of a new ^{16}O(e,e'p) experiment at JLAB which aimed for much better statistical precision than the E89-003 and included measurements at higher p_{miss}.

1.6.2. Previous ^{12}C(e,e'p) experiments

^{12}C has been previously studied in several experiments (Table 1.3) and in principle is well understood. Proton elastic scattering from ^{12}C has been performed over a wide range of kinematics and this yields abundant information to be used in determining the final state interaction for the ^{12}C(e,e'p) reaction. Therefore, one can derive good predictions for both cross sections and response functions. This makes ^{12}C also a good candidate for the study of the reaction mechanism for proton knockout.

Quasielastic ^{12}C(e,e'p) experiments have been previously performed at Tokyo, Saclay, NIKHEF, SLAC, Bates and JLAB in various kinematics. A summary of these experiments is presented in Table 1.3.

SITE	KINEMATICS	Q^2 $(GeV/c)^2$	CENTRAL T_p (MeV)	REFERENCE
TOKYO	PERPEND.	0.29	159	Kenzo, N. et al. [Ken76]
SACLAY	PERPEND.	0.16	87	Mougey, J. et al. [Mou76]
		0.18	99	
SACLAY	PARALLEL	0.09-0.32	99	Bernheim, M. et al. [Ber82]
NIKHEF	PARALLEL	0.02-0.26	70	Steenhoven, G. et al. [Ste88]
SLAC	PERPEND.	1.11	600	Makins, N.C.R. et al. [Mak94]
BATES	PARALLEL	0.15	60-120	Ulmer, P.E. et al. [Ulm87]
BATES	PARALLEL	0.30-0.58	200-300	Weinstein, L.B.et al. [Wei90]
BATES	PARALLEL	0.75	518	Morrison, J.H. [Mor99]
		0.83	457	
JLAB	PERPEND.	0.64	350	Dutta, D. et al. [Dut03]
		1.28	700	
		1.84	970	
JLAB	PERPEND.	1.84	750	Monhaghan, P. [Mon08]
TOHOKU	PERPEND.	0.007	42	Tamae T. et al. [Tam09]

Table 1.3: Summary of previous $^{12}C(e,e'p)$ experiments.

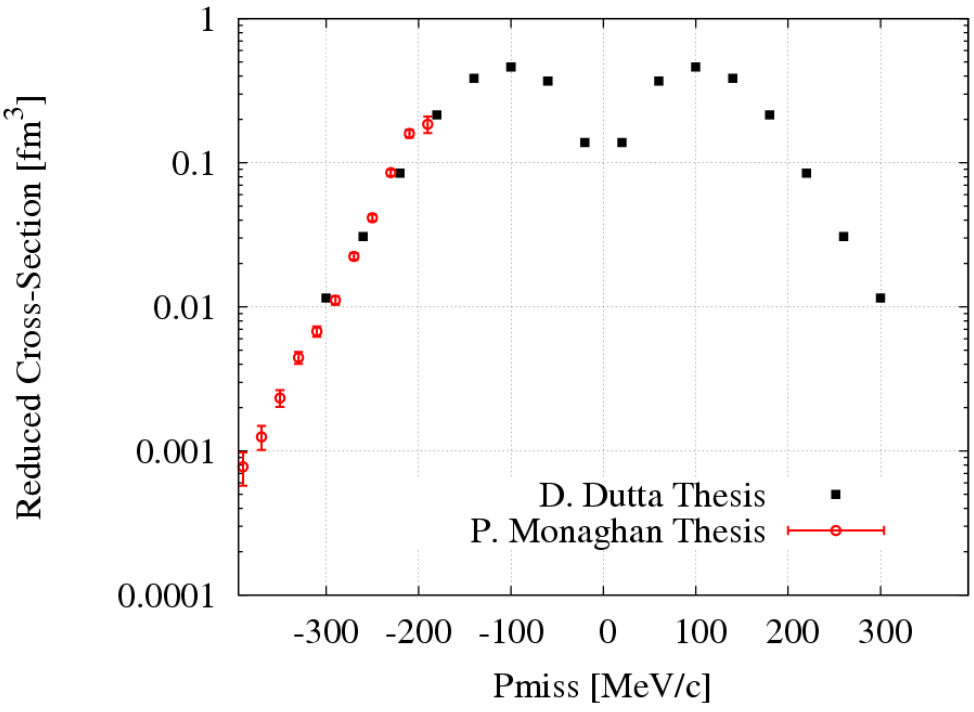

Figure 1.11: $^{12}C(e,e'p)$ reduced cross section for the $1p_{3/2}$ shell obtained in previous experiments performed at JLAB [Dut03, Mon08].

Nevertheless, recent theoretical reinterpretation of some of these experiments [Lap00, Fra01] claimed that there may be a dependence of the spectroscopic factors with Q^2. As this would imply a serious modification of either the standard view of the reaction mechanism based upon the IA, or of our definition and interpretation of spectroscopic factors, this analysis raised the need for more experiments to investigate in detail the possible Q^2 dependence of the spectroscopic factors.

One of the problems with the reanalysis of the experiments performed in [Lap00, Fra01] is that data at different Q^2 from experiments at different facilities were used. To address this, the Q^2 dependence of the spectroscopic factors is now being studied in new experiments performed at the same facility with the same targets and detectors spanning different Q^2 values [Dut03]. In these experiments, no Q^2 dependence of the spectroscopic factors was found. In this thesis, a further negative result for this search for Q^2 dependence is presented.

1.6.3. Previous ^{208}Pb(e,e'p) experiments

The atomic nucleus is often considered a dense system of fermions whose motion to first order can be treated as independent particles moving in a mean field. The ^{208}Pb nucleus is a textbook example of a mean-field theory friendly nucleus. This nucleus has been studied in the past at NIKHEF-K [Qui88, Bob94] and Saclay [Med99] using the (e,e'p) reaction.

SITE	KINEMATICS	Q^2 (GeV/c)^2	T_p (MeV)	REFERENCE
NIKHEF	PARALLEL	0.1-0.4	100	Quint, E. [Qui88]
NIKHEF	PERPEND.	0.037	100	Bobeldijk, I. [Bob94][Bob95]
NIKHEF	PARALLEL	0.26-0.49	161	Van Batenburg, M. [Bat01]
SACLAY	PERPEND.	0.55	161	Medaglia R. [Med99]
		0.70	263	

Table 1.4: Previous ^{208}Pb(e,e'p) experiments

In these measurements, spectroscopic factors for the valence states displayed in Table 1.5 were obtained for missing momenta less than 300 MeV/c, (save for the I. Bobeldijk et al. [Bob94] results). Some of these states are schematically shown in Figure 1.12. and a experimental E_{miss} spectrum from NIKHEF is displayed in Figure 1.6.

SHELL	E_x (MeV)	$E_{miss} = S_p + E_x$ (MeV)	Spec. Factor
$3s_{1/2}$	0.000	8.008	0.70
$2d_{3/2}$	0.351	8.359	0.73
$1h_{11/2}$	1.348	9.356	0.60
$2d_{5/2}$	1.683	9.691	0.63
$1g_{7/2}$	3.470	11.478	0.30

Table 1.5: Valence states in ^{208}Pb together with the spectroscopic factors obtained from the comparison of the relativistic DWIA predictions to NIKHEF-K data [Udi93, Udi96].

Results from these experiments have been analyzed within the IA with both non-relativistic and relativistic treatments [Udi93, Udi96]. Deviations from independent-particle motion for orbits near the Fermi energy are clearly present and are attributed to various correlations. Former works on this nucleus at high missing momentum, p_{miss} > 300MeV/c, [Bob94] attribute the excess strength in the cross section in this region as determined by the non-relativistic analysis, to long-range correlations. However, a relativistic analysis of the bound- and free-nucleon states shows no need to invoke long-range correlations [Udi96]. Instead, in the relativistic treatment of the (e,e'p) reaction, the spinor distortions of the lower component of the nucleon wave function account for the increased cross section seen at high missing momentum, in the case of the measurement of [Bob94]. In that experiment the measurement was done far from quasi-elastic conditions due to beam-energy limitations that cloud the interpretation using usual IA assumptions.

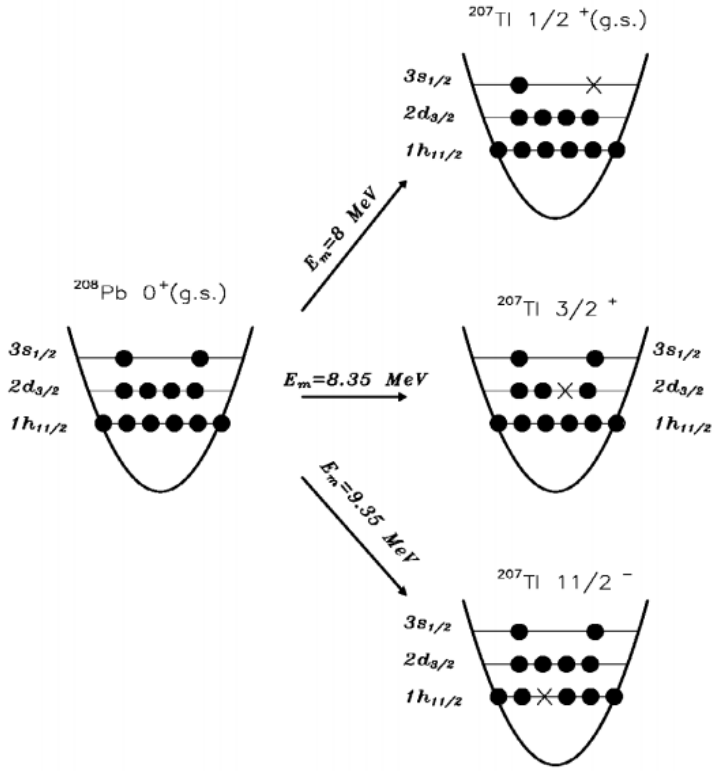

Figure 1.12: Diagram with some of the observed states in the ^{208}Pb(e,e'p)^{207}Tl. (Figure taken from [Udi93]).

1.7. Physics Motivation and Objectives of these Experiments

1.7.1. General Motivation

Exclusive (e,e'p) experiments allow for detailed study of properties of nucleons in nuclei and lepton-nucleus reaction mechanisms. Relativistic properties of the bound system are of interest in quantum field theory. Nuclei are a unique system for which binding energies have a magnitude comparable to the mass of the constituents, but not so large that the constituents themselves have lost their identity. Thus, binding effects are expected to modify the structure of the nucleons and of the lepton-nucleon coupling, as indeed some polarization transfer $(\vec{e},e'\vec{p})$ measurements in ^{4}He and ^{16}O [Stra03, Mal08, Die01] seem to indicate.

Note that in molecules and atoms, binding energies are so small compared to the mass of the electrons, that bound and free electrons can be treated in exactly the same manner, as an extreme non-relativistic picture suggests. At the other extreme, quarks bound in hadrons interact so strongly that they can no longer be treated as free quarks. It is thus clear that bound quarks have properties that are highly modified depending on the surrounding media. Nucleons in nuclei are in a very interesting intermediate regime. However, this makes it very difficult to develop consistent theories of possible medium modifications.

As a consistent and complete theory is lacking, experiments are used to fill the gap in our knowledge of the lepton-nucleon interaction for bound nucleons. This is of paramount interest for the many neutrino-nucleus experiments currently under way or in preparation [BooNE, KEK], aimed at detailed study of neutrino oscillations. The availability of models that can consistently predict both inclusive and exclusive electron-nucleus cross sections and that can also be applied also to neutrino-nucleus scattering will constitute an invaluable tool for the analysis of the experiments [Her09b, Her09c].

In this respect, it is worth mentioning the scaling approach to electron-nucleus reactions [Don88, Mai02] that leads to the superscaling approach to neutrino-nucleus scattering [Mar08, Her09b]. The superscaling approach allows the experimental body of electron-nucleus scattering data to be translated into predictions for neutrino-nucleus reactions. The detailed tests of nuclear-structure models, reaction mechanisms (to be incorporated into FSI for instance) and modification of the lepton-nucleon interaction inside the nucleus make the (e,e'p) reactions under exclusive conditions, where everything is under control, one of the most powerful experimental techniques available.

1.7.2. Experiment E00-102 - *(e,e'p) on ^{16}O*

The experiment E00-102 "*Testing the Limits of the Single-Particle Model in $^{16}O(e,e'p)$*" was performed in the fall of 2001 using a waterfall (H_2O) target to study the nuclear structure of ^{16}O. The Nuclear Physics Group of UCM took part in the preparation of the proposal and data taking and also contributed significantly to the data analysis. As the name of the proposal indicates, the main purpose of this experiment was to study the $^{16}O(e,e'p)$ reaction in quasielastic kinematics testing the limits of the Single-Particle Model. Indeed, The experiment E00-102 [Sah00] measured the $^{16}O(e,e'p)$ cross section with higher statistical precision and to much higher missing momentum and missing energy than did E89-003. Data were taken at p_{miss}< 350 MeV/c to statistically improve upon and compare with the existing data. Furthermore, data were also taken at p_{miss} > 350 MeV/c where no measurements had ever before been made. Both regions can be seen in Figure 1.13.

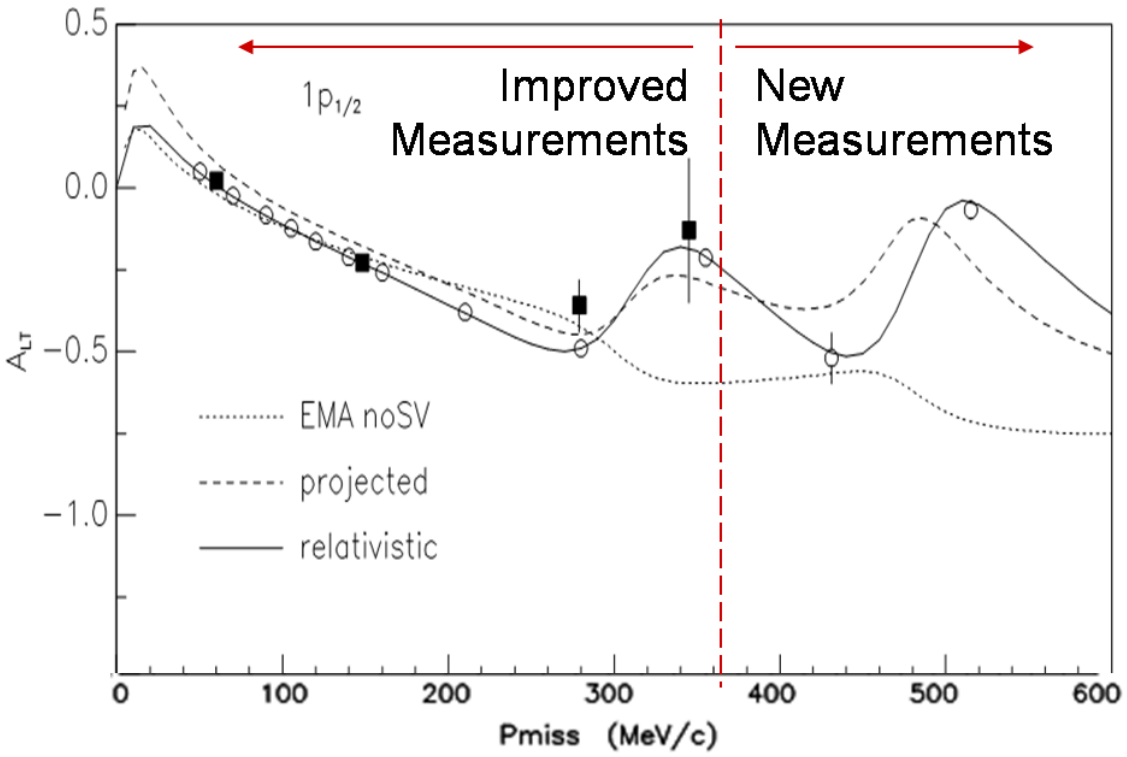

Figure 1.13: A_{TL} in $^{16}O(e,e'p)$ as a function of p_{miss}. Black squares represent the previous JLAB $^{16}O(e,e'p)$ experiment E89-003 [Gao99]. Lines and open circles show theoretical predictions and estimates of statistical uncertainty released prior to the experiment.

1.7.3. Experiment E06-007 - *(e,e'p) on* ^{208}Pb and ^{12}C

The experiment E06-007, "Impulse Approximation Limitations to the (e,e'p) on ^{208}Pb Identifying Correlations and Relativistic Effects in the Nuclear Medium" measured the reaction (e,e'p) on ^{208}Pb, ^{12}C and ^{209}Bi at x_B=1; that is, in quasielastic kinematics.

Both non-relativistic and relativistic treatments predict similar low missing momentum cross sections when they are scaled to data with the spectroscopic factor. Excess strength at high p_{miss} has been seen in a former experiment on ^{208}Pb. It can be attributed to long-range correlations in a non-relativistic scheme [Bob94]. Nevertheless, in the relativistic approach [Udi96] no additional effects beyond mean field are required, so the increase of the cross section at high missing momentum is attributed to relativistic effects. However, these conclusions were based on an experiment not performed in quasielastic kinematics, and thus effects beyond the IA could contribute and misguide the interpretation. New experiments at Q^2 large enough so the high missing momentum region can be explored in fully quasielastic kinematics will settle the issue of whether or not the momentum distribution obtained within a mean-field picture needs to be modified to explain the high missing-momentum data.

The asymmetry A_{TL}, which is accessible in unpolarized (e,e'p) reactions, is a relatively new and as yet little exploited observable for low-lying excited states. While it was not possible to measure this quantity at previous laboratories, yet an important effect of relativistic effects was predicted for this observable [Udi93]. The measurements reported in this thesis are the first ones to measure cross sections at negative p_{miss} (angles forward of the three momentum transfer) in ^{208}Pb. A_{TL} is sensitive to the theoretical approach (non-relativistic vs. relativistic) employed and then it is of primary interest.

As it was already mentioned, it has been claimed [Lap00, Fra01] from a reanalysis of several (e,e'p) experiments in ^{12}C at different momentum transfers that the spectroscopic factors measured in (e,e'p) reactions in exclusive conditions may display a momentum-transfer dependence. This dependence saturates at a Q^2 of around 1 (GeV/c)^2. Subsequent studies on ^{16}O including data from 0.2 to 0.8 (GeV/c)^2 did not find evidence for such Q^2 dependence (see for instance, [Udi01, Rad02]). The experiments in Hall A reported here can settle this issue since the cross sections for low p_{miss} at Q^2 between 0.81 to 1.97 (GeV/c)^2 can be accurately measured at the same facility and under similar conditions.

Therefore the objectives of this experiment were:

(I) Search for long-range correlation effects at high missing momentum.

a) Measure spectroscopic factors for states near the Fermi level.

b) Measure cross sections for these low lying states to 500 MeV/c in p_{miss}.

c) Search for any Q^2 dependence in the spectroscopic factors.

(II) Identify dynamical relativistic effects in nuclear structure.

a) Measure the cross section asymmetry A_{TL}. The relativistic mean-field model predicts an A_{TL} for p_{miss}< 300 MeV/c substantially different from the predictions of non-relativistic mean-field models due to dynamical enhancement of the lower component of the nucleon wave function. This effect in A_{TL} is more noticeable for (j=l-1/2) states [Cab98] like the $h_{11/2}$ shell in lead.

1.8. General Description of the Experimental Setup

The experimental setup for these experiments was of the conventional Hall A variety. The accelerator transported a continuous unpolarized electron beam with a current on the order of 50 μA to the target chamber. The experiments used the two High Resolution Spectrometers, one for detecting the scattered electrons and one for the ejected protons. A detailed description of the experimental setup in Hall A at Jefferson Lab is shown in Chapter 0.

1.8.1. Experiment E00-102

For this experiment, a beam energy of 4.620 GeV was used. The left HRS, set to detect electrons with a central momentum of k_f = 4.121 GeV/c, was fixed at 12.5° and was never moved. This determined the kinematical variables $|q|$ = 1.073 GeV/c, θ_q = 56.22°, ω = 0.499 GeV and hence Q^2 = 0.902 $(GeV/c)^2$ as shown in Figure 1.14.

The right HRS detected protons, had a central momentum set to p_p= 1.066 GeV/c and was positioned at different angles around q as shown in Figure 1.14. Kinematics with $\theta_p<\theta_q$ (in red) correspond to negative p_{miss} (referred to "minus" kinematics), those with $\theta_p>\theta_q$ (in green) correspond to positive p_{miss} (referred to "plus" kinematics) and $\theta_p=\theta_q$ (in blue) correspond to p_{miss}=0 (referred to "parallel" kinematics). Groundbreaking measurements performed at extreme positive p_{miss} are shown in purple.

Central values for all kinematics
E_i = 4.620 GeV
$\|q\|$ = 1.073 GeV/c
ω = 0.499 GeV
Q^2 = 0.902 (GeV/c)^2
θ_e = 12.5 deg. = 0.218 rad
k_f =4.121 GeV/c
T_p = 1.420 GeV

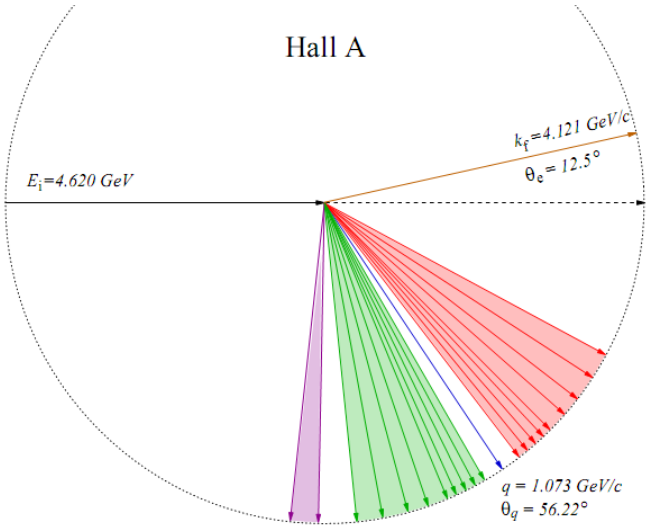

Figure 1.14: Kinematical settings for the experiment E00-102.

Figure 1.14 shows the kinematical setting of the experiment E00-102 ^{16}O(e,e'p) at JLAB. The 4.620 GeV electron beam entered Hall A from the left. The waterfall target was located inside the scattering chamber at the centre of the Hall.

The waterfall target was the same as the one used in the previous E89-003 experiment [Gao99]. It was composed of three foils with water continuously flowing. As the water was flowing there was no problem with overheating, so that rastered beam was not required. The presence of hydrogen in the target allowed for the H(e,e) and H(e,e'p) reactions to be used as a reference. A schematic view of the target configuration is shown in

Figure 1.15. A more detailed description is given in Section 4.5.1.

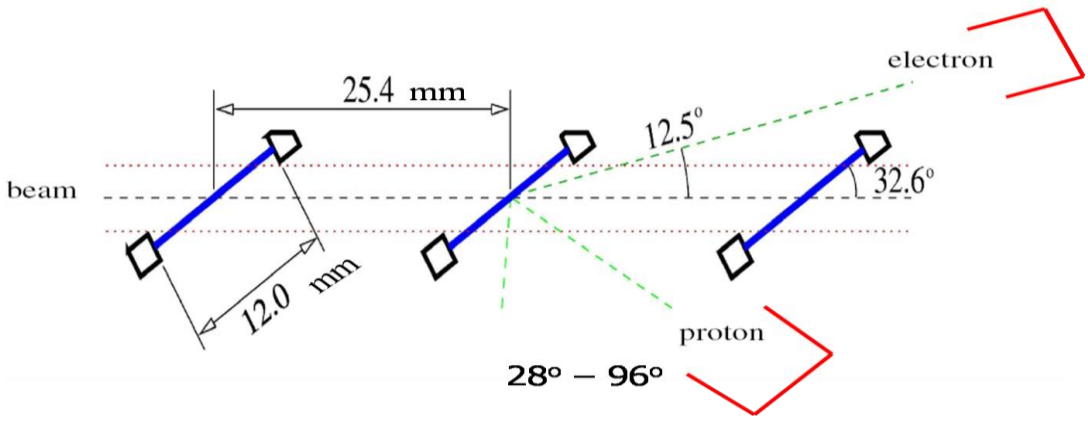

Figure 1.15: Schematic view of the waterfall target used in the experiment E00-102.

1.8.2. Experiment E06-007

The experimental setup was quite conventional in Hall A at JLAB. It used beam energy of 2.649 GeV. The left HRS was set to detect electrons with a central momentum of 2.216 GeV/c and was fixed at a scattering angle of 21.44°. This determined the kinematical variables $|q|$ = 1.000 GeV/c and ω = 0.433 GeV, and hence Q^2 = 0.81 (GeV/c)^2 as shown in Figure 1.16.

Central values for all kinematics
E_i = 2.649 GeV
$\|q\|$ = 1.000 GeV/c
ω = 0.433 GeV
Q^2 = 0.812 (GeV/c)^2
θ_e = 21.44 deg. = 0.3742 rad
k_f =2.216 GeV/c
T_p = 1.363GeV

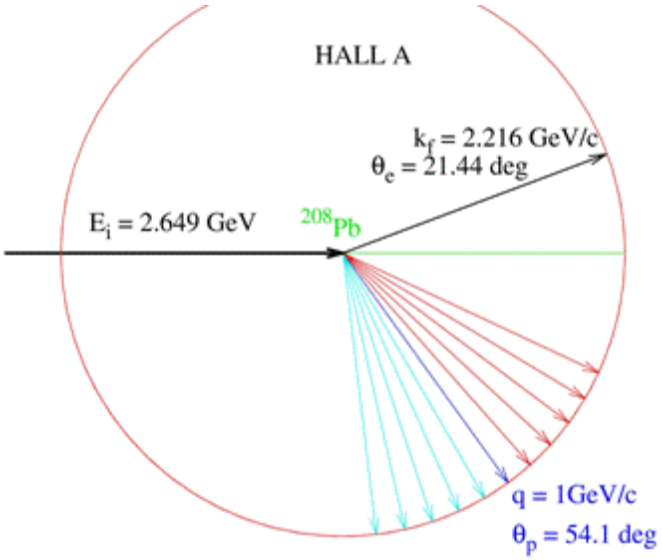

Figure 1.16: Fixed parameters for the experiment E06-007.

The right HRS was set with a central momentum of p_p= 1.066 GeV/c, and was positioned at different angles around q to measure p_{miss} in the range of [-500,500] MeV/c as shown in Fig. 1.19. The solid-target ladder contained several targets (^{12}C, ^{208}Pb, ^{209}Bi) and it was cooled, keeping the temperature below 30K at all times. A more detailed description of the target used in the experiment E06-007 is given in Section 4.5.2.

Additionally, some measurements at different Q^2 were performed on carbon and lead to study the possible dependence of the spectroscopic factors with Q^2. The kinematical settings for these special runs are shown in Table 1.6.

Kinematics	Q^2 [GeV/c]^2	q [GeV/c]	E_i [GeV]	ω [GeV]	E_f [GeV]	θ_e [degrees]	p_p [GeV]	θ_p [degrees]
Kin01	0.812	1.000	2.649	0.433	2.216	21.44	0.989	54.101
Kin12	1.40	1.400	2.649	0.745	1.904	30.60	1.388	43.816
Kin13	1.97	1.750	2.649	1.045	1.604	39.81	1.738	35.936

Table 1.6: Kinematics for the experiment E06-007 for the study of the Q^2-dependence of the spectroscopic factors.

2. Theory

It is not the goal of this chapter to give a full account of the theoretical developments regarding the analysis and interpretation of (e,e'p) reaction. These details have been discussed several times in the literature and previous works [Don86, Kel96, Udi93, Garr93, Fru84, Pic85, Wal06, Udi95]. Here, only the basics assumptions usually taken within the IA and the main features and theoretical ingredients used in this thesis are briefly described. The assumptions reviewed here are usually fully justified at the quasielastic kinematics of the experiments of this thesis. For instance, in this work it is assumed, as it is often done for the energies customarily involved, that the mass of the electron is negligible. Other assumptions are reviewed in what follows.

2.1. Single-Photon Approximation

Single-photon approximation allows for the neat separation of the leptonic and hadronic variables that enter into the process. As shown in Chapter 1, within this approximation, the dependence on the lepton kinematics can be easily identified. This assumption is generally sound, as the coupling of the leptonic probe to the nucleus is weak, as its strength is given by the structure constant α (approximately 1/137). However, under certain circumstances, double photon exchange may be an important correction. This is the case of Coulomb and radiative corrections, where the incoming and outcoming lepton exchange more photons than the one that actually is responsible of the nuclear transition for the reaction considered. As a summary, it can be said that the single-photon approximation for the lepton-nucleus interaction is generally valid, while radiative and Coulomb corrections must be considered as a technical nuisance that has to be included when comparing to actual experimental data.

2.2. Impulse Approximation (IA)

The IA assumes that the (single) photon exchanged interacts with only one nucleon, and that said nucleon is the one that is further detected in coincidence with the electron (see Figure 2.1). This assumption is reasonable in quasielastic conditions and if the wavelength of the exchanged photon is of the order of the nucleon size or less, that is, the energy transferred to the nucleus is 200 MeV or higher. Under these conditions, the most likely process is that the exchanged photon interacts with one single nucleon, transferring to it its energy and momentum and knocking it out of the nucleus. The remaining nucleons inside

the nucleus are considered as spectators.

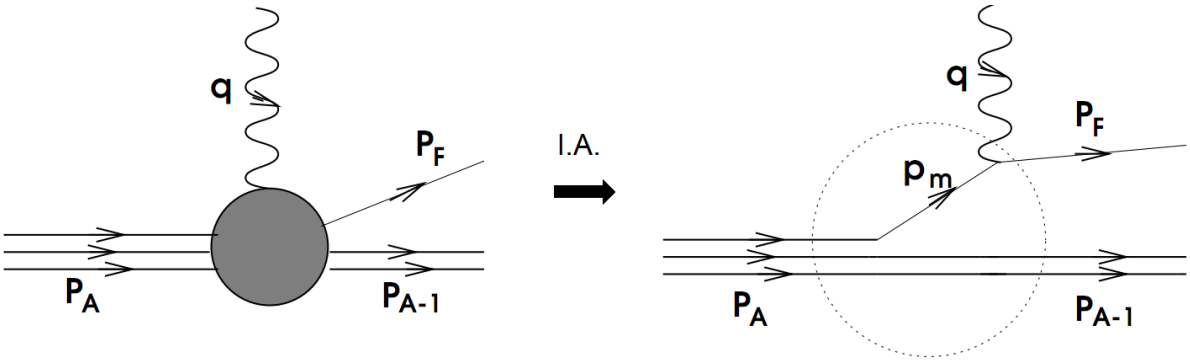

Figure 2.1: (e,e'p) reaction in first order Born Approximation and the Impulse Approximation (IA) picture. (Figure from Her09b).

The *direct diagram* considered in the IA requires a nucleon of moderate momentum (generally below the Fermi level) that receives a *direct hit* from the virtual exchanged photon and thus leaves the nucleus with the right momentum to be detected in the experiment (that is set for quasielastic kinematics). Under the usual kinematics conditions of (e,e'p) experiments, the knocked-out nucleon has a considerable momentum, typically above 400 MeV/c for older experiments at Mainz, Saclay and NIKHEF, and for the experiments analyzed in this thesis, around 1 GeV/c.

On the other hand, there is also a possible *exchanged diagram* where the detected nucleon is the spectator while the virtual exchanged photon is absorbed somewhere else in the nucleus. This *exchanged diagram* is proportional to the probability of finding a nucleon with rather high momentum in the target nucleus that gets removed from the nucleus due to excitations and break up induced by the virtual photon, but not due to having received the momentum from the virtual photon.

Apart from the small probability of this happening (a factor 1/A for this has been argued in [Fru84]), this exchanged diagram is clearly not favored because the probability of finding nucleons with high momentum in the target nuclei is orders of magnitude smaller than the one of finding them with low momentum. However, when studying kinematics where the experiment looks for initial nucleons with high momentum, one must be aware that the in this case the direct diagram may reach small values, and the exchanged diagram may eventually need to be inspected.

2.3. One-body operator

The IA naturally calls for considering the electromagnetic interaction of the lepton with the nuclear system as being described as a one-body operator. That is, the vertex at the nuclear side, that most generally will be an A-body operator *J(1,2, …..,A)*, can be simply written as a sum of the one body interactions as

$$\hat{J}(1,2,...A) = \sum_{i=1}^{A} \hat{j}(i) \tag{2.1}$$

Assuming the one-body structure of the interaction of the lepton with the nuclei, the interaction in the nuclear side can be factored out in easy-to-interpret ingredients. For the initial state, the initial nucleus is composed of A nucleons $|A,I\rangle$. In the final state, there are the A-1 nuclear system $|A-1,F\rangle$ and the knocked-out nucleon |N>. The matrix element representing the interaction at the nuclear side would then be

$$\langle A-1,F,N|\hat{J}(1,...,A)|A,I\rangle \tag{2.2}$$

The single-body plus impulse-approximation assumption (one may argue whether the IA implies the one-body approximation for the current too) lead to a factorization of the nuclear vertex as

$$\sum_i \langle N|\hat{j}(i)|\langle A-1,F|A,I\rangle \tag{2.3}$$

Two ingredients can be identified in this expression. First the *spectroscopic amplitude* or more properly *overlap integral* $|\Psi_{IF}\rangle = \langle A-1,F|A,I\rangle$. The interpretation of this quantity is easier in a single particle model, as it will be shown. It describes the overlap of the initial state *I* of the *A* particle target nucleus, usually in its ground state $|A,gs\rangle$, and the particular final state F of the residual system $|A-1,F\rangle$. Therefore, it represents the probability of finding an initial nucleon with the conditions set by the reaction, which selects the state F of the final system. In terms of this overlap, the matrix element is simply put as $\langle N|j|\Psi_{IF}\rangle$. This can be regarded as the matrix element connecting, via the interaction of the virtual photon, the knocked out nucleon with what can be seen as the wave function for the initial nucleon, or quasi-particle [Bro05] wave function Ψ_{IF}.

2.4. Beyond the Impulse Approximation

The described one-body operator approximation, fully consistent with the spirit of the IA, neglects Meson Exchange Currents (MEC). During MEC, the interaction of the virtual photon (or generally, the virtual vector boson of an electroweak interaction) may be affected by the presence of other nucleons, or the pion in flight that mediates the NN interaction [Dub76, Umi95, Umi95b].

Due to the high momentum of the virtual boson that is chosen for usual (e,e'p) kinematics, possible MEC contributions to the reaction should involve high momentum nucleons and therefore they will be much lower than the direct term considered for the IA. Furthermore, as MEC contributions are suppressed by a 1/A factor compared to the direct term, and for quasielastic kinematics their relative contribution decreases with increasing Q^2, they are not expected to be important for the kinematics and nuclei (with A>10) considered in this work. Actual calculations of MEC seem to confirm this fact [Dub76, Umi95, Umi95b, Ama10].

2.5. Mean field approximation

Complex nuclei are usually described using the mean-field picture, where nucleons are assumed to move independently of each other (aside from Pauli exclusion effects) in the nuclear mean field and are described as solutions of a single particle equation. Indeed, for independent particles, a product of *A* single-particle states, each of them solution of the single-particle equation with energies ε_i, is a solution of the *A*-body problem with total energy $E = \sum_i \varepsilon_i$. Being the nucleons identical particles, proper antisymmetrization of the wave functions requires that an antisymmetrized product (a Slater determinant) has to be used, instead of a simple product.

Under this mean-field approximation, the overlap integral can be easily computed as

$$\left|\Psi_{IF}\right\rangle \equiv \left\langle A-1,F\middle|A,I\right\rangle = \left|\Psi_a\right\rangle \qquad (2.4)$$

where "*a*" corresponds to the single-particle state from which the nucleon has been removed. Indeed, in the extreme mean-field picture, both the initial and the final nuclear systems are constructed from single-particle states of the same mean field, and thus the $\left|A-1,F\right\rangle$ system is just a particular *hole state* of the initial system. As it is possible to make holes (or remove nucleons) from different shell states, several possible final states of the $\left|A-1\right\rangle$ system could contribute to the reaction, and in general the residual system will not be in its ground state. The (e,e'p) reaction will map out the excitation energies of the residual system that can be reached by removal of one nucleon from the target nucleus.

One of the advantages of the (e,e'p) reaction, when performed under exclusive conditions, is that a particular state F of the residual system can be isolated or selected by setting the kinematics of the experiment for a particular excitation energy of the final nucleus. Experimental uncertainties cause that the excitation energies cannot be selected with arbitrary precision, so predictions for experimental (e,e'p) yields should include the contribution of all states that can be reached within the experimental range of excitation

energies. Nevertheless, in what follows, it will be assumed that the experiment can isolate the contribution of a individual final state, compatible with the removal of a nucleon from the single-particle level (or shell) *a*.

The *spectroscopic factor*, for a given shell under study *a*, is defined as the norm of the particular quasi-particle contribution to the overlap integral, that is, $S_a=<\Psi_a|\Psi_a>$ [Bro05]. In the mean-field model, this is simply the number of nucleons occupying the single-particle state *a* in the target nucleus. This is why it is very often said that the (e,e'p) reaction actually measures the *number of nucleons* in a given shell.

2.6. Relativistic Mean Field

The mean field used to compute the single-particle wave functions can be implemented both in a non-relativistic or relativistic fashion. The non-relativistic approach assumes a Schrödinger equation with central and spin-orbit term, and with other possible further interactions, such as spin-spin interactions. This has been employed for decades to describe nuclear structure and self-consistent solutions obtained within Hartree-Fock approaches with phenomenological NN interactions. It has proved to be quite successful in describing nuclear sizes, binding energies, single-particle levels and single-particle wave functions. These non-relativistic models actually produce momentum distributions that are in remarkably good agreement with the experimental data obtained from (e,e'p) reactions.

On the other hand, it is also possible to describe accurately the essential properties of nuclei in a relativistic picture, using self-consistent solutions of Dirac equations within either Hartree or Hartree-Fock approaches. In the relativistic approach, a lagrangian for nucleons, that incorporates the NN interaction obtained from effective single boson exchanges (with scalar, pseudoscalar and vector bosons) and whose properties are fitted to describe saturation properties of nuclear matter (binding energy and densities), is usually employed [Hor81, Ser86, Rein86]. This lagrangian can be solved in a self-consistent way to produce nuclear wave functions, densities and further relevant properties.

Both relativistic and non-relativistic phenomenological approaches to nuclear structure have been used for decades with very reasonable success and they were considered in this work equally valid to describe the nuclear initial states or the final state interaction of the knocked out nucleon with the residual system. There are very few observables that are, more or less arguably, really sensitive to the approach used to describe the nuclear

structure, being relativistic or not. The asymmetry A_{TL} measured in the (e,e'p) reactions is one of these few observables.

Mean-field parameters are often tuned to reproduce the observed experimental data. In non-relativistic approaches, the depth and the size of the Woods-Saxon potential employed as mean field are fine-tuned to reproduce the binding energy of the shell studied and the observed (e,e'p) cross-sections [Qui88, Lap93]. A similar procedure can be used in the relativistic case with the shape of the scalar and vector potentials (in contrast to the central plus spin-orbit terms used in the non-relativistic case).

In this work, cross-sections for ^{12}C, ^{16}O and ^{208}Pb nuclei are computed using single-particle wave functions from relativistic mean fields that are known to reproduce adequately previous (e,e'p) data for these nuclei. In ^{12}C the NLSH parameterization [Rein86], without further tuning, yields reasonable agreement with data [Kel05]. For ^{16}O, in Ref. [Udi01] this parameterization was slightly tuned in order to better reproduce former data in parallel kinematics taken at NIKHEF [Leu94] (yielding the NLSH-P parameterization). With the NLSH-P wave functions, ^{16}O(e,e'p) data from other experiments at Saclay and NIKHEF in perpendicular kinematics are also well described [Chi90, Spa92]. In the case of lead, the wave functions obtained with the HS parameterization of the relativistic lagrangian [Hor81] were used in this work. They yielded an excellent reproduction of the ^{208}Pb(e,e'p) data acquired in NIKHEF in parallel kinematics [Udi93, Udi95].

2.7. Spectroscopic Factors

For light systems (A<4), the overlap $\langle A-1|A\rangle$ between initial and final nuclear states sampled by the (e,e'p) reaction can be computed without resorting to the IPSM. Instead, a general many-body function is solved with a realistic NN interaction. For instance, the calculation of the ^{3}He(e,e'p)d reaction can be carried out to yield the cross section in terms of ^{3}He and deuteron wave functions that enter into the $\langle A-1|A\rangle$ overlap: <d|^{3}He>=Ψ_α(r). This overlap depends on the coordinates of the proton removed from ^{3}He which, within the IA, is the one that is detected [Alv03]. The (e,e'p) cross section is proportional to the *squared norm* of the overlap:

$$Z = \sum_\alpha \left(\int | < A-1 \mid A > dr \right)^2 \qquad (2.5)$$

In the IPSM, this overlap would coincide with a single-particle orbit and its norm will count the number of protons in said orbit [Udi93], that is, the norm of this overlap, *Z*, is the spectroscopic factor. The exact calculation of the overlap for light systems shows that the norm of the overlap is of the order of 70% of the IPSM value, that is, the value one would get by neglecting all correlations and computing it within the mean field.

For A>4 nuclei, it is often too complex to compute the overlap functions exactly. Thus, the IPSM is assumed and the (e,e'p) cross section is computed using the single-particle state corresponding to the *hole* made in the target nucleus. It is also assumed that all protons in the single-particle orbits within the binding energy range sampled by the experiment contribute to the cross section. The cross sections obtained are then compared to data. The theoretical cross sections must be rescaled to fit the data, and this scale factor yields information on the spectroscopic factors. It is remarkable that the shape of the cross sections so obtained compare quite well with the experimental data, as shown in Figure 2.2. For many nuclei, the scale factors needed are of the order of 60-70%, as shown in Figure 2.3.

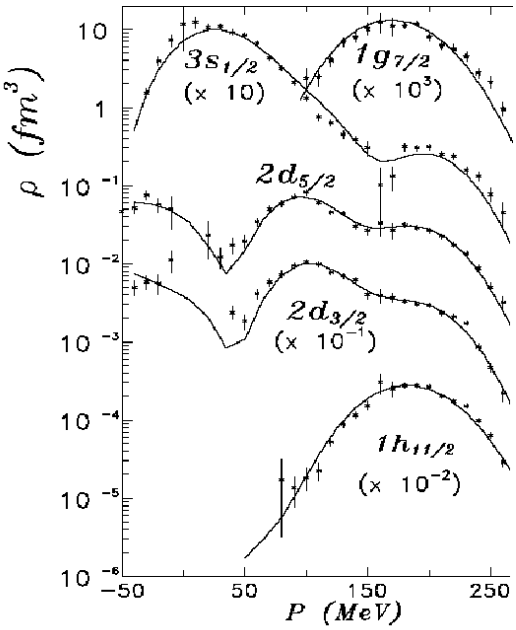

Figure 2.2: Reduced cross sections from a (e, e'p) experiment performed in ^{208}Pb at NIKHEF-K compared to the shell model predictions, scaled to data. Scale factors needed are of the order of 65%. Data from [Qui88]. Theory from Udias et al [Udi93].

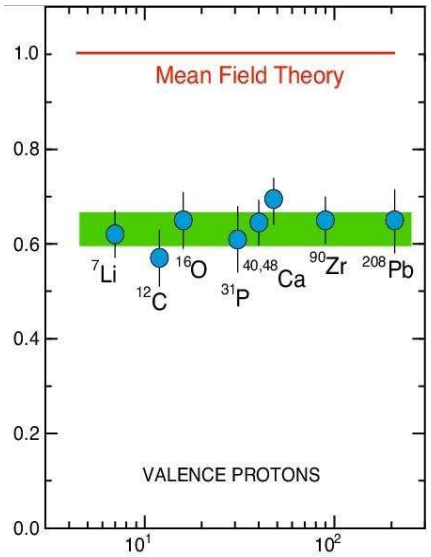

Figure 2.3: Spectroscopic factor from (e, e'p) experiments for valence shells of various nuclei. The observed values are only 60-70% of the shell model prediction, indicating that effects from N-N correlations are important. Figure from [Lap93].

2.8. Beyond mean field

While the bulk of nuclear structure and properties, especially for complex nuclei (A>8) can be understood within the mean-field approach, it is clear that nucleons are strongly correlated and that there are effects of these correlations that cannot be accounted for within single-particle models. Correlations put nucleons outside of their single-particle orbits. This causes that the spectroscopic factors for the dominant one-hole shell orbits

explored with the (e,e'p) reaction, are in general smaller than the ones that would correspond to pure mean field nuclear behavior. For instance, correlations that arise mainly between nucleons pairs, sometimes cause that the knock-out of one nucleon imply also the removal of its partner. In this case, the reaction drains more energy transfer, so part of the removal strength for that nucleon that in the mean field would appear at the particular single-particle missing energy, lies at higher missing energies. In many cases this makes that this strength is not seen in the experiment as the kinematical conditions are set to observe particular single-orbits.

The usual way of comparing theory to (e,e'p) experiments under exclusive conditions is to compute the mean-field prediction for the single-particle states seen in the experiment, assuming 100% spectroscopic factors, and scaling the predictions to the data. As discussed here, scale factors will be less than one (typically 60-70% as seen in Chapter 1) and the departure from unity yields an idea of the importance of correlations.

Effects beyond mean field not only deplete the spectroscopic factors of particular single-orbit shells from their 100% expected values within the mean field. Correlations also cause fragmentation of the spectroscopic strength into mixed configuration states, which cannot be interpreted as pure single-orbit states. This can be seen in the missing energy spectrum of ^{12}C or ^{16}O, where the $1p_{3/2}$ strength appears fragmented into several states, in the first case, or that additional states to p or s hole states can be seen in the second case [Ami97]. Furthermore, correlations cause that nucleons do not stay 'forever' in orbits compatible with mean field orbits. This makes the mean-field energy levels get a finite width.

In summary, effects beyond mean field [Mut94, Mut04, Mah87, Ma91]:

a) Deplete the spectroscopic factor of pure mean field orbits seen in the hole states of the target nuclei.

b) Fragment the strength of pure mean-field orbits into other complex configurations that should be understood only within configuration mixing.

c) Make the mean-filed energy levels get a finite width.

The strength not seen at the single-particle values of energy, would appear at higher or lower energies, not only in other discrete levels as discussed in b), but also as a continuous background, such as there is a chance of nucleons being removed from the target nuclei for almost any value of energy.

Thus, (e,e'p) reactions will not only provide information about the shell structure of nuclei, but also information about correlations. One long standing issue is actually disentangling the role of *short-range* and *long-range* correlations inside nuclei.

Short-range correlations are intuitively understood from the finite size of nucleons that cannot then be put arbitrarily close together and thus contravening *independent motion of nucleons*. These correlations will enter into play in the surroundings of each nucleon (then the name short-range) and thus their effect should be largely independent on nuclear size, at least for nucleons deep inside nucleus that will not see the nuclear surface. Therefore, the importance of these correlations can be estimated from infinite nuclear matter calculations, which thanks to translational invariance are amenable to solution. These calculations would imply that short-range correlations cause a depletion of no more than 15% in the spectroscopic factors [Pan84, Bob95, Bat01]. This is a very modest effect, which can only be understood taking into account that Pauli blocking effects, already considered in the mean field solutions, prevent nucleons from being too close and therefore, so short-range correlations are highly suppressed. From a different point of view, it can also be said that, even though nucleons could be scattered out of their mean field orbits due to nucleon-nucleon correlations, they can only go into unoccupied orbits due to the Pauli exclusion principle, and this is suppressed for deep shells due to the large difference in energy.

Conversely, correlations of long range also have a role inside nuclei. As a typical example, pairing correlations due to which nucleons tend to couple in pairs of zero angular momentum, may act quite irrespectively of the distance between the nucleons in the correlated pair. For these long-range correlations, surface and nuclear size effects are supposed to be important, and thus these are difficult to assess, though there are predictions for their effect in the literature on one side [Mah87], and on the other [Ma91].

Figure 2.4 shows the spectroscopic factors of ^{208}Pb measured at NIKHEF. For deep shells, where long range correlations are supposed to be highly suppressed, the spectroscopic strength seen in the experiment is of the order of 80% of the maximum (i.e., predicted by the mean field model). For valence shells close to the Fermi level, Pauli blocking is less effective and long range correlations are held responsible for additional depletion of the spectroscopic factors to 60-70% values.

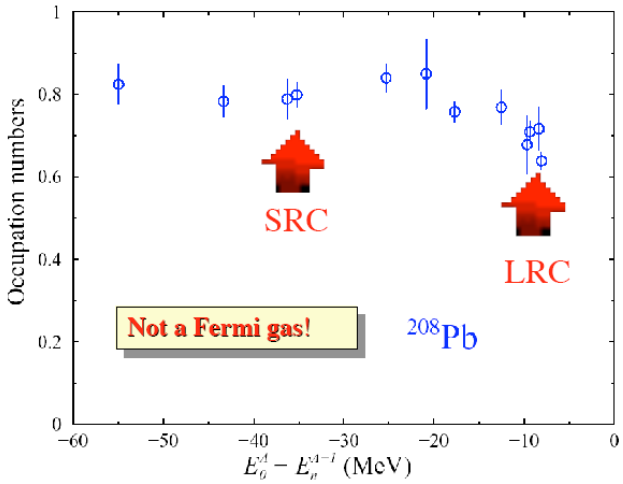

Figure 2.4: Spectroscopic strength measured with the (e,e'p) reaction in ^{208}Pb at NIKHEF-K (Figure from [Bat01]).

Indeed, it is generally assumed that it is the combined effect of short- and long-range correlations what causes the depletion of the spectroscopic factors near the Fermi level (that is, for valence shells) to the 60-70% of the full independent particle prediction. Further to the depletion of the spectroscopic factors, correlations might also have an effect on the shape of the momentum distribution. Indeed, short range correlations will enhance the chances of finding nucleons with high values of the momentum in the nucleus. However, for (e,e'p) reactions at quasielastic conditions, with focus in nucleons in shells near the Fermi level, this increase of the high momentum distribution is small [Ani06]. However, in a former experiment at NIKHEF-K [Bob94], an important increase of (e,e'p) events at high values of missing momentum (p_{miss} >300 MeV) was observed. Formerly this was attributed to long range correlations [Bob94] but also to relativistic effects [Udi96]. The fact that the experiment was performed quite far away from quasielastic kinematics, greatly difficult the interpretation of the results. At quasielastic kinematics, however, it has been shown that for quasielastic kinematics and Q^2 of the order of 1 (GeV/c)^2 [Ani06] that long range correlations, if they are responsible for the depletion of the spectroscopic factors to the 60-70% level, they will also change the shape of the missing momentum distribution at 350 MeV/c and higher, and under these conditions, this result will not be masked by relativistic effects.

Overall, the effect of long range correlations in exclusive (e,e'p) reactions is not clear neither from the theoretical or experimental point of view. With regard to the experimentally observed values of the spectroscopic factors of the order of 60-70% are in fair agreement with the only calculations of the overlap than can be done exactly, namely for very light

systems such as it is the case of the ^{3}He(e,e'p)d reaction. Exact (that is, not resorting to mean field approaches plus correlations within some model) theoretical calculations for the overlap for this case predict spectroscopic factor also of 60-70% [Alv03]. Further, in recent years, the role of tensor correlations in complex nuclear systems begins to draw attention [Schi02, Mon08].

2.9. Final State Interaction: Optical Potential

The matrix element in the calculation of the cross section involves the initial nucleon, the interaction with the photon, and the ejected nucleon. The initial part of the matrix element has already been discussed. For the final one, as it has been already discussed in the previous chapter, the interaction of the knocked-out nucleon with the residual system can be included in the DWIA. This means that the nucleon is assumed to interact by means of an average mean potential created by the residual system.

This (optical) potential is computed most often by fitting elastic proton nucleus cross sections either in a relativistic fashion [Coo93] or in a non-relativistic one [Blok85]. This potential must account for the propagation of the nucleon in its way out of the residual system. In its path, the nucleon can interact with other nucleons. For instance, it may exchange momentum and energy with other nucleon in a way that it is the second nucleon the one that is knocked out of the nucleus and further detected instead of the one that interacted with the photon. As said before, this is a process outside IA and that is suppressed due to the high momentum of the nucleon after its interaction with the photon. It is also possible that it can transfer only part of its energy to the residual system, excite the nucleus, excite a nucleon resonance, etc. In the case of an exclusive process, these excitations of the residual system will drain energy and thus increase the missing energy for such events. Thus, they can be identified and removed from the (e,e'p) data. This means that, apart from some coupled channels contributions that are usually small [Kel96] during the propagation of the knocked out nucleon, only the elastic channel has to be retained. This is why the optical potential fitted to elastic proton-nucleus scattering data is adequate to describe the motion of the final nucleon. This optical potential includes an imaginary term that precisely takes into account the 'absorption' of the nucleon or more accurately, the flux lost into inelastic channels excited by the nucleon in its way outside the nucleon.

In this work, relativistic optical potentials has been used, which means that the wave

function of the final nucleon is described as a solution of Dirac equation, with scalar (that is, which appears in Dirac equation modifying the mass) and vector (that is, that appears modifying the energy, or 0^{th} component of the 4-momentum of the particle) potentials. When fitting these potentials to elastic scattering data, simple shapes (Wood-Saxon or Fermi shape) are chosen and their parameters are determined with comparison to experimental data.

As the optical potentials fitted to elastic scattering do not fully constrain the (e,e'p) matrix elements, there remains some ambiguity or theoretical uncertainty introduced by the fact that different optical potentials, even if they yield similar agreement with elastic proton-nucleus scattering data, predict different (e,e'p) cross sections.

There have been identified differences between predictions of relativistic and non-relativistic (i.e., based upon the Schrodinger equation) optical potentials [Udi05] even when in both approaches they may fit elastic scattering data in a similar way. This is due to the fact that elastic scattering observables are only sensitive to the asymptotic behavior of the wave functions, while (e,e'p) matrix elements sample the very nuclear interior. The Darwin term, present in the relativistic case, reduces the effective density of the knocked-out nucleon in the nuclear interior, thus yielding smaller (e,e'p) cross sections in the relativistic case than in the non-relativistic one and thus implying larger values of the spectroscopic factors.

Furthermore, it has been seen that the choice a relativistic optical potential among the several parameterizations available, may introduce an ambiguity in the value of the spectroscopic factors, as the reduced cross-section at low values of the momentum transfer may change of the order of 15% [Udi01]. This happens even when, in general terms, it does not change the shape of the cross-section or A_{TL}, and the effects of the lower components of the spinors in the observables are the same with the different potentials.

However, for the values of nucleon momentum and nuclei (^{12}C, ^{16}O, ^{208}Pb) considered in this thesis, the several relativistic optical potentials available yield results in remarkably agreement with each other, so that the spectroscopic factors derived with different optical potentials are usually within 5% [Kel05, Fis04, Ani06]. Throughout this thesis, the EDAI parameterizations of B. Clark et al. either for ^{12}C (EDAI-C), ^{16}O (EDAI-O), and ^{208}Pb (EDAI-Pb) have been employed.

Appart from optical potentials, other microscopical approaches are also possible to

consider FSI. For instance, the relativistic folding approach are valid at the energies involved in this thesis. In the folding approach, the nuclear density is folded with an effective NN interaction, fitted to NN elastic scattering data, which, in the relativistic case, is parameterized as a sum of one boson exchanges [Lov81, Hor85]. This folding approach actually yields very good agreement to elastic proton scattering data from ^{16}O and ^{208}Pb.

Besides the purely phenomenological-based approach to FSI given by optical potentials, Glauber approaches together with the eikonal approximation [Cio05, Ryc03] are also employed. This is an appealing approach as it does not require input from experimental proton-nucleus scattering, only needs the Glauber NN interaction profiles taken from experimental NN scattering, The propagation of the nucleon through the remaining nucleons is computed from the series of NN collisions, which are described in the extreme forward-angle (eikonal) approximation. Thus, this approach in principle can be applied to every nuclei. For light systems [Jes99], it is arguably one of the most appropriate methods of dealing with FSI. However, for complex nuclei a full Glauber calculation, that would require integrating Glauber profiles over the 3A dimensions of the positions of the A nucleons, becomes impossible. Approximations are then possible (such as the thickness approximation as employed in Ghent's group calculations). The remaining nucleons with whom the propagating nucleon scatters are most often considered at rest (frozen nucleon approximation), although there have been also some calculations that remove this approximation and claim some effect may be seen of this in (e,e'p) reactions [Pet03].

A connection can be made between optical potential and Glauber approaches (see for instance [Nik96]) but most often the optical potential is not derived from Glauber schemes but rather, as previously described, from phenomenological fits to proton-nucleus scattering observables.

One has to have in mind that, even if the eikonal-Glauber approach has a strong conceptual appeal (as it would be able of describing FSI for any nuclei from a very modest phenomenological input) when it comes to reproducing the phenomenology in complex nuclei, a very small effect in the NN profiles might yield a large effect in the total Glauber amplitude of the whole nucleus (essentially a power of A of the profile). Thus, this approach fails to yield quantitative results [Lav04].

2.10. Factorization

The matrix element $\langle N|j|\Psi_{IF}\rangle$ introduced above (2.3) can be factorized (at least formally) in a simple way [Fru84, Vig04] by writing it as:

$$\int dP_2 \cdot dP_1 < N \mid P_2 >< P_2 \mid j \mid P_1 >< P_1 \mid \psi_{IF} > \quad (2.6)$$

This equation is read and interpreted in different ways in relativistic and non-relativistic languages.

- Non-relativistic - From this point of view [Fru84, Cio08], two closure expressions $\int dP \mid P >< P \mid = 1$ have been introduced, where $|P\rangle$ can be interpreted, in the non-relativistic case, as the wave function for a free (on-shell, positive energy only) nucleon. The integral may include the sum over spins and any other variables needed to span all possible states of the nucleon. Thus, the previous expression simply means that the matrix element needed to compute the (e,e'p) cross section can be written in terms of the overlap in momentum space (or as it is usually assumed, the momentum distribution for the initial nucleon) $< P_1 \mid \psi_{IF} >$, times a further term $< N \mid P_2 >$ that describes the propagation of the final nucleon through the residual system, and $< P_2|j|P_1 >$, that is the matrix element for the interaction of the exchanged boson with two free nucleons. This is the matrix element that would enter the elementary lepton-nucleon cross section σ_{ep}.

This formal factorization of the matrix element will not automatically lead to a factorization of the (e,e'p) cross section as the one introduced in Eqs. (1.24) and (1.25). This is due to the fact that, to obtain the (e,e'p) cross section, the above written matrix element must be squared and a sum on the third components of the angular momenta for the initial and final nucleons must be done. Within a plane-wave approach for the final state $< \mathrm{N} \mid \mathrm{P}_2 >= \delta(\mathrm{N},\mathrm{P}_2)$ and thus we are quite close to a factorized expression. The only requirement would be that the sum on third components of the angular momentum will not spoil the factorization in the cross section. Due to the spin-orbit coupling inherent to any nuclear single-particle state, this sum on angular components is in general different than the one for free nucleons, for which there is no spin-orbit coupling and thus orbital angular momentum is a good quantum number. Actually, it has been shown [Fru84, Cab89, Cab98b] that, due to the spin ½ of the nucleon, factorization is possible within PWIA, assuming only positive energy considered in previous expression, even if in the initial state there is spin-orbit coupling. What is more, it has been proved that within DWIA, if no spin-orbit coupling is introduced in the final state, factorization is still recovered under the same assumptions [Fru84]. Finally, in Ref. [Vig04] the conditions required to recover factorization

in the cross section starting from previous expressions were established. It was found that it is enough that no spin-orbit is present either in the initial or in the final state, or in both.

The term that represents the propagation of the nucleon in the final state, $< N \mid P_2 >$, in a diagrammatic view, contains a *direct term* that represents the cases when the nucleon does not interact, and a *scattering term* considering the cases when the nucleon interacts:

$$< \mathrm{N} \mid \mathrm{P}_2 >= \delta\left(\mathrm{N},\mathrm{P}_2\right) + \mathrm{S}\left(\mathrm{N},\mathrm{P}_2\right) \qquad (2.7)$$

The first term is the only considered within PWIA, and the second contributes in general. In light nuclei, the direct term dominates for low missing momentum, while the interference with the scattered term dominates when the direct term loses importance. The propagation of the nucleon in the final state is often computed within eikonal or eikonal-Glauber approaches, especially for light nuclei [Lav04] or with diagrammatical expansions [Lag85]. In the distorted wave approach, an 'exact' realization of <N|P2> in the presence of the residual nucleus is employed.

- Relativistic view - Within a relativistic view, the former expression for the factorized amplitude has to be read in a different way. In particular, the closure relationships must now include both *positive* and *negative* energy components [Vig04, Udi05]. In other words, it should include both 'u' spinors as well as 'v' negative energy spinors [Bjo64].

This has been at times misinterpreted as if 'negative energy' levels in the Dirac sea needed to be populated, but this is not the case. The energy of the nucleons considered is well defined and it is clearly a positive energy, in the sense that, asymptotically, the knocked out nucleon will be free and equal to a positive-energy (on the mass shell) detectable nucleon. On the other hand, bound nucleons are off the mass-shell just slightly, with a binding energy of the order of a few MeV, quite smaller than their rest mass.

In the presence of potentials, in the relativistic case, wave functions of both the bound nucleon and the knocked out one, are expanded into *free* (on the mass shell) solutions of Dirac equation which must necessarily involve positive and negative *free* (on the mass shell) solutions. Of course, the negative energy free solutions components of the wave function are fully absent in the free elementary electron-nucleon cross section that by its own definition, involves positive energy free wave functions to describe incident and outgoing nucleons.

In spite of these genuine dynamical effects (in the sense that without interactions there will not be negative energy content) that prevent exact factorization in the cross section in the relativistic view, the (e,e'p) cross section factorizes to a large extent, at least for

modest values of missing momentum at quasielastic kinematics (see Figure 2.5) [Udi01b]. It can be observed that, in the reduced cross sections for p_{miss} below 250 MeV/c, factorized results and the ones obtained within a fully unfactorized relativistic approach are very similar. This allows to maintain the interpretation of the *distorted momentum distributions* obtained from the data as giving an indication of the momentum distribution of the nucleons in the target nucleus, provided that this interpretation is not extended to very high values of missing momentum (>300 MeV/c) where only the fully unfactorized distorted calculation should be compared to data [Udi01b, Vig04b].

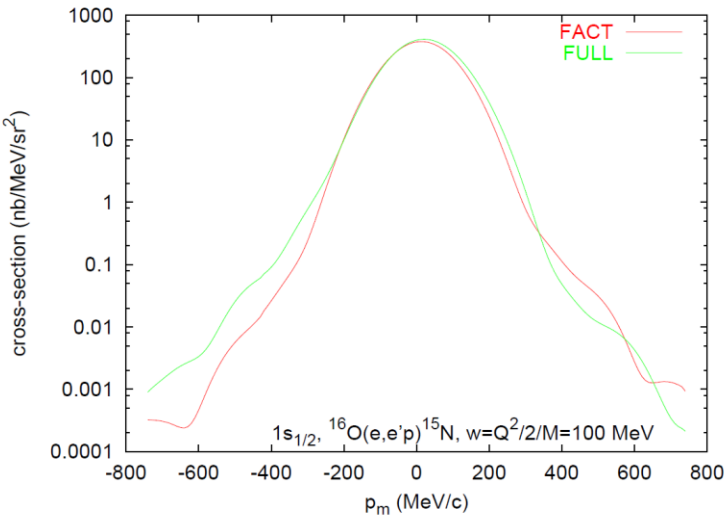

Figure 2.5: Reduced cross section in ^{16}O(e,e'p) with a factorized and a full calculation. (Fig. from [Udi01b]).

2.11. Negative energy components

Were if not for the negative energy components, one could actually built completely equivalent relativistic and non-relativistic models, provided the relativistic kinematics is fully included in the non-relativistic approaches. Otherwise, non-relativistic models would fail miserably [Ama96, Ama10].

The negative energy components or, equivalently, the fact that the nucleon wave functions for the bound and knocked out nucleons are off the mass shell, may have observable effects. Indeed, it has been shown that the A_{TL} asymmetry is very sensitive to any breakdown of factorization, either due to the negative energy components, the spin-orbit interaction, or to re-scattering effects. Indeed, as seen in the following figure, the factorized A_{TL} is clearly distinct from the one of interacting nucleons. In this figure it can be seen a behavior that is quite general for A_{TL}. At moderate p_{miss}, the direct term drives the

cross section than thus follows approximately the behavior of the free A_{TL}, apart from the negative (or off-shell) effects in A_{TL}. At larger values of p_{miss}, the direct term gets smaller and an oscillation in A_{TL} is seen, somewhere around 250-300 MeV, when the re-scattering term takes over the direct one. Thus, the region where the effect of negative energy components can be more conspicuous is for intermediate missing momentum, precisely where the cross sections peak and then good statistics can be obtained.

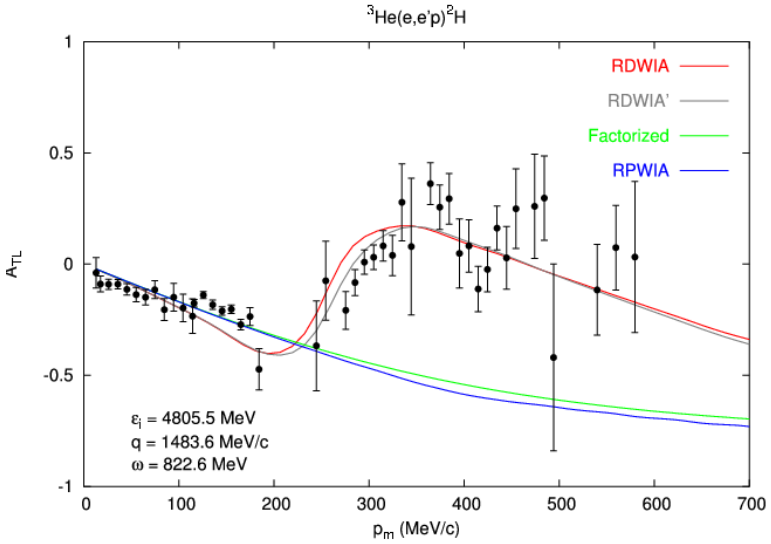

Figure 2.6: A_{TL} in ^{3}He(e,e'p) comparing factorized (green curve) and several non factorized calculations (Figure extracted from [Vig04b]).

In this region, differences between predictions of models with and without negative energy components are clear, particularly for *j=l-1/2* shells. This is a direct consequence of the relativistic model that has been predicted in [Cab01]. Indeed, the effect of negative energy components can be associated with the enhancement of the lower components due to the presence of the *S+V* potentials. The lower component of a solution of a free Dirac equation is of the form:

$$\psi_{down} = \frac{\vec{\sigma}\cdot\vec{p}}{\tilde{E}+\tilde{M}}\psi_{up} \qquad (2.8)$$

where due to the interaction, the denominator has effective values of mass and energy, $\tilde{M} = M + S,\ \tilde{E} = E + V$. With the usual values of the potentials, this means that the lower components of wave functions obtained from relativistic Dirac equation are twice as large as the ones for free (on shell) spinors. Actually, the effect of the negative energy components can be studied using, instead of the fully relativistic wave functions, wave functions built from on the mass shell spinors, for which the lower energy component is built from the upper one with an expression that involves the free values of *E* and *M*. The

spinors verify that their expected values of mass, energy and momentum verify $\left\langle \mathrm{M}^2 + \mathrm{P}^2 \right\rangle = \left\langle \mathrm{E}^2 \right\rangle$, provided *E*, *M* and *P* in former equation verify $E^2=M^2+P^2$. Comparing results with full and on-shell spinors (the latter giving predictions essentially similar to the non-relativistic ones) for A_{TL} with experimental data, will allow to assess the need of these dynamical off-shell effects to describe data. Use of these spinors is equivalent to the use of spinors obtained from the full ones applying positive energy projection operators [Udi05, Her05].

2.12. Off-shell ambiguity

The off-shell components of the wave functions have another effect. The Gordon transformation or Gordon decomposition that yields several (actually infinite) equivalent expressions to compute the matrix elements of free positive energy solutions of the free Dirac equation, is not longer valid. This is just a consequence of the fact that Gordon decomposition is derived using the free Dirac equation, while the spinors that solve a general equation with non-zero potential, will not, obviously, fulfil the free Dirac equation. The on-shell (or positive energy projected out) spinors introduced in previous paragraphs, however, can be shown to fulfil Gordon transformation.

Therefore, the several expressions of the current operator yield indistinguishable values for the elementary lepton-nucleon (free) cross sections, but yield different values when applied to off-shell wave functions.

From all possible forms of the current operator, three 'canonical forms' are more often employed, cc1, cc2, and cc3 [For83]:

$$
\begin{aligned}
CC1 \qquad & \overline{u}_f \cdot \Gamma^\mu \cdot u_i = \overline{u}_f \cdot \left[\left(F_1\left(q^2\right) + F_2\left(q^2\right) \right)\gamma^\mu - \frac{F_2\left(q^2\right)}{2M_p}\left(P_f + P_i\right)^\mu \right] \cdot u_i \\
CC2 \qquad & \overline{u}_f \cdot \Gamma^\mu \cdot u_i = \overline{u}_f \cdot \left[F_1\left(q^2\right)\gamma^\mu + i\frac{F_2\left(q^2\right)}{2M_p} \cdot q_\nu \cdot \sigma^{\mu\nu} \right] \cdot u_i \\
CC3 \qquad & \overline{u}_f \cdot \Gamma^\mu \cdot u_i = \overline{u}_f \cdot \left[\frac{F_2\left(q^2\right)}{2M_p}\left(P_f + P_i\right)^\mu + i\frac{2F_2\left(q^2\right)}{2M_p} \cdot q_\nu \cdot \sigma^{\mu\nu} \right] \cdot u_i
\end{aligned}
\tag{2.9}
$$

Where u are the positive energy spinors, and F_1 and F_2 the nucleon form factors.

Different (e,e'p) cross sections are obtained with these three operators. In the past, the differences between cc1 and cc2 have been taken as a measure of the *theoretical uncertainty* due to these off-shell ambiguities. It is important to remark that for on-shell nucleons the three prescriptions mentioned yield identical results. These on-shell results are very similar (within few percent in the derived spectroscopic factors, for instance) to the

ones obtained with the cc2 or cc3 prescriptions when applied to the full spinors. Therefore, it can be said that these prescriptions show a 'moderate' display of the nucleon off-shellness. On the other hand, the cc1 prescription, when applied to compute the matrix elements between the off-shell spinors usually encountered in this work, tend to give quite different results, implying changes in the spectroscopic factors obtained with this operator for off-shell spinors of the order of 10%. Unless otherwise specified, all the theoretical results presented in this thesis has been obtained with the cc2 prescription.

2.13. Gauge invariance ambiguity

There is another popular ambiguity which affects the calculation of the matrix element of the one-body current operator for DWIA calculations of (e,e'p) reactions. This has to do with current conservation and gauge invariance [Kel97]. In principle, the vector currents (EM or weak) are conserved and the matrix elements computed should be gauge invariant. In practice, due to simplifications in the current operators and the wave functions employed (for instance, by restricting to only one-body current operators), the matrix elements usually do not fulfill the continuity equation and depend on the choice of gauge. To solve this ambiguity, usually one resorts to the phenomenology, comparing calculations with different gauges and picking the one that yields results in best agreement with data. As in the case of off-shell effects, some facts will be useful in guiding our choice of gauge and current operator.

For instance, one must be aware that part of the lack of charge conservation is due to the flux lost into inelasticities, when the final state is described with an optical potential with imaginary part. This means that part of the 'charge' is simply lost into inelastic channels. This has less to do with gauge invariance than with limitations of the IA where the matrix element is computed as a direct sandwich with the optical potential solution. Considering lost channels will be enough to recover much of the 'lost' current and it should help to conserve current.

A most basic current conservation problem would occur when a potential that does not include losses into inelastic channels, that is, a real potential, shows gauge dependence. A calculation that may be used as a hint here, is the one for inclusive electron scattering, where the initial and final nucleons are computed with the same relativistic mean field real potentials [Her09b, Cab10]. Under these conditions, it can be shown that matrix elements obtained with the cc2 operator fulfill the continuity equation and yield identical matrix

elements for the most commonly employed gauges (Coulomb, Lorentz and Weyl gauges). The ones obtained with cc3 and the Coulomb gauge are rather similar to these obtained with cc2 and any gauge, while the matrix elements obtained with cc1 are very different, particularly with Weyl gauge and, to a less extent, the Lorentz one. These facts suggest the following actions:

i) Disregard the results with the Weyl gauge.

ii) Disregard cc1 results, due to large off-shell effects.

iii) Consider most reliable the results obtained with cc2 or cc3, within the Coulomb gauge. Unless otherwise specified, the Coulomb gauge has been employed in the theoretical calculations of this thesis.

The interested reader is referred to the literature for further comparison of these most common prescriptions. Particularly, the prescription popularized by de Forest [For83], that replaces the longitudinal component of the electromagnetic current for the target by a term proportional to the charge component such that $q_\mu J^\mu = 0$ for the modified current, and that has been shown [Pol06] to be equivalent to the Coulomb gauge choice.

2.14. Proton Form Factors

It is well known that nucleons are not point-like particles. Therefore, the structure of the nucleons should be taken into account when the (e,e'p) cross section is evaluated. The characterization of the structure of the nucleon is a defining problem of hadronic physics, much like the hydrogen atom is to atomic physics. Elastic nucleon form factors (FFs) are key ingredients of this characterization. The measurement of the electromagnetic FFs in elastic as well as inelastic scattering, and the measurements of structure functions in deep inelastic scattering of electrons have been a rich source of information on the structure of the nucleon.

The study of the spatial distributions of the charge and magnetism carried by nuclei, began in the early fifties. Quite early the interest turned to the nucleon; the first FF measurements of the proton were reported in 1955 [Hof55]. Until the last ten years the FFs obtained from cross section data had suggested that $G_{Ep} = G_{Mp}/\mu_p = G_D$, where μ_p is the proton magnetic moments, and the dipole FF G_D is given by;

$$G_D = \frac{1}{\left(1 + Q^2 \,/\, 0.71 GeV^2\right)^2} \tag{2.10}$$

Nevertheless, recent and unexpected results from JLAB using the polarization transfer technique to measure the proton electric over magnetic FF ration G_{Ep}/G_{Mp}, has revealed

that for Q^2 values larger than 2 (GeV/c)^2, G_{Ep} decreases faster than G_{Mp}/μ_p with a slope of -0.14 per GeV^2. Therefore the G_{Ep}/G_{Mp} ratio decreases linearly with increasing momentum transfer Q^2. The numerous attempts to explain the difference in terms of radiative corrections which affect the results from the Rosenbluth separation method very significantly, but polarization results only minimally, have led to the previously neglected calculation of two-hard-photon exchange whit both photons sharing momentum transfer.

Different parameterizations of the Q^2 dependence of the form factors have been proposed. In this work, the parametrization from Ref. [Arr04] based on Rosenbluth separation has been used. This choice is consistent with working in the single-photon exchange approximation (section 2.1) as discussed in [Arr04].

$$G_E(Q^2), \frac{G_M(Q^2)}{\mu_p} = \frac{1}{1 + p_2 Q^2 + p_4 Q^4 + ... + p_{2N} Q^{2N}} \qquad (2.11)$$

The parameters of the fit to the data obtained with the Rosenbluth separation technique and with the polarization transfer method are summarized in Table 2.1

	Rosenbluth		Polarization	
Parameter	G_E	G_M/μ_p	G_E	G_M/μ_p
p_2	3.226	3.19	2.94	3.00
p_4	1.508	1.355	3.04	1.39
p_6	-0.3773	0.151	-2.255	0.122
p_8	0.611	-0.0114	2.002	-8.34×10^{-3}
p_{10}	-0.1853	5.33×10^{-4}	-0.5338	-4.25×10^{-4}
p_{12}	0.01596	-9.00×10^{-6}	0.04875	-7.79×10^{-6}

Table 2.1: Fit parameters for the Rosenbluth and polarization form factors, using the parameterization of Eq. (2.11) ([Arr04]).

2.15. Study of the Q^2 dependence of the Spectroscopic Factors

Some recent works [Lap00, Fra01] pointed to the possibility of a Q^2 dependence of the spectroscopic factor. For ^{12}C there are several (e,e'p) experiments performed at different value of Q^2, so it is a good nucleus to look for such effect. In Figure 2.7 from [Udi01], the scale factors needed to scale the theoretical RDWIA reduced cross section to the experimental data in ^{16}O experiments are compared.

Nevertheless, some aspects should be taken into account:

1)-FSI- Scale factors are not independent on final state interactions (FSI). In particular,

calculations with FSI based upon optical potentials fitted to elastic proton scattering in one hand, and upon the Glauber approach on the other, give generally different scale factors [Lap00]. This is due to the different picture of the FSI interaction assumed in each case. Which one is dominant in (e,e'p) processes is yet to be known, and probably depends on the kinematics. Also, elastic proton data mainly constrain the asymptotic behavior of the optical potentials. (e,e'p) experiments are not very sensitive to this asymptotic or large region, rather to the behavior of the proton wave function (and thus the potential) in the inner nuclear region. This is the reason why optical potentials that yield essentially the same elastic (p,p') observables, can however lead to (e,e'p) scale factors that differ by 50% or more [Udi01]. However, under exclusive conditions, the optical potentials are quite adequate to estimate (e,e'p) yields.

In Figure 2.7 the results shown in the left and right panels differ only in the relativistic optical potential employed. The effect on the scale factor is clearly visible while none of the two can be preferred over the other based upon elastic (p,p') scattering only. A very effective way of dealing with this optical potential uncertainty is to use also data from inelastic nucleon scattering, restricting thus more the potentials in the nuclear interior [Kel89]. This is at the moment only available for non-relativistic potentials in a restricted range of energies.

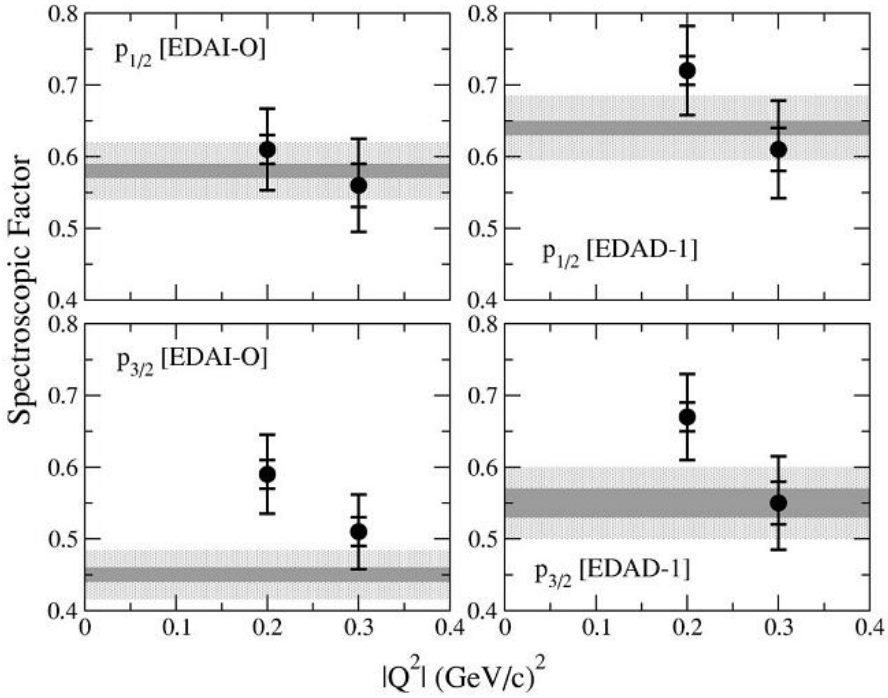

Figure 2.7: - Effect of the Optical Potential used in the FSI calculation. From [Udi01]

For higher Q^2 and/or a heavier nucleus as ^{208}Pb, scale factors are much more stable against different choice of the optical potentials [Udi93], mainly because all the available

relativistic parameterizations are much more similar than for ^{16}O at low momentum of the knocked out nucleon.

2) p_{miss} range - Usually, lower Q^2 experiments span a smaller range in p_{miss} than large Q^2 ones. Due to this, large Q^2 experiments give more weight to the large p_{miss} region, where the IA is not the only prevailing reaction mechanism. Other contributions would naturally lead to an increase of the cross section in the p_{miss} region where the single-particle spectral function is not dominant, and thus fitting scale factors with data in this region will yield higher scale factors. When comparing data from experiments taken at different Q^2 in order to deduce scale factors, it is advisable to restrict the analysis to data in the region of p_{miss} where the IA result is important.

2.16. Relativistic vs. Non-Relativistic Calculations

A large amount of theoretical work on *(e,e'p)* has been carried out on the basis of non-relativistic approximations to the nucleon current, like the standard distorted wave impulse approximation (DWIA) [Kel96] that uses a non-relativistic approximation to the nucleon current operator and wave functions. DWIA has been successfully used over the years to analyze *(e,e'p)* data using bound and scattered proton wave functions deduced from phenomenological non-relativistic potentials. The limits of validity of the non-relativistic DWIA approach have been studied [Meu01].

On the other hand, nuclear responses and differential cross sections for exclusive quasielastic electron scattering within the framework of relativistic mean field approximations have been also studied [Udi93b, Udi95, Udi96]. In the relativistic distorted wave impulse approximation (RDWIA) the one-body nucleon current is calculated with relativistic wave functions for initial bound and final outgoing nucleons, respectively, and with relativistic nucleon current operator J_N.

The bound state wave function is a four spinor with well-defined parity and angular momentum quantum numbers, and is obtained by solving the Dirac equation with scalar-vector *(S-V)* potentials determined through a Hartree procedure from a relativistic Lagrangian with scalar and vector meson terms [Hor91].

The wave function for the outgoing proton is a solution of the Dirac equation containing *S-V* global optical potentials [Coo93] for a nucleon scattered with asymptotic momentum p_F. Dirac equations for both scattered and bound wave functions are solved in coordinate space and their solutions are then transformed to momentum space where necessary.

Between the relativistic and non-relativistic approaches there are essential differences due to *dynamical effects.* These effects are due to the differences between relativistic and non-relativistic wave functions which depend not only on the four-spinor versus two-spinor structure, but also on the potentials used in the respective Dirac and Schrodinger equations for the bound and scattered nucleon. The main features of dynamical effects are

(a) A dynamical depression of the upper component of the scattered nucleon wave function in the nuclear interior, typically identified as the effect of the Darwin term coming from the derivative of the optical *S*-*V* potentials [Udi95].

(b) A dynamical enhancement of the lower components, mainly those of the bound nucleon wave function, due to the negative energy components.

RDWIA has been successfully applied to ^{208}Pb and ^{40}Ca at low Q^2 [Udi93b, Udi95], and to ^{16}O at high Q^2 [Udi99, Gao00]. The effect caused by the nonlocal Darwin term for ^{40}Ca and ^{208}Pb cases was studied in detail in Refs. [Udi93b, Udi95]. The Darwin term causes an apparent enhanced absorption when comparing the RDWIA differential cross section to the DWIA one at moderate p_m values, thus predicting larger spectroscopic factors [Udi93b, Udi95, Jin92]. For larger missing momentum values, the lower components of the relativistic wave functions start to play a more important role, enhancing the higher momentum components of the nucleon wave functions. In [Udi96] it was found that RDWIA calculations, compared to standard DWIA, tend to produce lower cross sections at p_m=300 MeV/*c* and larger cross sections at p_m=*300* MeV/*c*, improving agreement with experiment.

The effect of the dynamical enhancement of the lower components was studied in RPWIA [Cab98, Cab98b]. It was also studied in RDWIA at high Q^2 [Udi99]. In both cases it was found to play a crucial role in the *TL* responses. Previous experiments on ^{16}O at high Q^2 seem to confirm former RDWIA predictions as it was shown in Section 1.6.1. In particular, the effect of off-shellness of the spinors in the A_{TL} asymmetry at moderate values of the missing momentum, which is large for $p_{1/2}$ and small for $p_{3/2}$ shells, produces that only the predictions of relativistic calculations that include the dynamical enhancement of the lower components of bound Dirac spinors is consistent with data for the shell $p_{1/2.}$

3. Simulations

3.1. Introduction

A general problem invariably found during the analysis of (e,e'p) data is how to deal with spectrometer acceptances. Experiments are generally performed with spectrometers that have significant angular and momentum acceptances. On the other hand theoretical calculations are generally performed assuming central values for these acceptances. Thus, in order to correctly compare data to theory, acceptance issues as well as other instrumental effects such as mispointing of spectrometers or radiative corrections, must first be determined.

There are two different approaches to reconcile experimental data and theoretical calculations:

- Method 1 - Experimental acceptances may be unfolded to convert the experimental data into 'point-acceptance' equivalent results. Data should also be corrected by effects like radiative processes and Coulomb distortion. This procedure has been most often employed at NIKHEF-K and JLAB, although some model dependencies or bias in the data are introduced.
- Method 2 - Theoretical calculations may be averaged over acceptances with a Monte Carlo simulation that may also include radiative effects and Coulomb distortion. This simulation can be compared to data with only moderate cuts at the edges of the acceptances. This method requires a good understanding of the experimental acceptances, it is time consuming and must be done for every theoretical calculation that one wants to validate against the particular experiment.

The salient features of these options are briefly outlined.

METHOD 1 - Without a realistic Monte Carlo code, only a restricted subset of the data whose behavior is well understood can be used in the acceptance unfolding. Accordingly, in the resulting data analysis, the spectrometer acceptances should be cut restrictively in the variables θ_{tg} (the out-of-plane angle), ϕ_{tg} (the in-plane angle), and δp_{tg} (the deviation from the spectrometer central momentum). Using data (from so-called "white-spectra" measurements if available, or from simulations), it can be shown that when sufficiently restrictive cuts are applied, the distributions for the above-stated variables become "flat"

over their cut range. Under these conditions, measured spectra can be simulated using a uniform random-number generator. Thus, by randomly populating “physics” spectra with this type of simulation, the experimental phase-space for this much-reduced acceptance can be determined. This phase-space may then be employed to compute the cross section.

Data are then unfolded for acceptance effects. This implies binning the data for reduced ranges of the variables of interest (usually E_{miss}, p_{miss}, q, ω and ϕ). As a rule of thumb, bin size should be reduced when the variation of the cross section inside the bin gets larger than its statistical uncertainty. If bins are too small, the statistical error inside them becomes too large, while if bin size is too large, the experimental points necessarily "average-out" features of the cross section.

The experimental cross section for each particular bin can be compared to theoretical calculations obtained using the averaged values of the representative variables of the bin. It is important to note that these values, computed from their average in the data sampled inside each bin, may differ from their nominal central values in the bin. As a result, kinematics of each bin may not vary continuously with the contiguous ones, making it difficult to create theoretical calculations.

Finally, assuming the factorized approach described by Eq. (1.26), cross section of the proton knock-out from a particular shell (i.e. in a given E_{miss} range) is usually given as a function only of p_{miss}, Using reduced cross sections, most of its dependence with the particular kinematics of the experiment (like q and ω) are removed. This implies that bins with a different q and ω can be then merged into a single bin. Theoretical estimates based upon unfactorized calculations would yield information on the error implied in this procedure.

METHOD 2 - The increasing computer power available and the development of sophisticated Monte Carlo simulations allow for accurate modeling of the entire system, including target, detectors, electronics, radiative tails, etc. Thus, in principle, the whole range of acceptances present in the data may be considered, apart from minor cuts to avoid edge effects. In this case, the theoretical calculation must be input to the realistic Monte Carlo simulation and compared to minimally processed data [Flo99, Die01, Mon08]. While this procedure of comparing theory to data is truly model independent, it requires that the theoretical calculation must first be incorporated into the Monte Carlo of the experiment. Unfortunately, some theoretical models require a large computational cost in

order to be properly addressed.

As it was already pointed out, the conventional way of incorporating theoretical calculations into the Monte Carlo simulation was based on a factorized expression for the cross section (see Eq. (1.24)) and with momentum distributions from theoretical models as input. This method is not optimal because the degree to which factorization is not fulfilled depends on the theoretical model employed and, above all, factorization is not a good approximation [Vig04].

In this thesis, rather than using a single momentum distribution calculated for a particular “catch all” kinematics to represent an entire experiment, RDWIA structure-function calculations have been incorporated on an efficient event-by-event basis. In order to achieve this, responses are pre-calculated in a dense multidimensional grid in the variables p_{miss}, ω and q, comprising the entire experimental acceptances. "Dense" enough mean that the interpolated responses from the grid differ by less than 1% [Flo99, Die01] from the actual responses computed at pinhole-acceptance kinematics. During the simulations, the cross sections are computed from the interpolated responses according to Eq. (1.22). The payoff is twofold: first, these theoretical cross sections can be easily included as the source in the most realistic physics simulation imaginable. Second, focused studies of the effects of acceptance averaging on the results are now possible without resorting to the factorization approximation. In this approach, the only assumption made is that Eq. (1.22) holds; that is, that the one photon exchange approximation is valid.

3.2. MCEEP

MCEEP [MCEEP] is the de-facto Hall A simulation package developed initially by Paul Ulmer. With MCEEP, Hall A projects have access to well-developed software models of the High-Resolution Spectrometers, to name just a small subset of what the toolkit delivers (see below).

From its humble beginnings, MCEEP has evolved into a dynamic toolkit for analyzing data obtained in Hall A at Jefferson Lab. Many effects previously neglected in the simulations – multi-foil target models, spectrometer models, energy loss, multiple scattering and radiative corrections, are addressed in the current version of MCEEP.

Unfortunately, in order to keep computation times reasonable, overly simplistic models of the (e,e'p) reactions were employed in the past. To take MCEEP to the next level the physics models available to the user needed to be improved. Ideally, they should allow

state-of-the-art theoretical descriptions of (e,e'p) reactions, including fully unfactorized, relativistic calculations, with even the possibility of including Coulomb distortion effects of the electron wave function.

3.3. RDWIA Response Functions + MCEEP

In the past, MCEEP commonly used hard-coded momentum distributions supplied by the user to describe nucleon-knockout processes. End-user momentum distributions can be added to the code in a painless fashion and cross sections needed in the simulations were obtained from the momentum distributions assuming factorization. While this is a very efficient approach in terms of processing time and certainly sufficient for setting up experiments and making estimates of rates, for example, it is not sufficient for comparison of theory to experimental data or for studies of the effect of extended spectrometer acceptances. This is because in an extended-acceptance experiment, each event can correspond to somewhat different kinematics. Thus, every experimental bin corresponds in principle to a slightly different experiment and the results of the simulation are thus different for factorized versus unfactorized models. This issue has been address allowing for fully unfactorized calculations into MCEEP. To be specific, the responses are pre-calculated in a grid (our "hypercube") which spans the experimental phase space, and then they are used to interpolate responses within this hypercube to obtain cross sections on an event-by-event basis. These cross section values may then be cut or binned according to the wishes of the user, allowing for detailed studies of the effects of extended acceptances without any footprint induced by factorization upon the results.

This approach of using response functions in MCEEP instead of momentum distributions was initially developed by S. Strauch, J. Vignote and J.M. Udías for the analysis of polarization observables in a ^{4}He(e,e'p) experiment. Formerly, it was employed to include radiative corrections to theoretical models by Florizone et al. In this work, I have adapted and further developed this approach to incorporate it to the analysis of all experiments discussed in this thesis.

Similar approaches were attempted in some previous experiments. A grid of response functions together with a Monte Carlo code was used, for example, in Ref. [Wij99] using response functions from J. Kelly. In Ref. [Man93], a ^{12}C(e,e'p) experiment performed at MIT-Bates used the Monte Carlo code AEEXB [AEEXB] with a lookup table for the response functions obtained from the code PV5FF [Bof92]. In that case, the three-

dimensional grid was created with the energy of the detected electron and proton and the electron-scattering angle.

3.4. Example of the enhanced MCEEP simulations for the E89-003 experiment

The results of the extended MCEEP simulations will be illustrated with a short study of the previous ^{16}O(e,e'p) experiment E89-003 at JLAB. This experiment has already been analyzed [Gao99, Liy99] and results have been published [Gao00, Liy01]. Furthermore, good agreement between data and RDWIA model of Udías *et al*. [Udi99] was found [Fis04]. As our response functions are based on the same theoretical model, similar good agreement to data is expected.

The goals of this study were:

1) Apply restrictive cuts on the acceptances in the simulation (i.e. without acceptance averaging) to obtain the "bare" (i.e. using central values for the kinematical variables) theoretical results. This is a basic test for the internal self-consistency of the method.

2) Study the impact of acceptances cuts and criteria on the results can be assessed. This way, a deeper insight of what happens when a theoretical model is averaged over experimental acceptances can be gained.

A detailed description of these tests can be found in [Her07]. Here only the more relevant results are presented.

3.4.1. Pinhole acceptances

Using simulations with pinhole acceptances, the effects of averaging the theoretical calculations over the detector acceptances are removed. Therefore, the same result as for the bare theory is expected. In the bottom panel of Figure 3.1, it can be seen that the results obtained with "extremely reduced" spectrometer acceptances agree nicely with the theoretical curves. The cuts used for the extremely reduced acceptance results spanned $\pm$0.1 mrad in both θ_{tg} and φ_{tg} and $\pm$0.1% in δp for both spectrometers. Clearly, the simulated results collapse to the point-acceptance theoretical RDWIA calculations.

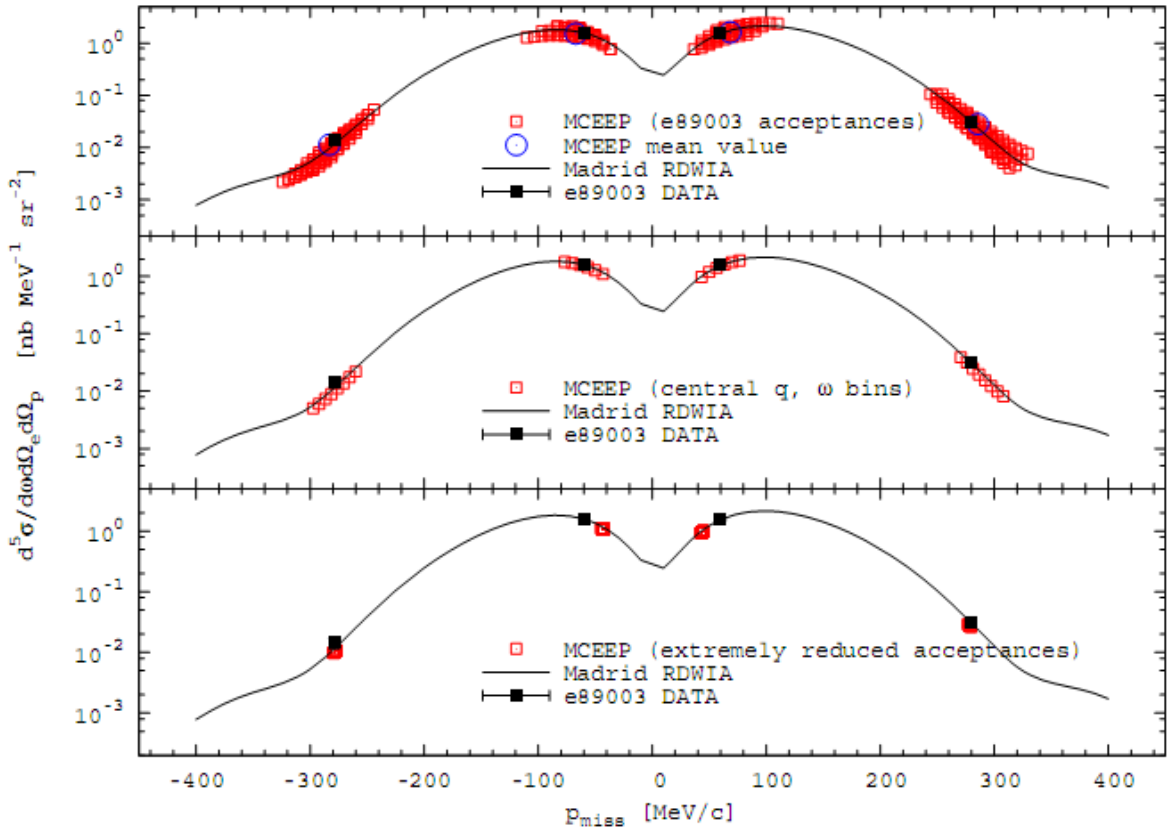

Figure 3.1: Differential $^{16}O(e,e'p)$ cross section ($1p_{1/2}$ shell). Data, theory and simulations

3.4.2. Impact of the acceptances on the results

The results from the extremely reduced acceptance simulations and the E89-003 data in Figure 3.1 (bottom pad) do not appear at the same missing-momentum values of the data published. This may easily be explained if the finite size acceptances are considered. The E89-003 data were plotted in a single bin located at the average value from the total number of events which passed both the cuts applied during the data analysis and occupancy restrictions placed upon the phase-space volume, that is, when care is taken that only bins of phase space that are appreciably populated are included.

The range in the angular acceptances and momenta of the detected particles are translated into a range in (q, ω and the out-of-plane ϕ). In Figure 3.1, the impact of having a finite range in q and ω is depicted in the top pad. Here, the entire number of bins in q and ω and the results they imply for the cross sections are shown. In the middle pad, only the central q, ω bins are shown, and the results are then more compatible with the bare theoretical calculations computed at central values of the kinematics.

These acceptance effects are in general larger for lower θ_{pq} as it is shown in Figure 3.2. It is clear from these plots that the reduced-acceptance distributions do not correspond to the “average” of the full-acceptance distributions.

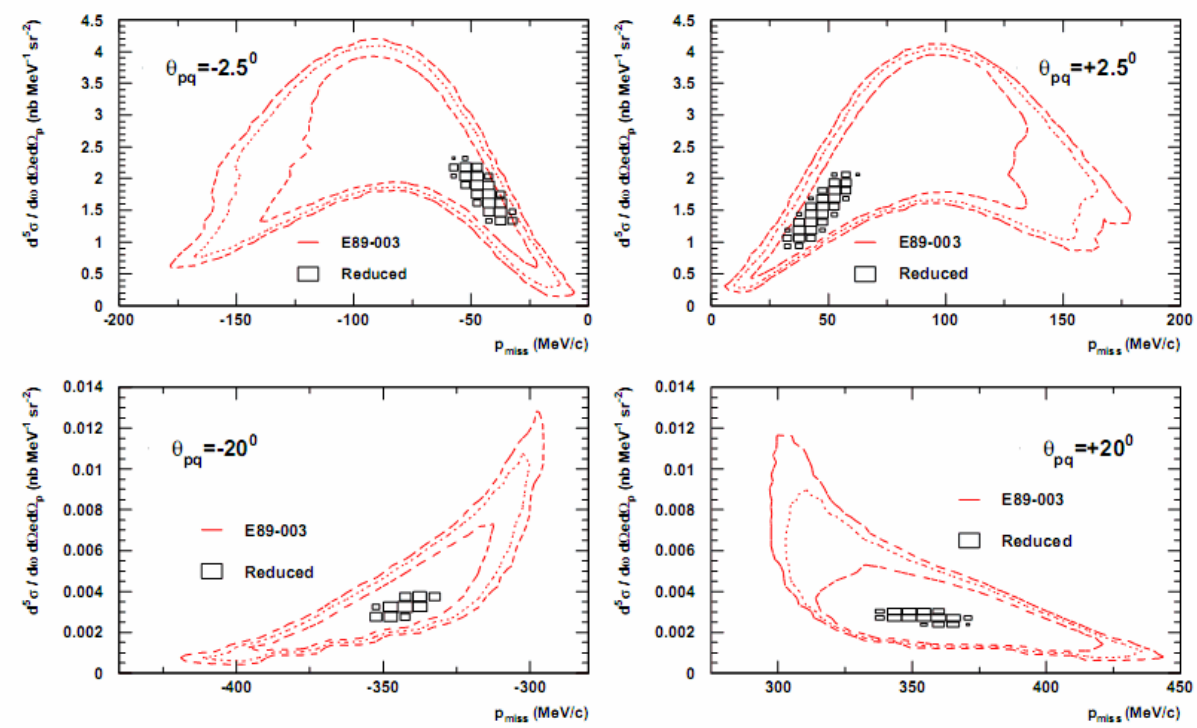

Figure 3.2: Simulated differential cross section for E89-003 kinematics with experimental versus reduced acceptances.

3.5. Input file parameters

3.5.1. Beam parameters

In order to get realistic simulations, the width and the energy spread of the beam should also be considered in the simulation. Furthermore, the offsets of the beam with respect to the central (x,y)=(0,0) coordinates of the target in the Hall coordinate system can be added. This allows for a better reproduction of the angular ranges of the experiment.

In contrast to the experiment E00-102, in the experiment E06-007 a rastered beam was used. In the simulation, this effect is combined with the offsets, improving the angular matching between theory and simulations.

3.5.2. Internal collimators

MCEEP allows for the use of internal collimators in the HRSs. During the simulation of the transport of the particles in the spectrometers, these collimators restrict the possible trajectories. By default, collimators are not included and thus simulations have wide acceptances. Without the default values of the collimators, the distribution of the yield vs. p_{miss} is not properly simulated. Nevertheless, changing the internal collimators to match the experimentally allowed values improves the agreement of data and simulations.

3.6. Energy Loss and Radiative Effects

The (e,e'p) reaction described by the simple, one photon exchange diagram shown in Figure 1.4 does not take into account that in any electron-scattering experiment, the incoming and outgoing charged particles radiate photons which are not observed. Radiative effects include:

A) Virtual Photons: The emission and re-absorption of virtual photons corresponds to the vertex correction, mass renormalization, and vacuum polarization of the exchanged photon. Therefore the emission of a virtual photon can only change the magnitude of the measured cross section, without altering the momenta of the particles. Usually this is a small effect (save for Coulomb distortions), and can be well computed from QED.

B) Real Photons: The radiation of a real photon changes the energy and momentum transferred in the (e,e'p) reaction. Furthermore, energy losses of the incident and scattered electron and extracted proton due to atomic ionizations along their path also have to be considered when describing the experimental reaction.

These radiative processes are an integral part of the (e,e'p) reaction, but they are not included in the theoretical (e,e'p) cross section. Therefore, similarly of what happens with experimental acceptances (Section 3.1), two approaches exist to deal with radiative processes:

A) In order to make the results independent of the target thickness and other features of the experimental setup, measured cross sections may be corrected for all radiative losses. This allows a meaningful comparison between the experiment and bare theory. In the correction process the measured cross section is adjusted to the values which would have been measured in the absence of radiation.

B) They can be incorporated into the simulation code to obtain a more realistic simulation which can be compared directly to the acquired data.

In this thesis, the first method was used. MCEEP simulations were done as realistic as possible, including all radiative processes. This way, source of errors induced by the unfolding procedure were avoided. This was already done in previous thesis [Mak94].

Three processes are considered for radiative corrections:

- **Ionization losses** - Energy is lost through excitation or ionization of atoms along the path of the charged particles.
- **External radiation** - External radiation is produced when the charged particle (electron or proton) radiates real and virtual photons in the presence of the Coulomb

fields of nuclei other than the one involved in the (e, e'p) reaction.

- **Internal radiation** - Internal radiation is produced when the charged particle (electron or proton) radiates real or virtual photons from the interaction with the Coulomb field of the nucleus involved in the (e,e'p) reaction. It was first calculated by Schwinger [Sch49] and later improved by Mo and Tsai [Mo69], and it has the largest overall contribution to the radiative correction.

Ionization losses and external radiation are proportional to the total amount of material that the charged particles have to traverse. In the experiments considered in this thesis, the target used and the windows of the target chamber were thin and internal radiative effects were in general the dominant effect.

Although radiative effects have been known for many decades [Sch49, Yen61, Mo69, Tsa74], there are still many recent works [Tem09, Ent01, Weis06, Afa08] aiming to define the best way to handle them, especially around the energy region (~1GeV) considered in this thesis. This is due to the fact that radiative corrections change the final cross section by a very significant amount, so the reliability of final results depends to a high extent on the accuracy of these corrections.

Extensive details about the calculation of the energy loss and external and internal radiative processes in MCEEP can be found in the user's guide [MCEEP].

The Peaking Approximation [Weis06] used in this work assumes that the real photons arising from radiative losses are emitted in the direction of the charged particles that emitted them. For the kinematics of the present experiment, the effect of proton radiation is relatively small. The formula "4.42" of [Mak94] derived for ultra-relativistic particles has been used to estimate the relative strength of the proton radiation. In the worst case, the correction to the cross section from proton-radiation effects is about 1%. Since this is well within the systematic and statistical uncertainties of these experiments, proton radiation has been neglected in the analysis (other than computing the corresponding E_{loss}). However, it should be noted that as one goes to higher values of Q^2, proton-radiation effects increase and the relative strength of these contributions was considered.

In Ref. [Weis06], the limitations of the Peaking Approximation were studied. The deviation between a full model that takes into account all possible angular directions and the Peaking Approximation at the kinematics of these experiments (Q^2~1GeV^2) is less than 1%, well within our systematic and statistical uncertainties.

4. Description of the Experimental Setup

4.1. Overview

The experiments described in this thesis were performed in Hall A of the Thomas Jefferson National Accelerator Facility (JLAB), formerly known as CEBAF (Continuous Electron Beam Accelerator Facility). JLAB is located in Newport News, Virginia and is a state-of-the-art facility featuring an electron accelerator, three experimental Halls (A, B and C), a free-electron laser and an Applied-Research Center. The accelerator was designed to produce high current (up to 200μA), 100% duty factor beams of up to 4 GeV to the three independent and complementary experimental halls. simultaneously.

In Hall A, two basically identical 4 GeV/c high resolution spectrometers (HRS-R and HRS-L) are used to detect scattered electrons and knocked-out protons respectively. The detector packages are installed in the focal plane of each spectrometer to determine the particle trajectories as well as to identify particles.

In the experiment E00-102, a waterfall target with three waterfall foils, built by the INFN group [Gar92] was used to study ^{16}O. In the experiment E06-007, special C+Pb+C and C+Bi+C target were used. Graphite foils were also used in the experiment for calibration purposes.

In this chapter, an overview of all the experimental apparatus is given. Further detailed information on both JLAB and Hall A can be found in [JLAB, Alc04]. A full review of the electron accelerator is provided in [Lee01].

4.2. Accelerator

The layout of the accelerator is shown in Figure 2.1.

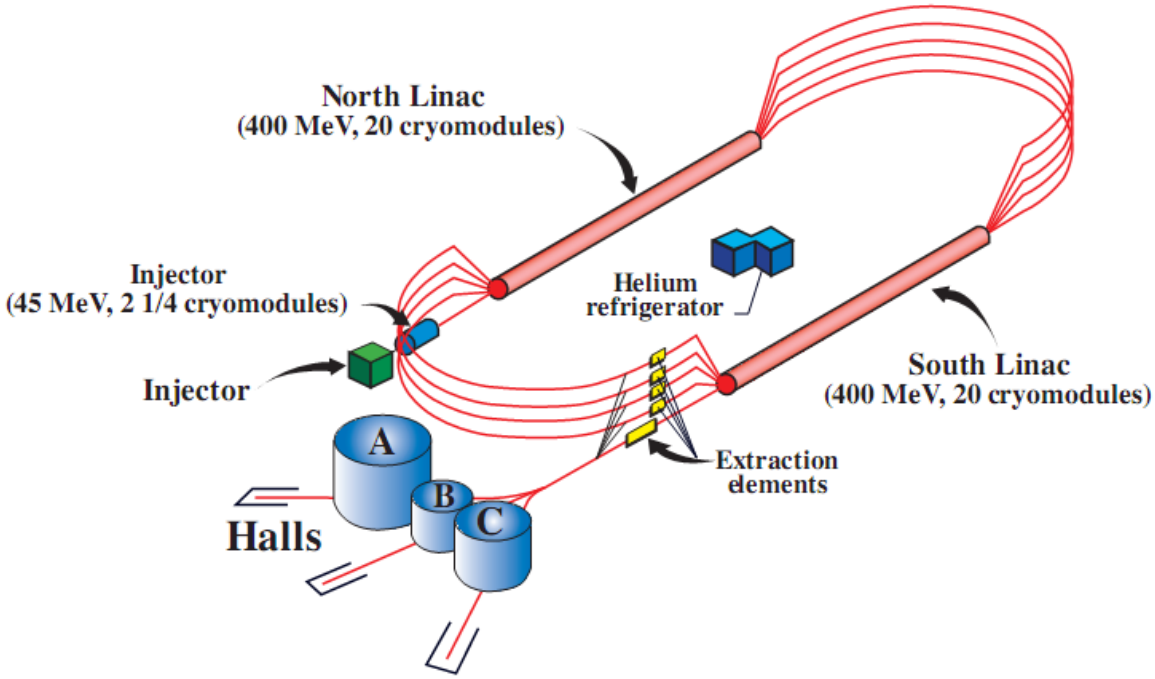

Figure 4.1: JLAB Accelerator configuration. Figure from [Alc04].

The electron beam is accelerated to 45 MeV in the injector before passing through a linac consisting of superconducting RF cavities with a design accelerating gradient of 5 MeV/m. Ongoing in situ processing resulted in an average gradient in excess of 7 MeV/m [Alc04]. This made it possible to accelerate electrons up to 5.7 GeV (higher than the designed maximum momentum of 4 GeV/c).

After undergoing a 180° bend in the recirculation arc, the beam passes through another linac. At this point, the beam can be either extracted and directed into any of the three halls, or sent back for additional acceleration in the linacs. The final energy of the beam depends on the total number of passes.

There are five different arcs for recirculation on the east of the machine, and four different arcs on the west end. The bending field of each individual arc is set to bend the beam of a different pass, that is, a beam of a different energy. The beam is separated at the end of each linac, sent to the corresponding arc, and then recombined before entering the next linac. At the end of the acceleration process, the beam is extracted and then delivered to the experimental halls. This allows different halls to use different values of the electron energies.

The beam has a micro-structure that consists of short pulses at a frequency of 1497 MHz. Generally, each hall receives one third of the pulses, resulting in a quasi-continuous train of pulses at a frequency of 499 MHz. Beams with different energies can be delivered to the different halls simultaneously.

Beam characteristics are summarized in Table 4.1

Maximum energy	5.7 GeV
Duty cycle	100%, CW
Emittance	$2x10^{-9}$ m
Energy spread (4σ)	10^{-4}
Maximum intensity	200 μA
Vertical size (4σ)	100 μm
Horizontal size (4σ)	500 μm

Table 4.1: Jefferson Laboratory beam characteristics [Gao99].

The experiment E00-102 used a four-pass beam, with an energy of 4.6 GeV, and beam currents ranging from 5 to 120 μA. The experiment E06-007 used an energy of 2.4GeV, with a beam current up to 40 μA.

4.3. Hall A Setup

The basic configuration of Hall A is shown in Figure 4.2

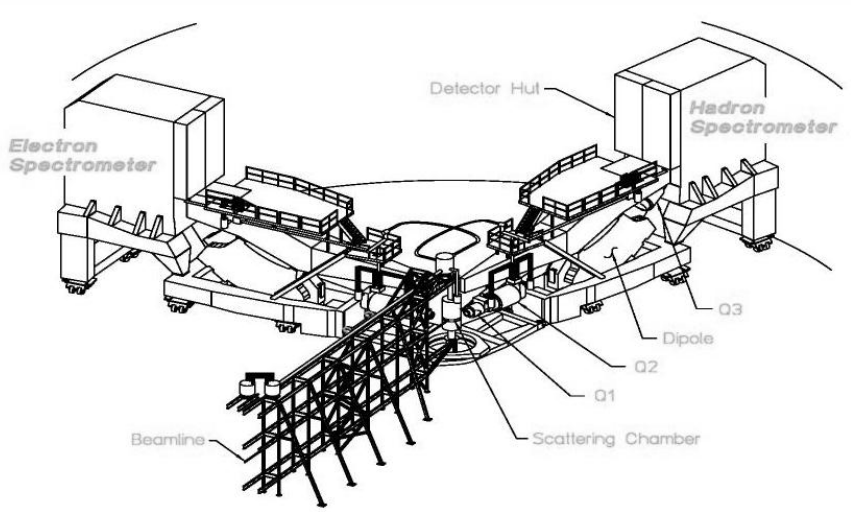

Figure 4.2: Hall A configuration.

After being extracted for use in Hall A, the electron beam is transported into the hall along the beamline, and onto the scattering chamber where the target is placed. Along the beamline (Figure 4.3), there are two BCMs (Beam Current Monitors, see Section 2.4.1)

and two BPMs (Beam Position Monitors, see Section 2.4.2) which provide precise measurements of beam current and position. The majority of electrons incident upon the target pass through without interacting and are transported to a well-shielded beam dump. Two spectrometers (see Section 2.6) are used to perform physics experiments. The electron spectrometer (HRS-L) measures the momentum and direction of the scattered electrons, and similarly, the hadron spectrometer (HRS-R) detects the knocked-out protons. The two spectrometers are essentially identical in terms of their magnetic components and optics. Note that by changing the polarities of the magnets, their roles can be interchanged. On the platform of each spectrometer, a shielding house (detector hut) was built to protect the detector packages and associated electronics from radiation damage, and to minimize the rates in detectors caused by particles not passing through the spectrometer.

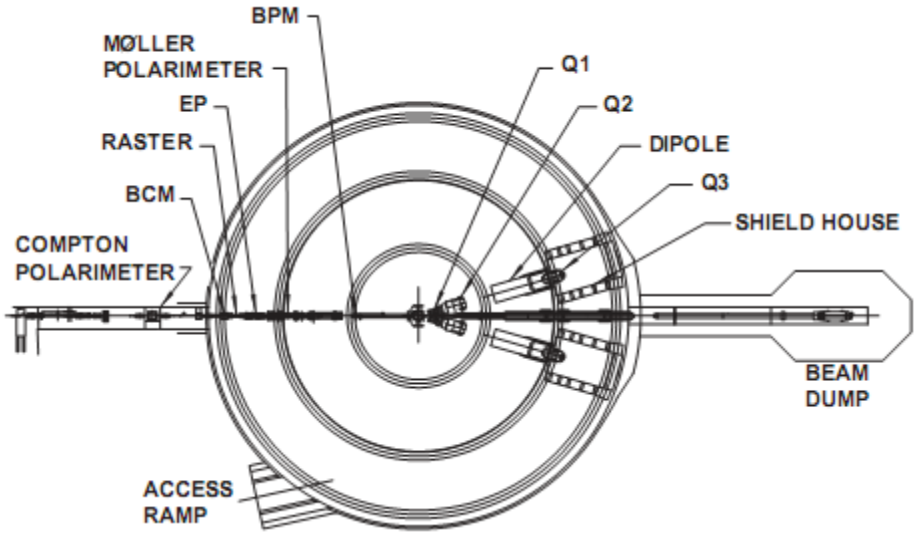

Figure 4.3: Schematic layout of Hall A. Figure from [Alc04].

4.4. Beamline

4.4.1. Beam Current Measurement

The beam current delivered to Hall A is measured by two beam current monitors (BCMs) located in the beamline about 24.5 meters upstream of the target with a Unser monitor sandwiched between them. They are used to monitor the beam current linearly and continuously.

In addition to the BCM, the value of the current from the injector (from the OLO2 injector cavity) is also available. As this total current is shared among the different experimental halls, no beam may be delivered to the halls during beam current calibration runs. A

Faraday Cup at the injector section of the main accelerator is also used to provide an absolute reference during calibration runs (see section 5.1.1).

Each BCM is a cylindrical resonant cavity made out of stainless steel, 15.48 cm in diameter and 15.24 cm in length, tuned to the frequency of the beam (1497 MHz). When the electron beam passes through the cavity, it excites the resonant transverse magnetic mode TM_{010} at 1497 MHz. A loop antenna couples RF power out of the cavity, giving an output signal proportional to the current, which is converted to a 10kHz signal. Each of the RF output signals from the two cavities is split into two parts, to be sampled or integrated.

The sampled data, are processed by a high-precision digital AC voltmeter, DMM (Digital Multi-Meter). This device provides a digital output each second which represents the root-mean-square (RMS) value of the input signal during that second. The resulting number $V^{(u,d)}$ is proportional to the average beam current for that second and it is fed into the data-acquisition stream at regular intervals of a few seconds.

The integrated data is sent to a RMS-to-DC converter which produces an analog DC voltage level. This voltage level drives a voltage-to-frequency converter (VtoF) whose output frequency is proportional to the input DC voltage level. These signals are then fed to fastbus scalers and finally injected into the data stream along with the other scaler information. These scalers accumulate during the run, obtaining a number proportional to the integrated voltage level and therefore they represent more accurately the true integral of the current and hence the total beam charge.

This RMS-to-DC conversion is linear for currents from about 5μA to 200μA. In order to extend the linear region to lower currents, a set of amplifiers with gain factors of 3x and 10x were introduced. As a result, each BCM provides a set of three signals. Therefore the upstream and downstream BCMs provide six signals that are fed to scaler inputs.

The Unser monitor sandwiched between the BCMs is used for calibration purposes. It cannot be used to monitor the beam continuously because the output signal drifts on a time scale of several minutes.

During a typical calibration run, the beam current is ramped from zero to the maximum value dwelling at each step for 60 to 90 s. In this manner, the beam charge can be determined with an accuracy of 0.5% down to a current of 1μA.

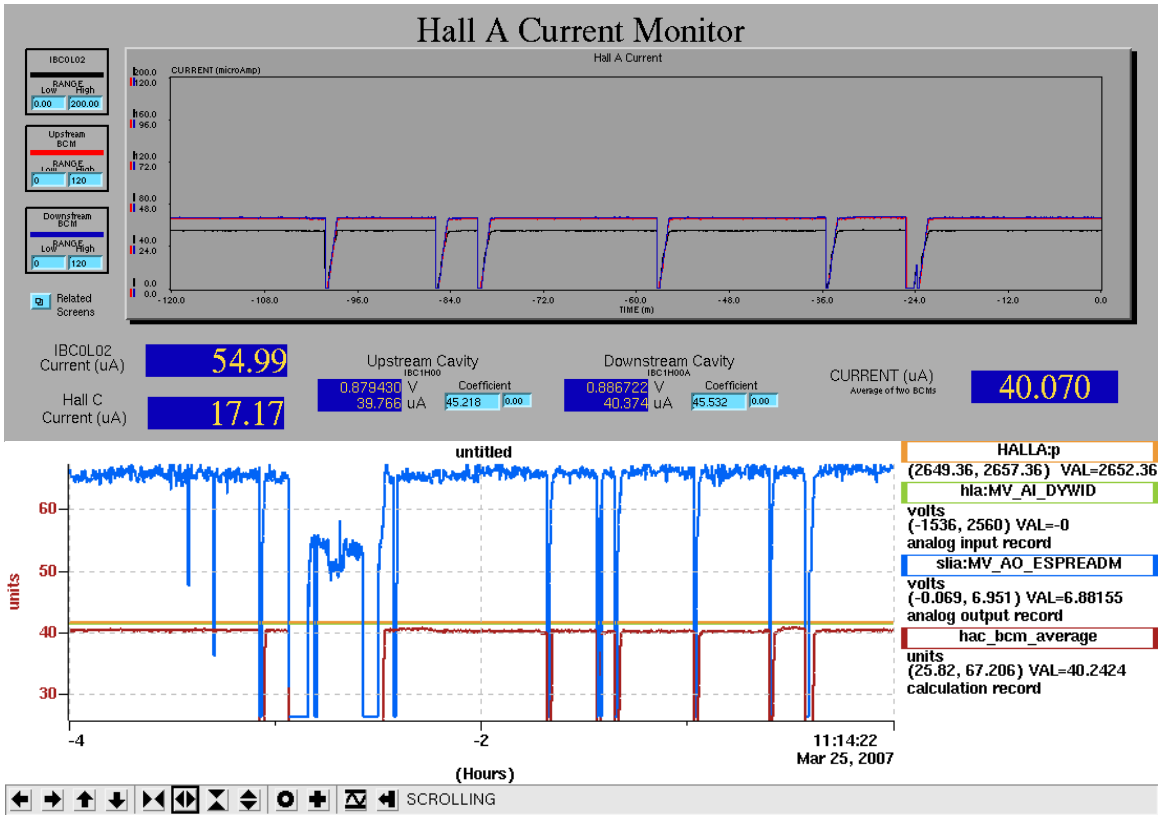

Figure 4.4: Typical Beam Current Monitor readout during the experiment E06-007.

4.4.2. Beam Position Measurement

The position of the beam along the Hall A beamline was monitored using two beam position monitors (BPMs) [Bar90] upstream of the target along the beamline. These two BPMs are respectively 7.3m (BPM A) and 1.1m (BPM B) away from the target [Alc04]. A BPM consists of a cavity with four wire antennas oriented parallel to the electron beam and located at the corners of a square as shown in Figure 4.5.

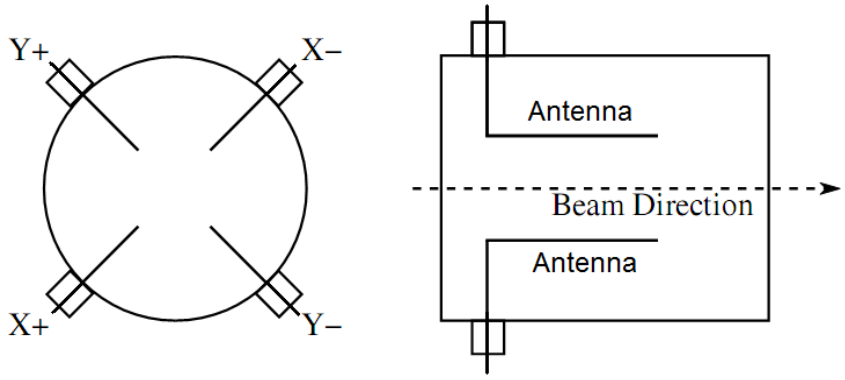

Figure 4.5: Schematic of a stripline beam position monitor. Left view is along the beam axis, right view is a cross section of the monitor.

Radiofrequency (RF) signal from each antenna is processed to yield a DC signal which is proportional to the product of the beam current and the distance between the beam and the antenna. These DC signals are integrated in the DAQ system on an event-by-event

basis and used to give the beam position in horizontal and vertical lab coordinates (x,y). The antenna signals vary with beam current so a gain switch is used to keep the DC output signals constant regardless of the beam current. At a beam current of 10 μA, the beam position can be determined down to 20 μm.

From the information provided by the two BPMs, one can figure out both the beam position on the target and the beam direction. The absolute position of the beam may be determined by calibrating the BPMs respect to surveyed wire scanners (Harps) located adjacent to each of the BPMs. These are surveyed at regular intervals and the results are reproducible at the level of 200 μm [Alc04].

4.4.3. Beam Energy Measurement

The energy of the incident electron beam can be measured in two independent ways: eP measurements and arc energy measurements.

The eP method uses a stand-alone apparatus to make an invasive measurement of the incident beam energy by measuring the angles of scattered electrons and protons in the elastic ^{1}H(e,e′p) reaction. This method was not used during these experiments.

The Arc Energy method is based on the fact that an electron moves in a circular trajectory in a magnetic field. The radius of the trajectory depends on the magnitude of the magnetic field and the momentum of the electron. Therefore, the electron momentum can be determined by measuring the radius of the arc through which it is deflected by a known magnetic field. The deflection of the electron beam in the arc section of the accelerator beamline is used to determine the beam energy. The measurement can be made when the beam is tuned in either dispersive or non-dispersive mode in the arc section of the beamline. The electron beam momentum (p in GeV/c) is then found from the magnetic-field integral of eight dipole magnets in the arc beamline and the resulting net bend angle through the arc (θ in radians) by:

$$p = k \cdot \frac{\int \vec{B} \cdot d\vec{l}}{\theta} \qquad (4.1)$$

where k = 0.299792 GeV rad / Tm ; the nominal bend angle is 34.3º.

Two measurements must be performed to determine the beam energy: the field integral of the eight magnets in the arc with respect to a reference magnet (the 9th dipole) and the actual bend angle of the arc using a set of wire scanners. Further details regarding this instrumentation can be found in [Alc04].

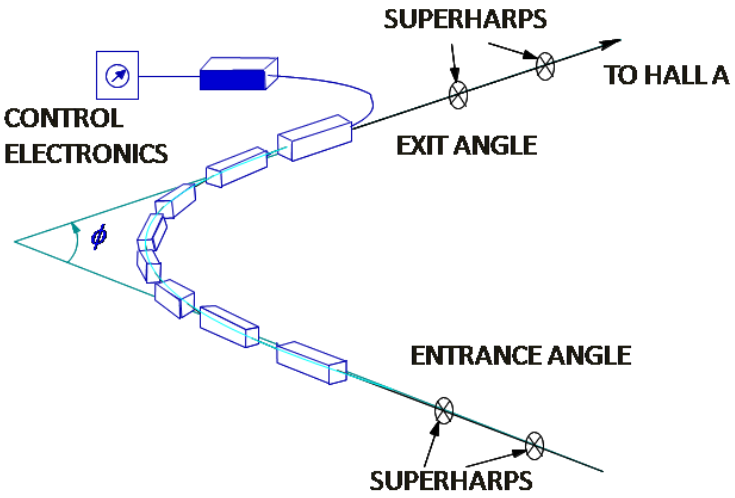

Figure 4.6: Arc beamline section with the magnets used to deflect the beam.

The beam-energy values used during the analysis are taken as the Tiefenbach values recorded in the data stream. The Tiefenbach value is calculated from the launch and exit angles of the beam through the arc, obtained using the beam position monitors in the hall,. The relative error on the Tiefenbach energy is less than 5×10^{-4}.

4.4.4. Beam Rastering System

The power deposited by the electron beam into the target must be dissipated in order to maintain the target properties. A heat exchanger in the cryogenic loop is sufficient to handle the average power deposited in the target. Nevertheless, the size of the beam at the target is typically a few hundred micrometers in both the horizontal and the vertical direction. Therefore, the possibility of local boiling and bubble formation is a concern.

To prevent the target from being overheated locally, the heat load is spread over a larger volume by sweeping the beam over a small area of the target using a device called raster [Alc04, Yan05]. The raster in Hall A is driven by a pair of horizontal (x) and vertical (y) aircore dipoles located 23 meters upstream of the target.

Before 2002, the waveform of the magnet current was sinusoidal. The rastering frequency was around 20 kHz, with an irrational ratio for x and y component to avoid a closed Lissajous pattern. Unfortunately, with that raster equipment, as the sinusoidal waveform approached its peak, it slowed down in order to reverse direction at the edge of the scan region. This caused much more beam energy to be deposited along the boundaries and at the corners, contributing to an uncertainty in target length, which in turn

affects the accuracy of the experimental data.

As described in [Yan05], since August 2002, a linear raster system with a high linear velocity and reduced turning time has been operating in Hall A. This system provides a highly homogeneous (95%) raster density distribution over the entire raster region. It achieved 98% linearity with 1000m/s linear sweep velocity. The turning time at the vertex of the raster pattern is about 0.2 μs, which is reasonably small compared to the typical 20μs of the beam traveling time from edge to edge of the target.

The experiment E00-102 was performed in 2001, before the new raster equipment was available. Nevertheless, it did not use rastered beam for production runs. On the other hand, the experiment E06-007 used extensively the new raster system, with a large rectangular pattern of about 2.5 mm x 6.0 mm as shown in Figure 4.7.

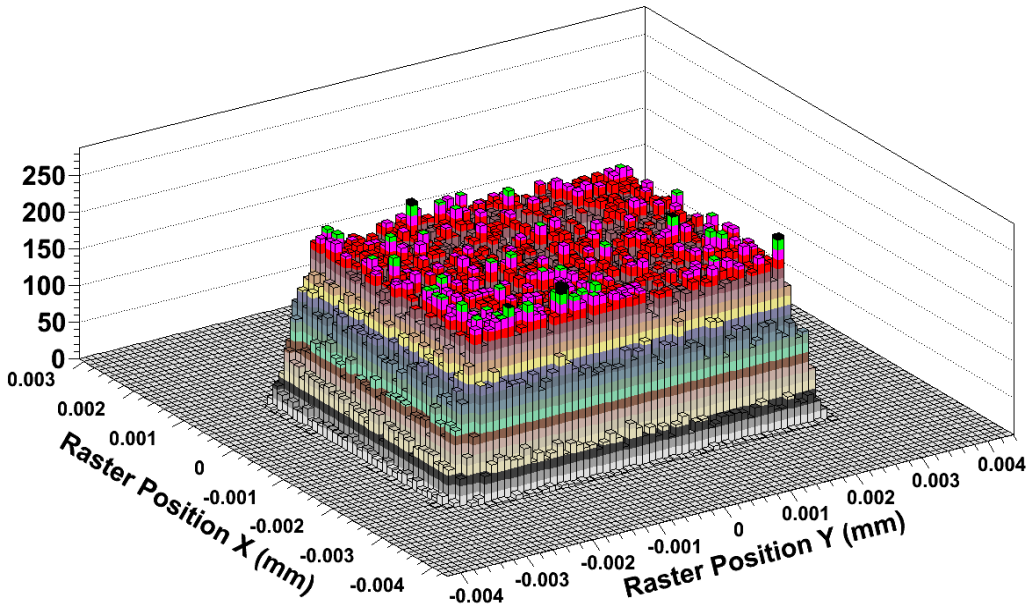

Figure 4.7: Raster position in a production run on ^{209}Bi in experiment E06-007 [RUN 2].

4.5. Target System

4.5.1. Experiment E00-102

The waterfall target constructed by a group from INFN was placed inside the scattering chamber. The basic design and configuration of the apparatus is presented in detail in [Gar92]. In the target cell, water was forced through vertical slits to form three flat, vertical, identical rectangular foils. These foils were stable due to surface tension and the adherence of the water to the 2 mm × 2 mm stainless-steel poles. The water, continuously pumped from a reservoir outside the scattering chamber, passed through a heat exchanger into the target cell, and then back into the reservoir. All targets parts in contact with water were made of stainless steel.

A configuration with three identical waterfalls was used, with each waterfall nominally 125 mg/cm^2 (0.25 cm) thick, and oriented at 32.6° to the incident beam direction. This configuration was better than a single waterfall three times as thick because the energy loss in the target was reduced. The foil angles were optimized with respect to the apertures of the spectrometers and the trajectories of the ejected particles, so that neither the scattered electrons nor the knocked-out protons went through a second waterfall for any of the kinematical settings. The layout of the three foils is displayed in Figure 4.8.

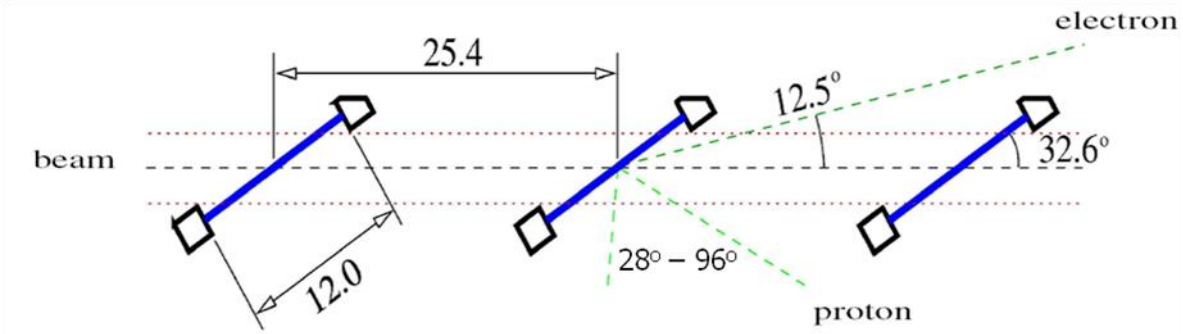

Figure 4.8: The waterfall-target configuration.

The target can was a rectangular box with a size of 20 cm x 15 cm x 10 cm, and it contained air at atmospheric pressure. Beam entrance and exit windows were made of 50 μm and 75 μm beryllium foils, respectively, which allowed for large beam currents (~70 μA) to pass through. The two side windows are made of 25 μm stainless steel, a trade-off between having enough strength to sustain the pressure difference between the air in the inner can and the vacuum in the scattering chamber while at the same time minimizing multiple scattering and radiative effects. The outer target chamber was kept under vacuum

in order to reduce energy loss and multiple scattering of beam electrons, scattered electrons and ejected protons.

Water targets are particularly useful for this experiment because of the hydrogen content of the water molecule. Since the kinematics of this experiment is quasielastic, H(e,e) can serve as a continuous luminosity monitor, and H(e,e'p) can be used to determine the *q*-direction precisely. Thus, this experiment is both self-calibrating and self-normalizing.

Once the target foils were formed, the thickness of the foils increased with the pump speed up to a maximum value, which depended essentially on the dimensions of the slits through which the water passed. Target thickness stability was monitored continuously by measuring the pump speed and the flow rate. A cooler was used to keep the water at a constant temperature. The dependence of the target thickness upon the water pump speed was mapped by looking at the spectrometer singles trigger rates at different pump tachometer settings [And05]. The experiment pump speed was chosen to make the waterfalls as thick as possible without driving the pump too hard.

As the electron beam carried a large amount of power, localized boiling in the waterfalls was induced. This reduced the water density. In order to look for this effect, the water pump speed was held constant and a scan with increasing beam current was performed. Small effects (< 5%) were seen as the current was increased [And05].

There was also a target ladder which held five thin solid targets beneath the waterfall cell. A mechanical system allowed the vertical movement of this ladder in order to change the target which was placed in the beam. One of these targets was a density-calibrated BeO foil with a thickness of 369.2 ± 2 mg/cm^2 [And05] which was used to determine the thickness of the water foils based on their $1p_{1/2}$ ^{16}O(e,e'p) yields. The effective thickness of the waterfall foils, taking into account their orientation respect to the beam, is presented in Table 4.2 [Rei05].

Foil number	1	2	3
Thickness (mg/cm^2)	281	290	234

Table 4.2: Waterfall foil thickness in the experiment E00-102.

Note that these thicknesses were only used for energy-loss corrections and as a consistency test, as the luminosity was obtained from H(e,e) events (see Section 6.3.1). A variation of a few percent in the thickness was expected from run to run due to the dynamic nature of the target.

4.5.2. Experiment E06-007

(e,e'p) experiments on heavy metal nuclei using electron beams have historically been limited because of the difficulty in employing sufficiently large electron-beam currents to make the measurements feasible. Lead and bismuth have very low thermal conductivity and very low melting points. Previous studies using electron beams [Bra00, Bob94] restricted beam currents to less than 1.5 μA and have used rotating metal foil targets to distribute the heat over large enough areas to prevent target meltdown. Experiments E06-007 [Ani06] and E06-002 [Mic06] at Jefferson Lab proposed to use electron beam currents from 50 μA to 100 μA, corresponding to power dissipations of 60 W to 120 W in targets of lead and bismuth. A calculation of heat transport radially away from the beam within the metal foils reveals that it is practically impossible to bring the low temperature close enough to the electron beam and keep the foils below their melting temperature. A new design for carrying the heat away from the foils has successfully debuted in experiment E06-007. This experiment was the first to subject heavy-metal targets to extended periods of bombardment using high beam currents.

Information about the targets used in E06-007 can be found in [TarE06]. In order to create a lead target that could resist the high incident current without melting, a special design was developed for this experiment. The electron beam was rastered over a pattern of 4 mm x 6 mm on the lead target in order to prevent excessive local beam heating due to the highly focused electron beam. Further, additional cooling of the heavy-metal targets was required. The poor thermal conductivity of these targets precludes using heat transport radially along the body of the targets. A suitable backing for these targets needs to have a high thermal conductivity to extract thermal energy perpendicular to the metal surfaces. The high thermal conductivity of diamond made it an excellent choice for carrying the heat away from the metal foils. Further, the missing energy spectrum from carbon does not interfere with the spectra of main interest from the heavy metal targets. Carbon vapor deposition (CVD) diamond foils are commercially available. The heavy metal targets (≈0.17 mm thick) were sandwiched between thin (≈0.15 mm) sheets of CVD diamond and held in a ladder frame which was actively cooled by flowing 20 K helium gas through the frame.

The experiment required that the target was tilted at 30 degrees with respect to the beam, as shown in Figure 4.9, so the actual target thickness seen by the electron beam was larger than the thicknesses just quoted (see Table 4.3). A picture of the target ladder

is shown in Figure 4.10.

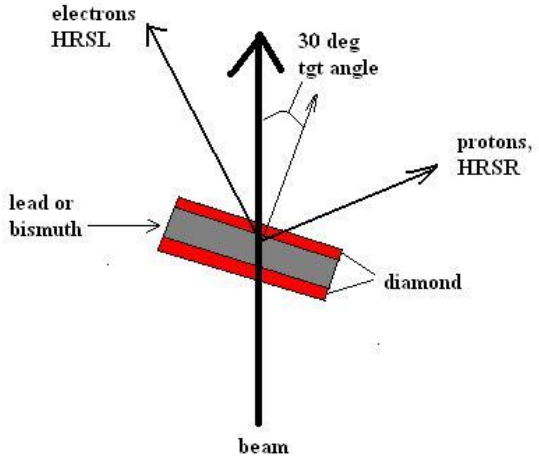

Figure 4.9: E06-007 target configuration. Targets were tilted 30º with respect to beam direction to reduce the impact of proton absorption in the target.

The target ladder used in the experiment (RUN 1) contained 5 different foil targets as shown in the pictures of the target chamber in Figure 4.10. The second part of the experiment (RUN 2), not analyzed in this thesis, used a different target setup. More details about the targets used in RUN 2 can be found in Ref. [TarE06].

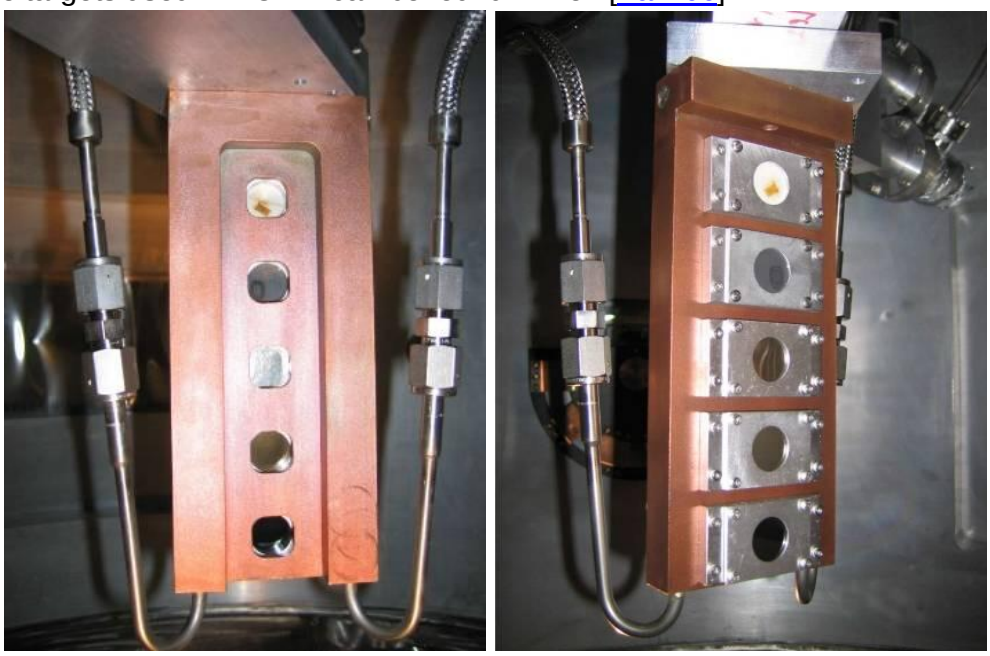

Figure 4.10: Pictures of the solid target ladder. Upstream (left) and Downstream view (right).

For this experiment (RUN 1), the diamond-metal-diamond sandwiches were held together by compression. The first lead target used (target #4 in Table 4.3). failed after a few days running at 80 μA. Examination of the experimental spectrum showed that the diamond foils were still present, but the lead had melted away under the rastered beam.

The second lead target (target #3 in Table 4.3) was exposed to a 50 μA beam for two weeks without evidence of failure. The ^{208}Pb(e,e'p) results shown in this thesis correspond to this target #3.

Table 4.3 presents the target foil positions, thicknesses and chemical purities of the targets present in the experiment E06-007. Remark that more than the actual weight or dimensions of the target, the most important parameter of the targets is their thickness (g/cm^2) as it directly affects the luminosity.

#	Target		Weight (g)	Purity (%)	Density (g/cm^3)	Size (cm × cm)	Thickness (g/cm^2)
1	BeO			99.00			0.149 (1)
2	C (graphite)		-	99.95	1.8	-	0.0838(1)
3	C+Pb+C	Diamond 1	0.3075	100	3.515	2.537 × 2.537	0.04776
		Lead 4	1.134	99.09	11.35	2.413 × 2.413	0.1947
		Diamond 2	0.2962	100	3.515	2.535 × 2.530	0.04619
4	C+Pb+C	Diamond 3	0.2989	100	3.515	2.535 × 2.537	0.04647
		Lead 5	1.128	99.09	11.35	2.413 × 2.413	0.1937
		Diamond 4	0.2541	100	3.515	2.537 × 2.537	0.03946
5	C+Bi+C	Diamond 5	0.2704	100	3.515	2.535 × 2.54	0.04776
		Bismuth	1.351	99.999	9.8	2.520 × 2.515	0.1947
		Diamond 6	0.3366	100	3.515	2.535 × 2.543	0.04619

Table 4.3: Properties of the targets employed in the experiment E06-007 (RUN 1) [TarE06].

As one of the targets was damaged during the experiment, measures were taken to assure that target integrity was maintained during the data runs employed in the analysis. Thus, single rates and distribution of coincidence counts in the target area were studied for all analyzed runs. From these tests, we found no reason to suspect that target #4 was damaged. Nevertheless, a thorough post experiment examination of target integrity and thickness uniformity would be advisable.

4.6. High Resolution Spectrometers

In order to separate the closely spaced nuclear final states and to control the systematic uncertainties in the study of (e,e'p) reactions, Hall A spectrometers were designed to have high resolution in the determination of particle momentum, position and angles. Each high resolution spectrometers consists of three quadrupoles (Q1, Q2 and Q3) and one dipole

(D). The magnets are superconducting and arranged in the QQDQ configuration shown in Figure 4.11. The bending angle is 45° in vertical plane. The nominal momentum range of each spectrometer is from 0.3 GeV/c to 4 GeV/c. Nevertheless, before the experiment E00-102, the HRS was tested to check that it could achieve the 4.1 GeV/c needed for the experiment. The momentum acceptance is ~9%, and the momentum resolution is 10^{-4}.

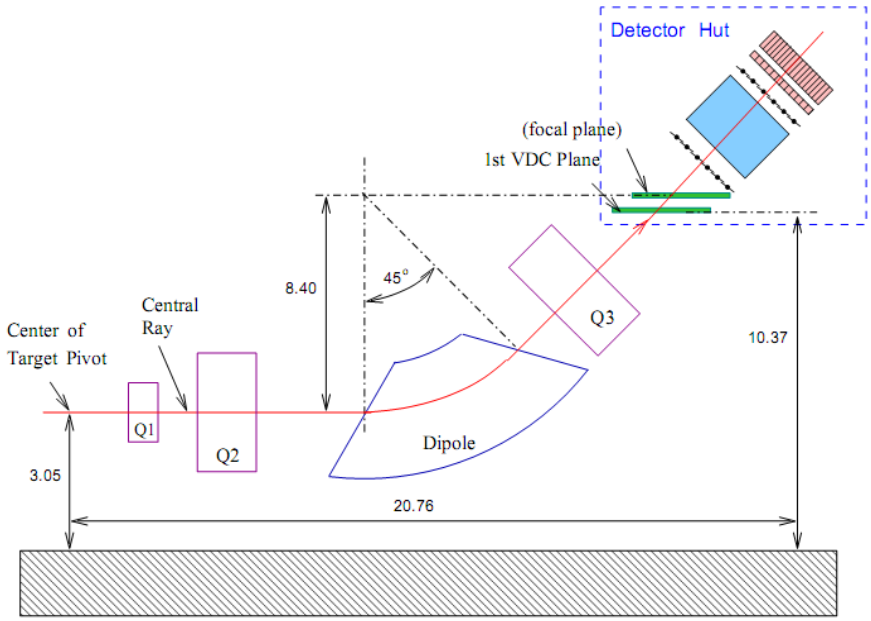

Figure 4.11: Hall A High Resolution Spectrometer and nominal design values.

Each spectrometer is point-to-point in the dispersive direction. Q1 is convergent in the dispersive (vertical) plane. Q2 and Q3 provide transverse focusing. The dipole which bends the charged particles has both its entrance and exit inclined at 30° with respect to the central axis. The magnetic field of the dipole increases with the radial distance, which provides a natural focusing in the dispersive direction. Main characteristics of the spectrometer are listed in

Table 4.4.

Configuration	QQDQ
Bending angle	45°
Optical length (m)	23.4
Momentum range (GeV/c)	0.3 to 4
Momentum acceptance (%)	±4.5
Momentum resolution (FWHM)	1.0×10^{-4}
Horizontal angular acceptance (mr)	±30
Transverse angular acceptance (mr)	±60
Solid Angle (msr)	6
Angular Resolution - Horizontal (mr)	0.6
Angular Resolution – Vertical (mr)	2.0

Table 4.4: Main characteristics of the High Resolution Spectrometers [Alc04]

4.7. Detector Packages

In these experiments, the beam-left HRS was used to detect scattered electrons, while the beam-right HRS was used to detect knocked-out protons. The polarities of the magnets and the detectors used can be customized for each experiment to detect negative or positively charged particles in either spectrometer. The detectors in each spectrometer are illustrated in Figure 4.12 and are located inside the shielded detector hut at the top of each HRS. The A1, A2 and RICH detectors on the left arm and the Gas Cerenkov detector in the right arm were not used during the experiment E00-102.

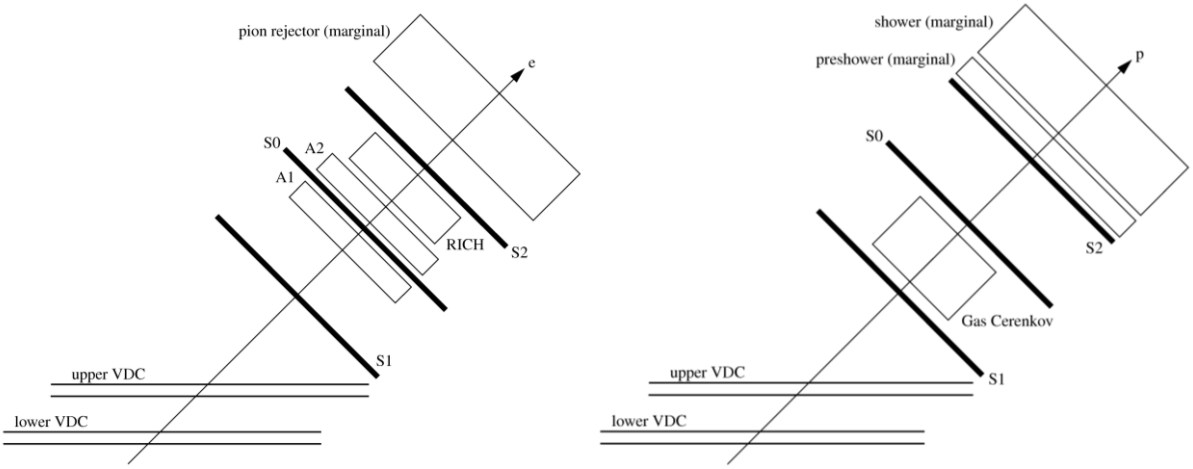

Figure 4.12: A side view of the detector stacks in each spectrometer for the experiment E00-102. (Left) Electron spectrometer; (Right) Proton spectrometer.

Both detector stacks contain a pair of vertical drift chambers (VDCs) used for particle tracking and a pair of scintillator planes (S1 and S2) used to form the trigger for the data acquisition system. The electron detector stack also contained a gas Cherenkov detector and a lead glass preshower/shower detector for particle identification. The hadron detector stack also included another scintillator detector, S0, which could be use to generate auxiliary triggers. All detectors used in the experiments E00-102 and E06-007 are briefly described below.

4.7.1. Scintillators

There are two scintillator planes S1 and S2 on each spectrometer. They form the principal trigger system for events in each spectrometer. The scintillator plane S1 is located 1.5 m downstream of the center of the first VDC. The distance between S1 and S2 is about 2 m.

The S1 plane consists of six overlapping scintillator bars (Figure 4.13), while the S2 plane has sixteen scintillator bars. Each bar has a photomultiplier tube (PMT) at each end of the bar.

The scintillator bars in both the S1 and S2 planes are oriented perpendicular to the central ray, in the horizontal direction. The two planes are arranged perpendicular to the central ray through the spectrometer, i.e. at an angle of 45º to the vertical. The active area of the S1 plane is 170 cm x 35 cm, while S2 has a slightly larger active area of 220 cm x 54 cm.

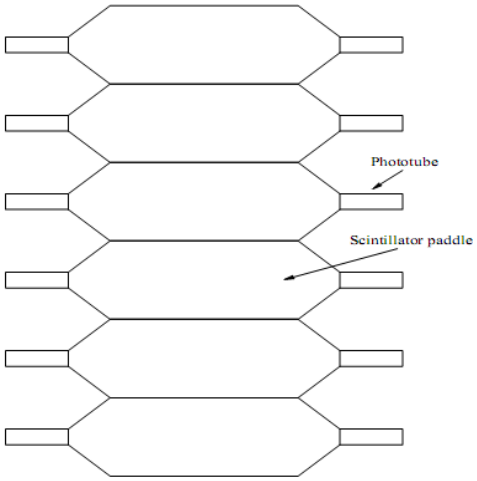

Figure 4.13: A schematic display of the scintillator plane. Each scintillator plane has six paddles. A phototube is installed on each side of each paddle.

Time and amplitude signals from the scintillators are digitized into TDC and ADC values. The width of TDC spectrum is about 1 ns, which is mainly due to the photon time walking in the scintillator, as well as the reaction time of the phototube and associated electronics. The peak position in the TDC spectrum is the time difference between the start and stop signals. The TDC start signal provides timing information to generate different types of triggers and to calculate the velocity of the particle with the time-of-flight technique. The coincidence time is the raw timing difference between the two spectrometers for a single event. The FWHM of the corrected coincidence timing peak can be about 1.4 ns after careful calibration (see Section 5.3.4).

4.7.2. Trigger system

Trigger electronics determine whether or not an event is to be recorded by the data-acquisition system. Since the two spectrometers are alike, their trigger systems are very

similar, and the coincidence trigger results from an AND operation of the two single spectrometer triggers. The trigger system is constructed from commercial CAMAC and NIM modules (discriminators, delay units, logic units and memory lookup units).

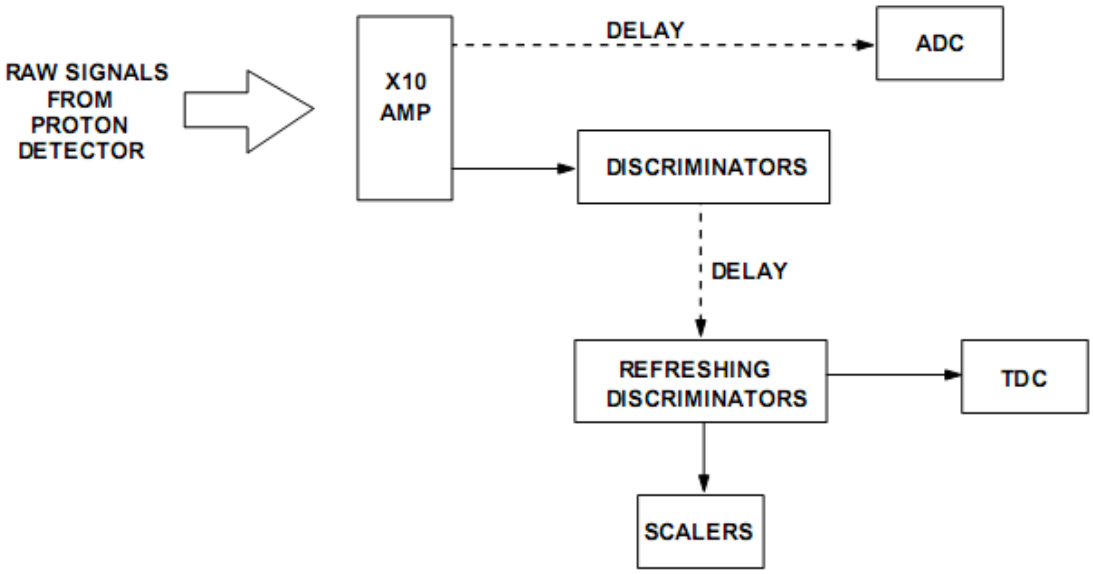

Figure 4.14: Schematic view of the signal proccesing in the trigger system.

Figure 4.14. shows how the signals are digitalized. Signals from the two sides of each scintillator paddle were sent to a logical unit AND to generate the timing signals for that scintillator paddle. In parallel, the analog signals were sent to ADCs. The timing signals were delayed, and then sent to both TDCs and scalers.

Only a certain hit pattern (S-ray) in the scintillators is identified as a good trigger. The S-ray is defined in the following manner: if the paddle n of one scintillator plane (composed of 6 paddles) fires, then on the other scintillator plane, the hit must be from one of the three paddles n-1, n, n+1, or the overlap between two of them.

Single-spectrometer triggers are formed from the mean-timed AND of the two scintillator planes. Coincidence triggers are generated from the AND of the two spectrometer triggers. There are basically five types of triggers, generated from the timing information provided by the scintillators:

T3: Main left arm trigger	T1: Main right arm trigger
T4: Loose left arm trigger	T2: Loose right arm trigger
T5: Coincidence of T1 and T3	

Table 4.5: Description of the five types of triggers generated.

Triggers (T1, T3) are formed when both scintillator planes (S1 and S2) are fired, normally implying that a charged particle passed through the spectrometer. Loosed

triggers in T2 and T4 are used to estimate efficiency. These occur when only one scintillator plane, S1 or S2, is fired. Trigger T5 is a coincidence of T1 and T3, normally implying that two particles detected by the two spectrometers are produced at the target simultaneously. The fraction of data recorded from each type of triggers can be chosen by setting appropriate prescale factors. In these experiments the prescale factor for coincidence events was always set to unity so that no coincidence events were prescaled away.

The Trigger Supervisor (TS) module, built by the CEBAF Data Acquisition Group, synchronizes the readout crates and administers the dead time logic for the entire system. It also enforces the user-selected prescales used to record only some fraction of each type of events. A diagnostic trigger created by a 1024 Hz pulser provides means for generating ADC pedestals as well as assessing electronic and computer dead time.

4.7.3. Vertical Drift Chambers

Within the detector package of each spectrometer, there are two paired vertical drift chambers (VDCs) [Fis01, Alc04] which determine the trajectories of the charged particles at the focal plane. Figure 4.11 shows how these two VDCs are positioned. As can be seen, they are identical and parallel to each other. The bottom one is placed near the actual focal plane. The top one is about 35 cm above the bottom chamber, and shifted by about 35 cm with respect to the bottom one in the dispersive direction. The size of each VDC is about 240 cm x 40 cm x 10 cm. The active area is 211.8 cm x 28.8 cm. The nominal central ray is within 0.5 cm of the center of the bottom VDC.

There are four wire planes for each VDC pair. Each wire plane has 368 signal wires. The signal wires are separated by 4.243 mm, and the distance between the wires and the high voltage planes is 13 mm (Figure 4.15). The wires are oriented at ± 45° with respect to the dispersive direction.

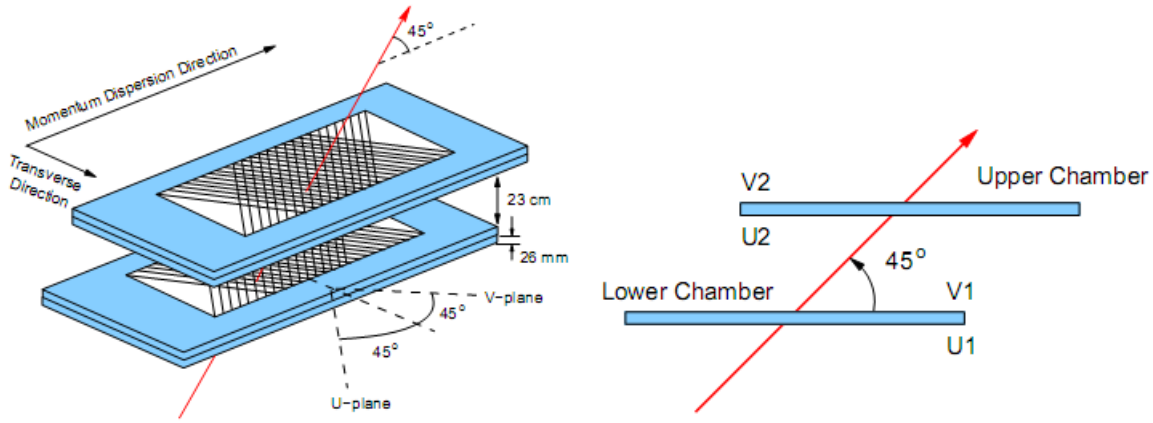

Figure 4.15: A diagram of the VDC wire planes showing the orientation of the wires relative to the central ray (left figure) and a side view of the VDC pair (right figure).

Each VDC consists of two gas windows, two wire planes, and three high voltage (HV) planes. Each gas window is made of 6 µm thick Mylar film coated with aluminum to shield the signals from noise. Each wire plane is sandwiched between two high voltage planes. The distance between a wire plane and a neighboring high voltage plane is 13 mm. The three high voltage planes are 6 µm thick Mylar film coated with a 0.5 µm layer of gold for good conductivity. The middle high voltage plane is coated with gold on both sides, while the other two high voltage planes are single sided. There are 400 wires on each wire plane. The first and last 16 wires on each wire plane are grounded to shape the electric field. The remaining 368 wires are all 20 µm diameter signal wires which are made of tungsten coated with gold.

Figure 4.16 shows a typical particle trajectory through the VDC creating a five-cell event; that is, the five wires closest to the trajectory register a hit. The electric field lines between the wires and the cathode planes (mylar foils) and the electrons drift along the path of least time - the geodetic path - and induce a signal in the wires are also shown.

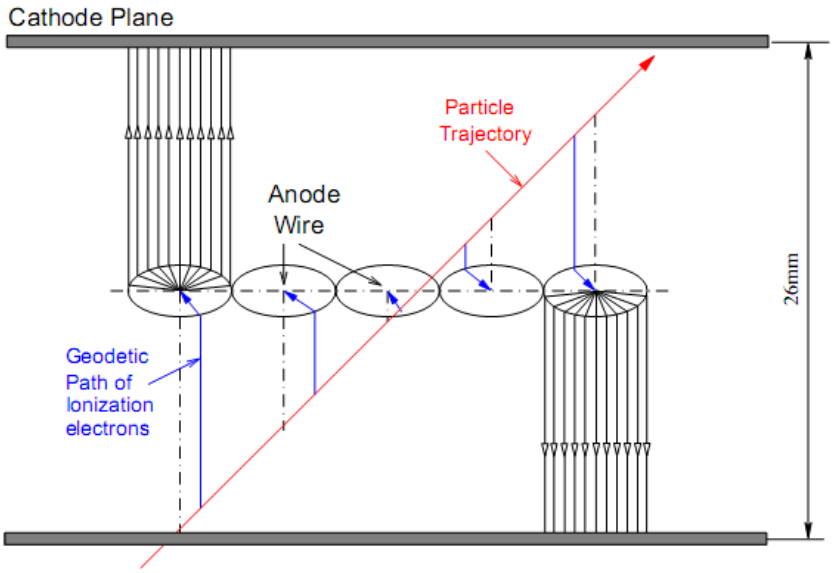

Figure 4.16: A typical particle trajectory through the VDC.

The gas used for VDC is an argon (62%) and ethane (38%) mixture. The operational high voltage is about -4.0 kV. When a charged particle passes through the VDC, the atoms of the gas are ionized along its trajectory. The electrons drift along the electric field lines towards the wire. In the vicinity of the wire, the electric field increases as 1/r and the electrons can gain enough energy within a single mean-free path to cause ionization. The ionized electrons will again gain enough energy to induce more ionizations. This process is called an avalanche. As the avalanche approaches the wire, a negative signal is induced by the rapid depletion of the ions.

A TDC is used to measure the time elapsed between the initial ionization and the induction of the signal on the sense wire. Knowledge of the drift velocity of the electron in the chamber gas allows for the derivation of the drift distance and eventually the perpendicular distance between the particle trajectory and the wire. Generally, five or six adjacent wires fire for each trajectory. However, in these experiments, only 3 wires were required to acquire sufficient tracking information for a plane.

The intersection point between the trajectory and the wire plane may be determined from the distances between the trajectory and the wires. As there are four wire planes on each spectrometer, four intersection points are usually obtained. These lead to two positions (x_{fp} ,y_{fp}) and two angles (θ_{fp},ϕ_{fp}) for each trajectory at the focal plane. Each wire is positioned with accuracy better than 50 μm [Fis01]. The relative position of the VDCs is known down to 100 μm. The main contribution to the ultimate position resolution comes from the drift-time measurement. The final FWHM focal plane position resolution due to

the VDC pair is about 200 μm.

4.8. Data Acquisition

Data taken at JLAB are primarily collected using the CEBAF Online Data Acquisition system (CODA) [Alc04]. CODA provides software tools to take the raw data from ADC, TDC and scaler modules, build events from the various pieces of information read out and then record the event data. Data is usually first written to a local disk and then transferred to a long-term storage system.

Raw signals from the detectors are first amplified and then split, with one copy to ADCs and the other to TDCs via constant fraction discriminator (CFD) modules. All of these front-end modules are located in the detector hut on each HRS. The Trigger Supervisor (TS) module decides if signals from the detector correspond to valid triggers or not.

Data from the ADCs and TDCs are collected by the CODA Read Out Controllers (ROCs).. ROCs then pass the data to the CODA Event Builder (EB), which uses the pieces of information from the various ROCs to construct a single data structure for each event. Finally the data is passed from the EB to the Event Recorder (ER), which writes data to a local disk. Various other pieces of information are inserted into the data stream at frequent intervals; for example, the beam current and beam position values.

There are several types of events in the data stream. The first few events in the data file of each run are status events, which are included whenever the state of the run changed. In addition, there are some user-defined status events. Most events in the data file are physics events, which contained information from only one spectrometer (single arm) or both spectrometers (coincidence). For these experiments, the size of a typical coincidence event was about 1.0 kB, and a single arm event was about 0.5 kB. In addition to the two types of events above, there are scaler events which were read out every 10 seconds, and EPICS events which included the beam position and beam current information.

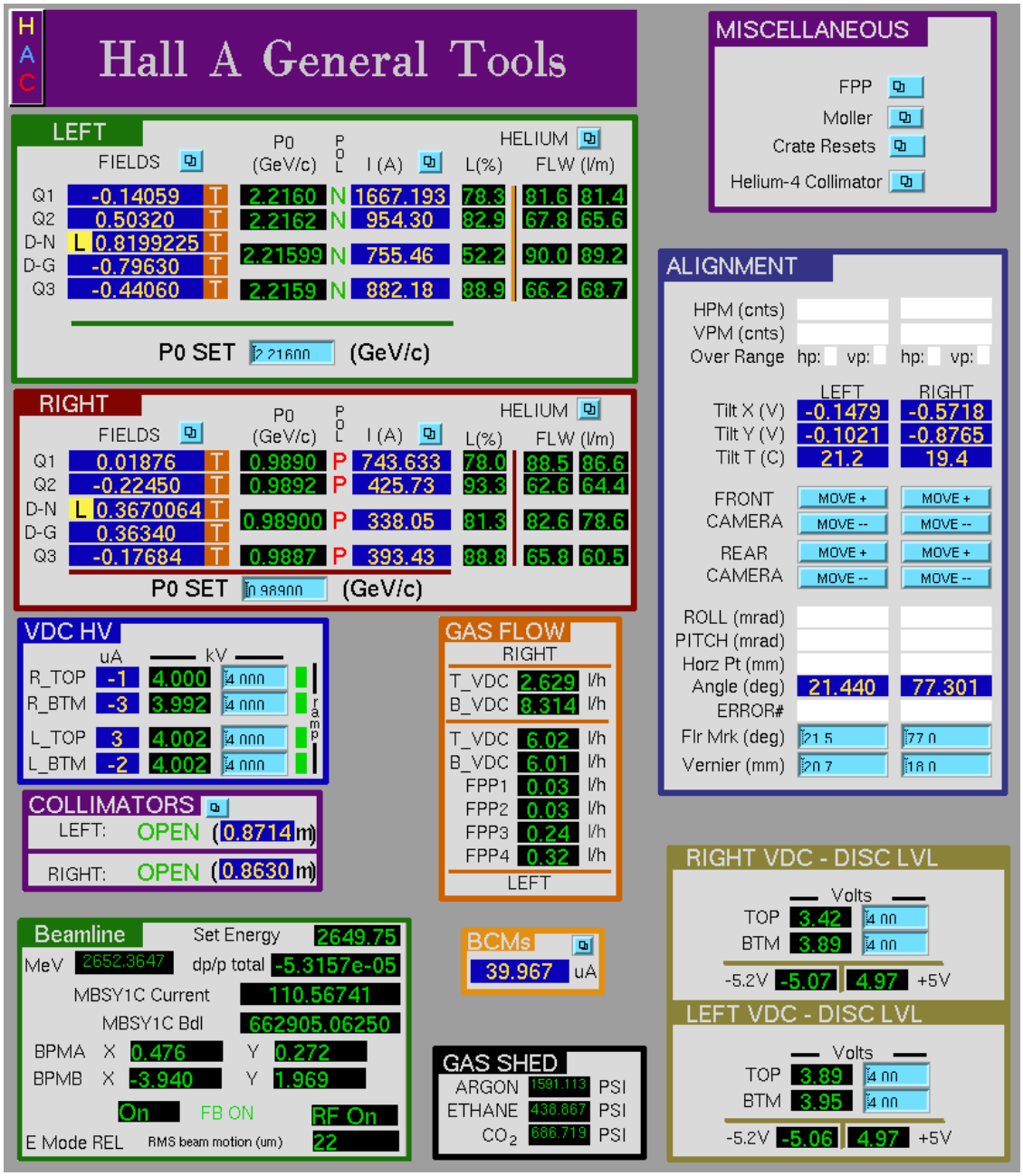

Figure 4.17: Hall A Main Control Screen. Settings are from kin 8 of E06-007 (Table 8.2).

4.9. Data Analysis Software

The physics analysis software used in this thesis was the Hall A C++ Analyzer [Analyzer], referred here as "Analyzer". This code is built using an object-oriented (OO) approach on top of the ROOT libraries from CERN [ROOT]. It was adapted from the FORTRAN-based code ESPACE [Event Scanning Program for hall A Collaboration Experiments] previously used in early Hall A experiments.

Raw data from the data acquisition (DAQ) are decoded and analyzed by this event-processing program. The event processor creates data summary files in .root files which

contain the computed data in ntuple format. Final physics results are then extracted from the summary files with either ROOT or Analyzer. At the end of the analysis of a raw data file, Analyzer creates also a summary text file with some statistics and scalers information.

The code itself is relatively flexible and user-friendly. A detailed description can be found at Ref. [Analyzer]. Some main features for Analyzer are presented below:

- It can read and decode raw data.
- It carries out the VDC analysis computing the focal plane position (x_{fp} , y_{fp}) and trajectory angles (θ_{fp},φ_{fp}).
- It reconstructs the momentum (direction and magnitude) and interaction vertex at the target for the detected charged particles based on the coordinates of the particle detected at the focal plane in each HRS and the optics database.
- It can perform a so-called *optics optimization*: an interactive fitting procedure to the optics study data in order to get the correct optical matrix elements
- It contains a logic package *which allows for c*reating spectra with logic tests and cut conditions as well as filtering data according to predetermined conditions.
- It can correct the raw time-of-flight event-by-event for path length and velocity variations. It can also correct for energy losses of charged particles before and after the reaction.
- It may display data in user-defined histograms and graphical user interface (GUI).

4.10. Coordinate Systems

The data analysis requires the particle trajectories do be defined in the following right-handed Cartesian coordinate systems.

4.10.1. Hall Coordinate System (HCS)

The origin is the center of the Hall, defined as the intersection of the "ideal" unrastered electron beam with the plane perpendicular to the beam that contains the vertical symmetry axis of the target system. The z-axis is in the beam direction, the y-axis points vertically upwards and the x-axis points to the left of the beam line, perpendicular to the y- and z-axes. Its origin is defined to be the center of the hall, with the z-axis pointing along the electron beam direction. This coordinate system is shown in Figure 4.18.

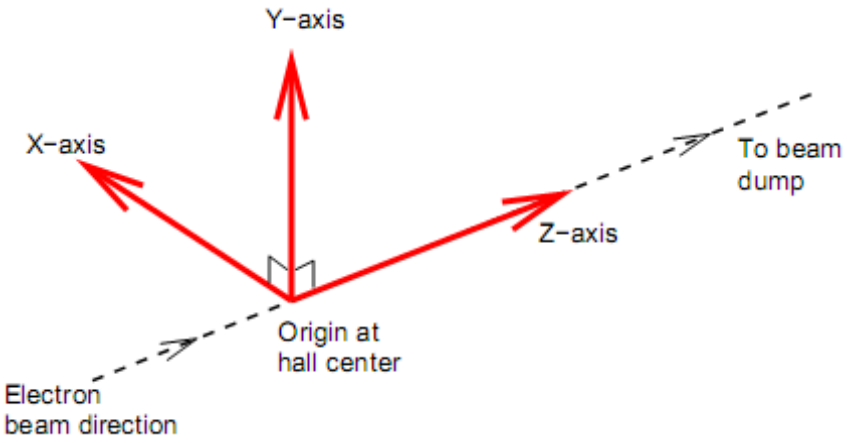

Figure 4.18: Hall A Coordinate System.

4.10.2. Target Coordinate System (TCS)

The origin is defined as the point 1.25 m from the center of the central hole in the sieve slit plate1, perpendicular to the sieve plate surface and pointing toward the target. The z_{tg}-axis is defined as the line perpendicular to the sieve-slit plate of each spectrometer, pointing towards the central hole in the sieve plate. The x_{tg}-axis points vertically downwards and the y_{tg}-axis form the right-handed triplet. The in-plane (φ_{tg}) and out-of-plane angles (θ_{tg}) of the scattered particle, are defined in this coordinate system as:

$$\begin{aligned} \tan\theta_{tg} &= \frac{dx}{dz} \\ \tan\phi_{tg} &= \frac{dy}{dz} \end{aligned} \qquad (4.2)$$

Figure 4.19 shows these angles. Note that the z_{tg}-axis points along the central axis of the spectrometer and is rotated an angle θ_0 from the electron beam direction.

The deviation δp_{tg} of the particle momentum (p) from the central momentum of the spectrometer (p_0) is given by

$$\delta p_{tg} = \frac{p - p_0}{p_0} \tag{4.3}$$

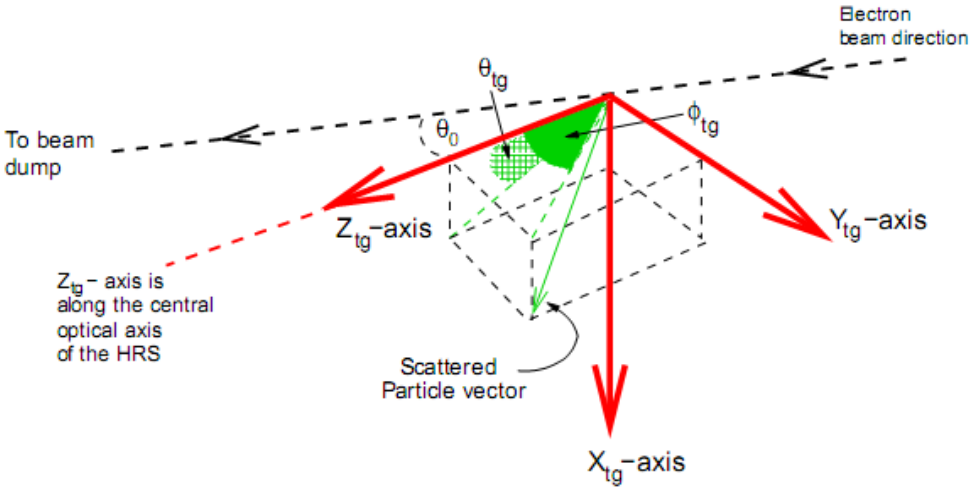

Figure 4.19: Target Coordinate System.

4.10.3. Detector Coordinate System (DCS)

The track through the VDC is determined as described in Section 4.7.3 in terms of wire plane coordinates, u and v (see Figure 4.15). For further analysis, it is advantageous to convert these coordinates into detector coordinates: x_{det} and y_{det}. Taking into account the 45º orientation of the wires as described in Section 4.7.3, the coordinate transformation is obtained by a rotation of 45° around the z-axis (perpendicular to the detector plane, pointing upward):

$$x_{\mathrm{det}} = \frac{\sqrt{2}}{2} \cdot (u + v); \qquad y_{\mathrm{det}} = \frac{\sqrt{2}}{2} \cdot (u - v) \tag{4.4}$$

The origin of the Detector Coordinate System (DCS) is the intersection of wire 184 in the U1 plane and the projection of wire 184 in the V1 plane onto the U1 plane.

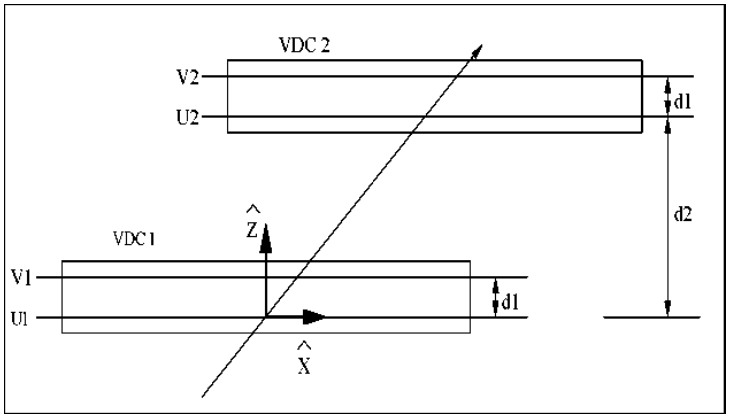

Figure 3.5: A side view of the DCS. d1 is 26 mm and d2 is about 35 cm.

4.10.4. Focal Plane Coordinate System (FCS)

This is a rotated coordinate system where the z_{fp}-axis is rotated by an angle $\rho(x_{fp})$ between the local central ray of the spectrometer and the vertical axis in the VDC wire plane. This means z_{fp}-axis rotates along the long symmetry axis of the VDC as a function of the relative momentum δp_{tg}, as shown in Figure 4.20.

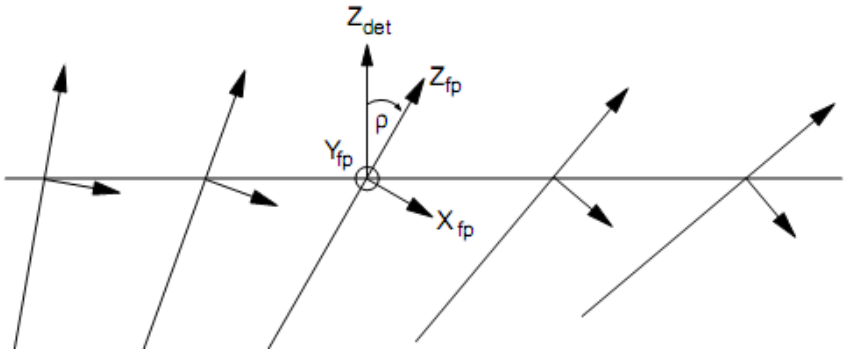

Figure 4.20: Focal Plane Coordinate System.

4.11. Event Reconstruction

4.11.1. Reconstruction of Focal Plane Variables

The trajectories of the charged particles at the focal plane are determined from the cross-over positions $(u_1, v_1)\text{and}(u_2, v_2)$ of the two tracks, measured in the two VDCs of each spectrometer (Figure 4.21).

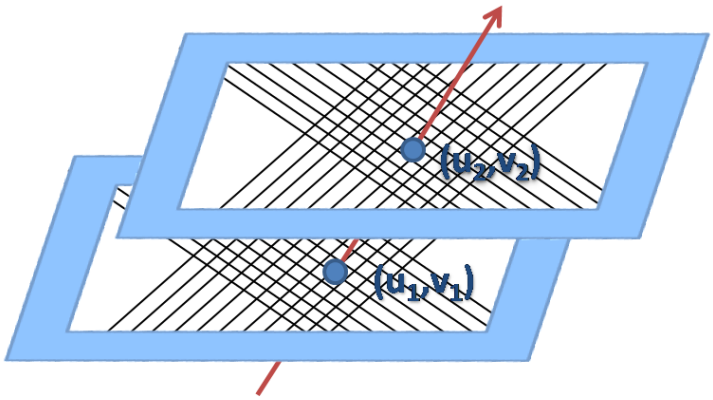

Figure 4.21: Cross-over position (u_1,v_1) and (u_2,v_2) of the tracks obtained from each VDC.

In order to get the trajectory, the following steps are followed [Alc04]:

1) Hit selection and cluster identification.

2) TDC corrections - In principle, tracks can be reconstructed using only the cluster center coordinates, which can be obtained from the known wire locations; however, the spatial resolution per plane available in this way is of order of the wire separation 4.2 mm; which is not sufficient to meet the precision requirements of the Hall A spectrometers.

Better resolution can be obtained by analyzing the TDC timing information. TDC data allow for extraction of the projected drift distances d_i within each wire cell C_i. Once the distances d_i are known, the crossing point of the track in the wire plane can be determined with high precision by means of a linear fit of drift distances vs. wire positions. The typical per-cluster position resolution obtained with the Hall A VDCs obtained with this procedure is 225 μm FWHM [Fis01].

3) Local cluster fitting.

4) Most-probable track selection - In case of multiple clusters, the most probable track ("Golden Track") is chosen.

When the *u,v* coordinates in each VDC have been obtained, the position and angles of the particle passing the focal plane can be calculated easily:

$$\left(u_1, v_1\right) \,\&\, \left(u_2, v_2\right) \longrightarrow \left(x_{\det 1}, y_{\det 1}\right) \,\&\, \left(x_{\det 2}, y_{\det 2}\right) \longrightarrow \left(x_{fp}, y_{fp}, \theta_{fp}, \phi_{fp}\right) \tag{4.5}$$

4.11.2. Reconstruction of Target Variables

The variables at target θ_{tg}, φ_{tg}, y_{tg} and δp_{tg} are obtained from the variables measured at the focal plane (x_{fp}, y_{fp}, θ_{fp}, φ_{fp}) by the VDC pair. δp_{tg} is defined as the relative momentum of the detected particle with respect to the central momentum p_0 of the HRS

$$\delta p_{tg} \equiv dp \big/ p_0 = (p_{tg} - p_0) \big/ p_0 \tag{4.6}$$

The position of the particle and the tangent of the angle defined by its trajectory along the dispersive direction are given by (θ_{tg},x_{tg}). Effectively, the x_{tg} is set at 0 during the optics calibration by requiring that the beam spot is within 100 μm of the y-z plane of the target coordinate system. The focal-plane coordinates and the target coordinates are linked by a set of matrix elements Y_{ijkl}, T_{ijkl}, P_{ijkl} *and* D_{ijkl}, where

$$\begin{aligned}
y_{tg} &= \sum_{ijkl} Y_{ijkl} x_{fp}^i \theta_{fp}^j y_{fp}^j \phi_{fp}^k \\
\theta_{tg} &= \sum_{ijkl} T_{ijkl} x_{fp}^i \theta_{fp}^j y_{fp}^j \phi_{fp}^k \\
\phi_{tg} &= \sum_{ijkl} P_{ijkl} x_{fp}^i \theta_{fp}^j y_{fp}^j \phi_{fp}^k \\
\delta p_{tg} &= \sum_{ijkl} D_{ijkl} x_{fp}^i \theta_{fp}^j y_{fp}^j \phi_{fp}^k
\end{aligned} \tag{4.7}$$

The vertical mid-plane symmetry of each spectrometer requires that, $T_{ijkl} = D_{ijkl} = 0$ for odd (k+l), $Y_{ijkl} = P_{ijkl} = 0$ for even (k+l).

In order to completely reconstruct the reaction vertex, it is necessary to include the information from beam position as obtained by BPMs and raster variables

$$\begin{pmatrix} x_{fp} \\ y_{fp} \\ \theta_{fp} \\ \phi_{fp} \end{pmatrix} \xrightarrow{OPTICS} \begin{pmatrix} y_{tg} \\ \theta_{tg} \\ \phi_{tg} \\ \delta p_{tg} \end{pmatrix} \xrightarrow[+RASTER]{+BPM} \begin{pmatrix} x_{tg} \\ y_{tg} \\ z_{tg} \\ \theta'_{tg} \\ \phi_{tg} \\ \delta p'_{tg} \end{pmatrix} \tag{4.8}$$

With the BPMs and the raster properly calibrated (see 5.1.1 and 5.1.4), the position x_{tg} (that is, the vertical direction in the Hall Coordinate System) and z_{tg}. (the position along the beam) can be obtained. Furthermore, the momentum δp_{tg} and out-of-plane angle θ_{tg} can be corrected for slight deviations of the beam from its nominal central path. This is considered in Section 5.3.3.

As it can be seen in Figure 5.16, the reconstruction of z_{tg} requires good resolution in the variable y_{tg}, as well as corrections for the possible mispointing of the spectrometers (see Section 5.3.2).

4.11.3. Reconstruction of Physical Variables

Using the information from the incident electron beam $\vec{k}_i$, the scattered electron $\vec{k}_f$ and the ejected proton $\vec{p}_p$, it is possible to obtain all the relevant physical variables in the (e,e'p) reaction. It is convenient to separate the reconstruction process into two main parts: the leptonic vertex and the hadronic vertex.

Leptonic Vertex: $\left(\vec{k}_i, \vec{k}_f\right) \longrightarrow \left(\vec{q}, \omega\right)$

Based the isotropy of the process the momentum of the incident beam can be set to be in the z-axis of the Laboratory Coordinate System (LCS) without loss of generality. Therefore, there are 4 input variables (the energy of the incident beam and the 3-momentum of the scattered electron) to reconstruct the 4 variables of the virtual photon exchanged (energy ω and 3-momentum $\vec{q}$):

$$\begin{matrix} \vec{k}_i = (0,0,k_i) \\ \vec{k}_f = (k_{fx}, k_{fy}, k_{fz}) \end{matrix} \longrightarrow \begin{matrix} \omega = k_i - k_f \\ \vec{q} = \left(-k_{fx}, -k_{fy}, k_i - k_{fz}\right) \end{matrix} \tag{4.9}$$

Hadronic Vertex: $\left(\vec{q}, \omega\right) + \vec{p}_p \longrightarrow \left(E_m, p_m, q, \omega, \phi\right)$

With the information in hand of the virtual photon exchanged, we can focus on the (γ,p) reaction. We can now look at the hadronic vertex as a generalized (γ,p) reaction where the gamma ray, being virtual, is not bound to the $q^2 - \omega^2 = 0$ relation.

Using again the isotropy of the process, the momentum of the virtual photon can be set to be along the z-axis of a new reference system. The x-axis of this reference system is set to be in the scattering plane (formed by the incident and ejected proton). This can be

called the "*q*-Coordinate System". The 3-momentum of the ejected proton will be referred in this new *q*-coordinate system $\vec{p}_p \rightarrow p_p, \theta_{pq}, \phi_{pq}$ instead of in the LCS.

Thus, there are 5 variables as inputs and 5 variables as the final result:

$$\begin{matrix} \omega \\ \vec{q} = (0,0,q) \\ \vec{p}_p \rightarrow p_p, \theta_{pq}, \phi_{pq} \end{matrix} \longrightarrow \begin{cases} q, \omega, \phi_{pq} \\ p_{miss} = p_{miss}(q, p_p, \theta_{pq}) \\ E_{miss} = E_{miss}(\omega, p_p, p_{miss}) \end{cases}$$

4.11.4. Radiative Effects in the Reconstruction of Physical Variables

If radiation is present, the previous scheme for the reconstruction of physical variables is modified. Using the Peaking Approximation (Section 3.6) and neglecting radiation from the ejected proton, the radiated photons will be only emitted in the direction of the incident electron (CASE A) or in the direction of the scattered electron (CASE B). Therefore, only the magnitude of the radiated photon k_γ is unknown. Fortunately, the information from the position of the E_{miss} peaks (only certain values of E_{miss} are expected in case of no radiation) can be used to recover this unknown information.

It is convenient to differentiate, in this case, the asymptotic (measured) values of the variables from the vertex values (the actual values of the variables in the interaction point):

	ASYMPTOTIC (MEASURED VALUE)	VERTEX (ACTUAL VALUE)
CASE A (Incident electron radiates kγ)	$\vec{k}_i, \vec{k}_f$	$\vec{k}_i' = \vec{k}_i - \vec{k}_\gamma, \vec{k}_f$
CASE B (Ejected electron radiates kγ)	$\vec{k}_i, \vec{k}_f'$	$\vec{k}_i, \vec{k}_f = \vec{k}_f' + \vec{k}_\gamma$

Table 4.6: Differences between asymptotic (measured) variables and vertex variables.

The main problem that radiation causes, from the point of view of the reconstruction of the physical variables, is that the direction of the $\vec{q}$ vector changes, and although the proton 3-momentum is not affected by radiation, the "*q*-Coordinate System" changes and so the coordinates of p_p referred to this system do change.

$$\vec{k}_i', \vec{k}_f' \rightarrow (\vec{q}', \omega') \xrightarrow{+\vec{p}_p} (q', \omega', p_p, \theta_{pq'}, \phi_{pq'}) \rightarrow (E_m', p_m', q', \omega', \phi_{pq'}) \quad (4.10)$$

It is important to remark that the angle ϕ_{pq} between the scattering plane and the reaction plane is significantly modified by radiation and because of the reduced range measured in this variable (close to 0 or π, for most kinematics) this effect cannot be easily corrected.

5. Data Analysis I – Calibrations, Efficiencies and Corrections

5.1. Calibration of Beam Parameters

5.1.1. Beam Current Calibration

The general procedure for calibrating the beam current in Hall A is summarized in Figure 5.1.

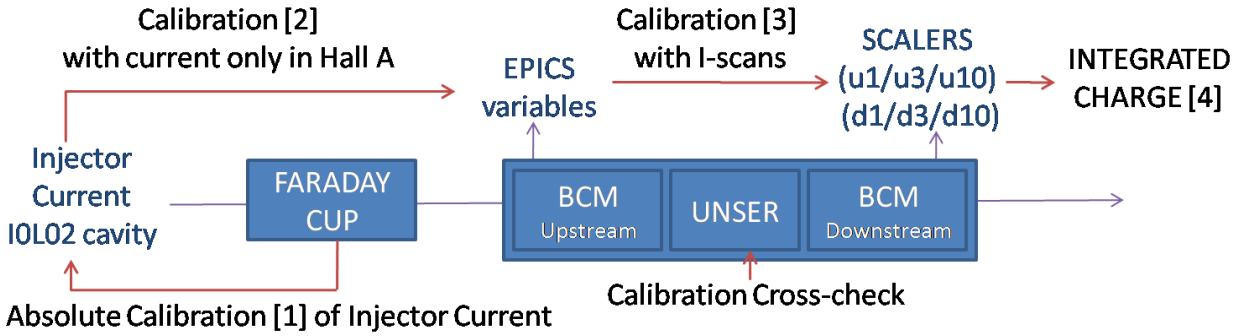

Figure 5.1: Schematic description of the steps followed for the beam current calibration.

During the BCM calibration runs, different current settings are measured when beam is only sent to Hall A. The current from the Faraday cup, OLO2 cavity (Faraday, IOLO2) and the average voltage level of BCM cavities (V^u,V^d) are measured at the same time and data is written to a bcm_log file.

In order to take into account offsets in EPICS and scalers measurements, data runs when no current was present in the hall (for example, in calibration runs or cosmic-ray runs) were analyzed. These offsets are not supposed to vary during the experiment, but this was checked on different days during the experiment.

- **Experiment E00-102**

No special efforts were devoted to obtaining a precise calibration of the beam current during the experiment E00-102, as the beam charge measurement was only used as a reference value. In this experiment, luminosity was obtained from the number of H(e,e) recorded events. This method was proven to be an effective way of reducing systematic errors in the previous E89-003 experiment [Gao99]. Therefore, it was assumed that the beam charge from the scalers, as obtained from the end-of-run information, was already

well calibrated. No significant errors are expected as the BCMs were precisely calibrated in a previous experiment and this calibration has proved to be stable as a function of time.

- **Experiment E06-007**

The calibration runs used correspond to the bcmlog_125(127) files acquired one week before the start of the experiment. This type of calibration has previously been proven to be stable over experiments lasting several.

The steps followed to perform the BCM calibration were:

STEP 1 - Absolute Calibration of OLO2 Injector Current

The OLO2 Cavity Monitor and Faraday Cup at the accelerator injector section were used to provide an absolute current reference. OLO2 was compared to Faraday Cup measurements to check that the absolute beam current values were reliable. A comparison of the ratio of the current as measured with both methods for currents higher than 5 μA is shown in Figure 5.2. They agree to 0.3%.

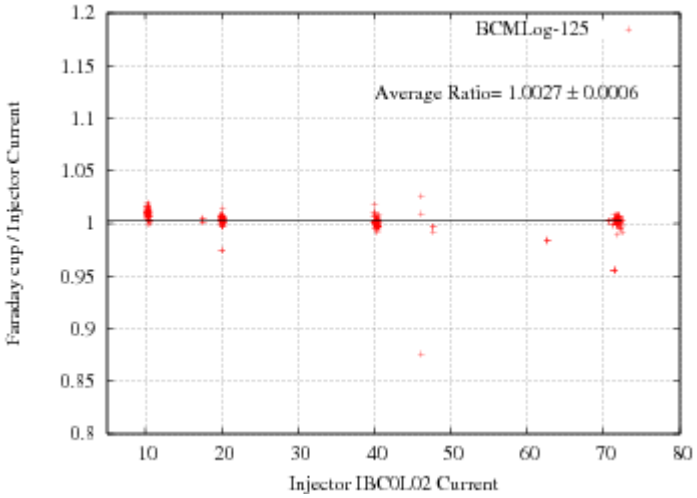

Figure 5.2: Comparison of the Faraday Cup and the Injector OLO2 Current measurements.

STEP 2 - EPICS Calibration

The EPICS calibration constants were obtained from a linear fit of OLO2 vs. the EPICS value corrected by the corresponding offset of BCM cavities

$$I_{OLO2} = K_{EPICS}{}^{u,d} \cdot \left(V^{u,d} - offset_{EPICS}^{u,d} \right) \tag{5.1}$$

These offsets were determined from EPICS measurements when the beam was off. The measured voltages V^u and V^d from the BCM (upstream and downstream respectively) when no current was present in the hall were averaged over the run to obtain the offset EPICS values. The resulting values for the calibration can be found in Table 5.1 and the plots of the OLO2 current vs. the EPICS values are displayed in Figure 5.3. The value of

the constants obtained for both the upstream and downstream BCM are compatible with those obtained in other experiments. Currents below 5 μA were not used for the final fitting procedure, as they had a non-linear behavior and typical currents in this experiment were around 40 μA.

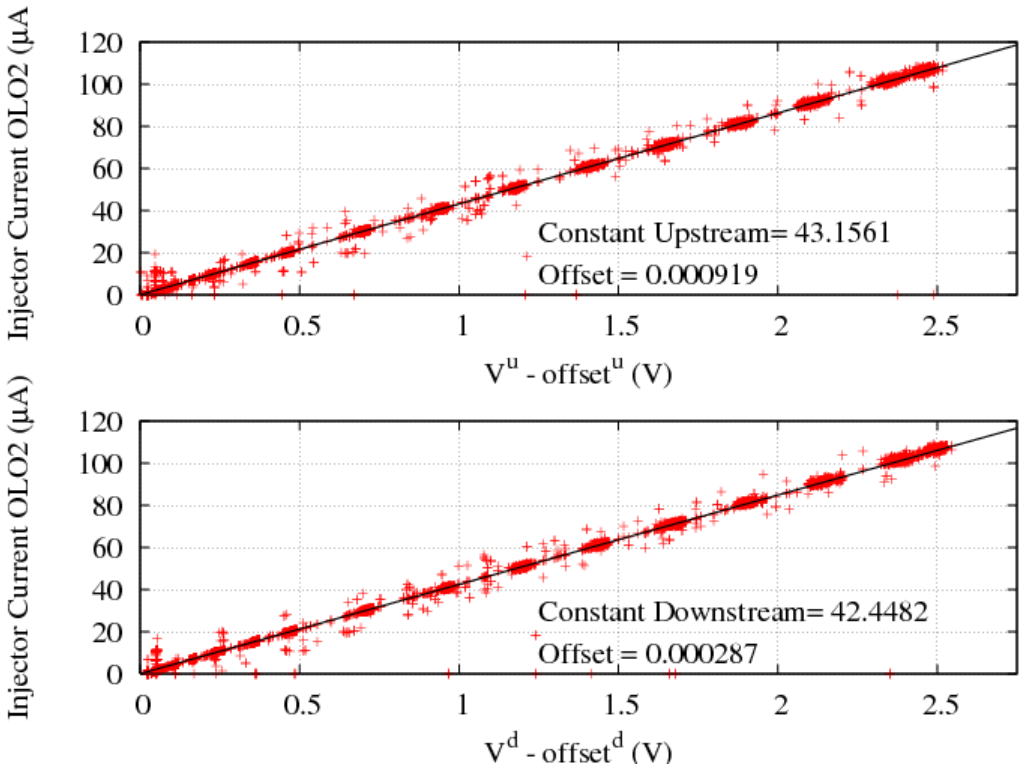

Figure 5.3: Injector Current vs EPICS variables (top pad -- upstream, bottom pad -- downstream).

	Upstream	Downstream
Offset	0.0009191 ± 1e-07	0.00028730 ± 5e-08
Constant	43.2 ± 0.05	42.5 ± 0.06
Constant (I>5μA)	43.3 ± 0.02	42.6 ± 0.02

Table 5.1: Results from EPICS calibration.

With the EPICS calibration constants obtained from the fitting procedure, the averaged beam current during the data-taking period is given by:

$$I_{av} = K_{EPICS} \cdot \left(V^{u,d} - offset_{EPICS} \right) \tag{5.2}$$

STEP 3 - Scalers Calibration

The beam current and hence the charge, $Q_a = I_a\ t$, can be obtained from the BCM scaler reading as follows [Sul06]

$$I_a = \frac{N_a\ /\ t - offset_a}{k_a} \tag{5.3}$$

$$\rightarrow Q_a = \frac{N_a - offset_a \cdot t}{k_a} \tag{5.4}$$

where a = 1, 3, 10 is the gain factor, t is the time for each run (in seconds) and N_a is the BCM scaler reading for each gain factor.

The BCM scaler offsets are determined from the calibration runs during periods without beam delivered to the experimental hall. The time dependence of these offsets were checked periodically and were found to be reasonably stable during the experiment.

Table 5.2 shows the offset rate in Hertz for the upstream and downstream BCMs for the three amplification factors. These offset values were determined by averaging the scaler readings for each BCM over the entire run.

	U1 (Hz)	U3 (Hz)	U10 (Hz)	D1 (Hz)	D3 (Hz)	D10 (Hz)
Run 1335	353.959	449.124	769.504	161.289	133.073	326.945

Table 5.2: Offset rate of BCM scalers.

The BCM scalers calibration constants k_a were determined from intensity-scan runs (I-scan). For E06-007 these calibration runs were performed during the experiment in March 2007. These short runs with a different incident beam intensity on each target were used as a quick test of single rates and linearity.

Once that the EPICS BCM variables are well calibrated, a relative calibration between scaler BCM values and EPICS BCM current can be obtained. The values of the calibration constants obtained are given in

Table 5.3. Compared to calibrations from other neighboring experiments, these results vary by < 1%.

Current	U1	U3	U10	D1	D3	D10
5.62	2368.87	7288.25	28010.50	2333.33	7233.49	22848.08
9.77	2367.87	7284.67	26507.30	2337.04	7242.17	22877.50
19.91	2366.45	7279.48	25761.77	2337.90	7242.01	22879.11
40.26	2366.19	7277.08	26787.56	2339.68	7244.73	22740.94
4.86	2369.84	7291.41	28384.30	2336.07	7242.90	22877.60
19.83	2367.49	7282.48	26275.95	2338.95	7245.49	22890.23
39.94	2365.37	7274.34	25031.78	2341.17	7249.47	22782.08
50.36	2365.30	7273.11	22919.79	2341.55	7249.50	20712.17
MEAN =	2367.17	7281.35	26209.87	2338.21	7243.72	22575.96
ERROR =	0.58	2.31	609.60	0.97	1.80	266.93

Table 5.3: Scalers BCM calibration constants for E06-007.

In this work, U3 was used to determine the charge via Eq. (5.4). U3 typically behaves in a more stable fashion than its counterparts and it has been the common choice in several previous experiments.

5.1.2. Beam Position Calibration

To obtain the correct beam position information, the necessary optimizations and calibrations were performed. During these measurements, a bulls-eye scans with unrastered beam were steered away from its nominal position to several different positions. Data were taken simultaneously with the BPMs and surveyed wire scanners (Harps) located adjacent to each of the BPMs. These runs give the absolute beam position in the Hall A Coordinate System and allow for the BPMs to be calibrated against the Harps. After the analysis of the Harp runs and the acquisition information, the offsets and slopes for the BPM analysis were determined and put into the database.

- **Experiment E00-102**

During the experiment E00-102, several bulls-eye scans were performed [Rei02]. Figure 5.4 shows an overview of all bulls-eye scans in the upper left corner. It corresponds to CODA runs (1208-1212, 2919-2925) and Harp runs (1425-1429, and 1444-1450). The other three plots are for one single run (Coda run 2919). The width of the distribution for these runs was typically 100 μm in the horizontal direction (x-axis) and 200 μm in the vertical direction (y-axis), two to three times as large as the width given by the Harps.

Figure 5.5 shows the calibration of the BPMs against the Harp scan. Harp results were already corrected for the nearest survey. As can be seen, the database was already optimized and BPM and Harp scans yielded consistent beam positioning information.

The analysis of unrastered production runs (like the ones acquired with the waterfall target) requires the use of a database and a *rastconsts.dat* file obtained from the calibration procedure described above. The beam position is analyzed on an event-by-event basis, and thus no two pass analysis is necessary. A small amount of noise coming from the BPM ADCs is present in the position readings, but its contribution (30-50 μm) is small compared to other uncertainties in this measurement.

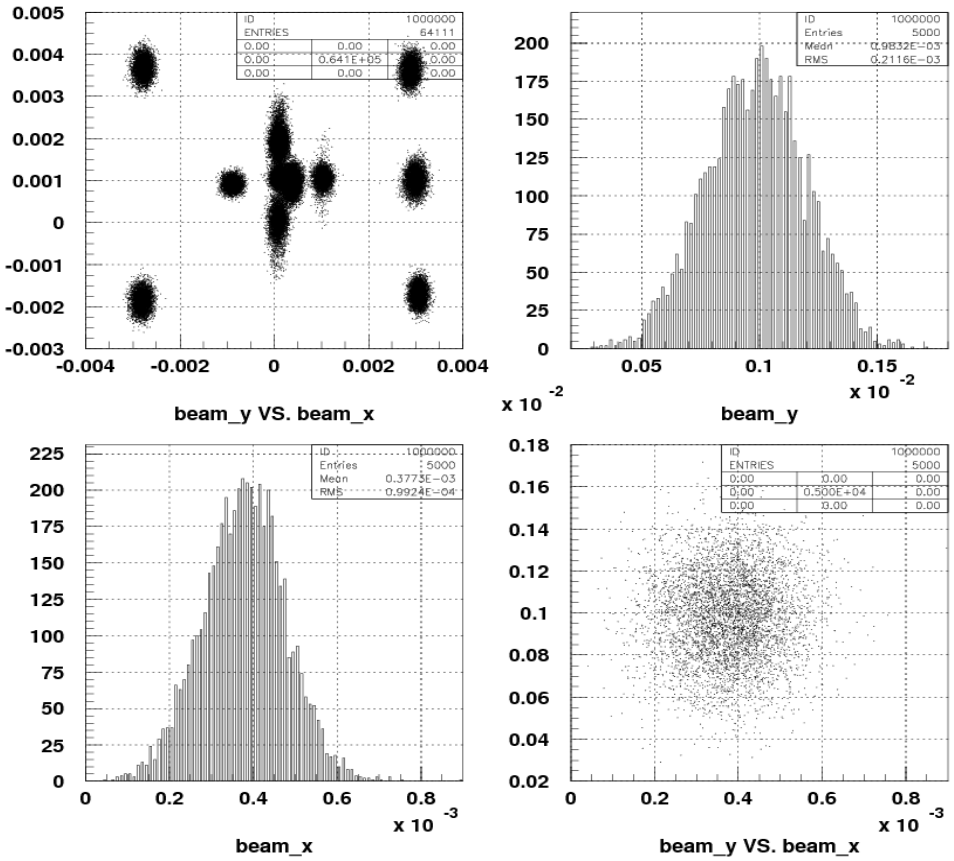

Figure 5.4: Bulls-eye scan: overview of all runs (Top left), beam x and beam y distributions for a single run (in meters). Figure extracted from [Rei02].

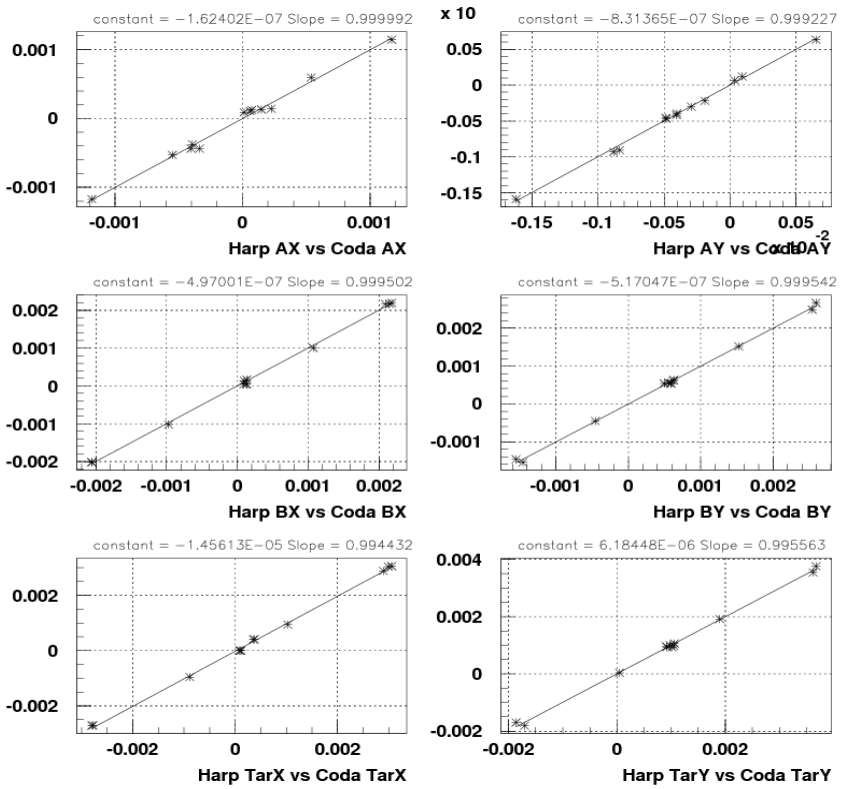

Figure 5.5: Bulls-eye scan: beam position obtained by BPMs versus that obtained with the Harps. Figure extracted from [Rei02].

Shifts in the beam position over time are automatically corrected for. Figure 5.6 shows the time evolution of the beam position for a typical production run (with the raster off). Here, the width of the distribution of beam positions is usually better than 50 µm.

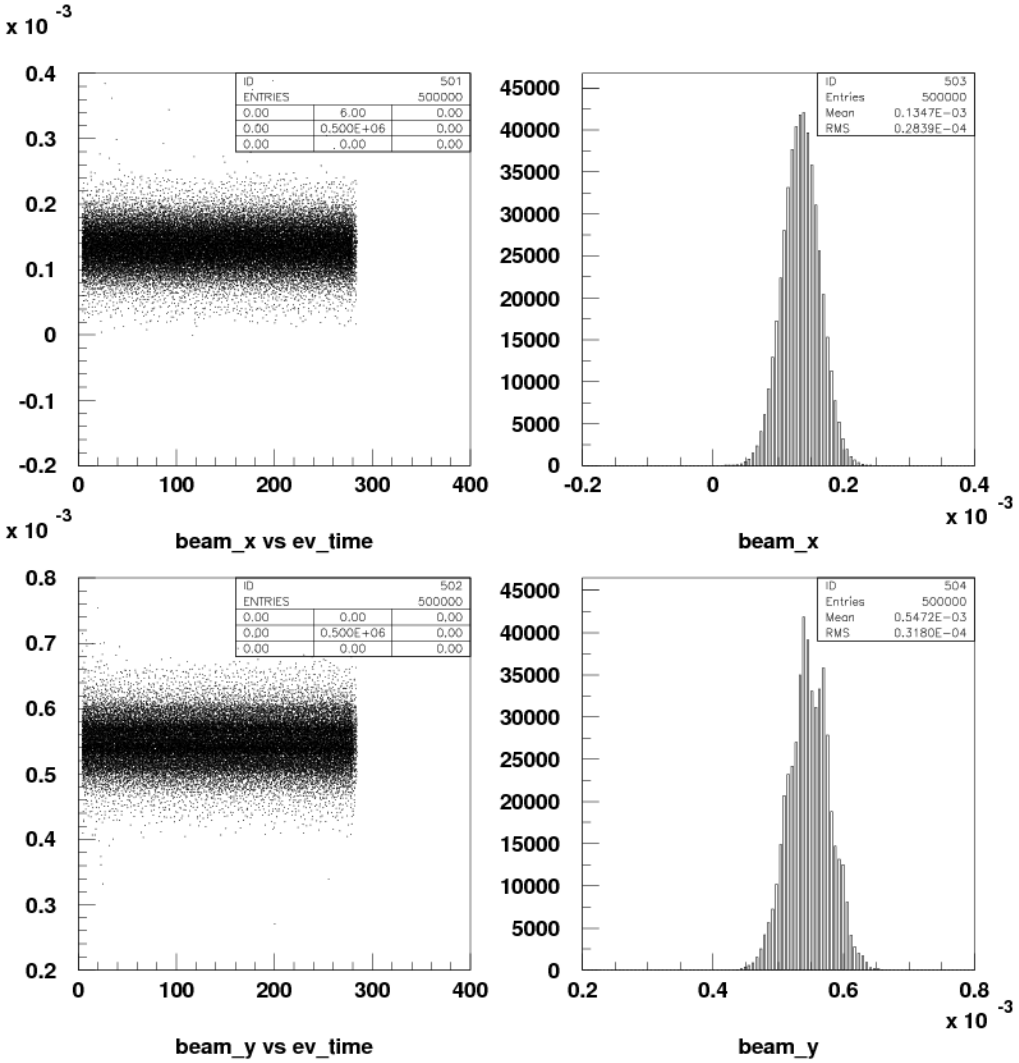

Figure 5.6: Example of a production run (with raster off): beam position as function of time and the distribution of the beam position in the x and y direction. Figure from [Rei02].

- **Experiment E06-007**

A bulls-eye scan was also performed during the experiment E06-007 (RUN 1). The beam position was measured at 5 different positions and Harp scans runs (2311-2315) corresponding to CODA runs (1079-1083) were recorded. In each of those runs, 1M events were recorded using a beam current of 5 µA and a beam energy of 1.143 GeV. These runs were acquired at the beginning of the experiment using a graphite target and with both left and right spectrometers simultaneously acquiring elastic data from the ^{12}C(e,e) reaction. With the center of the beam placed at different positions, the singles rates acquired in each spectrometer give a straightforward measurement of when the

target frame was being hit by the beam, as this situation corresponds to a very visible rate increase. These measurements were later used to define the maximum raster size. Additionally, several "Aperture Scans" were performed with both BeO and graphite targets.

The nominal positions of the beam in these runs and the rate of single events detected in each arm are shown in Table 5.4.

Position	(-4.0,2.0)	(-2.0,-1.0)	(-6.0,-1.0)	(-2.0,5.0)	(-6.0,5.0)
Harp Scan Run	2311	2312	2313	2314	2315
Coda Run	1079	1080	1081	1082	1083
T1 / T3 (kHz)	8.5 / 11.0	9.5 / 9.8	7.5 / 12.0	9.9 / 10	11 / 20

Table 5.4: Data runs and singles rates acquired for the bulls-eye scan.

During the experiment E06-007, a rastered beam with large size was used. Because the rastering of the beam is very fast (18.3 kHz) compared to the readout of the BPMs, the reconstruction of the beam position with the BPMs alone is not sufficient, and the result has to be phase corrected.

To obtain the necessary correction, the data analysis for each run proceeded in two steps. In a first pass, the analyzer software analyzes some subset (typically 10k events) based on the macro *get_rast_const.C*. From this analysis, the average beam position as well as the raster size are obtained. At the same time, one also gets the average raster current and the distribution of this quantity. This information is put into individual *rastconsts.dat* files. During the second pass, these files are used to obtain the phase corrected beam position.

5.1.3. Beam Energy Calibration

During data acquisition, the position of the missing energy peak of the ground states of ^{16}O(e,e'p) [experiment E00-102] and ^{12}C(e,e'p) [experiment E06-007] were used to monitor possible changes in beam energy.

- **Experiment E00-102**

The results from eP and Arc beam-energy measurements during the experiment E00-102 are shown in Table 5.5. [Rei05, And05]. Repeated measurements of the beam energy using both eP and arc methods gave a mean value for the electron beam energy of 4618.4 MeV and demonstrated self-agreement to within $<3\cdot10^{-4}$ over the course of the entire experiment.

Method	Date	Result (MeV)	Error (stat.) (MeV)	Error (sys.) (MeV)	Error (tot.) (MeV)
Arc	Oct 29	4618.6			0.9
Arc	Nov 2	4617.5			0.9
eP	Nov	4619.08	0.32	1.01	1.3
eP	Dec 7	4618.34	0.22	1.01	1.2
Average		4618.4			

Table 5.5: Beam-energy measurements during the experiment E00-102 [Rei05, And05]

The presence of hydrogen in the target gives the possibility of a continuous check of the beam energy. Measurements from left-arm elastic H(e,e) events (acquired during the entire experiment) and H(e,e'p) measurements (acquired in some runs at different times of the experiment in parallel kinematics) allowed for independent determinations of the incident energy [Alc04].

Analysis of both single-arm and coincidence data from the experiment E00-102 showed kinematic irregularities [Lac07]: the missing-energy spectrum in coincidence events appeared somewhat shifted, and the expected relationship between beam energy, scattered particle energy and scattering angle did not hold for elastic events. Therefore the beam energy and scattering angle were offset corrected (within 2σ of the measured value) to get consistent results. A discussion of this offset correction is presented below.

COINCIDENCE EVENTS: Coincidence events in run 2086 (parallel kinematics) were analyzed using the nominal kinematic settings (E_0=4618.4MeV). E_{miss} was calculated for each event and the total histogram, with a dominant H(e,e'p) peak and two small ^{16}O(e,e'p) peaks, is shown in Figure 5.7. It can be noticed that the elastic peak is positioned at -2.1MeV.

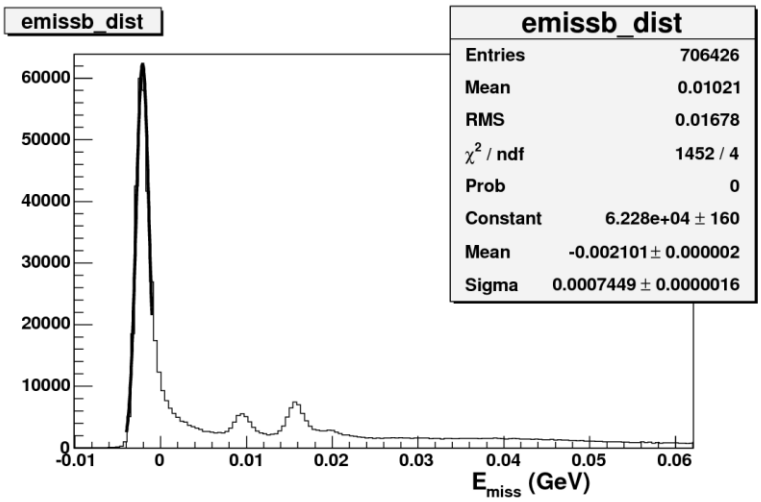

Figure 5.7: E_{miss} distribution for run 2086 (parallel kinematics) using E_0=4618.4 MeV [Lac07]

LEFT-ARM SINGLES: An interesting measurement from H(e,e) singles is ΔE. ΔE is

defined as the difference between the measured energy of the scattered electron and the energy expected for an electron scattered elastically at the measured scattering angle [Alc04]:

$$\Delta E = E' - E'(\theta) = E' - \frac{E_0}{1 + \frac{E_0}{M_p}(1 - \cos\theta)} \tag{5.5}$$

where *E'* is the measured scattered electron energy that includes energy loss corrections (Section 5.2), and θ is the angle between the incident and scattered electron and E_0 is the incident beam energy. θ is calculated from the measured 3-momentum of the scattered electron $\vec{p}$ and the initial electron momentum $\vec{p}_0$ (in the beamline direction).

$$\cos(\theta) = \frac{(\vec{p} \cdot \vec{p}_0)}{|\vec{p}| \cdot |\vec{p}_0|} \tag{5.6}$$

Figure 5.8 shows the ΔE distribution for the same run 2086 in parallel kinematics. The data are analyzed using the nominal kinematic setting, but with E_0 increased by 2.1 MeV to E_0=4620.5 MeV to obtain the correct E_{miss} distribution.

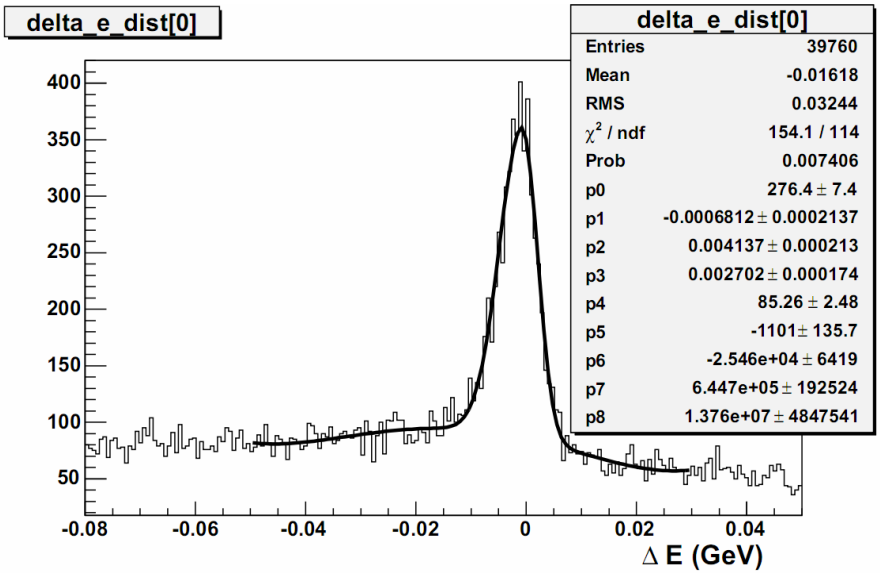

Figure 5.8: ΔE distribution, from all foils in a run with parallel kinematics. The parameters p4-p8 are the polynomial parameters a_0-a_4, p0 correspond to B, p1 to x_0 and p2,p3 to σ_1, σ_2. Figure extracted from [Lac07].

The elastic peak is seen to sit on top of a slowly varying smooth background. The ΔE distribution was fit with a function of the form

$$f(x) = a_0 + a_1 x + a_2 x^2 + a_3 x^3 + a_4 x^4 + g(x) \tag{5.7}$$

where the first five terms are a fourth-order polynomial to represent the background and the term g(x) is a "two-sided" gaussian intended to fit the elastic peak

$$g(x) = \begin{cases} B \cdot \exp\left(-\left(x - x_0\right)^2 / 2\sigma_1\right) & ,, x \le x_0 \\ B \cdot \exp\left(-\left(x - x_0\right)^2 / 2\sigma_2\right) & ,, x > x_0 \end{cases} \quad (5.8)$$

During the analysis of left-arm elastic events, it was also noticed that the ΔE distribution was not peaked at ΔE = 0. This was corrected by introducing a slight modification to the nominal angle of the left spectrometer from θ_{left}=12.5 to θ_{left}=12.535, as shown in

Table 5.6:

θ_{left} (deg)	ΔE (MeV)
12.5	-2.35
12.525	-0.74
12.535	-0.05

Table 5.6: Adjustment of the nominal central angle of the left HRS.

- **Experiment E06-007**

In experiment E06-007, no additional measurements of the beam energy apart from the ones given continuously by the Tiefenback device were made. This value of the beam energy was available as a variable and it was used in the data analysis. Additionally, beam energy values were checked during the experiment using as a reference the position in the E_{miss} spectrum of the dominant $1p_{1/2}$ peak of carbon with respect to the nominal E_{miss}=16.0MeV. In Figure 5.9 it can be seen that the position of the peak in E_{miss}, obtained using the value of E_0 given by the Tiefenback varied less than 0.5 MeV. The offset of roughly 0.75 MeV was caused by the energy loss.

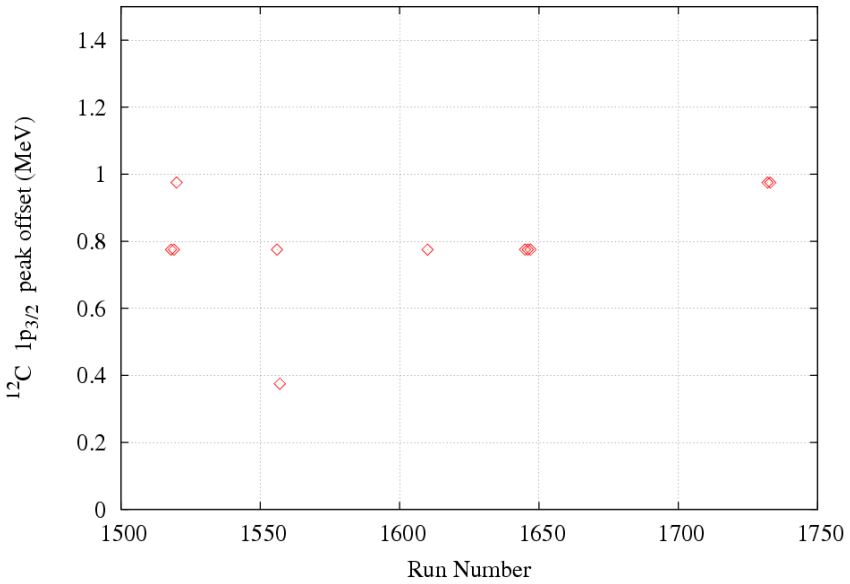

Figure 5.9: Energy offset of the $1p_{1/2}$ peak in the E_{miss} spectrum of $^{12}C(e,e`p)$.

5.1.4. Beam Raster Calibration

- **Experiment E00-102**

The experiment E00-102 did not use the raster in the production runs. Therefore, a precise calibration of the raster was not necessary. Nevertheless, some calibrations were performed for the test runs acquired with the BeO target. Further details can be found in [Rei02].

- **Experiment E06-007**

The experiment E06-007 used a large raster size. Therefore, a good raster calibration was necessary in order to obtain a raster correction that allowed for an accurate reconstruction of the variables at the target. The raster calibration was obtained on a run-by-run basis using the *get_rast_const.C* code. This code was run before the data from each run was analyzed. Using a fraction of the detected events, it evaluated the raster constants and the database was automatically updated. Subsequently, the entire run was analyzed.

5.2. Correction for Energy Losses

Energy loss in these types of (e,e'p) experiments is a fairly well known process. The models used to describe the total energy deposited by the incident and scattered electron and the ejected proton agree well with experimental data. Nevertheless, it is important to note that energy loss is a stochastic process, so that only the averaged energy loss can be corrected and some straggling due to differences from this mean energy loss will result in a degradation in the energy resolution.

In order to obtain an accurate energy-loss correction, it is necessary to take into account all materials that the particles pass through, together with their thickness and density. This includes not only the target itself, but the chamber walls and other windows in the HRS. A detailed list of all these materials in typical Hall A experimental setups can be found in [Qat05].

Target thickness must also take into account as the incident beam in general is not perpendicular to the target foils ($\Theta \neq 90$). Therefore

$$foil\_thickness = \frac{thickness}{\sin(\Theta)} \tag{5.9}$$

As energy loss changes the momentum of the scattered electron and knocked-out proton, this effect was corrected on a event-by-event basis during the reconstruction of the

physical variables.

Simulations in MCEEP were obtained with an option that allows for correcting for the mean energy loss. Further details regarding the energy-loss simulation options in MCEEP can be found in section 4.2 of the MCEEP documentation [MCEEP].

- **Experiment E00-102**

The main materials that were taken into account and the total thickness are shown in Table 5.7.

Target Chamber (Al) entrance and exit	Foil 1 (Water)	Foil 2 (Water)	Foil 3 (Water)
0.0891 g/cm^2	0.281 g/cm^2	0.290 g/cm^2	0.234 g/cm^2

Table 5.7: Target thickness used to calculate the energy loss in E00-102 [TarE00].

A dedicated new module in Analyzer [Lac07c] was used to correct the reconstructed energy of the incident and scattered electrons as well as the energy of the detected proton for mean energy loss. This module uses different target thickness depending on the foil where the (e,e'p) reaction took place. As a result, the E_{miss} spectra reconstructed by Analyzer for each foil are compatible.

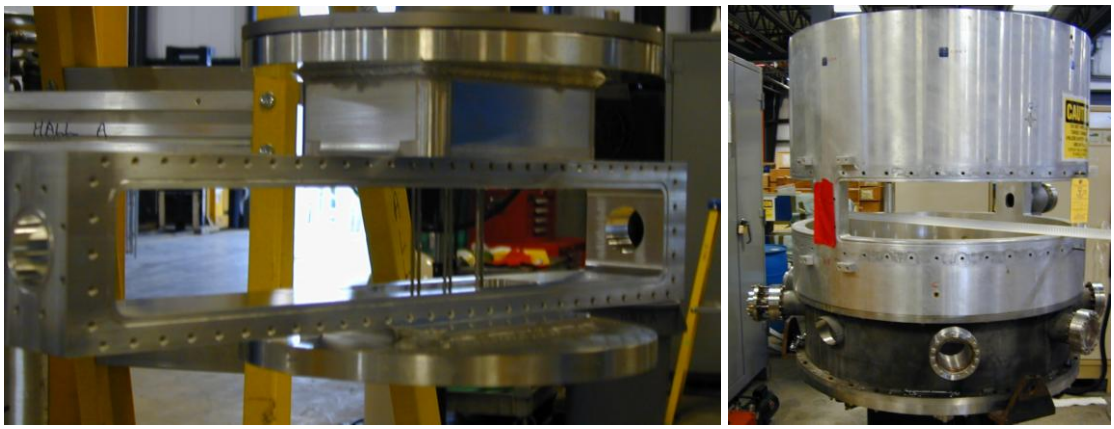

Figure 5.10: Waterfall target and scattering chamber [TarE06].

- **Experiment E06-007**

Due to the special targets used in this experiment, with three thin joined foils C+Pb+C and C+Bi+C [TarE06], energy loss corrections were not straightforward. The thickness of the foils (around 0.17 mm) is much smaller than the best achievable resolution of the HRSs along the beam (4 mm FWHM) [Alc04]. Therefore, the foil in which the reaction takes place is unknown and energy loss corrections on a event-by-event basis as done in

the experiment E00-102 cannot be applied.

Therefore, efforts were made to improve the simulations used to compare with the data. It was necessary to adapt MCEEP to be able to simulate realistic energy losses with these compound targets. The thickness of the windows of the target chamber (Al, 0.0891 g/cm^2) and other materials like air, were already included in MCEEP, as they were commonly used in other experiments. Nevertheless, the energy loss produced by the diamond foils of this experiment had to considered appropriately.

The method to include the effect of the additional energy loss due to the diamond foils was:

1) A MCEEP simulation was performed using the 2 diamond foils as a target. It was imposed that the reaction vertex occurs in the middle of them (z=0 plane) and the energy loss due to the windows was set to zero. The energy losses of the e,e' and p due to the diamond foils for each event were stored in a file.

2) A second MCEEP simulation was then performed, now with the lead (or bismuth) target, but adding to each event an extra energy loss which is randomly picked from the previously simulated file.

In this manner, good agreement between data and simulation was obtained. This was checked by comparing the position of the ^{12}C(e,e'p) peak from the $p_{1/2}$ shell in the graphite target with one from the diamond+Pb+diamond foils.

5.3. Calibration of the High Resolution Spectrometers

5.3.1. Optics Calibration

The two spectrometers (HRSE and HRSH) have the same configurations (QQDQ) and optical features. The matrix elements of the optics database Y_{ijkl}, T_{ijkl}, P_{ijkl} and D_{ijkl} (defined in Section 4.11.2) are determined using data. These data are special in the sense that certain of the kinematic quantities of the detected particles are known, so that the matrix elements may be varied until the analysis code reconstructs them correctly.

^{12}C(e,e′) data are usually used for calibrating the optics databases. These data are acquired with a sieve-slit plate placed at the entrance of each HRS. The sieve-slit plate is a 5 mm thick stainless steel plate with a regular pattern of 49 (7 x 7) holes drilled through it. Two of the holes have twice the diameter of all the others, to allow for the determination of the sieve-plate orientation at the focal plane.

Angular Calibration:

The T_{ijkl} and P_{ijkl} matrix elements (used in determining θ_{tg} and φ_{tg}) are calibrated using events scattered from a single carbon foil target which pass through the aforementioned sieve-slit plate, inserted at the entrance of each spectrometer. Knowledge of the target location, as well as the location of each sieve plate together with their corresponding sets of holes comes from the spectrometer survey. Figure 5.14 shows typical reconstructed angles θ_{tg} and φ_{tg} from a ^{12}C(e,e′) calibration run.

Momentum Calibration:

The central momentum p_0 of the HRSs is obtained from the dipole-field strength B through the relation

$$p_0 = \sum_{i=0}^{3} \Gamma_i \cdot B_0^i \tag{5.10}$$

where Γ_i are magnetic constants which have to be determined.

The relation between the focal-plane position of a particle passing through the spectrometer and its momentum p is

$$\begin{aligned} p &= p_0 + dp = p_0 \cdot (1 + \delta p) \\ \delta p &= \frac{dp}{p_0} = \frac{p - p_0}{p_0} = \sum_{ijkl} D_{ijkl} x_{fp}^i \theta_{fp}^j y_{fp}^j \phi_{fp}^k \end{aligned} \tag{5.11}$$

The D_{ijkl} matrix elements and the constants Γ_i are also calibrated using the measured momentum of electrons elastically scattered from a carbon foil target (55.8 mg/cm^2). The sieve-slit plate is not required in this case. Optics database calibration procedures are discussed in detail in [Liy01b,Liy02]. The energy E_f of the scattered electrons for each state of the ^{12}C(e,e') can be expressed in terms of its corresponding excitation energy E_x, the incoming beam energy E_i, the mass of target M_t and the scattering angle θ by

$$\begin{aligned} E_f &= p_f = f_{rec}^{-1} \cdot \left[E_i - E_{loss1} - E_x \cdot \left[1 + \frac{E_x}{2M_t} \right] \right] - E_{loss2} \\ f_{rec} &= 1 + 2(E_i - E_{loss1}) \cdot \sin^2(\theta / 2) / M_t \end{aligned} \tag{5.12}$$

where E_{loss1} and E_{loss2} are the mean energy losses before and after scattering respectively. Figure 5.11 shows the elastic peaks used to adjust these matrix elements.

In practice, several different runs are performed for the ^{12}C(e,e') reaction with the elastic peak and the first few states of ^{12}C moved to different positions across the focal plane by varying the dipole field B. The energy differences between the first few states of ^{12}C and the high momentum resolution of the spectrometers are used to reduce the uncertainty in the extraction of the constants.

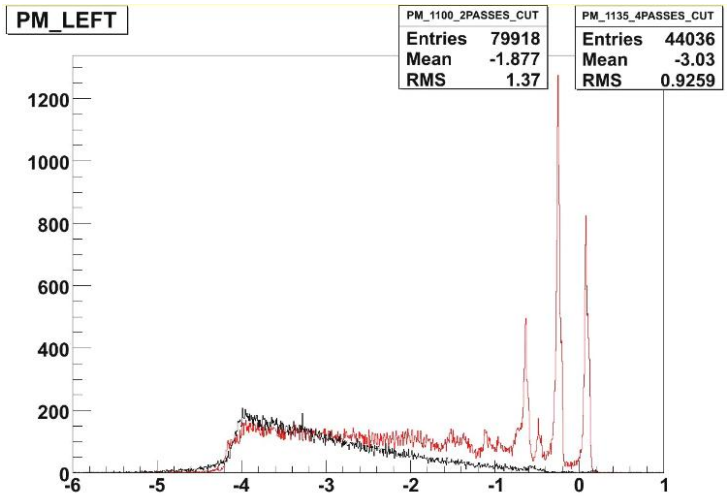

Figure 5.11: Reconstructed momentum from the $^{12}C(e,e')$ reaction. The red spectrum corresponds to a beam energy of 1.3 GeV, while the black one corresponds to 2.6 GeV.

Figure 5.11 shows typical $^{12}C(e,e')$ calibration data. The first peak on the left corresponds to the reaction leaving ^{12}C in its ground state while the other peaks correspond to the first few excited states. The spectrum in black correspond to data acquired with 2.6 GeV. In this case the peaks are dominated by a background of quasielastic events and cannot be appreciated.

The values of the magnetic constants Γ_i for each spectrometer are shown in Table 5.8. [Liy01b]. As expected, both HRS have similar magnetic properties. These values, obtained in 1999, proved to be valid in the experiments reported in this thesis, as the matrix element D_{000}, (which represents a possible global offset between p and p_0), is compatible with $D_{000}=0$.

Spectrometer	Γ_0	Γ_1 (MeV/kG)	Γ_2	Γ_3 (MeV/kG)
HRS-L	0.0	270.2 ±0.15	0.0	-1.6E-03 ± 0.7E-03
HRS-R	0.0	269.8 ±0.15	0.0	-1.6E-03 ± 0.7E-03

Table 5.8: Magnetic constants Γ for the HRS central momentum [Liy01b].

Reaction-Point Calibration:

Finally, the Y_{ijkl} matrix elements (used to determine y_{tg}) are determined using events scattered from a set of seven carbon-foil targets offset from one another along the direction of the beam. The locations of the 7 target foils is determined by a survey of the target system prior to data taking.

- **Experiment E00-102**

The missing-energy resolution obtained with the optics database in this experiment was about 1.8 MeV(FWHM) (see Figure 5.12). As the experiment E00-102 used an incident energy of 4620 MeV, this resolution is consistent with that obtained in the previous ^{16}O(e,e'p) experiment E89-003 that achieved a missing energy resolution of 0.9 MeV (FWHM) [Gao99] with a nominal beam energy of 2445 MeV.

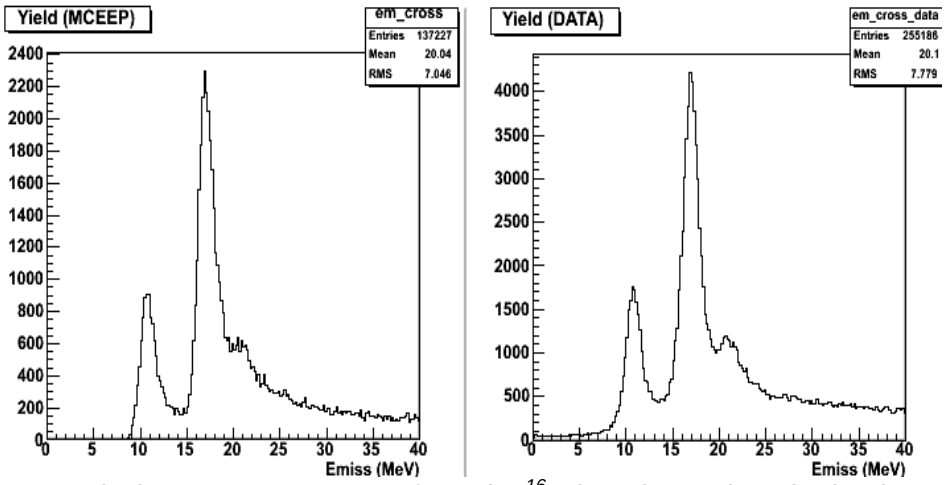

Figure 5.12: Missing-energy spectrum from the ^{16}O(e,e'p) reaction obtained at p_{miss}~70 MeV/c during the experiment E00-102. E_{miss} resolution is ~1.8 MeV (FWHM).

Special efforts were devoted to calibrating the reaction point. The reaction point along the beam (known as react.z) gives information about the foil in which the reaction took place (see Figure 5.13). This is important not only for accurate E_{loss} corrections and proper angular corrections (necessary for extended targets), but also because it allows for a cut on the foils that reduces the number of accidentals (see Figure 5.21).

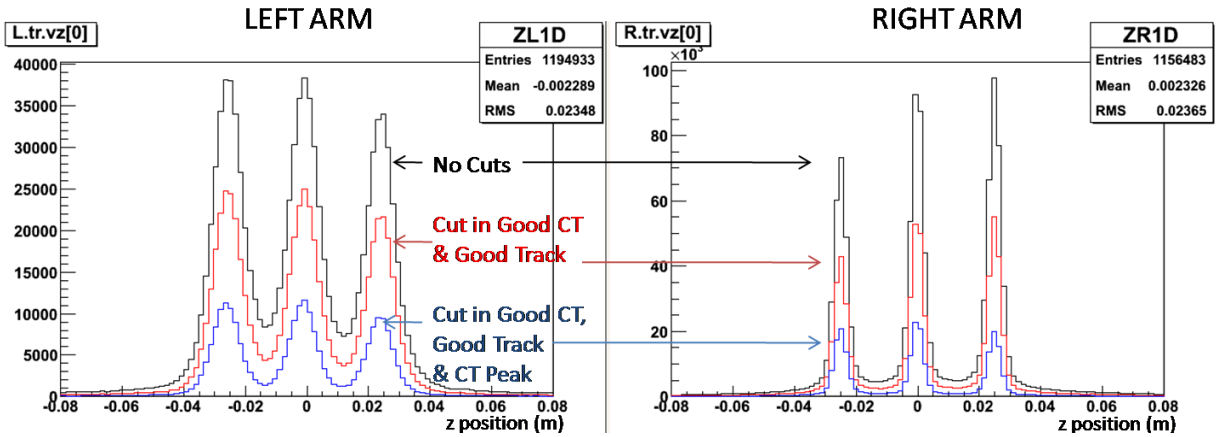

Figure 5.13: Reconstructed position along the beam line by each HRS for the 3 foils in the experiment E00-102 after different cuts were imposed upon the data.

As the target foils were rotated 32.6º towards the right arm (see Section 4.5.1), this arm was generally orthogonal to the plane of the target foils. Therefore, the resolution in the reaction point along the beam is better for the right arm.

- **Experiment E06-007**

Angular calibration:

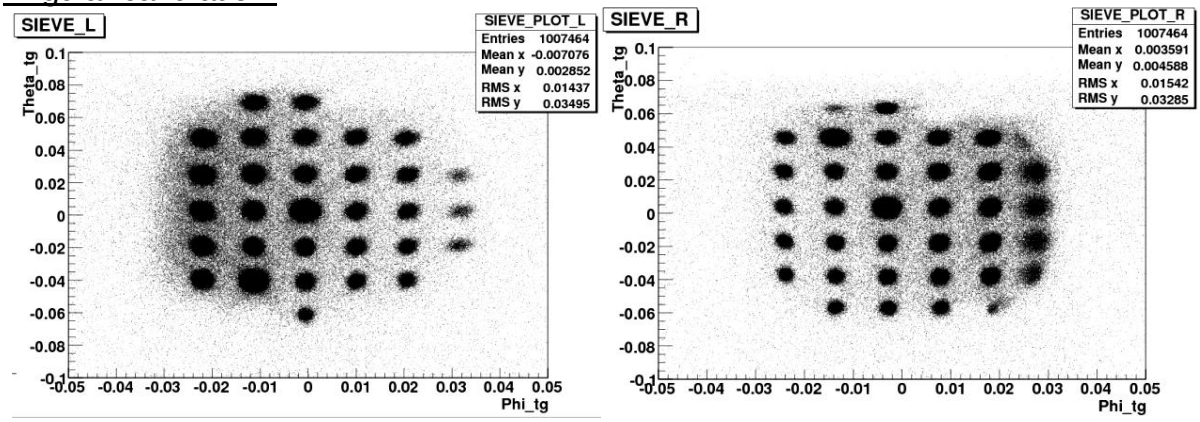

Figure 5.14: Sieve-slit plate reconstructed by Analyzer after calibration.

Momentum calibration:

As this experiment required good energy resolution, special efforts were devoted to the calibration of the optics, corresponding to the momentum reconstruction in each HRS.

The code "Optimize++" described in [Liy02] is based on a χ^2 minimization obtained by Minuit. This gradient-based method has the serious drawback of not allowing simultaneous variation of a large number of variables. Due to the fact that an optics calibration typically involves the minimization of a large number of D_{ijkl} coefficients, in practice, only a few of these parameters can be optimized in each step, and the others must be held constant. Furthermore, in many cases, there exists local minima where a local solution may exist that is in fact far from the global optimum result.

Instead, a genetic algorithm developed by Udías et al. (which has already been successfully applied to the minimization of nuclear properties [Fer08]) was used to obtain an improved version of Optimize++. In this thesis, the χ^2 minimization required by Optimize++ was improved by developing a code based on this genetic algorithm that replaces the previous gradient-based minimization routine. This way, all parameters could be optimized simultaneously and there were no problems with local minima. Optimization could be done overnight without human intervention.

It was shown in [Gao99] that calibrating the optics with singles $^{12}C(e,e')$ elastic data obtained for a lower beam energy than that to be used in the experiment could be

problematic; that is, there is no guarantee that the resulting optics database will be optimized. In the documentation of Optimize++, it is suggested to use an E_{miss} spectrum of $^{12}C(e,e'p)$ acquired with the same beam energy to be used for the rest of the experiment. Therefore, apart from using elastic $^{12}C(e,e')$ data, matrix elements can be improved by reconstructing a discrete missing-energy peak for a particular A(e,e'p)B reaction. This method also allows for matrix elements for both spectrometers to be calibrated simultaneously. This procedure also employed in the developed version of Optimize++ The χ^2 to be minimized was based on a combination of χ^2 that maximized the resolution for the elastics data and a χ^2 that maximized the resolution for the (e,e'p) peak.

The resulting resolution after this calibration is ~0.9 MeV (FWHM) (see Figure 5.15). This value is consistent with the hardware limit of the experimental apparatus.

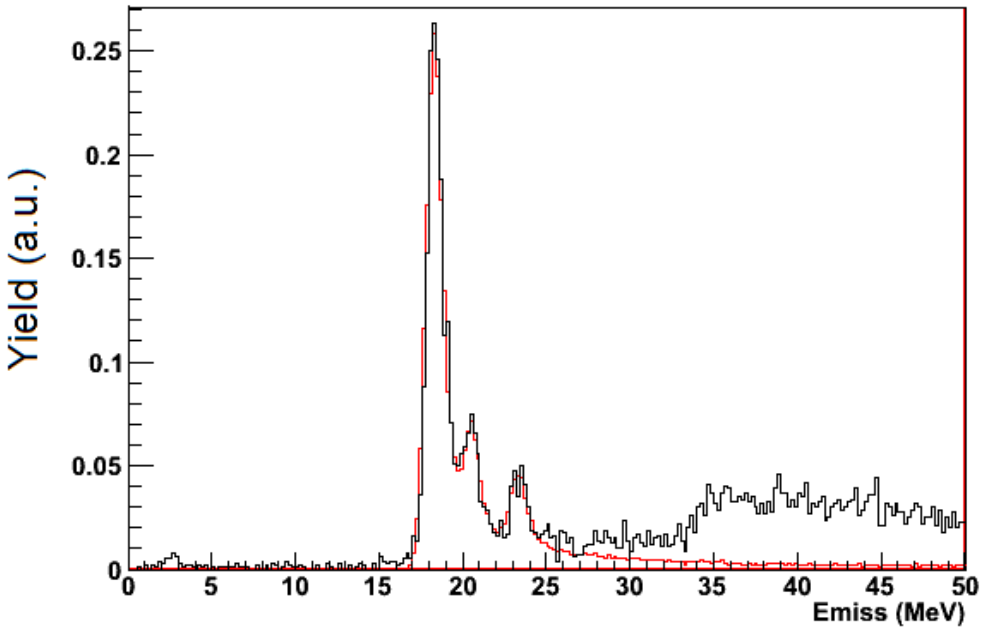

Figure 5.15: Kin0 (-100 < p_{miss} < 100 MeV/c) $^{12}C(e,e'p)$ E_{miss} spectrum after the momentum optics calibration for E06-007 (see text for details).

Figure 5.15 shows the peaks from the proton knock-out from the p-shell in ^{12}C. The red line corresponds to a MCEEP simulation, where only the p-shell was included, and the black line corresponds to measured data. Note that the region above 25 MeV corresponds to the $s_{1/2}$ states as well as the continuum. In this experiment, the Y_{ijkl} matrix elements were not calibrated as multiple foils were not used and the position of the target was known from a survey performed at the beginning of the experiment.

5.3.2. Spectrometer Mispointing

The HRSs are not constrained to remain along a constant radius with respect to the hall center as they rotate around the central pivot. This means that spectrometer central ray can miss the hall center by as much as ±3 mm in the horizontal plane and ±0.5 mm in the vertical plane [Alc04]. This is known as spectrometer mispointing. Unfortunately, these displacements are not fully repeatable; that is moving the spectrometer to the same angular location at different times leads to different horizontal and vertical displacements within the above mentioned range. Fortunately, these displacements can be measured and taken into consideration.

Furthermore, the target can have an offset (z_{lab}) with respect to the center of the hall. A survey of the target system at the beginning of the experiment provides target-foil offsets.

These two effects can be seen in Figure 5.16. The horizontal mispointing Δl obtained from each HRS (left (L) and right (R)) is

$$\begin{aligned} \Delta l_L &= y_{tg} + z_{lab} \cdot \sin\theta_{0,L} \\ \Delta l_R &= -y_{tg} + z_{lab} \cdot \sin\theta_{0,R} \end{aligned} \tag{5.13}$$

where y_{tg} is the reconstructed target position perpendicular to the central axis of the spectrometer and θ_0 is the spectrometer central angle with respect to the beam line. The correction $\Delta\theta_0$ to the central scattering angle of each spectrometer is found from the mispointing and the distance L_m=8.458 m between the hall center and the floor marks used to determine θ_0.

$$\Delta\theta_0 = \frac{\Delta l}{L_m} \tag{5.14}$$

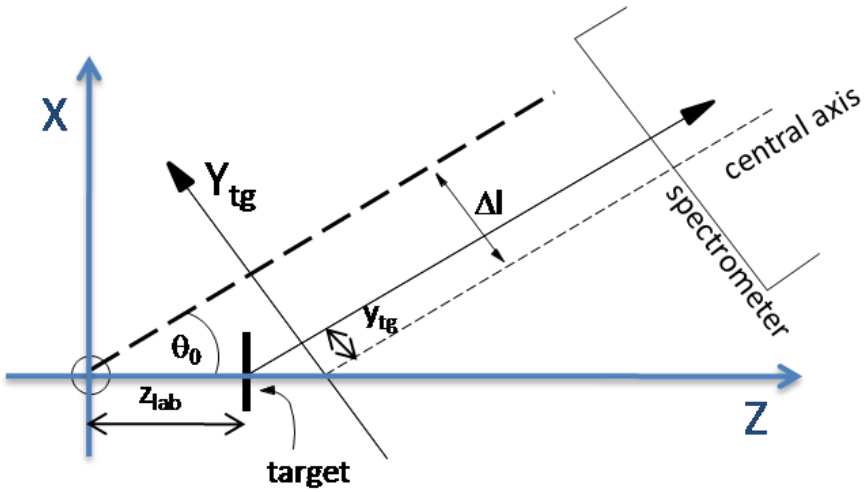

Figure 5.16: Definition of the mispointing variables in the Hall coordinate system.

- **Experiment E00-102**

Possible mispointing of the HRS was monitored and corrected for when required by checking the interaction point of the beam within the 3 foils (referred as react$_z$). React$_z$ is obtained from the information of the three-momentum $\vec{p}_0$ of the incident beam and the reconstructed three-momentum of the detected particle in each HRS $\vec{k}_{e'}, \vec{p}_p$. These reconstructed three-momenta used the optics calibration, the nominal position of the spectrometers as well as possible mispointings.

As can be seen in Figure 5.17, the reconstructed reaction points of the beam with each foil target was constant during the entire experiment after mispointing corrections were applied. Solid points correspond to the first mispointing analysis [Rei05]. Open points correspond to a posterior mispointing re-analysis of those runs performed after spectrometer movements. The dashed lines correspond to the surveyed position of each waterfall foils. Further information about the procedure for obtaining the mispointing offsets calibration can be found in [Roc03].

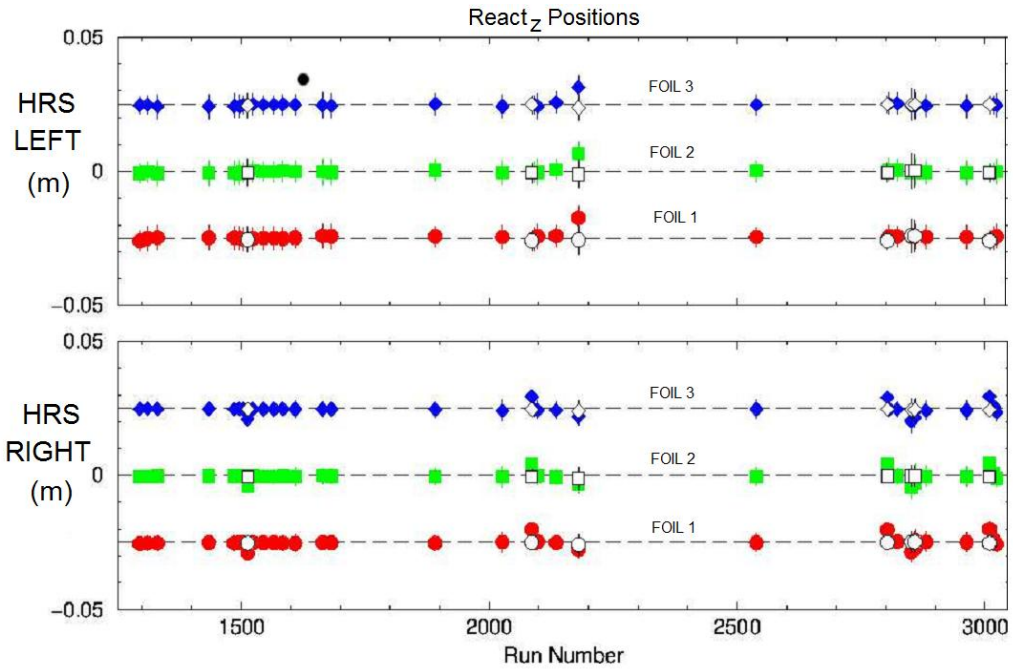

Figure 5.17: React$_z$ position for each of the 3 foils as obtained from each HRS in the experiment E00-102. Figure from [Rei05].

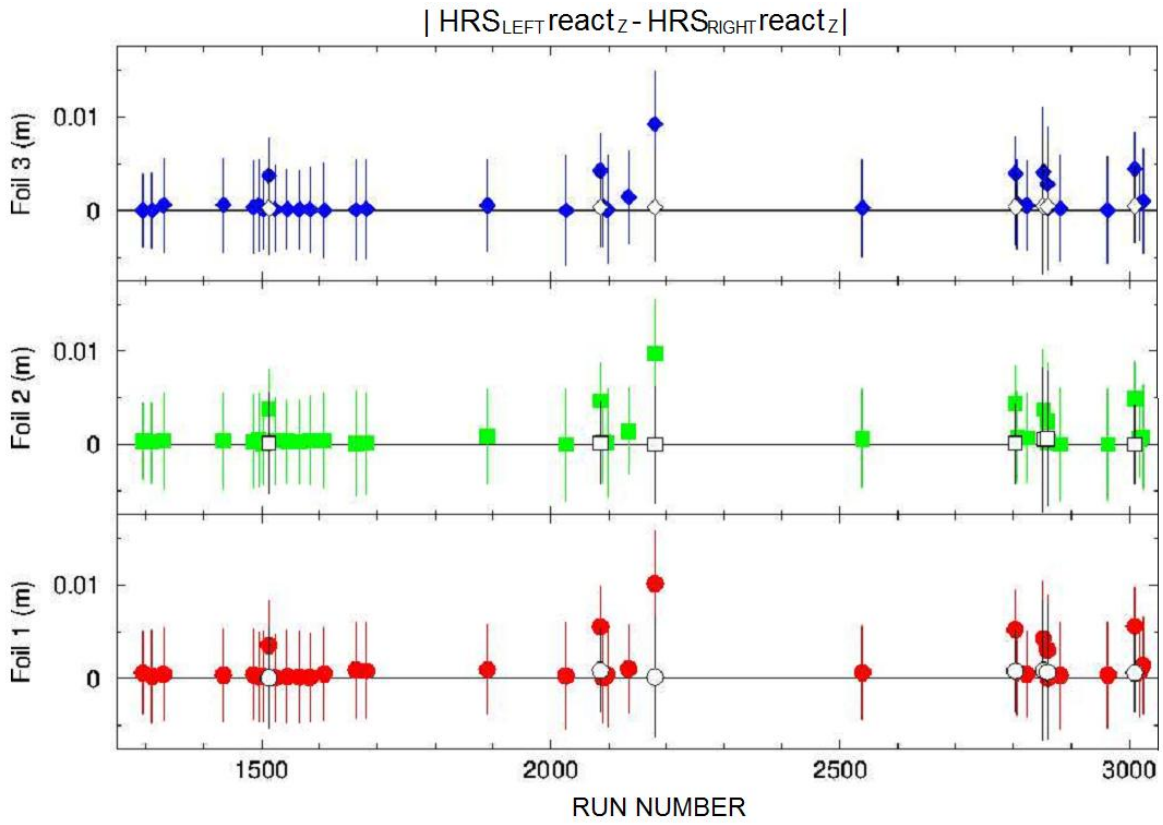

Figure 5.18: Differences between the react$_z$ position obtained from each HRS during the experiment E00-102. Figure from [Rei05].

- **Experiment E06-007**

The experiment E06-007 used a single thin target and the react.z value was set to the nominal value of the target position from the survey. Therefore, this value could not be used for mispointing calibrations. The left arm used the mispointing found from the initial survey, but the right arm was not corrected for possible mispointing at each kinematical setting. The error caused by this uncorrected effect was considered a part of the experimental systematic error.

5.3.3. Raster Correction

As described in Section 4.11.2, the optics of the HRS assume that the reaction point occurs at a vertical distance to the center of the hall, x_{tg}=0. If the beam position at the target deviates from this value (something that inevitably occurs with a rastered beam) and this deviation is not taken into account, the variables at the target will be incorrectly reconstructed. This has a large impact on the reconstructed momentum of the detected particles, as a deviation in the Hall vertical direction Δx_{tg} creates a deviation in the focal plane Δx_{fp} which directly affects the reconstructed momentum $\Delta \delta p_{tg}$.

Raster corrections were studied using data acquired using the graphite target with both

rastered and unrastered beams. If the raster correction is properly applied, both sets of data should give the same results for energy resolution and angles.

The raster correction is applied as described schematically in Eq. (4.8). First, the variables at the target are reconstructed in each spectrometer from the focal-plane variables and the calibrated optics. Then the variables δp_{tg} and θ_{tg} are corrected by

$$\begin{aligned} \theta'_{tg} &= \theta_{tg} + \Delta\theta_{tg} \quad ,, \quad \Delta\theta_{tg} = x_{tg} \cdot \theta_{Corr} \\ \delta p'_{tg} &= \delta p_{tg} + \Delta\delta p_{tg} \; ,, \quad \Delta\delta p_{tg} = x_{tg} \; / \; \delta p_{Corr} \end{aligned} \tag{5.15}$$

with the new values of $\delta p_{tg}'$ and θ'_{tg} thus obtained, the 3-momentum of the detected particle is re-evaluated.

This method assumes that a first-order correction is enough for correcting the distortion caused by the raster on these variables. During data analysis, it was suggested that due to the large raster size used in this experiment, a higher order raster correction could be necessary [Urc08]. In this work, only the first-order correction as implemented in the THaExtTarCor module in Analyzer was used. The constants θ_{Corr} and δp_{Corr} used for correcting the raster were stored in the database db_run.dat file. The same constants were used along the entire experiment.

θ_{Corr} (rad/m)	δp_{Corr} (m^{-1})
0.61	3.05

Table 5.9: Raster correction constants used in the experiment E06-007.

As it is shown in Figure 5.19, when the raster is properly taken into account, similar energy resolution is obtained both with and without it.

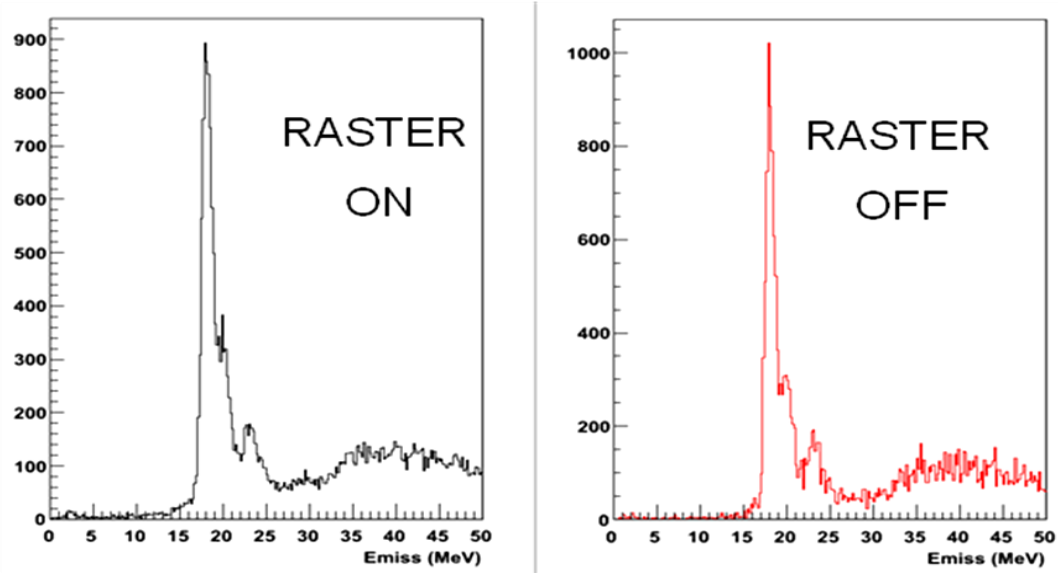

Figure 5.19: ^{12}C(e,e'p) E_{miss} spectrum acquired with unrastered and properly corrected rastered beam. Similar energy resolution is obtained in both cases.

5.3.4. Coincidence Time Calibration

The coincidence time (CT) is defined as the difference in time between the two spectrometer triggers of a coincidence event. For a true coincidence; that is, with the detected electron and proton coming from the same (e,e'p) reaction, this time corresponds to the difference in time of flight (TOF) through the spectrometers of both particles together with possible timing variations in the scintillators. Since the detected electrons are relativistic and the proton-momentum range is not so large, the CT distribution for true events should demonstrate a sharp, well-defined peak. CT is a useful measurement, as it allows "true" and "accidental" events to be disentangled:

- True coincidence events involve two particles emerging simultaneously from the same interaction in the target. If the mass and momentum of each particle and their path length between the target and the spectrometer are taken into account, a narrow peak from these real events is expected in the CT spectrum.
- Accidental coincidence events are caused by two uncorrelated single-arm events which, by chance, fall within the coincidence-timing window of interest. Therefore, accidental events will contribute to the continuous flat background in the CT spectrum. The number of accidentals depends on the square of the singles rates, so it increases with the beam current and target thickness.

The ratio of real-to-accidental coincidence events should be as large as possible to get statistically precise data. In order to increase this ratio, CT peak should be made as sharp as possible; that is, its width should be minimized. This enables the smallest possible time window for CT events to be employed, thus reducing the amount of accidental background passing the cut. The limits of this cut were chosen as $\pm 3\sigma$ from the peak location of a Gaussian function fitted to the peak in the CT spectrum.

The CT peak is artificially broadened by several phenomena which may individually be addressed [Gao99, Liy99]:

A) Timing variations in the scintillators. The timing for a single-arm trigger is determined by the right-hand side photomultiplier tubes (PMTs) of trigger-scintillator plane S2. Therefore, the timing fluctuates based upon the location of the particle in the S2 plane. This fluctuation can be compensated for by taking a mean-time in the analysis, as the average of the two TDC values (TDCs stopped by event signals on the left- and right-hand side of the trigger-scintillator paddle in question), with an offset added to center the peak at zero. The correction to the single arm timing is then given by

$$TDC_{corr} = TDC_{uncorr} + \frac{\left(TDC_L + TDC_R\right)}{2} + OFFSET \tag{5.16}$$

Different scintillator paddles have different timing offsets which need to be calculated and subtracted from the raw CT.

B) Variation in proton TOF due to variations in proton velocity. This effect is corrected by using the proton velocity obtained from either

-The TOF between the two scintillator paddles S1 and S2, with a typical resolution of 7% (σ) [Alc04]. An example of this so-called "β" distribution obtained in the experiment E00-102 can be seen in Figure 5.38.

-The reconstructed momentum *p* of the particle from the VDC measurements

$$\beta = \frac{p}{E} = \frac{p}{\sqrt{p^2 + m^2c^4}} \tag{5.17}$$

where m represents the mass of the particle (electron or proton) in the spectrometer.

The second method was used in the data analysis, the momentum *p* can be determined with better precision than can β from the TOF between S1 and S2.

C) Variation in electron and proton TOF due to path differences. *Path difference* is a spectrometer optical characteristic and it can be determined as a function of the focal-plane variables x_{fp}, y_{fp}, θ_{fp} and ϕ_{fp}. The TOF from the target to scintillator plane S2 for the central ray is

$$t_0 = l_0 \,/\, v_0 \tag{5.18}$$

where l_0 is the path-length along the central ray (l_0 ~ 29m) and v_0 is the nominal velocity of the particles, taken from the HRS dipole central-momentum settings. t_0 is on the order of 100-200 ns, so it is necessary to take into account the variations in the path length and proton beta to reach a FWHM in the CT distribution of better than 2ns.

In general, the TOF of a particle is given by

$$t = \frac{l}{v} = \frac{l_0 + \Delta l}{\beta \cdot c} \tag{5.19}$$

where *v* is the actual velocity of the particle calculated using the TOF between S1 and S2 scintillator planes and Δl is the path difference calculated from the spectrometer optics, through the measured focal-plane variables x_{fp}, y_{fp}, θ_{fp} and ϕ_{fp}. Finally, the difference between the actual TOF *t* of the particle and the TOF t_0 obtained with a central ray with momentum in the center of the acceptances is

$$t - t_0 = l_0 \cdot \left(\frac{1}{v} - \frac{1}{v_0}\right) + \frac{\Delta l}{v} \tag{5.20}$$

This value is obtained in each spectrometer and the measured CT is corrected by it.

- **Experiment E00-102**

Due to varying cable lengths and module processing times, scintillator pulses from different trigger paddles took different amounts of time to be processed by electronics. Calibration of the β value of the protons measured in the right HRS from the time of flight between S1 and S2 was performed as shown in Figure 5.20 [And05]. Before the β calibration, six individual scintillator paddles can be seen, one of which has substantially different gain characteristics. After β calibration, the scintillator paddles are indistinguishable and behave as a single scintillator paddle.

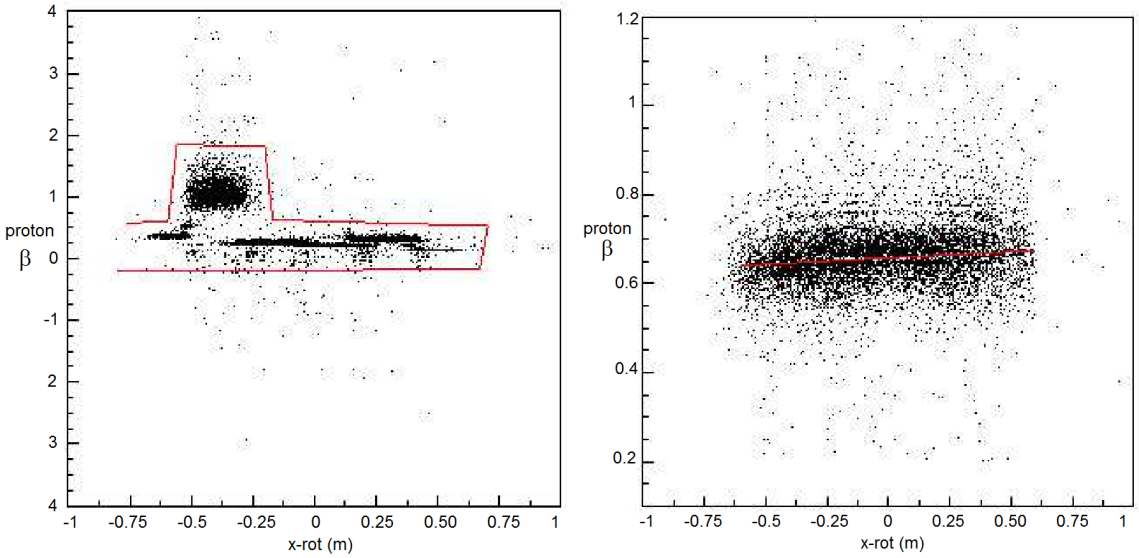

Figure 5.20: (Left) Sample raw proton β spectrum for the right spectrometer before calibration. The x-rot variable represents the vertical position of the track at the scintillator plane. (Right) Sample proton β spectrum after calibration. Figure from [And05].

Figure 5.21 shows the corrected CT spectrum. The prominent peak at around 0 ns corresponds to real coincidence events, while the background is due to accidentals. The TOF obtained without any cuts (in blue) shows several bumps due to mistimed events. With a cut in the CT difference of the values obtained at each spectrometer (in red), those bumps are removed. For a real coincidence event, the two spectrometers reconstruct the same reaction vertex. Therefore, a cut condition requiring that the two single-arm events come from the same waterfall foil increases the real-to-accidental coincidence ratio (see the black distribution plotted in Figure 5.21).

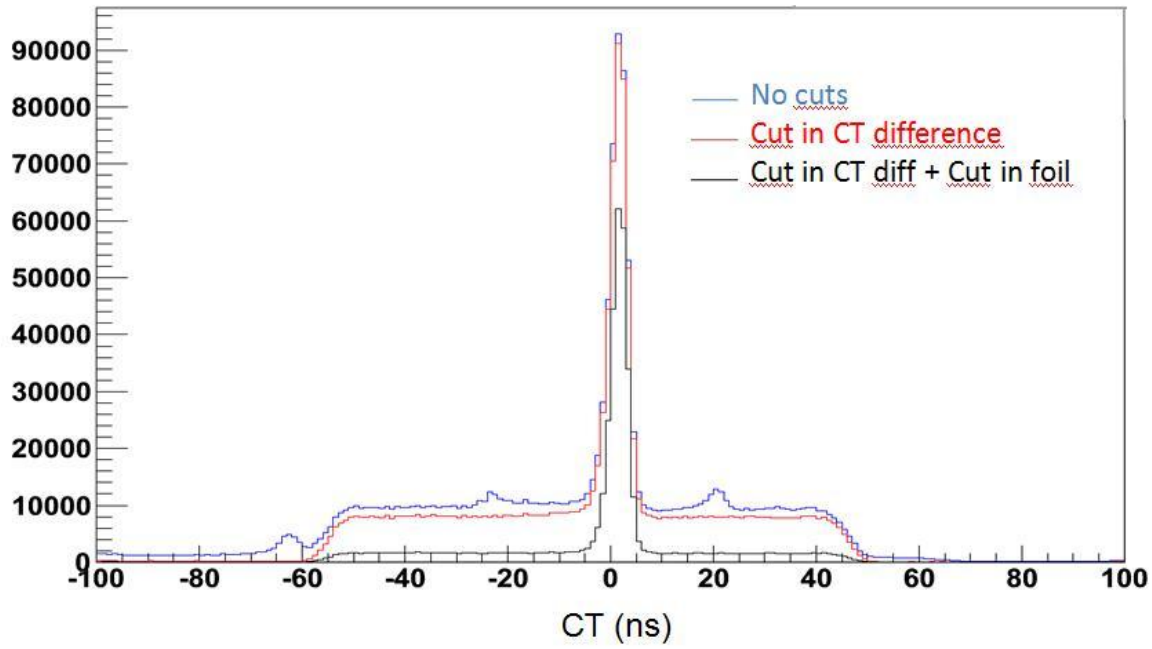

Figure 5.21: Calibrated CT spectrum for the experiment E00-102 with various cut conditions imposed.

Conversely, it can be seen in Figure 5.22 that with a cut in the CT peak, the reconstruction of the interaction vertices in the target foils is greatly improved.

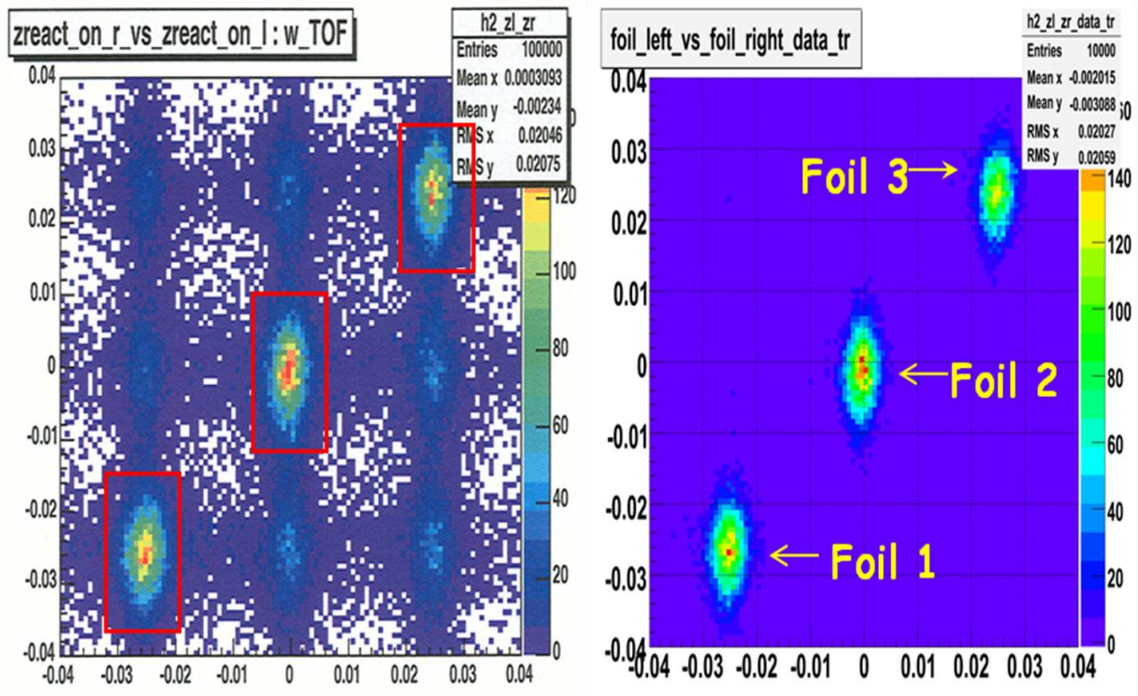

Figure 5.22: Position of the target foils reconstructed by each spectrometer (from [Foe07]). (Left pad) Without cuts in CT (Right pad) With a cut on the peak of the CT.

- **Experiment E06-007**

In this experiment, the CT spectrum seen during data acquisition, as reconstructed by Analyzer based on a database from a previous experiment, already had a reasonable good resolution. Nevertheless, in order to increase the signal-to-noise ratio in the high p_{miss} region, where random coincidences become dominant, it was necessary to improve the CT resolution. This was obtained by a proper calibration of the path-length correction applied to each particle. The Δl term in (5.20) is obtained from the measured focal-plane variables x_{fp}, y_{fp}, θ_{fp} and ϕ_{fp}. and it can be calibrated in a similar fashion as the rest of optics calibration described in Section 5.3.1. The Analyzer database was updated with the new coefficients for the Δl reconstruction and it was not necessary to change these coefficients during the whole experiment.

A resolution of around 3 ns in the CT spectrum was obtained with the calibrated database as shown in Figure 5.20. In this case, the real-coincidence peak is placed at 290 ns.

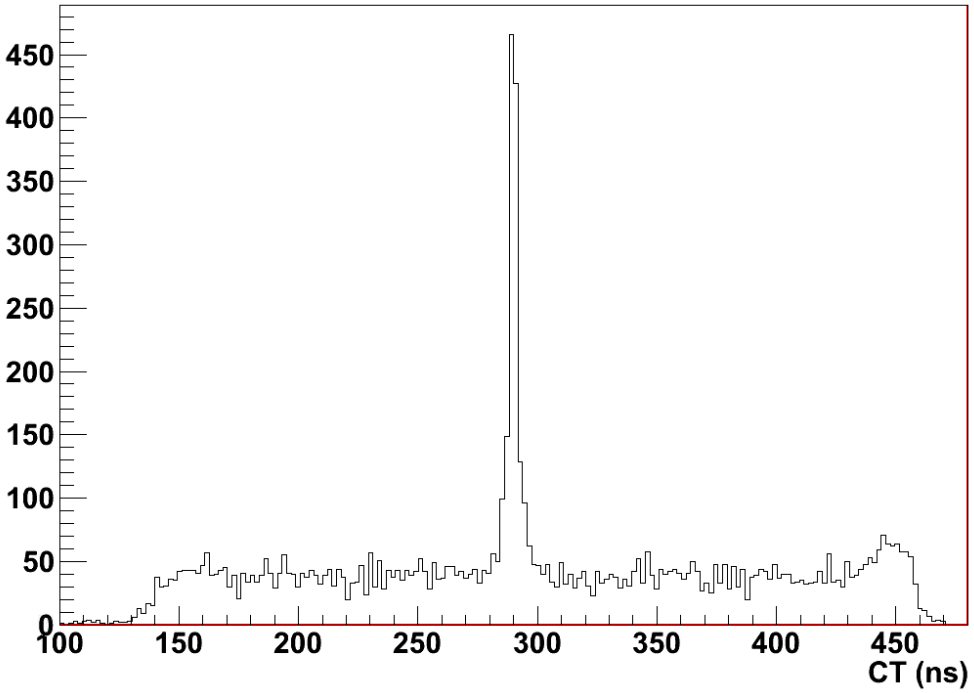

Figure 5.23: Calibrated CT spectrum for the experiment E06-007. It corresponds to a carbon run (Kin7, p_{miss}=-300MeV/c).

5.4. Efficiency Corrections

5.4.1. Deadtime Correction

There are two deadtime corrections to be applied to the data: the electronics deadtime correction and the computer deadtime correction. The resulting effect can be combined into a total deadtime. In practice, it is convenient to work with livetime (LT) instead of deadtime:

$$LT = (1 - DT) \tag{5.21}$$

- Computer deadtime (CDT) refers to events not being recorded because the DAQ can process at most one event every ~700 μs. This loss of events can be quantified by measuring the trigger input (from scalers) and the trigger output (recorded in the data file).
- Electronics deadtime (EDT) is due to the deadtime of various electronic components and the pulse width of the trigger signals τ passed to the scalers. If two independent pulses arrive at a scaler within a time interval shorter than τ, then only one pulse may be recorded. The amount of electronics deadtime depends on the scaler rate of the experiment. EDT is more difficult to measure than CDT (see [Jon00, Mic01]).
- Total deadtime (TDT) is the result of the combination of the CDT and the EDT:

$$\begin{aligned} TDT &\equiv 1 - TLT \;,, \quad TLT = CLT \cdot ELT \\ CLT &\equiv 1 - CDT, \quad ELT \equiv 1 - EDT \end{aligned} \tag{5.22}$$

A straightforward method to estimate the TDT is to obtain the relation between the rate of recorded events and the incident beam current. This study was performed for both the experiments E00-102 and E01-020 [Lac06]. A more accurate method to measure this total deadtime is to use a pulser signal which looks like a scintillator pulse through the path of the 4 PMTs required to make a trigger in each arm and to a TDC channel to "tag" the pulser event. This pulser is also sent to a scaler. The ratio of the number of recorded pulser events to the number of generated pulser events represents the total livetime.

The electronic livetime can be obtained from the CLT and the TLT measurements as

$$ELT = TLT / CLT \tag{5.23}$$

- **Experiment E00-102**

During this experiment, the pulser information was not available and it was necessary to obtain the total livetime (TLT) from the recorded rates as a function of the coincidence rate T_5. The code *dtchk* was used. Further details are presented in [Lac06].

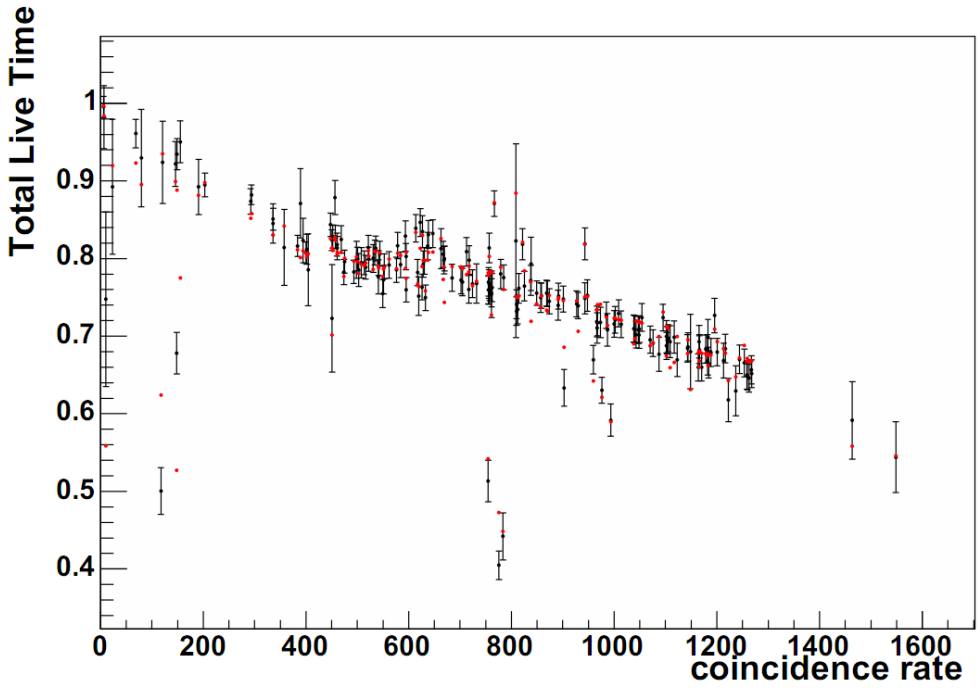

Figure 5.24: Total live time as a function of the coincidence rate in the experiments E00-102. (From [Lac06]). (See text for further details).

The computer deadtime was obtained from the ratio of the scalers of coincidence events T_5 and the actual recorded coincidences N_5 corrected by the corresponding prescale factor

$$CDT_i = \frac{T_i}{N_i \cdot ps_i} \tag{5.24}$$

In order to obtain the electronic deadtime, it was separated into the contribution from each arm

$$ELT = ELT^{LEFT} \cdot ELT^{RIGHT} \tag{5.25}$$

A linear dependence upon the trigger rates R1 and R3 was assumed for each of ELT^{LEFT} and ELT^{RIGHT}.

$$\begin{aligned} ELT^{LEFT} &= 1 - d_1 \cdot R1 \\ ELT^{RIGHT} &= 1 - d_3 \cdot R3 \end{aligned} \tag{5.26}$$

The parameters d_1, d_3 were obtained from a fit performed by the minimization of

$$\chi^2 = \sum_{i=1}^{N} \left(\frac{TLT_i - CLT_i \cdot ELT_i^{LEFT} \cdot ELT_i^{RIGHT}}{\sigma_i} \right)^2 \tag{5.27}$$

where the index i denotes the i^{th} run in the data set and σ_i is the statistical error in that run. After removing bad runs from the data sample, the fit returns

$$\begin{aligned} d_1 &= \left(5.956 \pm 0.022\right) \cdot 10^{-7} s \\ d_3 &= \left(7.263 \pm 0.015\right) \cdot 10^{-7} s \end{aligned} \tag{5.28}$$

The result from the fit is displayed with red points in Figure 5.24 together with the black points of the measured livetime from the recorded rates.

Figure 5.25 represents the ELT estimated for each run *i* as $ELT_i = TLT_i \,/\, CLT_i$ (black points) and the ELT obtained from the fit $ELT_i = \left(1 - d_1 \cdot R1_i\right) \cdot \left(1 - d_2 R2_i\right)$ (red points). It can be seen that electronic livetimes as low as 85% were seen. This was unexpected, as it implies that somewhere in the electronics there was a component with a gate width on the order of 500 ns. However, all components like discriminators were supposed to be set to have output widths of 100 ns. (see [Mic01]).

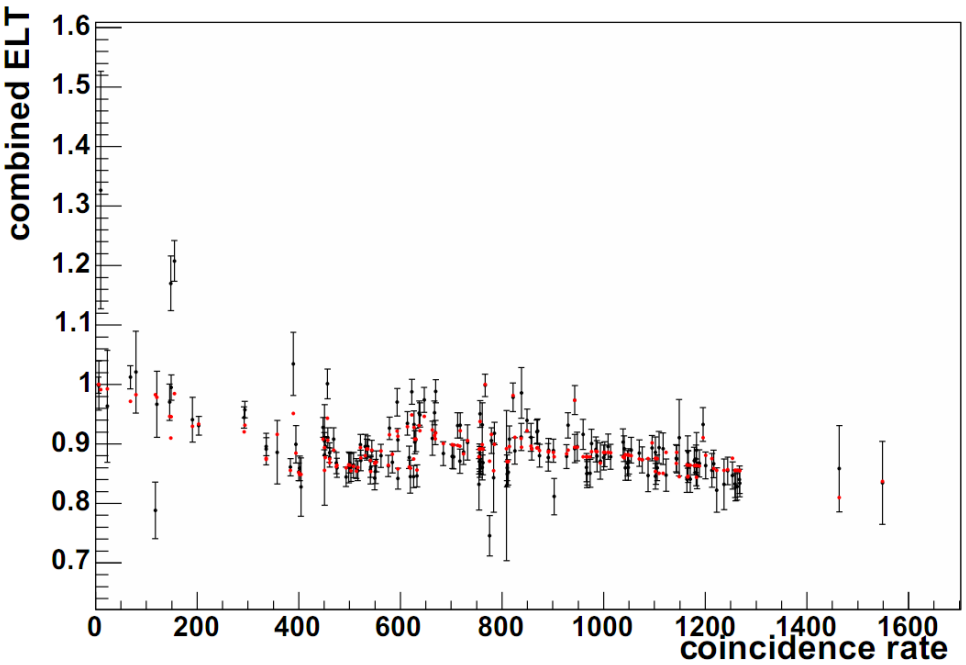

Figure 5.25: Electronic livetime as a function of the coincidence rate in the experiment E00-102. (From [Lac06]). (See text for further details).

- **Experiment E06-007**

In this experiment the pulser signal was used to obtain the total livetime required to correct the recorded coincidences. The module THaNormAna [Mic04] was incorporated into the data analysis software Analyzer, creating variables in the output ROOT file that not only determined a global livetime factor for each run, but also allowed for monitoring of the total livetime during the run.

Typical total livetimes in this experiment were on the order of 96%. The systematic error for the deadtime correction with this method was assumed to be 10% of the deadtime, about 0.4%. As a reference, Table 5.10 shows the total livetime obtained in several runs acquired with different Q^2 with beam currents between 35 μA and 40 μA.

No attempts were made in this experiment to obtain the electronic and the computer deadtime separately.

	Total livetime from pulser		
Example	Q^2=0.812 (Kin1)	Q^2 = 1.40 (Kin 12)	Q^2=1.97 (Kin 13)
1	0.962	0.965	0.953
2	0.962	0.964	0.955
3	0.962	0.963	0.951

Table 5.10: Total livetime in several E06-007 runs at different kinematics.

5.4.2. Trigger Efficiency

Scintillators are used to provide the experiment trigger. While extremely efficient, they are not perfect and the event loss due to this inefficiency must be quantified. The trigger efficiency for each spectrometer represents the probability that a charged particle results in a production trigger. Since this trigger is generated by the scintillator planes in each spectrometer, the corresponding trigger inefficiency represents the inefficiency of the scintillators and the electronics associated with the triggers being generated by these detectors.

The trigger-scintillator inefficiency can be caused by inefficiencies in the traveling tubes on each scintillator bar, absorption of scintillation light along the paddles to the photomultiplier tubes (PMTs), geometric holes between scintillator paddle comprising the trigger plane and fluctuations in the energy deposited by charged particles passing through the scintillator paddles.

The trigger efficiency is estimated by measuring the fraction of good events that caused a trigger in one of the scintillators but not in both. The triggers T_4(T_2) measures the number of these incomplete triggers in the left (right) HRS respectively. The total number of valid triggers registered in the left HRS is given by (T_3 (singles) + T_5 (coincidences)) and in the right HRS by (T_2 (singles) + T_5 (coincidences)). The individual trigger types are discussed in Section 4.7.2. Therefore, the trigger efficiency ε_e (ε_p) for electron (proton) detection is determined by:

$$\varepsilon_e = \frac{T_3^{'} + T_5^{'}}{T_3^{'} + T_4^{'} + T_5^{'}} \tag{5.29}$$

$$\varepsilon_p = \frac{T_1^{'} + T_5^{'}}{T_1^{'} + T_2^{'} + T_5^{'}} \tag{5.30}$$

where $T_i^{'}$ represents the number of triggers of type *i* after correction for the corresponding prescale factor ps_i and livetime

$$T_i^{'} = T_i \cdot ps_i \; / \; LT_i \tag{5.31}$$

The total trigger efficiency is the product the trigger efficiencies in both arms

$$\varepsilon_{trig} = \varepsilon_{trig-e} \cdot \varepsilon_{trig-p} \quad (5.32)$$

In order to ensure that the detected particles passed through the scintillators, the same acceptance cuts used in the data analysis were imposed on these events before evaluating the efficiency. The trigger efficiencies obtained did not vary with acceptances reduced even further.

- **Experiment E00-102**

The trigger efficiency obtained from Eqs. (5.29)-(5.32) was determined for each run. The values obtained from different runs are shown in Table 5.11. Good agreement was obtained with a previous trigger-efficiency evaluation presented in [Rei05]. The results for some runs in parallel kinematics (kin q) are shown in Table 5.11.

Run	2086	2803	3010
ε_{trig} - e	0.9725	0.9737	0.9688
ε_{trig} -p	0.9877	0.9861	0.9876
ε_{trig}	0.9605	0.9602	0.9568

Table 5.11: Trigger efficiency obtained in different runs during the experiment E00-102.

It is important to note that as H(e,e) events are used for luminosity normalization in this experiment, only the trigger efficiency on the right-arm should be corrected. Furthermore, the proton-detection efficiency obtained from anticoincidence events (see Section 5.4.6) results from a combination of trigger efficiency and proton absorption, so both efficiency measurements are complementary.

- **Experiment E06-007**

Trigger efficiency was also obtained for each run based on Eqs. (5.29)-(5.32) using only those events that fall inside the common acceptance cuts imposed during the data analysis (see Section 5.5). The efficiencies for both the left and right HRS at different runs are shown in Figure 5.26. This trigger efficiency was corrected on a run-by-run basis. In general, this measured efficiency was about 0.97% with 1% uncertainty.

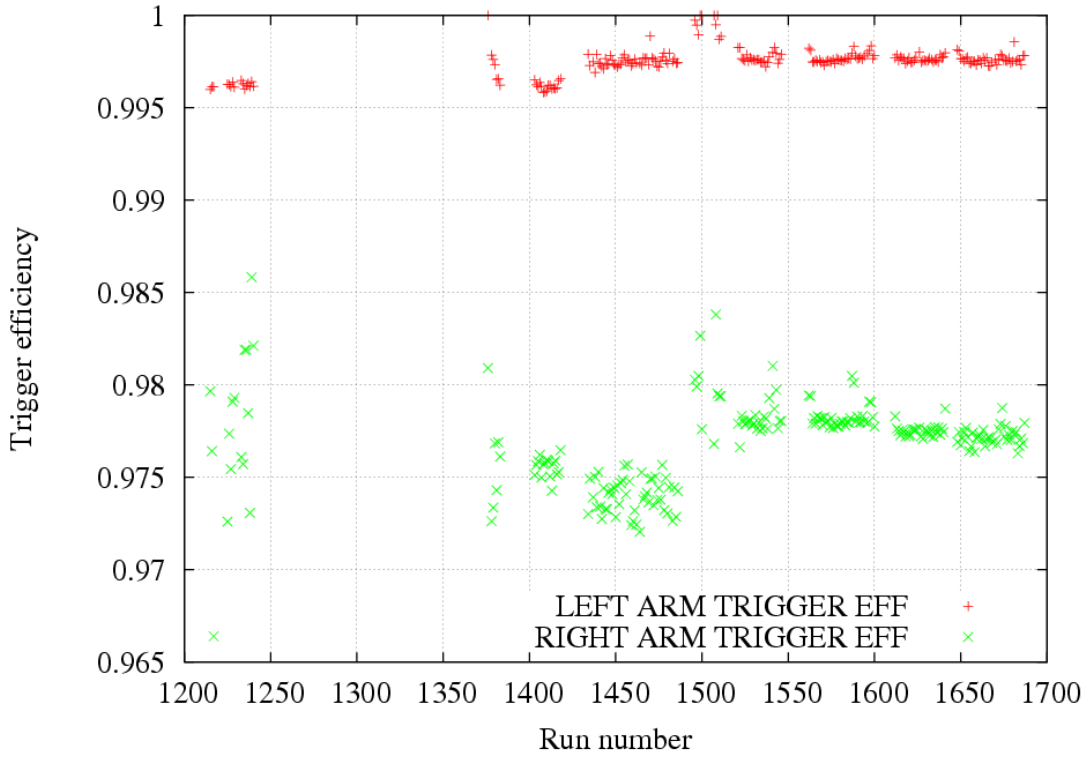

Figure 5.26: Trigger efficiency in the experiment E06-007 for the left and right HRS.

5.4.3. VDC Wire Efficiency

The efficiency of a single sense wire in the wire chambers is the probability that the wire fires when a charged particle passes sufficiently close to it. It can be estimated with the formula:

$$\varepsilon_{wire} = \frac{N_1}{N_0 + N_1} \tag{5.33}$$

where N_1 (N_0) is the number of times the wire fired (did not fire) when 2 wires adjacent to it fired. The efficiency determined with this formula is monitored during the experiment with an online macro provided with a graphical user interface (GUI).

This VDC efficiency was only used for monitoring the VDC, as the corresponding correction factor was included into a "global" tracking efficiency described in the next section.

- **Experiment E00-102**

In the right HRS, the efficiency was determined to be greater than 0.99 for all wires within the acceptance region of the spectrometers used in the cross-section analysis (Figure 5.27, right panels). In the center of the acceptance, this efficiency was about 0.996. Unfortunately, in the left HRS (Figure 5.27, left panels), the efficiency was lower. This was due to the high rate of particles reaching the chamber, as this HRS was placed at a very

small scattering angle (12.5º). The wire efficiency for this arm for the pertinent acceptance region was on average 0.980 ± 0.005.

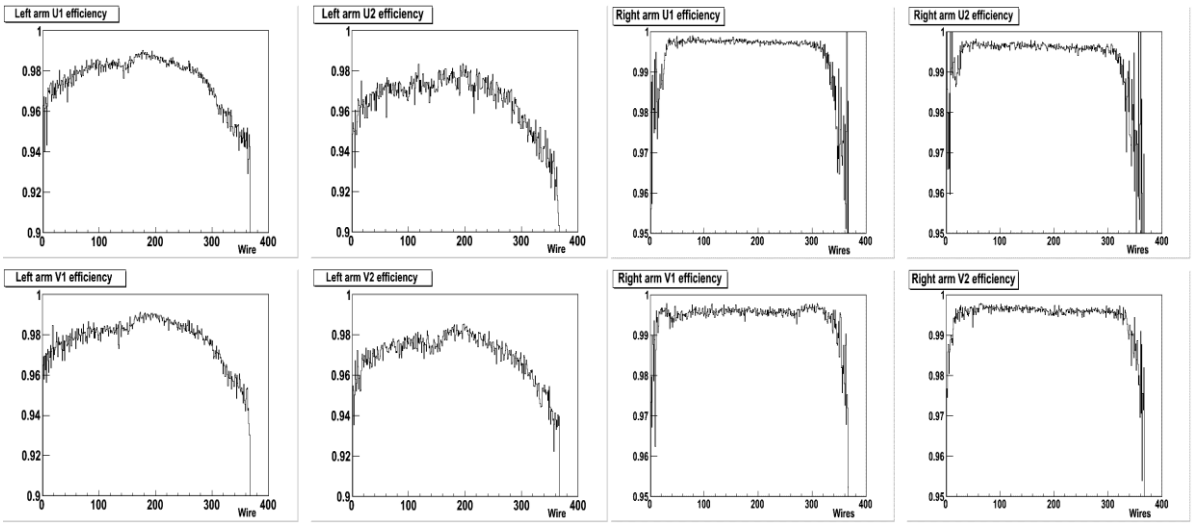

Figure 5.27: Efficiency of VDC wires in E00-102 determined using Eq. (5.33) for KinB+ for the left and right HRS. Note the different scales for the vertical axis.

- **Experiment E06-007**

The efficiency was determined to be greater than 0.98 for all wires within the acceptance region of the spectrometers used in cross-section analysis. On average, in the region inside the acceptances used in the data analysis, this efficiency was 0.995 ± 0.001 for the left HRS and 0.996 ± 0.001 for the right HRS. These values were stable throughout the experiment.

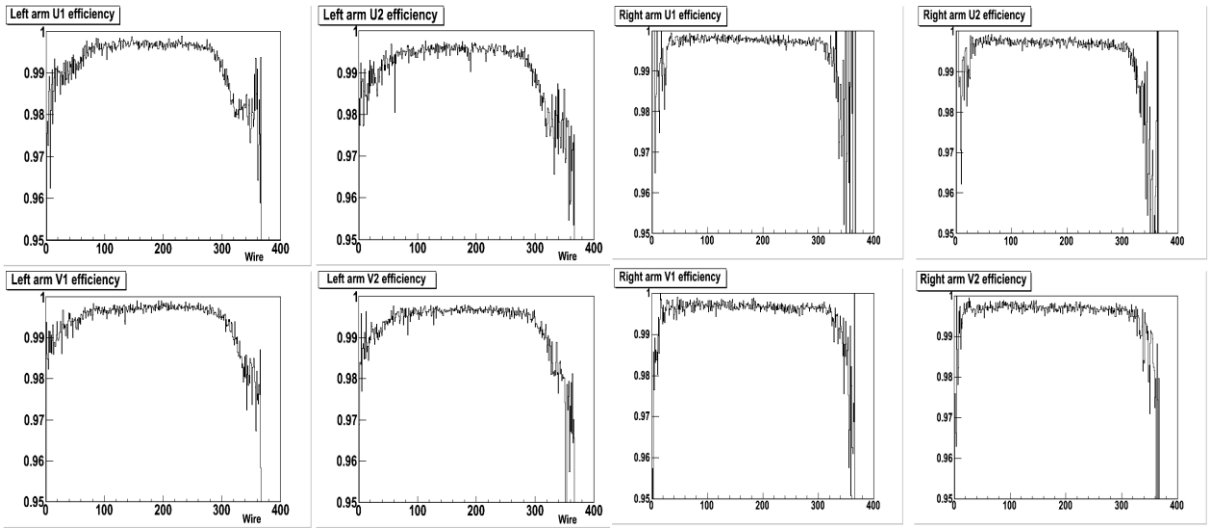

Figure 5.28: Efficiency of VDC wires in E06-007 determined using Eq. (5.33) for Kin 3 for the left and right HRS.

5.4.4. Tracking Efficiency

The tracking efficiency is the probability for a charged particle to be observed by the VDCs and correctly reconstructed by the tracking software. This efficiency is used to correct the data yield for events lost due to incorrect track reconstruction by dividing the detected data yield by the efficiency found for the electron and proton spectrometers.

For each event, the software Analyzer finds clusters of struck wires in each VDC wire plane and then fits various trajectories (tracks) through these clusters. The number of tracks obtained in each HRS for a typical run for each of the experiments E00-102 and E06-007 are shown in Figure 5.30 and Figure 5.32. The single trajectory corresponding to the best fit through all four wire planes of each VDC pair is selected as the *golden track*.

As it was described in [Mon08], the track reconstruction efficiency obtained using golden-tracks combines the VDC efficiency, the software event-reconstruction efficiency and any other inefficiencies in the spectrometers which affect the track reconstruction. The procedure used to obtain the tracking efficiency is as follows:

- A sample dataset of electron (proton) events was defined by selecting events in the respective spectrometer without using any information from the VDCs. The cuts used to define the sample dataset for each spectrometer were:
  1. For each event, the golden-track was selected in each arm.
  2. A cut on the raw TDC values which are used to form the coincidence time.
  3. A cut in beta for each particle obtained from the TOF between the scintillator planes in each HRS.
  4. Acceptance cuts on the θ_{tg} , φ_{tg} and δ_{tg} variables of the particle in the opposing spectrometer for which the track reconstruction efficiency was not being determined. Thus, when calculating the efficiency for the electron spectrometer, acceptance cuts on the proton spectrometer were used and vice-versa.
- After applying these cuts, the number of events remaining in the sample dataset is N_{sample}. Once the sample data were selected, the track-reconstruction efficiency was defined as

$$effic_{TRACKING} = \frac{N_{CUT}}{N_{SAMPLE}} \tag{5.34}$$

where N_{cut} is the number of events remaining after applying cuts based upon VDC information in the spectrometer for which the track-reconstruction efficiency is being

determined. By varying the cuts on the acceptance variables, the efficiency can be determined as these cuts are made progressively narrower, so that events which are reconstructed well outside the spectrometer acceptance are removed. The efficiency gradually decreases until a limit is reached near the outer edge of the nominal spectrometer acceptance. Making further cuts to a narrower acceptance range results in a very sharp drop in the efficiency as larger number of good events are rejected.

- The electron (proton) track-reconstruction efficiency is represented as a function of the cut applied and a linear fit in the region outside the nominal acceptances is performed. The offset of this line represents the probability that a good event is incorrectly reconstructed. This not only takes into account lost good events due to their reconstructed θ_{tg}, φ_{tg}, y_{tg} and δ_{tg} variables falling outside the acceptances, but also events within the nominal acceptances but with incorrectly reconstructed momenta or angles. These events will eventually be rejected by different cuts during the analysis.

• Experiment E00-102

In the experiment E00-102, as was shown in Figure 5.27, the VDC in the electron (left) arm was less efficient than that in the hadron arm. This was caused by the high event rate in that spectrometer due to the small scattering angle (12.5º). Nevertheless, in this experiment, this factor is already taken into account in the H(e,e) data used to normalize the ^{16}O(e,e'p) data, so only the tracking efficiency of the hadron arm was applied to correct the data. The track-reconstruction efficiency was determined for the different kinematics. The values used are given in Table 4.1.

These results were confirmed by the tracking efficiency obtained for each arm following the procedure described above. Figure 5.29 shows the tracking efficiency obtained for a typical run of the experiment E00-102 corresponding to p_{miss}=-280MeV/c (Kin F-). A sharp drop below the nominal acceptance δp<0.05 is clearly seen. The linear fit of good events that are incorrectly reconstructed and fall outside the acceptances gives as abscissa the corresponding tracking efficiency. The significantly lower tracking efficiency of the electron arm can be observed.

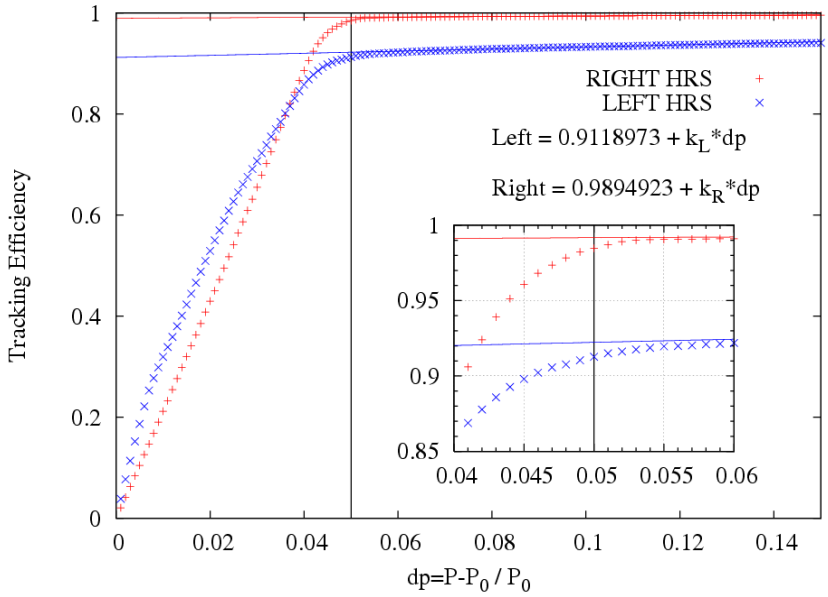

Figure 5.29: Tracking efficiency in E00-102 obtained from a linear fit of good events that are incorrectly reconstructed and fall outside the acceptances of the HRS.

Figure 5.30 shows the number of tracks measured in each spectrometer. The events with zero tracks in one arm correspond basically to singles, i.e. not coincidences. Note that these counts are affected by the prescale factor chosen. A small portion of multiple-track events (those with number of tracks >1) can be seen (especially in the electron arm), but they are very small in number with respect to the single-track events.

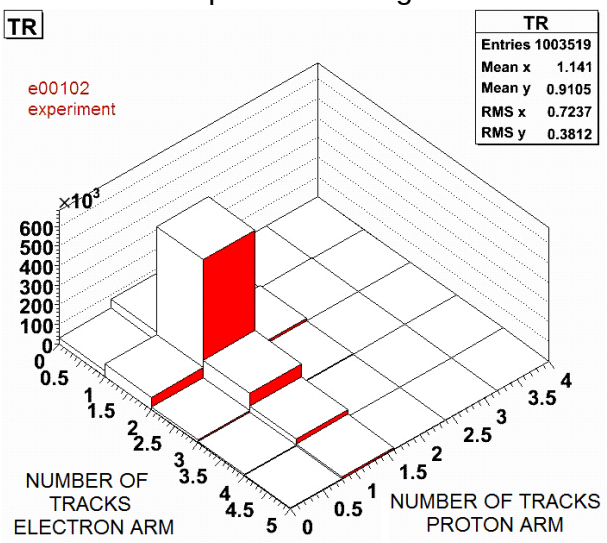

Figure 5.30: Number of tracks measured in each HRS for the events recorded in a data acquisition of the experiment E00-102.

Kinematics	Left	Right
Kin q (p_m=0)	0.962	0.988
Kin f_m (p_m=-280MeV/c)	0.912	0.989
Kin f_p (p_m=280MeV/c)	0.865	0.981

Table 5.12: Tracking efficiency for different kinematics of the experiment E00-102.

- **Experiment E06-007**

Track-reconstruction efficiency was also obtained for the data of experiment E06-007, and the results are shown in Figure 5.31. In this case, the efficiency of both arms are quite similar, as the left spectrometer was placed at 22.5º rather than 12.5º.

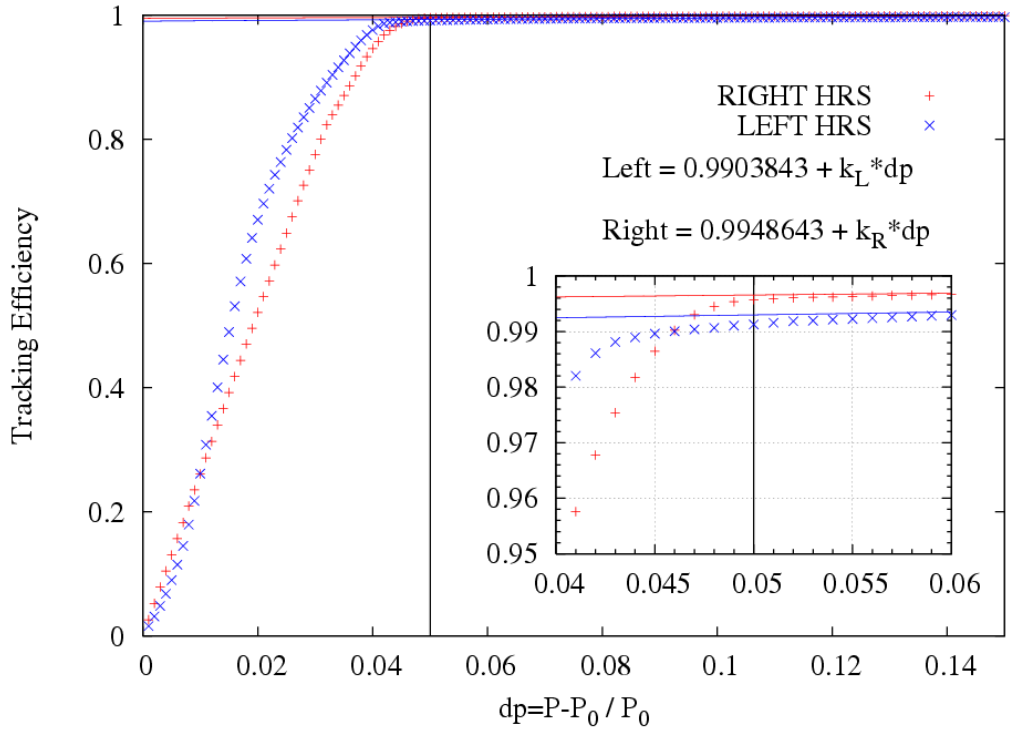

Figure 5.31: Tracking efficiency in E06-007 obtained from a linear fit of good events that are incorrectly reconstructed and fall outside the acceptances of the HRS. The figure corresponds to Kin 2 (p_m=100MeV/c) for lead.

The tracking efficiency was very similar at different kinematics. The mean and standard deviation of the mean of these results is given in Table 5.13.

Tracking efficiency		
Left	Right	Total
0.990 ± 0.002	0.995 ± 0.002	0.985 ± 0.003

Table 5.13: Tracking-efficiency values in The experiment E06-007.

The number of tracks measured in each spectrometer for a typical run in this experiment is shown in Figure 5.32. In this case, the number of single events (with zero tracks in one of the arms), is much more important because a smaller prescale factor was used. The ratio of coincidences with multiple-track events in any of the spectrometers relative to coincidences with single tracks is similar to the experiment E00-102.

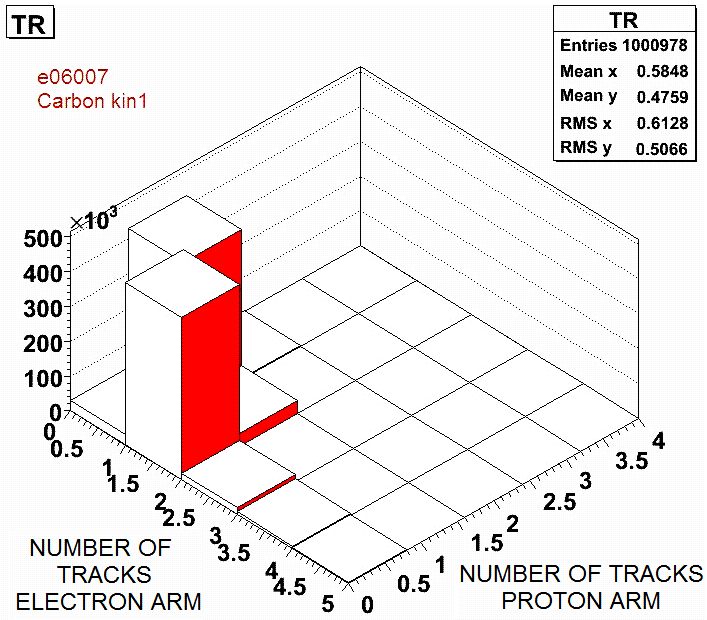

Figure 5.32: Number of tracks measured in each HRS for the events recorded in a Kin1 ^{12}C run of the experiment E06-007.

5.4.5. Proton Absorption

The knocked-out protons travel through material in the target, spectrometers and detector-stacks before they create a trigger in the scintillators. Therefore, there is some probability of the proton being absorbed or scattered in these materials due to nuclear interactions before making a trigger. Such a loss is called *nuclear absorption*.

In order to obtain a correction for this proton absorption, it was assumed that once a nuclear reaction occurs, the proton can no longer produce a trigger [Cha03][Qat05]. The mean free path, in cm, between nuclear collisions in each material *i* can be determined using

$$\lambda_i = 1 / \left[\left(\frac{\rho_i \cdot N_{AV}}{A_i} \right) \cdot \left(Z_i \cdot \sigma_{pp}(p_p) + N_i \cdot \sigma_{pn}(p_p) \right) \right] \tag{5.35}$$

where $\sigma_{pp}(p_p)$, $\sigma_{pn}(p_p)$ represent the total proton-proton and proton-neutron cross section (respectively) [Eid04, PDG] for protons with a momentum p_p, N_{AV} is the Avogadro constant (6.022e23/mol) and ρ_i represents the density (g/cm^3) of material *i*. Total proton absorption is obtained as

$$proton\ absorption = 1.0 - \exp\left(-\sum_i^n \frac{l_i}{\lambda_i} \right) \approx \sum_i^n \frac{l_i}{\lambda_i} \tag{5.36}$$

where the summation is over all the different materials listed in Table 5.14 and l_i represents the thickness (cm) of each material.

Cross sections $\sigma_{pp}(p_p)$, $\sigma_{pn}(p_p)$ for 1 GeV/c protons (valid for both the experiments E00-102 and E06-007) are very similar [PDG], so the following approximation was used:

$$\sigma_{pN}\left(p_p = 1GeV\right) \equiv \left[\sigma_{pp}\left(p_p = 1GeV\right) \approx \sigma_{pn}\left(p_p = 1GeV\right)\right] \approx 30mb = 0.30 \cdot 10^{-25} cm^2 \quad (5.37)$$

With this approximation, the mean free path given in Eq. (5.35) is simplified

$$\lambda_i = 1 / \left[\rho_i \cdot N_{AV} \cdot \sigma_{pN}\right] \quad (5.38)$$

Inserting Ec. (5.38) into the proton absorption from Eq. (5.36) results in

$$proton\ absorption \approx \left[\sum_i^n \frac{l_i}{\rho_i}\right] \cdot N_{AV} \cdot \sigma_{pN} = \left[\sum_i^n t_i\right] \cdot N_{AV} \cdot \sigma_{pN} = T \cdot N_{AV} \cdot \sigma_{pN} \quad (5.39)$$

where t_i represents the thickness in (g/cm^2) of material *i*, and T the total thickness (g/cm^2) of the materials along the path of the proton. Table 5.14 shows the list of these materials. Table 4.11 from [Qat05] was used as a reference. Proton absorption in the scintillator was already accounted for using the previous trigger-efficiency correction, so only materials upstream the first scintillator were considered. The target orientation with respect to the proton trajectory has been taken into account in the effective thickness.

Material	Density ρ (g/cm^3)	Thickness t (g/cm^2)
E06-007 Lead Foil	11.35	0.225
E06-007 Diamond Foil	3.515	0.0533
E00-102 Waterfall Foil (Average)	1.00	0.270
E00-102 Stainless Steel Target Window	7.8	0.25E-02
Aluminum (Scattering Chamber)	2.70	0.891E-01
Kapton (Spectrometer Entrance)	1.42	0.361E-01
Titanium	4.54	0.454E-01
Air	0.121E-02	0.968E-01
Mylar (Wire Chamber)	1.39	0.167E-01
Wire VDC (effective)	19.39	0.772E-03
Ar / Ethan	0.107E-02	0.214E-01

Table 5.14: List of materials and their properties used for the proton-absorption correction.

	E00-102	E06-007
TOTAL T (g/cm^2)	0.58	0.58
ABSORPTION (%)	1.0 ± 0.5	1.0 ± 0.5

Table 5.15: Total material thickness along proton's path and absorption.

The final estimate of proton absorption for both the experiments E00-102 and E06-007 is summarized in Table 5.15. A correction factor $\varepsilon_{p,abs}$=0.990 ± 0.005 was obtained. The relatively large uncertainty (systematic error) in this correction is due to the approximations made in the method, uncertainties in the thicknesses of the materials and the differences in the proton path for different kinematics and reaction points inside the target.

5.4.6. Proton detection efficiency

- **Experiment E00-102**

The presence of hydrogen in the waterfall target allowed the measurement of the proton detection efficiency in the right HRS. This measurement is based on the fact that H(e,e'p) is a two-body reaction and therefore once the scattered electron is detected, the momentum and direction of the corresponding proton is known. If the proton falls inside the acceptance of the right HRS but it is not detected, this must be due to some inefficiency. The procedure is implicitly based on the fact that the angular spread of the protons is small and that for all electrons inside the central acceptance of the left HRS, the proton from the H(e,e'p) reaction will be within the HRS acceptance.

The data taken with the right HRS along q (parallel kinematics, kin q) was used for this measurement. These parallel kinematics data were acquired at different occasions uniformly distributed throughout the duration of the experiment. The central momenta of both spectrometers were set so that the electrons and protons from the H(e,e'p) reaction would be detected in the flat efficiency region of the focal plane. A rigid cut was made on the electron arm solid angle to ensure that the proton from each H(e,e'p) event would reach the proton arm focal plane. Anti-coincidence events were used to obtain the proton efficiency using the relation

$$\eta_p = \frac{N_C}{N_C + N_A} \tag{5.40}$$

where N_C represents the number of detected electron-proton coincidences and N_A represents the number of anti-coincidences (with only a signal in the electron arm). Both counts were corrected by the corresponding prescale factors and livetimes. More details about the method can be found at [Lac06b].

A histogram of the kinematically-corrected relative momentum for the coincidence events (Figure 5.33) and anti-coincidence events (Figure 5.34) was generated. The peak corresponding to H(e,e) sits on top of the ^{16}O(e,e') quasielastic peak. In general, the hydrogen peak is considerably higher than the background. Nevertheless, in the anti-coincidence spectrum, the background is dominant.

ROOT was used to fit the background of the kinematically-corrected anti-coincidences events using 4th-order polynomials and to subtract it. The resulting spectrum is shown in Figure 5.34.

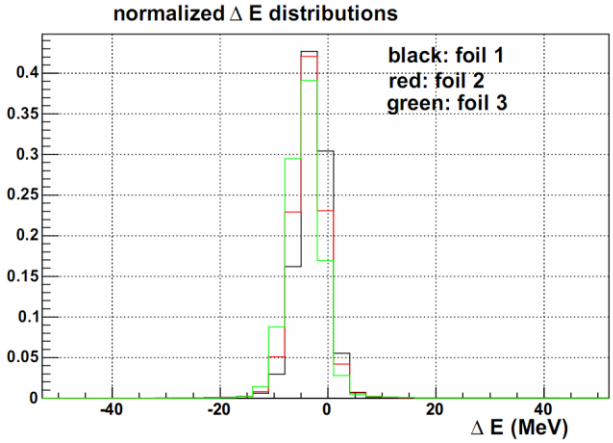

Figure 5.33 Kinematically corrected momentum of elastically scattered electrons detected in coincidence with a proton in the hadron arm. Figure from [Lac06b].

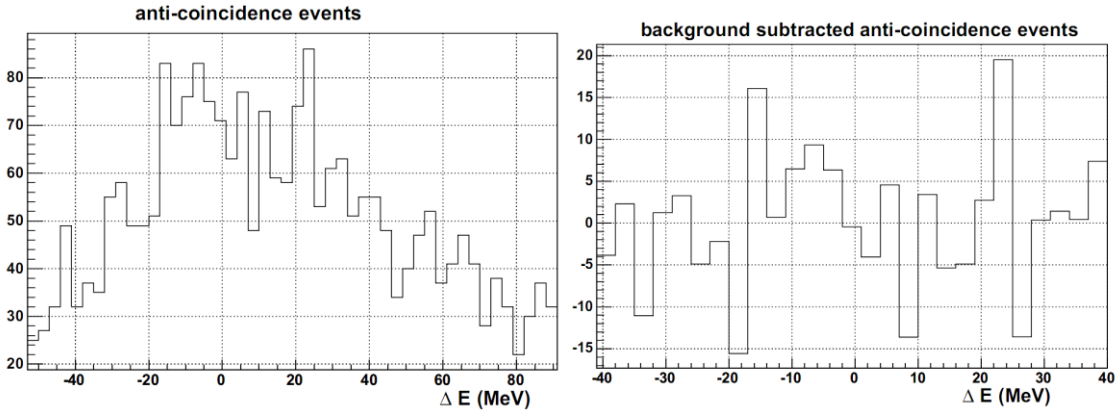

Figure 5.34: Kinematically corrected momentum of singles events from anti-coincidences. Before (left) and after (right) background subtraction. (Fig. from [Lac06b]).

The ratio of the counts N_C obtained from the integration over the elastic peak range shown in Figure 5.33 to the counts N_A obtained in the same range from Figure 5.34 (right panel) is about 3.7%. This indicates that the proton-detection efficiency is about 96.4 ± 3%. This inefficiency is reasonably consistent with proton absorption in the material it traverses on the way to the focal plane together with the inefficiency in the trigger electronics (Table 5.16). Nevertheless, due to the low statistics of the anticoincidences (a large prescale factor was unfortunately used for the singles in the electron arm) the efficiency obtained from the anti-coincidences has a large uncertainty. The final proton-detection efficiency was obtained combining both measurements and taking into account their uncertainties.

	N_C	N_A	Proton-detection efficiency from anti-coincidences	Proton Trigger eff. × Proton Absorption Corr.	Final proton efficiency
All Kin-q runs All foils	680114	25347	0.96 ± 0.03	0.98 ± 0.01	0.978 ± 0.016

Table 5.16: Proton-detection efficiency in the experiment E00-102.

5.4.7. Raster-Cut Correction

- **Experiment E06-007**

In the experiment E06-007, an additional cut was applied to the data to remove a small fraction of events where the raster may have directed the beam onto the aluminum target frame during RUN1. Figure 5.35 (left panel) shows clearly that the beam hit the aluminum frame, increasing the number of detected coincidences. After the cuts were imposed, the raster pattern was flat (right panel) . This can be compared with the raster pattern obtained in the second part of the experiment (RUN2) (see Figure 4.7).

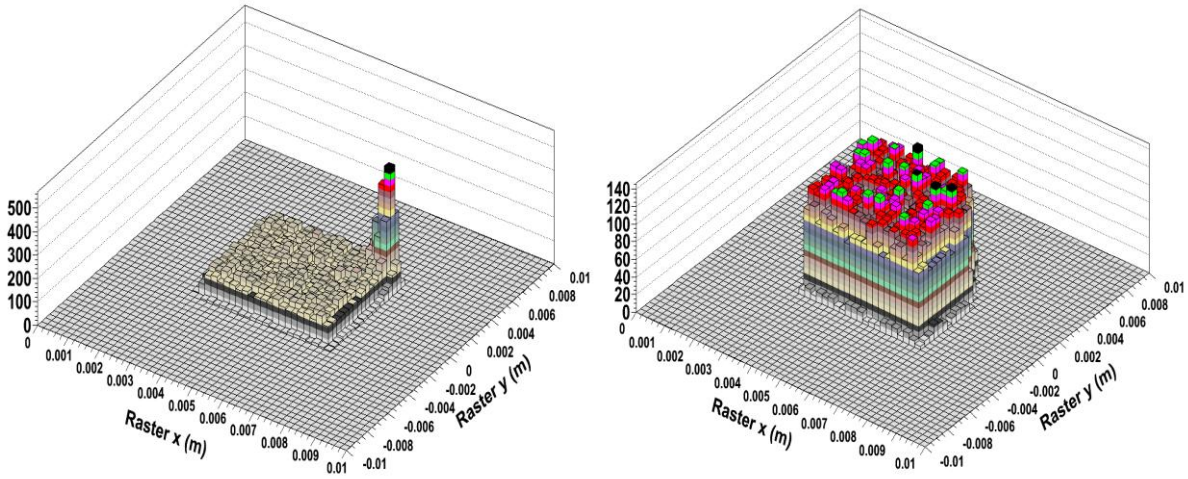

Figure 5.35: Raster pattern measured using the graphite target during RUN1 of the experiment E06-007. (Left) Before the cut (Right) with the cut imposed in the raster position.

This cut was necessarily taken into account when computing the effective luminosity of each run with an additional f_{CUT} factor (see Section 6.3). f_{CUT} represents the fraction of area removed by the cut imposed on the raster (x,y) position. This value was about 0.93, although it was not the same for all runs, as several raster sizes were used during the experiment. The correction factor was computed on a run-by-run basis and included in the effective luminosity of each run.

The accuracy of this raster-cut correction was verified using two different methods:

1) Different raster cuts were applied to the data and differences in the extracted cross section were studied.

2) Several runs on the graphite foil were acquired with and without rastering. The resulting cross sections were compared.

Based upon these careful studies, the systematic error caused by this raster cut was estimated to be around 3%.

5.5. Acceptances

There exist several approaches to take into account the edges of the detector acceptances. These regions are not so well understood and the efficiency of the detectors decrease [Gao99]. Therefore, they are difficult to simulate and to take into account in the analysis.

A) The "traditional" approach [Gao99] has been to make conservative orthogonal cuts in each variable, working just with the central acceptances. This method is easy to implement, but at the expense of rejecting at the very least half of the total detected events. This can be seen for example in Figure 5.36, where only the events in the red box were accepted.

B) On the other hand, R-functions were introduced in the E89-044 data analysis [Rva03], which proved to be a useful tool to take into account the multi-dimensional edges of the detector acceptances. With R-function cut, the number of accepted events increased dramatically.

The so-called R-function was generated for each event in both the data analyses and simulations to optimize the cuts on different acceptance variables, i.e. θ_{tg}, ϕ_{tg}, y_{tg}, δp_{tg}. The R-function is defined to be the minimal distance to the acceptance boundary in terms of several two-dimensional polygons. It helps to select events in the central region of the spectrometer acceptance in a systematic and efficient way, where the optics matrix elements were well tuned.

Six two-dimensional boundaries were defined for each spectrometer, out of any two combinations of the four acceptance variables, θ_{tg}, ϕ_{tg}, y_{tg}, δp_{tg}. Each boundary is a polygon defined in a two-dimension plot of the data. For each event, the magnitude of the distance to the boundary was normalized based on the maximal length. The sign of the distance was taken to be positive for events inside the polygon. The R-function for each single spectrometer is defined to be the minimal distance to the six boundaries, while for both spectrometers, it is defined by twelve two-dimension boundaries.

The coordinates of the vertices of the polygonal boundaries defined by the data were written into a file, which was then read by the analyzer to calculate the R-function in both data and simulation.

- **Experiment E00-102**

CENTRAL ACCEPTANCES: An illustration of the right arm spectrometer angular-

acceptance cuts used initially in the analysis of the data from this experiment [And05] can be seen in Figure 5.36. The red box indicates initial cuts made in θ_{tg} and ϕ_{tg} so that only the particles detected in the central acceptance region of the spectrometer were analyzed. The lack of events in the upper and lower right-hand corners of the scatter plot was due to trajectory masking caused by the NMR probes in the spectrometer dipole magnet.

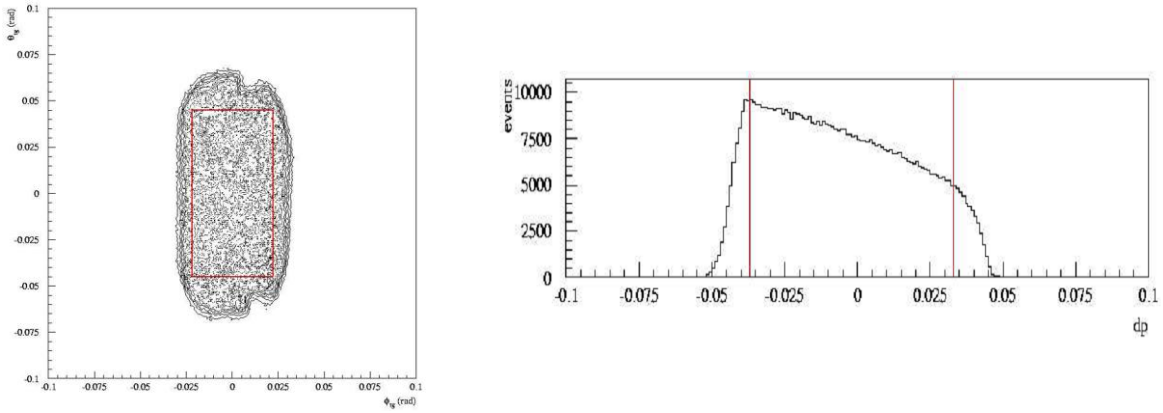

Figure 5.36: Central acceptances used in the initial data analysis (From [And05]).

R-FUNCTION: The R-function values were obtained for each event using Analyzer. The events surviving this cut in the angular acceptance are plotted in Figure 5.37. With cuts on the R-function, the acceptance dependence of the data-to-simulation ratio can be reduced. For a very large range of acceptance cuts, the change in the data to simulation ratio was only a few percent, therefore the uncertainty in the cross section due to acceptance cuts was taken to be 1% .The cut R>0.05 was used for all the E00-102 data analysis.

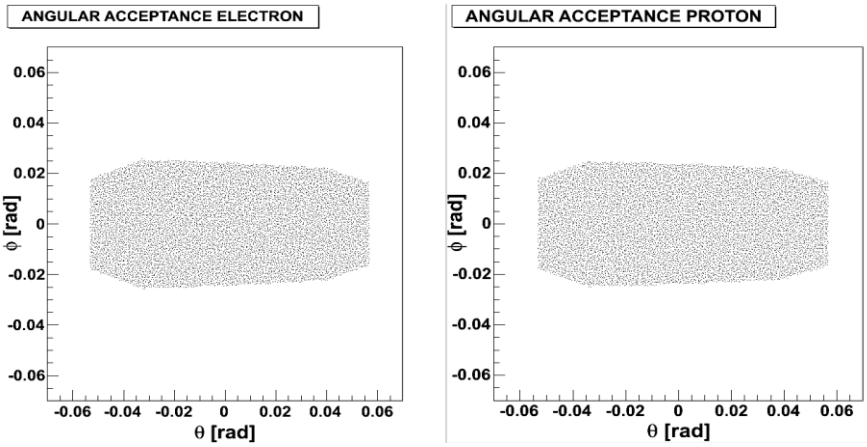

Figure 5.37: Left and Right HRS acceptances after the R-function cut R>0.05.

- **Experiment E06-007**

In the experiment E06-007, no R-functions were used and "traditional" central acceptance cuts in ϕ, θ *and* δp were applied to both arms. The cuts in these variables are

summarized in Table 5.17.

VARIABLE	LEFT HRS		RIGHT HRS	
ϕ_{tg} [rad] [Floor angle]	-0.02	0.02	-0.02	0.02
θ_{tg} [rad]	-0.04	0.04	-0.04	0.04
$\delta p = (p-p_0)/p$	-0.035	0.025	-0.035	0.025

Table 5.17: Cuts in acceptances in E06-007

With these cuts, the solid angle subtended by, in each arm was

$$\Delta\Omega_e = \Delta\theta_e \cdot \Delta\phi_e = 0.0032\ Sr^2$$
$$\Delta\Omega_p = \Delta\theta_p \cdot \Delta\phi_p = 0.0032\ Sr^2 \quad (5.41)$$

5.6. Randoms Subtraction

As described in Section 5.3.4, the Coincidence Time (CT) spectrum was used to separate real and random coincidences, as well as to remove the contamination of random coincidences within the prompt timing peak.

- **Experiment E00-102**

In this experiment, some real events were lost from the CT peak due to mistiming (see Figure 5.38). The top panel shows that there were events with CT values outside the CT window; that is, greater than 200 ns. The bottom panel shows the E_{miss} spectrum corresponding to mistimed events in the CT region marked with red in the top panel. There are clearly some real events as best evidenced by the peaks at 12.1 and 18.4 MeV corresponding to proton knockout from the $1p_{1/2}$ and $1p_{3/2}$ states of ^{16}O respectively. These peaks would not appear if the events were purely random. These data are centered at p_{miss}=60MeV/c.

Both HRS are instrumented with TDCs to make complementary CT spectra. They are created with a local start and stopped using a trigger accepted by the opposite spectrometer. Therefore, the two complementary CT spectra created (one for each arm) have opposite start and stop (see Figure 5.39). In this plot, the events with the expected timing should lie in a line (Region A, inside the red rectangle), while all other events are mistimed. To compensate for this problem, the number of real events outside Region A was quantified for each kinematics using the information from the E_{miss} spectrum,, and correction factors were determined.

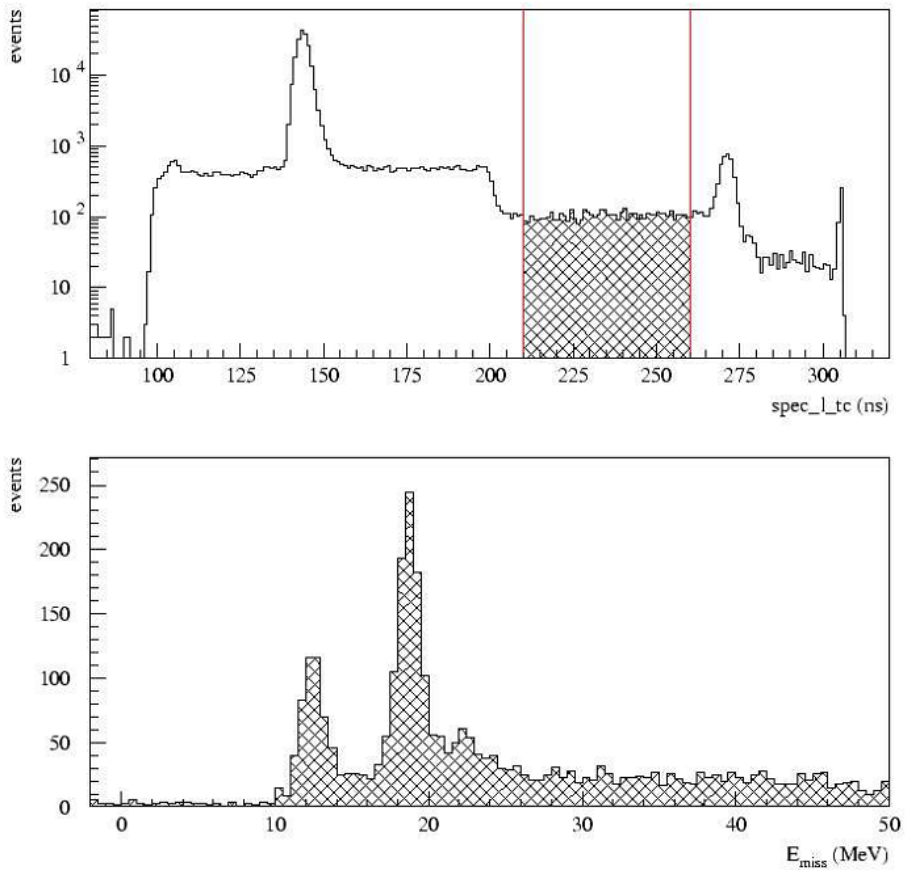

Figure 5.38: An illustration of mistiming in the CT spectra in the experiment E00-102. Events far from the CT peak, like the ones between the red lines, should be random coincidences without peaks in the E_{miss} spectrum (Fig. from [And05]).

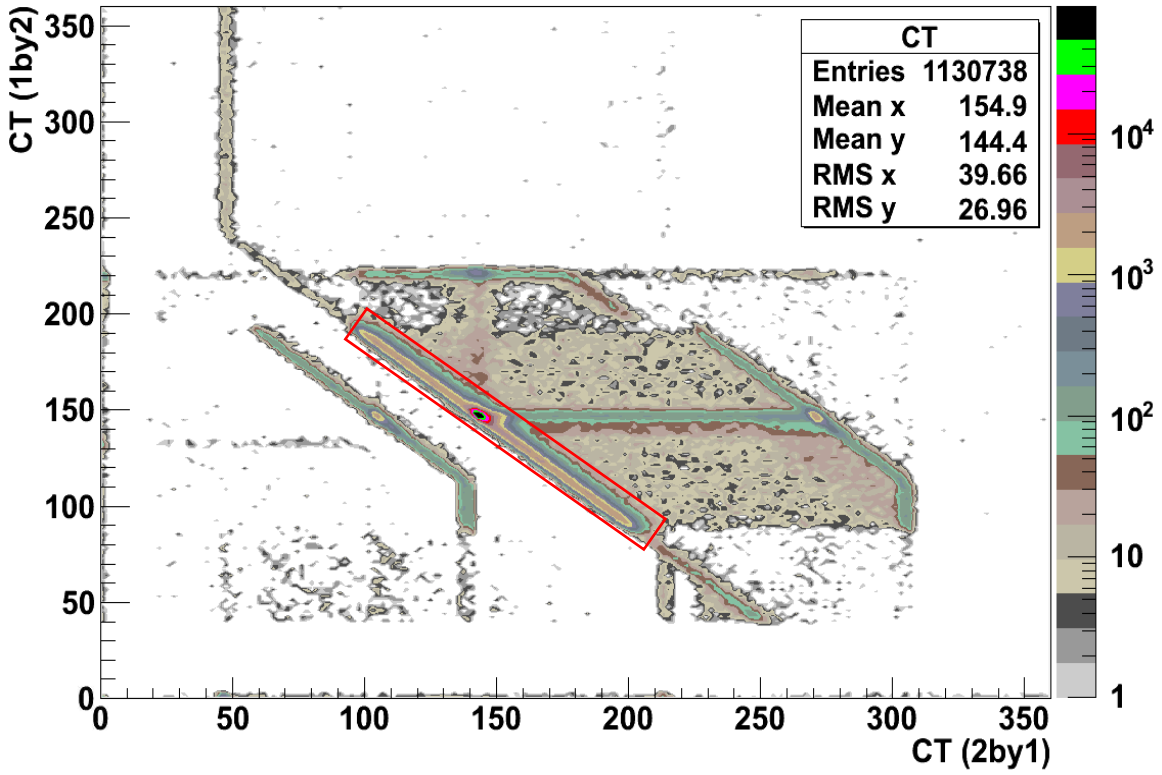

Figure 5.39: CT scatterplot generated from the two spectrometers. Only events in Region A (in red) correspond to well-timed events.

1) Looking only at the events in Region A, a plot was made of the CT (see Figure 5.40). The number of events in the foreground region and in the background region was determined. The foreground yield consisted of both real and random-coincidence events. The background yield consisted entirely of random-coincidence events. The total number of real events Y_{real} was calculated by subtracting the weighted background from the foreground. The weight was the size of the TDC interval used for the foreground divided by the total width of the TDC intervals used for the background

$$Y_{real} = Y_{fg} - \left(\frac{\omega_{fg}}{\omega_{bg1} + \omega_{bg2}} \right) Y_{bg} \tag{5.42}$$

Y_{fg} was the sum of the events in the foreground region and Y_{bg} was the sum of the events in the background regions. ω_{fg}, ω_{bg1} and ω_{bg2} were the widths of the respective TDC intervals.

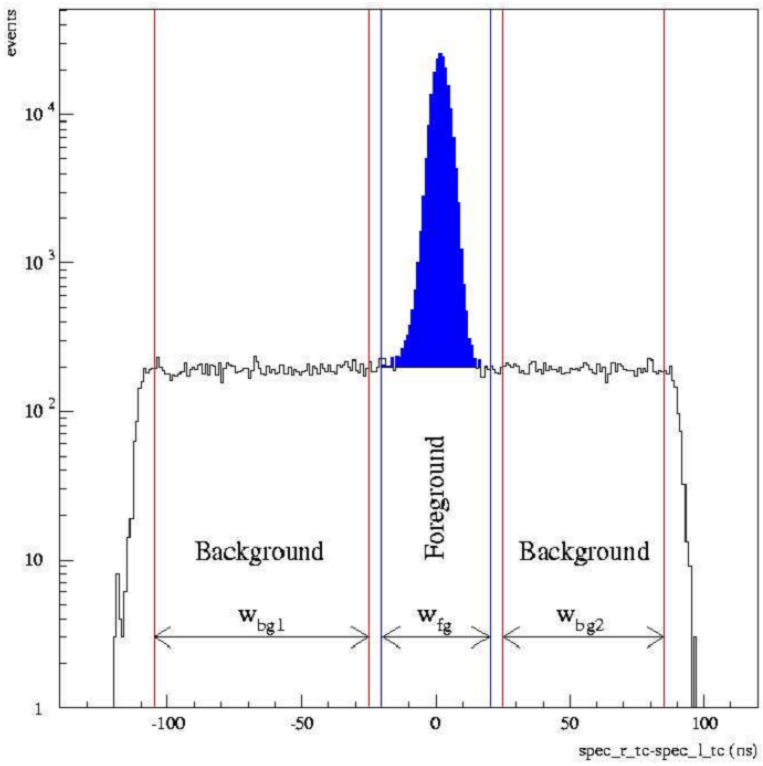

Figure 5.40: CT spectrum for region A (without mistiming events).

2) To determine the number of real events located outside Region A due to mistiming, the E_{miss} spectrum for those events was used (see Figure 5.41). The E_{miss} spectrum consisted of real events superimposed upon a random-coincidence background. The number of random coincidences was determined with a linear fit in the non-physical range (-70MeV<E_{miss}<10MeV) where there were no peaks. The number of random coincidences

in the region E_{miss} > 10 MeV was determined by extrapolating the fit function. The total number of real events lying outside Region A was then determined by subtracting the fitted function from the data, and summing the resulting distribution of events for 10 < E_{miss} < 150 MeV.

3) The number of real events inside Region A and the number of real events outside Region A were hence determined and the mistiming was corrected based upon this ratio

$$Y_{real,cor} = \left(1 + \frac{Y_{real,B}}{Y_{real,A}}\right) \cdot Y_{real,A} = K \cdot Y_{real,A} \tag{5.43}$$

Here $Y_{real,A}$ was the real yield from region A, $Y_{real,B}$ was the real yield from events outside region A and $Y_{real,cor}$ was the corrected real yield. This correction assumes (and it was checked) that all real events had the same probability of being mistimed.

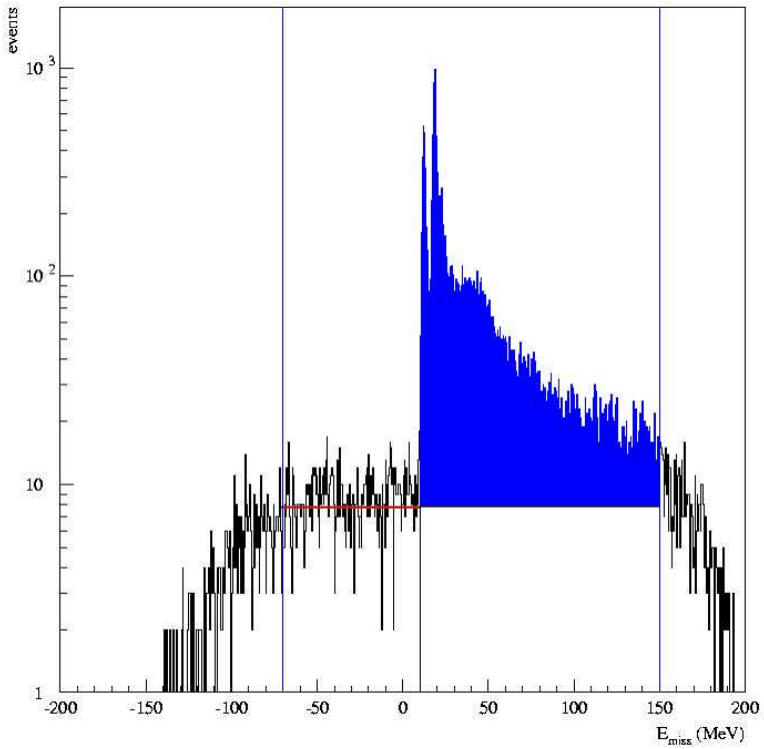

Figure 5.41: E_{miss} spectrum of mistimed events with background subtraction from a linear fit in the non-physical region in the E_{miss} spectrum.

The mistiming correction factor obtained for each kinematics was applied as an efficiency correction to the total number of real coincidences before computing the cross section (see Chapter 1).

- **Experiment E06-007**

In the data acquired in experiment E06-007 (Run 1 and Run 2), there was no problem with mistiming events as can be seen in Figure 5.42. The E_{miss} spectrum off the CT peak does not show any structure in the region $0 < E_{miss} < 20$MeV.

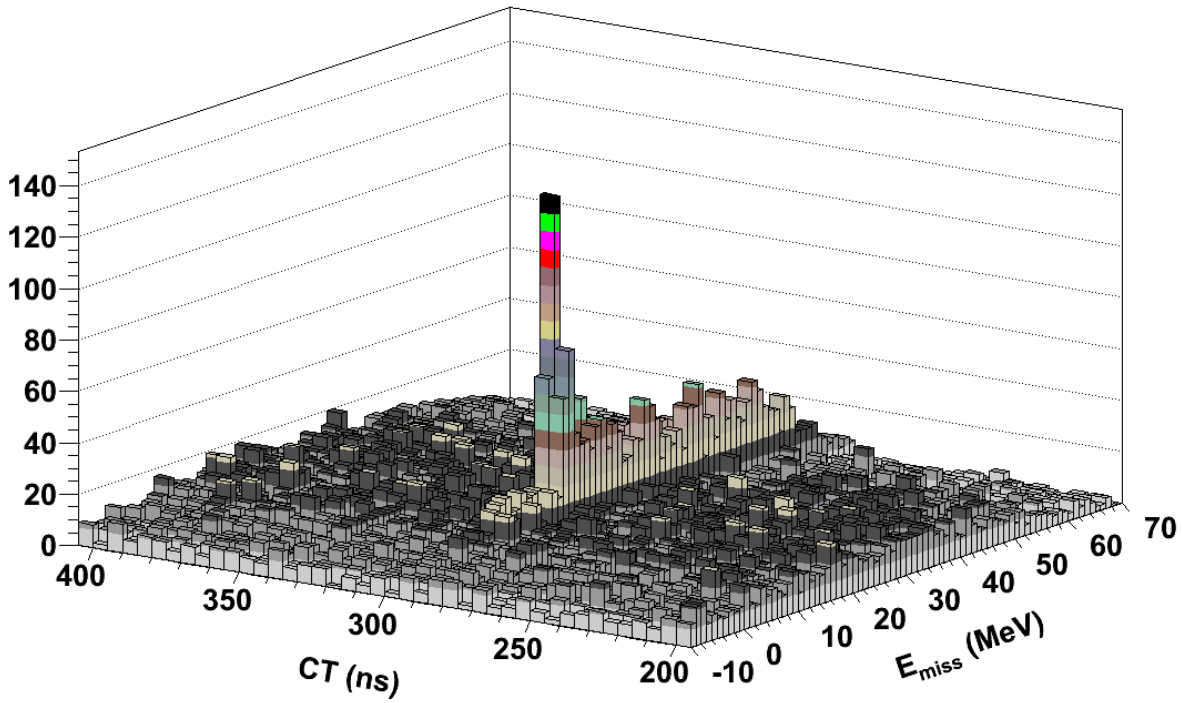

Figure 5.42: E_{miss} spectrum vs. CT corresponding to a high p_{miss} run of E06-007.

6. Data Analysis II – Cross section and A_{TL} extraction

In this thesis, simulations were used as a reference at all steps performed in the data analysis. This way, the impact of any cut applied to the data on the final result could be easily checked. The analysis can be separated into the steps presented in Figure 6.1.

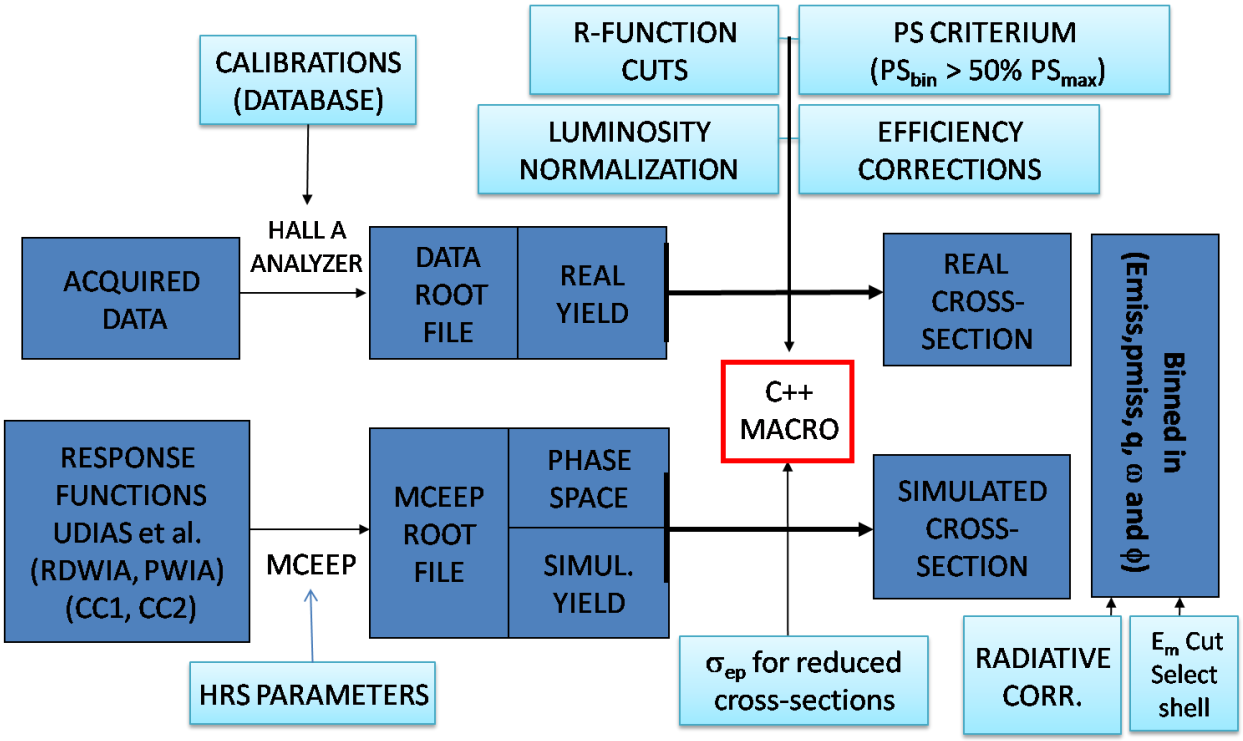

Figure 6.1 – Flow chart of the experimental analysis.

6.1. Generation of ROOT files with N-tuples

To begin with, data were retrieved from the Hall A storage system and processed via Analyzer. A calibrated database containing the optics properties of the HRSs, characteristics of the scintillators (pedestals, offsets) and some parameters of the experimental setup are required to reconstruct the events. A ROOT file with the main physical variables for each recorded event is obtained as well as a summary text file containing basic statistics for each file together with scalers. Simultaneously, several simulations of the experiment were performed with MCEEP based on different theoretical models and a realistic model of both HRSs and the experimental setup. The output files

were converted into ROOT files [ROOT] for a subsequent processing.

6.2. Event-by-event processing

In the second step, both reconstructed data and simulations are processed by a C++ macro developed for the experiments E00-102 and E06-007. This macro processes all the events in both the experimental data files and simulated files performing the following actions:

1. It applies all acceptances cuts based on R-functions (Section 5.5) and CT.
2. It selects only those events with single tracks in the VDC. At the end of the process, the number of events is corrected for this restrictive cut.
3. It computes, with the kinematical variables of each event, the $\sigma_{ep,CC1}$ cross section based on the prescription of De Forest [For83] and the proton form factors based on a fit of Rosenbluth data [Arr04]. The factor $\left[E_p \cdot p_p \cdot \sigma_{ep.cc1} \cdot R\right]^{-1}$, where *R* represents the recoil factor as defined in Eq. (1.21), is used as a weight for each event to compute the reduced cross section.
4. It stores the events in histograms. In ROOT, only 1-, 2- or 3-dimensional histograms are available. Therefore, in order to store the events in "5-Dimensional" histograms N(E_{miss}, $p_{miss,}$ q, ω, ϕ), an index $i_{qw\phi}$ was given for each (q, ω, ϕ) bin. This way, experimental and simulated events were stored in N(E_{miss}, $p_{miss,}$ $i_{qw\phi}$) 3-dimensional histograms. In the experiment E00-102 the number of bins used was large as the data were copious. As the data for E06-007 were far fewer, only one single bin in q,ω, ϕ was used.

Events from the simulation are stored in two histograms: one is filled with unweighted events for obtaining the phase space (i.e. how each variable is populated based upon just due to kinematical reasons) and a second where each event is weighted by the theoretical cross section, as modeled by the response-functions. This weighted histogram is then compared with the histogrammed data.

Events from experimental data are stored in two different histograms depending on the coincidence time. Events that fall outside the CT peak ($\pm 3\sigma$) are considered accidental events and are stored separately for the random-subtraction procedure as described in Section 5.6.

Finally, at the end of each data run, the macro applies efficiency corrections, multitrack corrections and livetime corrections to the data.

6.3. Calculation of Cross Sections

After all individual runs of the same kinematics are processed, global normalization factors are applied to the data and a random subtraction are performed. As a result, the total number of true coincidences is obtained.

The measurement of the cross section for the (e,e'p) reaction requires knowledge of the luminosity *L* and the overall efficiencies and corrections that should be applied to the data. The luminosity is defined as the product of the total number of incident electrons and the number of target nuclei per unit area

$$L = \left(\frac{Q}{e}\right) \cdot \left(t \cdot \frac{N_{AV}}{A}\right) \tag{6.1}$$

where *Q* represents the total accumulated charge in the configuration under consideration, *e* is the electron charge, N_{AV} is Avogadro's number, *A* is the atomic weight and *t* is the thickness of the target in g/cm^2.

In (e,e'p) experiments, the cross section is measured over finite angular and momentum acceptances for both the electron and the proton. Therefore, the measured cross section is six-fold differential. As data were binned in a five-dimensional space $\left(E_{miss}, p_{miss}, q, \omega, \phi\right)$, the six-fold differential cross section for each bin B$\left(E_{miss}, p_{miss}, q, \omega, \phi\right)$was obtained by dividing the number of events in that bin (N_B) by an effective luminosity L_{eff}, and the acceptance (or phase space) volume of the bin V_B.

$$\left\langle \frac{d^6\sigma}{d\omega d\Omega_e dT_p d\Omega_p} \right\rangle_B = \frac{N_B}{L_{eff} \cdot V_B} \tag{6.2}$$

The symbols < >$_B$ represent the averaged value in the phase space volume of the bin *B*. This cross section approaches the theoretical cross section (obtained with the central values of the bin) only if the latter does not vary appreciably over the volume of the bin. The effective luminosity L_{eff} includes all the efficiencies ε and the coincidence livetime (LT) described in Section 5.4. Also, any additional cuts applied to the data (like a cut in the raster in experiment E06-007) are corrected for here by applying a f_{CUT} factor

$$L_{eff} = L \cdot \left(\varepsilon \cdot LT \cdot f_{CUT}\right) \tag{6.3}$$

The phase space volume V_B of each bin B is defined as

$$V_B = \int_B d\omega d\Omega_e dT_p d\Omega_p \tag{6.4}$$

This phase space volume was obtained from a Monte-Carlo simulation. The HRSs of Hall A have the feature that the acceptance is flat over approximately 5 msr of solid angle and

(-3.7% to +3.3% in dp/p) [Gao99]. Thus, Nps_{TOT} events were randomly generated within this flat acceptance region over the variables ω, ϕ_e, θ_e, T_p, ϕ_p and θ_p. These simulated events were binned into the variables E_m, p_m, ω, q and ϕ and the same acceptance cuts used with the measured data (see Section 5.5) were imposed. The resulting number of events Nps_B in each bin B $\left(E_m, p_m, q, \omega, \phi\right)$ was used to compute the phase space volume:

$$V_B = \frac{Nps_B}{Nps_{TOT}} \cdot \Delta\omega\Delta\Omega_e\Delta T_p\Delta\Omega_p \tag{6.5}$$

where $\Delta\omega\Delta\Omega_e\Delta T_p\Delta\Omega_p$ are the ranges of the acceptances considered in the simulation, selected slightly larger than the actual cuts imposed upon the data to avoid edge effects.

The five-fold differential cross section for a discrete state is obtained from the six-fold differential cross section given in Eq. (6.2) by integrating over the corresponding E_{miss} region of the state. It is necessary to make use of the recoil factor (Jacobian) $R = \left|\partial E_m / \partial T_p\right|^{-1}$ defined in Eq. (1.21):

$$\left\langle \frac{d^5\sigma}{d\omega d\Omega_e d\Omega_p} \right\rangle_{\substack{E_{miss}=[E_1^{miss},E_2^{miss}] \\ B}} = \int_{E_2^{miss}}^{E_1^{miss}} \left\langle \frac{d^6\sigma}{d\omega d\Omega_e dT_p d\Omega_p} \right\rangle_B \cdot \left\langle R \right\rangle_B \cdot dE_{miss} \tag{6.6}$$

where $\left\langle R \right\rangle_B$ represents the averaged value of the recoil factor in the phase space volume of the bin *B*. Note that the recoil factor *R* is basically unity for the perpendicular kinematics and the nuclei of the experiments of this work.

6.3.1. Experiment E00-102

The overall coincidence efficiency ε in the effective luminosity L_{eff} given in Eq. (6.3) can be decomposed as

$$\varepsilon = \varepsilon_e \varepsilon_p \varepsilon_{coin} \tag{6.7}$$

where ε_e, ε_p, ε_{coin} are the electron-, proton- and coincidence-trigger efficiencies respectively. The factor $\varepsilon_p \cdot \varepsilon_{coin}$ represents the total proton detection efficiency described in Section 5.4.6. In the experiment E00-102, the product of the luminosity *L* and the electron-arm efficiency was obtained by comparing the number of H(e,e) events recorded in the left-HRS $N_{H(e,e)}$ with the fairly well known cross section for the H(e,e) reaction integrated over the electron arm angular acceptances

$$\sigma_{H(e,e)} = \int_{\Delta\Omega_e} \frac{d\sigma_{H(e,e)}}{d\Omega_e} \cdot d\Omega_e \tag{6.8}$$

This method allowed obtaining uncertainties below 4% in the previous E89-003 experiment [Fis04].

The number of experimental H(e,e) events was obtained in a stand-alone macro using

the same (R-function) cuts applied to the ^{16}O(e,e'p) data. This number of H(e,e) events was obtained as the integral of the peak corresponding to the kinematically corrected momentum of the electron single arm events after background subtraction, as described in Section 5.1.3. The H(e,e) reaction was also simulated with MCEEP (using a subroutine that MCEEP provides to compute the cross section $\sigma_{H(e,e)}$) and processed with the usual R-function acceptance cuts. This way, the H(e,e) cross section obtained was averaged with the same acceptances as the data and radiative tails were consistently considered; that is, they were equally included in both the measured data and in the simulation. The resulting cross section was denoted $\sigma_{SIM,H(e,e)}$.

The effective luminosity was therefore computed as $L_{eff} = \left(L \cdot \varepsilon_e\right) \cdot \left(\varepsilon_p \varepsilon_{coin}\right) \cdot LT$, with

$$L \cdot \varepsilon_e = \frac{N_{H(e,e)}}{\sigma_{SIM,H(e,e)}} \tag{6.9}$$

The livetime (LT) factors were obtained as described in Section 5.4.1.

Table 6.1 summarizes the number of bins and range of the variables used in the data analysis of the experiment E00-102.

	E_m (MeV)	p_m (MeV/c)	q (MeV/c)	ω (MeV)	ϕ (rad)
Min	-5	0	975	470	0
Max	70	800	1150	520	π
Bin Size	1	20	21.875	6.25	π/18
Number of Bins	75	40	8	8	18

Table 6.1: Sizes and number of bins chosen for the E00-102 data.

6.3.2. Experiment E06-007

In the experiment E06-007 there was no hydrogen in the target and a luminosity normalization based on the number of detected H(e,e) events, as done in E00-102, was not possible. Therefore, special efforts were devoted to obtain an accurate calibration of the beam-charge measurements and a reliable method to obtain deadtime corrections.

Target thickness, being solid targets, was assumed constant during the course of the experiment, as no boiling effects were expected. The rates of single events (S) measured in the electron arm at different days during the experiment were used as a diagnostic of target thickness. These single rates were corrected by prescale factors used during each run, and the livetime (LT) obtained from the pulser

$$S' = S \times PS \times LT$$

These corrected singles rates (S') in the electron arm should be constant if no changes

occur to the target.

The additional cut imposed upon the data to avoid a small square of the raster pattern that resulted in the beam hitting the aluminum target frame (see Section 5.4.7) was considered in the effective luminosity using an additional f_{CUT} factor in Eq. (6.3).

In this experiment, data was binned only in (E_{miss},p_{miss}); that is, with a single bin in q, ω and ϕ. In this case, the bin size in E_{miss} was smaller as sufficient energy resolution was required to separate the individual states in lead and carbon.

The bin size and range of the variables are summarized in Table 6.2.

	E_m (MeV)	p_m (MeV/c)
Min	-10	0
Max	80	500
Bin Size	0.25	20
Number of Bins	360	25

Table 6.2: Sizes and number of bins chosen for E06-007 data.

6.4. Radiative Corrections

The theoretical description of the energy loss and radiative processes present in these (e,e'p) experiments with a beam energy of several GeV was introduced in Section 3.6. MCEEP simulations, performed to be compared with the data, already have these effects incorporated, so a direct comparison between them and the acquired data can be performed.

Therefore, in this thesis, experimental data have not been corrected by radiative processes to avoid posible bias introduced in the radiative unfolding procedure. Instead, all these effects have been introduced in the simulations. This method has been followed in the analysis of other experiments [Mak94].

6.5. Reduced Cross Section

The reduced cross section was obtained by dividing the measured cross section by the factor $\left[E_p \cdot p_p \cdot \sigma_{ep.cc1} \cdot R\right]^{-1}$:

$$\left\langle \sigma_{RED} \right\rangle = \left\langle \frac{1}{\left[R \cdot E_p \cdot p_p \cdot \sigma_{ep.cc1}\right]} \cdot \frac{d^5\sigma}{d\Omega_e d\Omega_p d\omega} \right\rangle \qquad (6.10)$$

The factor $\left[E_p \cdot p_p \cdot \sigma_{ep.cc1} \cdot R\right]^{-1}$ was computed for each event with the corresponding values of the kinematic variables. It was used as a weighting factor when the data and simulations were histogrammed in the [E_m,p_m,q,ω,ϕ] variables. This way, computing the reduced cross section was straightforward.

6.6. A_{TL} Extraction

Data at both sides of *q* were used to obtain the transverse-longitudinal asymmetry A_{TL}.

$$A_{TL} = \frac{\sigma_m - \sigma_p}{\sigma_m + \sigma_p} \tag{6.11}$$

where σ_m represents *minus* kinematics ($\theta_{pq} < 0$, i.e. $\theta_p < \theta_q$) and σ_p represents *plus* kinematics ($\theta_{pq} > 0$, i.e. $\theta_p > \theta_q$). It is important to note that, being a relative measurement, A_{TL} is less sensitive to systematic uncertainties. For instance, it is not affected by possible errors in the luminosity. On the other hand, as it is defined as a difference of cross sections, its statistical error in these experiments is considerably large. The statistical error of A_{TL} can be obtained from the uncertainty of σ_m and σ_p as

$$\Delta A_{TL} = \frac{\left(\Delta\sigma_m{}^2 + \Delta\sigma_p{}^2\right)^{1/2}}{\left(\sigma_m + \sigma_p\right)} \cdot \left(1 + A_{TL}{}^2\right)^{1/2} \tag{6.12}$$

6.7. Systematic uncertainty

An estimate of the systematic uncertainties in these experiments is presented in Table 6.3.

Quantity	Uncertainty	% effect on cross section
Beam energy	0.2%	0.4
Electron scattering angle	0.3 mr	0.3
Proton scattering angle	0.3 mr	0.4
Proton solid angle	2.0%	2.0
E00102 Luminosity (relative)	1.7%	1.7
E00102 Luminosity (absolute)	4.0%	4.0
E06007 Luminosity (absolute)	5.0%	5.0
Total uncertainty E00102		4.8
Total uncertainty E06007		5.4

Table 6.3: Summary of systematic uncertainty in the experiments E00-102 and E06-007.

The total systematic uncertainty for the ^{16}O(e,e'p) cross section is a little less than 5%. It is dominated by the uncertainty of H(e,e) cross section, which has been used to obtain the absolute luminosity. On the other hand, uncertainty in the experiment E06-007 was mainly caused by the raster cut and additional uncertainties in the raster pattern, both affecting the luminosity.

7. Experiment E00-102 - ^{16}O(e,e'p)

7.1. Kinematics of this Experiment

For this experiment, a beam energy of 4.620 GeV was used. The left HRS, set to detect electrons with a central momentum of 4.121 GeV/c, was fixed at 12.5° and was never moved. This determined the kinematical variables |q| = 1.073 GeV/c and ω = 0.499 GeV, and hence Q^2 = 0.902 (GeV/c)^2 as shown in

Table 7.1. The kinematical parameters were defined in Section 1.4.

Central values for all kinematics	
E_0 = 4.620 GeV	σ_{MOTT} = 1729 nb / sr
$\|q\|$ = 1.073 GeV/c	$\lambda = Q^2 / q^2$ = 0.7834
ω = 0.499 GeV	$tan^2(\theta_e/2)$ = 0.0120
Q^2 = 0.902 (GeV/c)^2	V_L = 0.6137
θ_e = 12.5º = 0.218 rad	V_T = 0.4037
E_{ef} = 4.121 GeV	V_{LT} = 0.6987
T_p = 0.989GeV	V_{TT} = 0.3917

Table 7.1: Fixed parameters for the experiment E00-102.

The right HRS, set to detect protons, was positioned at the angles listed in

Table 7.2, with a constant momentum setting of 1.066 GeV/c. The experimental kinematics are shown schematically in Figure 7.1. Settings with negative p_{miss} are said to be at *minus* kinematics and those with positive p_{miss} are said to be at *plus* kinematics.

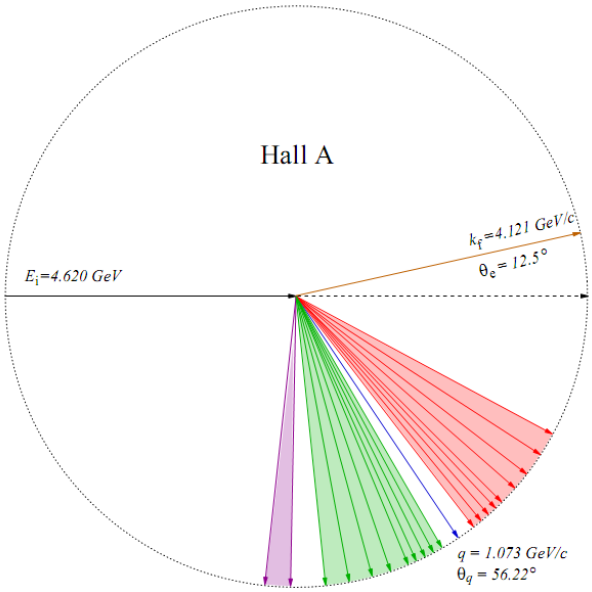

Figure 7.1: Diagram of the kinematical settings for the experiment E00-102.

In experiment E00-102, the 4.620 GeV electron beam entered Hall A from the left. The waterfall target was located inside the scattering chamber at the centre of the hall. The electron spectrometer was set at θ_e = 12.5° (brown) with a central field of 4.121 GeV/c, determining the magnitude and direction of the momentum transfer (blue) to be 1.073 GeV/c at θ_q = 56.22°. Measurements of ejected protons were made over a range of angles yielding a range in p_{miss} (see Table 7.2). The *minus* kinematics are shown in red and *plus* kinematics are shown in green. Groundbreaking measurements performed at extreme positive p_{miss} *are shown in magenta*.

KINEMATICS	Pmiss (MeV/c)	θ_{pq} (deg)	θ_p (deg)
I-	-515	-27.95	28.27
H-	-430	-23.27	32.95
G-	-345	-18.60	37.62
F-	-280	-14.90	41.32
E-	-210	-11.20	45.02
D-	-175	-9.40	46.82
C-	-140	-7.50	48.72
B-	-105	-5.60	50.62
A-	-70	-3.75	52.47
q	0	0	56.22
A+	+70	+3.75	59.97
B+	+105	+5.60	61.82
C+	+140	+7.50	63.72
D+	+175	+9.40	65.62
E+	+210	+11.20	67.42
F+	+280	+14.90	71.12
G+	+345	+18.60	74.82
H+	+430	+23.27	79.49
I+	+515	+27.95	84.17
J+	+635	+34.87	91.09
K+	+725	+39.88	96.19

Table 7.2: Overview of the kinematical settings for the experiment E00-102.

7.2. Experimental Results

p_{miss} (MeV/c)	Reduced Cross Section σ_{red} (GeV^{-3}) $1p_{1/2}$ shell		
	E00-102 Data	Relativistic RDWIA simulation	Non-Relativistic RDWIA simulation
-330	0.0546(47)	0.0366(18)	0.0340(12)
-310	0.0962(67)	0.0753(48)	0.0557(17)
-290	0.174(10)	0.163(62)	0.1127(18)
-270	0.400(15)	0.3935(75)	0.3031(50)
-250	0.847(18)	0.915(17)	0.7554(71)
-230	1.682(36)	1.907(17)	1.6822(81)
-210	3.081(60)	3.610(26)	3.311(13)
-190	5.771(88)	6.291(25)	5.929(11)
-170	9.67(11)	10.146(20)	9.709(19)
-150	14.13(21)	14.928(24)	14.482(41)
-130	20.04(34)	19.887(89)	19.45(11)
-110	23.91(51)	23.72(13)	23.74(34)
110	28.03(54)	26.00(29)	25.18(45)
130	22.82(27)	20.73(20)	20.72(16)
150	15.64(22)	15.08(13)	14.886(88)
170	10.14(10)	9.934(74)	9.772(48)
190	5.68(16)	5.965(39)	5.829(27)
210	2.959(59)	3.270(19)	3.135(14)
230	1.413(44)	1.6385(90)	1.4965(81)
250	0.610(34)	0.7325(72)	0.6562(76)
270	0.308(14)	0.3234(41)	0.2726(44)
290	0.156(16)	0.1555(23)	0.1105(14)
310	0.0981(73)	0.0935(29)	0.0677(16)
330	0.084(12)	0.0704(11)	0.0602(67)

Table 7.3: $^{16}O(e,e'p)$ reduced cross section from the experiment E00-102.

The measured ^{16}O(e,e'p) reduced cross sections from the experiment E00-102 for the $1p_{1/2}$ shell, are presented in Table 7.4. The results from relativistic and non-relativistic RDWIA simulations are also included. Uncertainties (statistical only) are indicated with parentheses, so that 0.0084(12) means 0.0084 ± 0.0012. Recall that simulations include all acceptance, cuts and radiative effects, thus they are to be compared directly to data.

Figure 7.2 shows these experimental results together with simulations obtained with (in red) and without (in blue) the dynamical relativistic effects described in Chapter 2. The overall agreement between the experimental data and the simulations is noticeable good. It can also be seen that the reduced cross section tend to agree better with the relativistic results at high missing momentum.

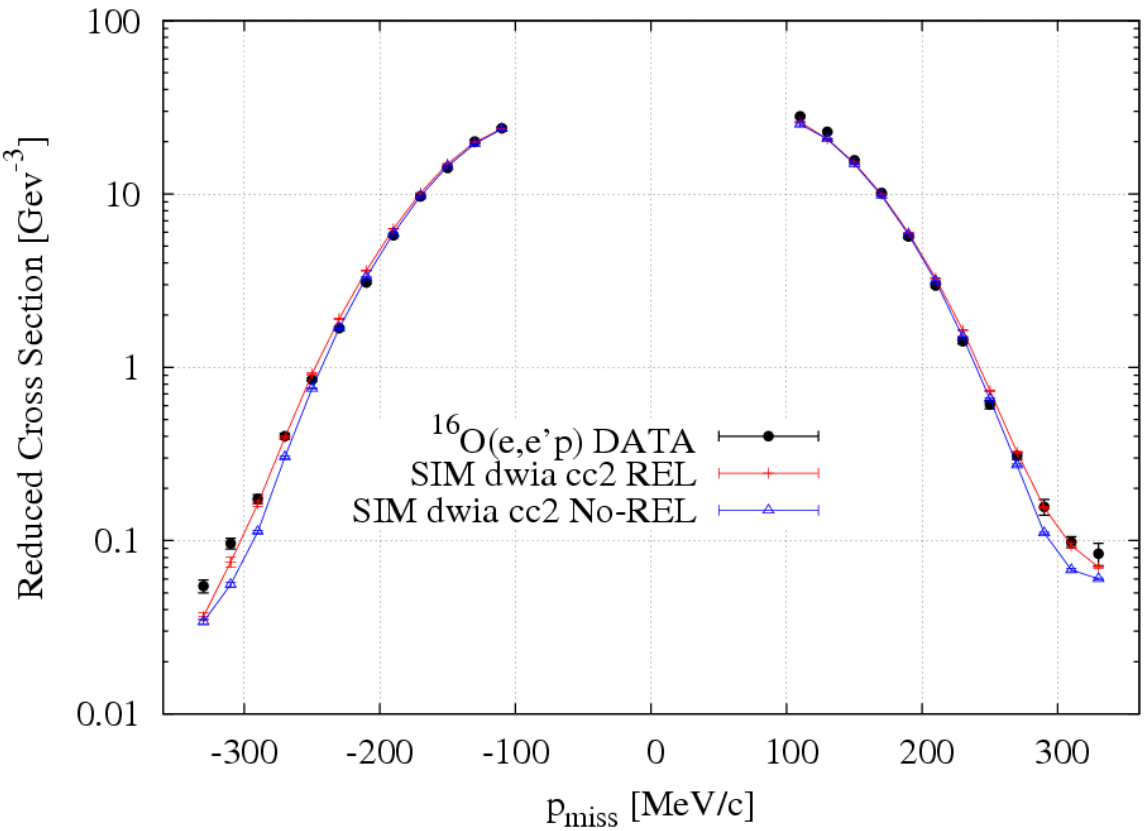

Figure 7.2: ^{16}O(e,e'p) experimental reduced cross section. The results from simulations based on the two theoretical approaches discussed in the text are also shown.

The experimental observable A_{TL} from the experiment E00-102 as a function of p_{miss} for the $1p_{1/2}$ shell of ^{16}O obtained as described in Section 6.6 is presented in Table 7.4.

p_{miss} (MeV/c)	A_{TL} ($1p_{1/2}$)		
	E00-102 DATA	Simulation DWIA Relativistic	Simulation DWIA Non-Relativistic
110	-0.132(45)	-0.089(12)	-0.130(50)
130	-0.210(26)	-0.138(80)	-0.186(60)
150	-0.165(18)	-0.168(60)	-0.244(80)
170	-0.234(17)	-0.232(70)	-0.295(80)
190	-0.301(20)	-0.299(90)	-0.314(80)
210	-0.392(21)	-0.357(90)	-0.394(10)
230	-0.409(29)	-0.377(80)	-0.378(46)
250	-0.467(34)	-0.458(10)	-0.382(42)
270	-0.492(66)	-0.453(49)	-0.297(56)
290	-0.372(87)	-0.432(44)	-0.178(58)
310	-0.31(11)	-0.277(60)	-0.297(56)
330	-0.19(11)	-0.118(59)	-0.178(58)

Table 7.4: A_{TL} for the $1p_{1/2}$ state of ^{16}O from the experiment E00-102.

The experimental A_{TL} values together with the results from simulations and data from former experiment E89-003 is shown in Figure 7.3.

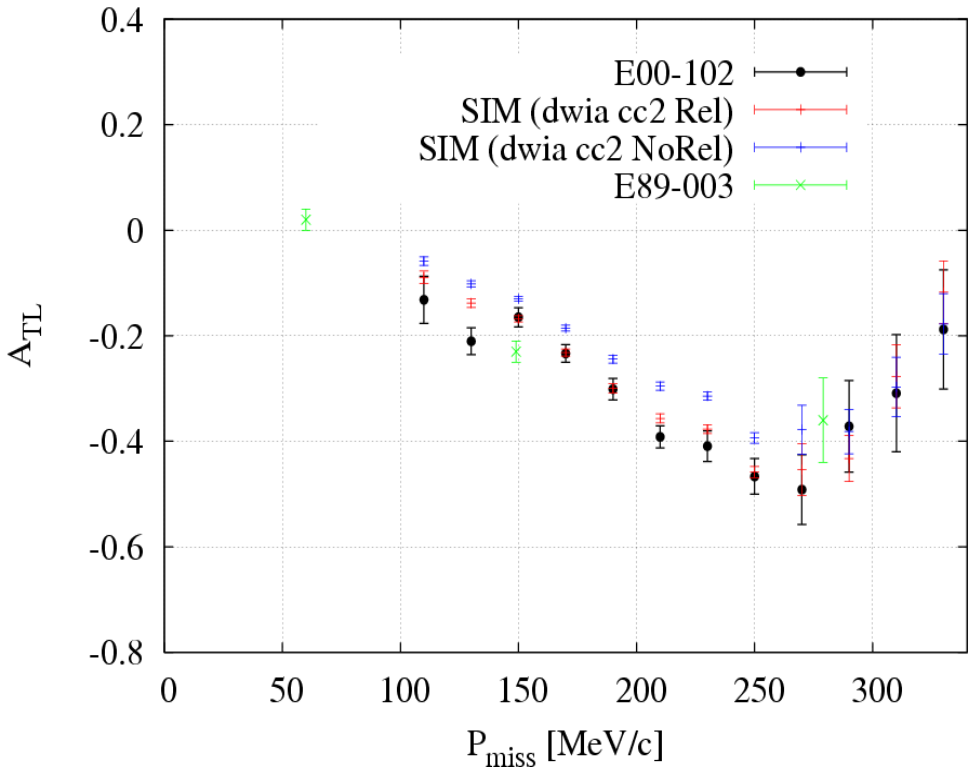

Figure 7.3: Experimental A_{TL} from the experiment E00-102, together with simulations and data points from the former E89-003 experiment. The experimental data seem to favor the relativistic results.

7.3. Comparison with Previous Experiments

The spectroscopic factor of 0.71 ± 0.05 for the p_{12} shell obtained in this experiment is in good agreement with the previous experiments [Fis04].

Figure 7.3 shows the comparison of the experimental A_{TL} of the $1p_{1/2}$ shell from the experiment E00-102 together with the results from the previous E89-003 experiment. It is important to note that these experiments were not performed at the same kinematics. In this plot, the improved uncertainty obtained in the experiment E00-102 with respect to E89-003, is clearly seen.

7.4. Comparison with theory and simulations

Data from this experiment have been compared with simulations based on response functions obtained with DWIA theoretical models with fully relativistic dynamics and with spinors with non-relativistic structure; that is, no negative energy content or on the mass shell. A description of these models was given in Chapter 2.

The region below 300 MeV/c in p_{miss} where the calculations are more reliable shows a deviation between data and DWIA results with non-relativistic spinors which cannot be explained by statistical uncertainties. DWIA results with fully off-shell spinors are in a much better agreement with cross section over the entire momentum range under consideration as well as asymmetry data. It is important to note that this agreement with the large number of points obtained in this experiment together with their reduced uncertainties is much more compelling evidence in favor of relativistic dynamics than in former experiments. Further, in the case of the reduced cross section, the only fitted parameter is the spectroscopic factor (as was the case in former experiments), while in the case of the asymmetry, there are no fitted parameters at all.

Note that the optical potentials were taken from elastic proton scattering off ^{16}O and that the bound-state wave function was obtained from RMF parameters slightly tuned from the NLSH parameter set [Rein86] to reproduce the (e,e'p) data of the NIKHEF-K experiment of Leuschner et al. (see [Udi01]). These data were obtained in parallel kinematics at moderate values of missing momentum, where there was no effect due to the relativistic structure of the spinors.

7.5. Summary and Conclusions

Cross sections for the ^{16}O(e,e'p) reaction have been measured in the quasielastic region with Q^2 = 0.902 (GeV/c)^2 in perpendicular kinematics. The results have been compared to fully radiated and acceptance-folded simulations based on unfactorized DWIA calculations that include spinors with both non-relativistic and relativistic structure. The conclusions can be summarized as follows:

- Cross sections agree with the standard DWIA calculations (both relativistic and non-relativistic) with spectroscopic factors around 71% for $1p_{1/2}$ states for missing momentum up to 300 MeV/c. However, at the larger value of momentum, the relativistic calculations agree better with data.
- The asymmetry A_{TL} has been compared to calculations without dynamical relativistic effects (that is without the negative-energy components in the wave functions) and to fully relativistic DWIA calculations [Udi93]. Data clearly favors the fully relativistic calculation. There are no free parameters in the theoretical calculations. The excellent agreement with the data must be interpreted as a great success of the fully relativistic Impulse Approximation and one of the most compelling experimental justifications of the need to modify the structure of spinors that describe nucleons bound in nuclei.
- This experiment has provided a theoretically challenging and experimentally unique data set for the quasielastic ^{16}O(e,e'p) reaction at Q^2 = 0.902 (GeV/c)^2 over a very large range of missing momentum at with accurate measurements of both the reduced cross section and asymmetry A_{TL}.

8. Experiment E06-007 - *(e,e'p) on* ^{208}Pb and ^{12}C

8.1. Kinematics of this Experiment

For this experiment, beam energy of 2.649 GeV was used. The left HRS set to detect electrons with a central momentum of 2.216 GeV/c, was fixed at 21.44° and was never moved. This determined the kinematical variables |q| = 1.000 GeV/c and ω=0.433 GeV, and hence Q^2 = 0.82 (GeV/c)^2, as summarized in Table 8.1.

Central values for all kinematics	
E_0 = 2.649 GeV	σ_{MOTT} = 45.67 nb/sr
$\|q\|$ = 1.000 GeV/c	$\lambda = Q^2 / q^2$ = 0.82
ω = 0.433 GeV	$tan^2(\theta_e/2)$ = 0.03584
Q^2 = 0.820 (GeV/c)^2	V_L = 0.6742
θ_e = 21.44 deg. = 0.3742 rad	V_T = 0.4458
E_{ef} =2.216 GeV	V_{LT} = 0.7586
T_p = 1.363GeV	V_{TT} = 0.4100

Table 8.1: Fixed parameters for the experiment E06-007.

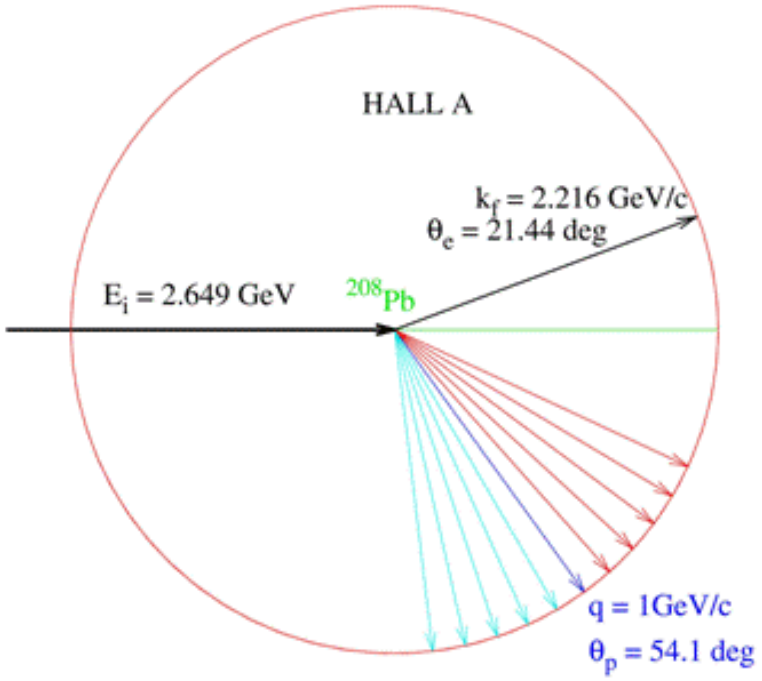

Figure 8.1 Diagram of the kinematical settings for the experiment E06-007.

Kinematics	q [GeV/c]	Eo [GeV]	ω [GeV]	Ee [GeV]	θe [degrees]	Pp [GeV]	θp [degrees]	pm [GeV/c]
Kin01	1.000	2.649	0.433	2.216	21.44	0.989	54.101	0.000
Kin02	1.000	2.649	0.433	2.216	21.44	0.989	59.830	0.100
Kin03	1.000	2.649	0.433	2.216	21.44	0.989	48.371	0.100
Kin04	1.000	2.649	0.433	2.216	21.44	0.989	65.625	0.200
Kin05	1.000	2.649	0.433	2.216	21.44	0.989	42.576	0.200
Kin06	1.000	2.649	0.433	2.216	21.44	0.989	71.440	0.300
Kin07	1.000	2.649	0.433	2.216	21.44	0.989	36.762	0.300
Kin08	1.000	2.649	0.433	2.216	21.44	0.989	77.299	0.400
Kin09	1.000	2.649	0.433	2.216	21.44	0.989	30.902	0.400
Kin10	1.000	2.649	0.433	2.216	21.44	0.988	83.222	0.500
Kin11	1.000	2.649	0.433	2.216	21.44	0.988	24.980	0.500
Kin12	1.400	2.649	0.745	1.904	30.60	1.388	43.816	0.000
Kin13	1.750	2.649	1.045	1.604	39.81	1.738	35.936	0.000

Table 8.2: Overview of the kinematical settings.

8.2. ^{12}C(e,e'p) Results

8.2.1. Experimental Results

The final ^{12}C(e,e'p) cross sections are presented in Table 4.1. Quoted uncertainties are statistical.

p_{miss} (MeV/c)	^{12}C(e,e'p) Reduced Cross Section σ_{red} (GeV^{-3}) for all $1p_{3/2}$ states		
	E06007 Data	Relativistic RDWIA simulation	Non-Relativistic RDWIA simulation
-312.5	0.36 (22)	0.2392 (60)	0.2541 (60)
-287.5	1.01 (25)	0.691 (12)	0.722 (13)
-262.5	2.04 (49)	1.674 (45)	1.733 (46)
-237.5	6.5 (17)	5.96 (28)	5.96 (28)
-212.5	7.94 (73)	10.55 (22)	10.57 (22)
-187.5	13.71 (81)	17.77 (32)	17.82 (32)
-162.5	26.0 (19)	24.94 (82)	25.02 (82)
-137.5	33.7 (20)	40.6 (13)	40.3 (13)
-112.5	43.0 (17)	46.7 (11)	46.5 (11)
-87.5	45.4 (17)	48.8 (11)	48.6 (11)
-62.5	41.2 (27)	37.3 (15)	37.1 (15)
-37.5	23.3 (28)	20.4 (12)	20.2 (12)
12.5	12.4 (18)	11.62 (67)	11.42 (66)
37.5	22.5 (12)	21.93 (55)	21.57 (54)
62.5	35.6 (14)	34.91 (82)	34.34 (81)
87.5	48.2 (21)	48.2 (18)	47.3 (17)
112.5	48.3 (11)	50.8 (12)	49.3 (12)
137.5	39.62 (53)	43.96 (81)	42.27 (78)
162.5	28.09 (64)	35.16 (98)	33.47 (93)
187.5	24.90 (87)	22.02 (79)	20.48 (73)
212.5	16.29 (37)	13.88 (25)	12.63 (22)
237.5	9.92 (34)	8.21 (18)	7.26 (16)
262.5	5.50 (62)	4.44 (25)	3.78 (21)
287.5	0.82 (22)	1.552 (44)	1.201 (34)
312.5	0.42 (11)	0.693 (13)	0.4886 (90)
337.5	0.31 (10)	0.2604 (60)	0.1570 (40)

Table 8.3: Measured ^{12}C(e,e'p) reduced cross section in the experiment E06-007.

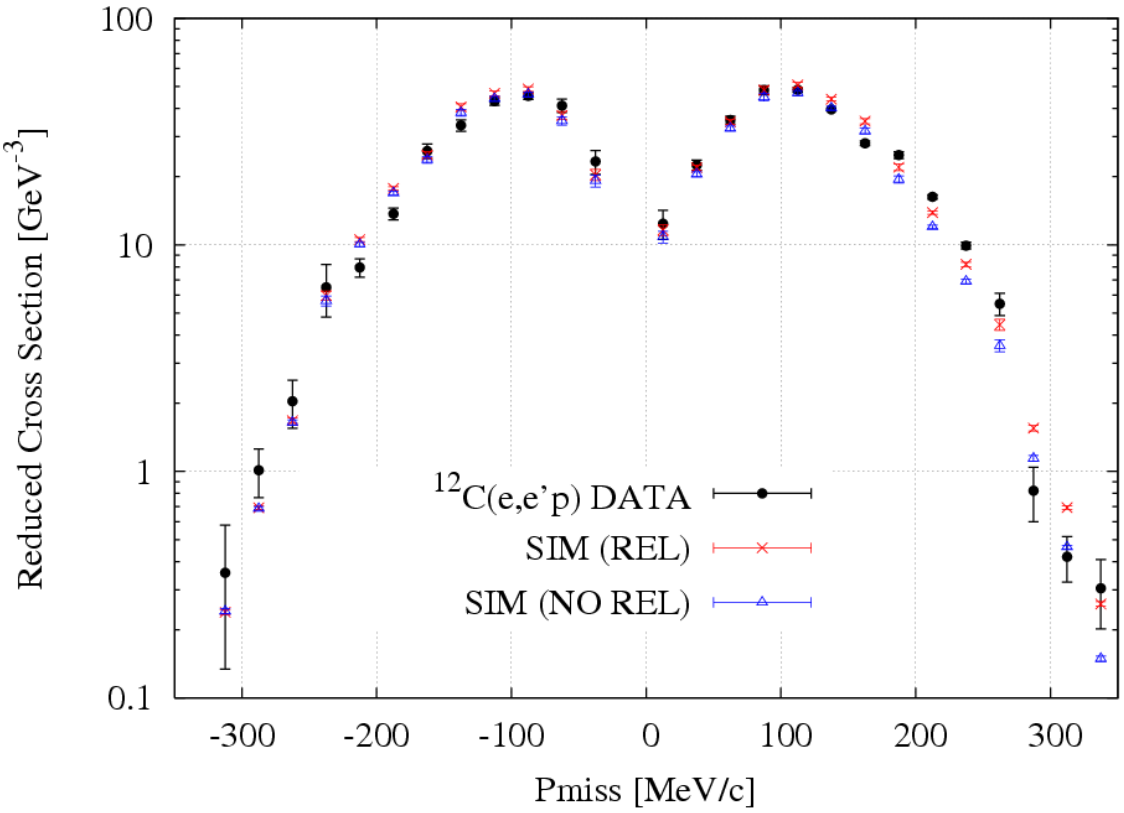

Figure 8.2: ^{12}C(e,e'p) experimental reduced cross section. The results from simulations based on the two different theoretical approaches described in this thesis are also shown.

The asymmetry A_{TL} obtained from the experiment E06-007 as a function of p_{miss} for the extraction of one proton from the $1p_{3/2}$ state of ^{12}C is summarized in Table 8.4.

p_{miss} (MeV/c)	A_{TL} ($1p_{3/2}$)		
	E06-007 DATA	Simulation DWIA Relativistic	Simulation DWIA Non-Relativistic
37.5	0.236 (95)	0.213 (34)	0.217 (33)
62.5	0.238 (46)	0.209 (21)	0.215 (21)
87.5	0.040 (26)	0.073 (15)	0.080 (15)
112.5	-0.189 (31)	-0.161 (28)	-0.154 (27)
137.5	-0.357 (26)	-0.304 (25)	-0.294 (25)
162.5	-0.395 (26)	-0.451 (24)	-0.434 (23)
187.5	-0.578 (25)	-0.568 (35)	-0.549 (34)
212.5	-0.725 (40)	-0.622 (49)	-0.599 (48)
237.5	-0.726 (50)	-0.703 (29)	-0.678 (28)
262.5	-0.831 (48)	-0.830 (37)	-0.803 (36)
287.5	-0.88 (14)	-0.890 (10)	-0.872 (99)
312.5	-0.76 (31)	-0.899 (51)	-0.865 (50)
362.5	-0.70 (90)	-0.813 (39)	-0.766 (38)

Table 8.4: A_{TL} for the $1p_{3/2}$ state of ^{12}C.

The experimental A_{TL} together with the results from simulations are shown in Figure 8.3. It can be seen that a large statistical uncertainty exists for p_{miss} >300 MeV/c. This is due to the fact that only a few runs were acquired at those kinematics, as ^{12}C was used in the experiment E06-007 mainly just for calibration purposes and as a reference for the data acquired with heavy nuclei.

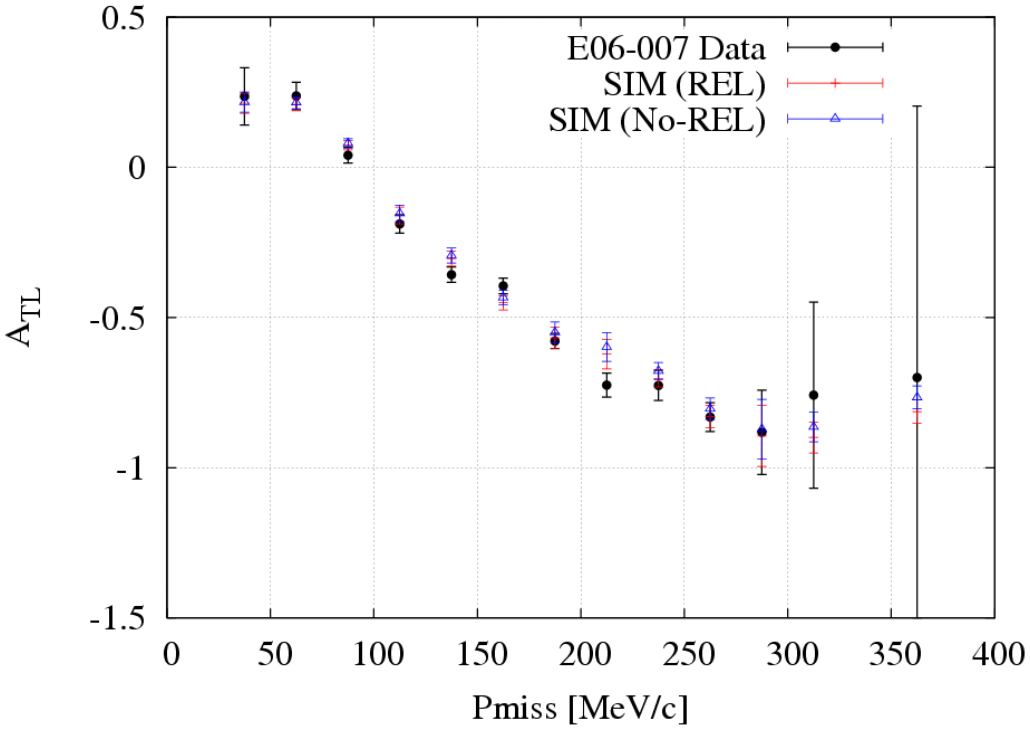

Figure 8.3: Experimental A_{TL} from experiment E06-007 together with the result from the simulations.

Recall that for *j=l+1/2* shells, the expected effect of relativistic dynamics is rather small. This explains that the results of simulations for both non-relativistic and fully relativistic spinors are practically identical and in very good agreement with the experiment.

8.2.2. Comparison with Theory and Previous Experiments

The data from this experiment have been compared with MCEEP simulations based on response functions obtained with the different theoretical models. The spectroscopic factors obtained from the comparison of the measured data with the simulations are summarized in Table 8.5. Note that these factors include all the three states in which the strength appears fragmented (see Figure 5.15) in the E_{miss} region between 15 and 25 MeV. The spectroscopic factor is in good agreement with former JLAB determinations as presented in Table 8.6.

SHELL	Spectroscopic factor (Experiment E06-007)	
	RELAT.	Non-RELAT.
$1p_{3/2}$	0.85 (5)	0.81(5)

Table 8.5: Spectroscopic factors for the valence states in ^{12}C from the experiment E06-007.

	Spectroscopic factor ^{12}C $1p_{3/2}$ shell		
EXPER.	Q^2 $(GeV/c)^2$	E_{miss}	Spectroscopic factor EDAIC
Saclay [Mou76]	0.16	15–22	0.572
Saclay [Mou76]	0.18	15–22	0.684
JLAB [Dut03]	0.6	15–25	0.909
SLAC [Mak94]	1.1	15–25	0.887
JLAB [Dut03]	1.2	15–25	0.950
JLAB [Dut03]	1.8	15–25	0.886
JLAB E06-007 (RELAT. DWIA)	0.82	15–25	0.85(5)

Table 8.6: Spectroscopic factors from previous experiments as derived from the analysis in [Kel05] compared to the values obtained in this work.

8.2.3. Summary and Conclusions

Cross sections and A_{TL} for the $^{12}C(e,e'p)$ reaction have been measured in the quasielastic region with Q^2 = 0.82 $(GeV/c)^2$ in perpendicular kinematics as a by-product of the diamond foils present in the lead and bismuth targets. This serves as also a cross check of both the experiment apparatus and the analysis procedure. Reduced cross sections, A_{TL} and spectroscopic factors are in good agreement with theoretical estimates and with former experimental results from JLAB and SLAC. The spectroscopic factors are larger than the ones derived in former experiments at MAINZ [Blo95], but these later data are known to suffer from normalization problems [Kel05].

8.3. ^{208}Pb(e,e'p) Results

8.3.1. Experimental Results

p_{miss} (MeV/c)	^{208}Pb(e,e'p) Reduced Cross Section σ_{red} (GeV^{-3}) Valence States E_{miss}=[6.75,10.75] MeV)		
	E06-007 Data	Relativistic RDWIA simulation	Non-Relativistic RDWIA simulation
	Value	Value	Value
-310	0.17(45)	0.831(22)	0.797(19)
-290	1.20(37)	1.41(25)	1.32(22)
-270	1.13(50)	2.716(68)	2.52(63)
-230	17.3(21)	19.84(50)	18.98(48)
-210	30.9(13)	36.99(46)	36.24(46)
-190	33.6(11)	45.9(49)	45.83(49)
-170	28.1(15)	41.71(75)	42.19(75)
-150	22.8(69)	33.50(12)	33.0(12)
-130	26.1(37)	31.38(46)	30.97(46)
-110	43.3(38)	48.03(60)	47.96(60)
-90	57.7(44)	68.2(10)	68.6(10)
-70	64.8(71)	66.3(17)	66.5(17)
-50	60.4(59)	67.2(16)	66.9(16)
-30	76.7(73)	94.6(33)	93.9(33)
-10	115(15)	133.7(99)	134.7(99)
10	128(12)	129.4(73)	130.3(73)
30	92.1(46)	100.4(23)	100.9(23)
50	67.9(35)	70.0(12)	69.2(12)
70	55.4(36)	61.8(11)	61.0(11)
90	58.9(39)	65.3(16)	63.2(15)
110	44.1(19)	51.48(71)	48.73(68)
130	29.9(91)	35.36(34)	32.81(32)
150	30.6(12)	33.25(59)	30.19(54)
170	39.3(31)	44.00(18)	38.90(16)
190	42.4(13)	49.92(80)	42.16(69)
210	42.88(99)	44.94(54)	36.52(44)
230	34.3(11)	31.84(48)	24.52(38)
250	22.2(16)	17.16(52)	12.23(38)
270	1.41(40)	1.660(16)	1.034(91)
290	0.84(10)	0.940(26)	0.708(18)
310	0.47(63)	0.640(13)	0.572(12)
330	0.254(68)	0.510(17)	0.468(17)
350	0.12(11)	0.363(27)	0.319(25)

Table 8.7: ^{208}Pb(e,e'p) reduced cross section for the aggregate of the valence states $3s_{1/2}$, $2d_{3/2}$ $1h_{11/2}$ and $2d_{5/2}$ (E_{miss}=[6.75,10.75] MeV).

The measured ^{208}Pb(e,e'p) cross sections in perpendicular kinematics for the aggregate of the valence states ($3s_{1/2}$, $2d_{3/2}$ $1h_{11/2}$ and $2d_{5/2}$) are listed in Table 8.7.

These measurements are compared to results from simulations that fully include effects of radiation and acceptance folding, and employ two models with different ingredients, as described in previous chapters.

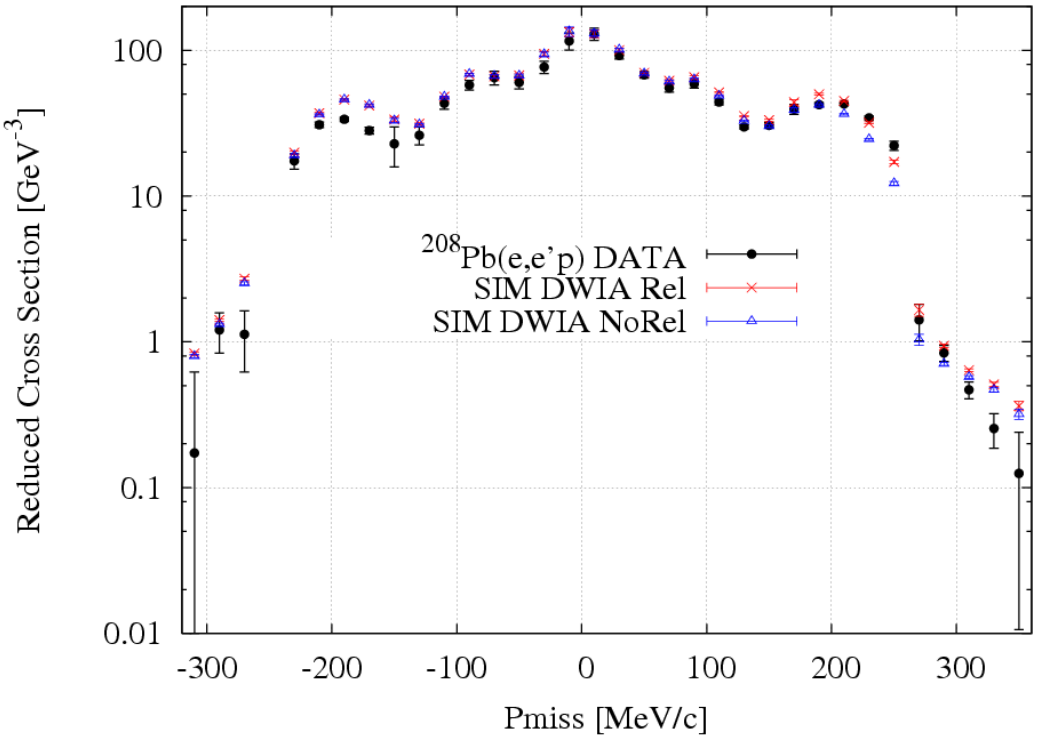

Figure 8.4: ^{208}Pb(e,e'p) reduced cross section for the aggregate of the valence states $3s_{1/2}$, $2d_{3/2}$ $1h_{11/2}$ and $2d_{5/2}$.

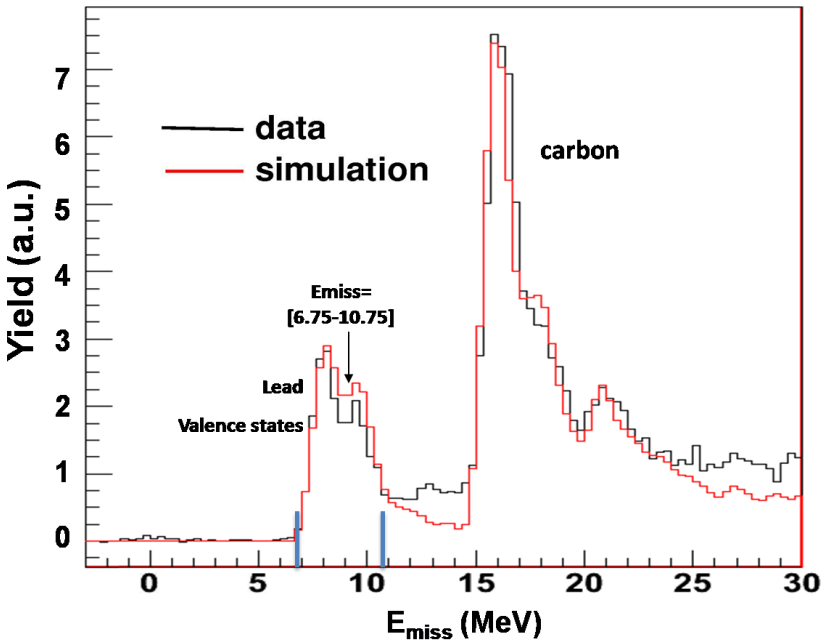

Figure 8.5: E_{miss} spectrum obtained with the diamond-lead-diamond target. The blue bars indicates the E_{miss} region used to obtain the cross section. It correspond to Kin1 ($|p_{miss}|$< 100 MeV/c).

Figure 8.5 shows the E_{miss} spectrum obtained at low p_{miss} ($|p_{miss}|$<100MeV/c). Two peaks in the valence-states region of lead, corresponding to the $3s_{1/2}$ + $2d_{3/2}$ and the

$1h_{11/2}$ + $2d_{5/2}$ shells can be seen. This was expected, as the energy resolution of this experiment does not allow to separate each individual level in E_{miss}, similarly of what happened in Saclay experiment [Med99]. Note that in this experiment it was not possible to distinguish the $1g_{7/2}$ peak (placed at E_{miss} = 11.5 MeV).

Table 8.8 lists A_{TL} as a function of p_{miss} for the aggregate of the valence states $3s_{1/2}$, $2d_{3/2}$ $1h_{11/2}$ and $2d_{5/2}$ of ^{208}Pb in the range 6.75 < E_{miss} < 10.75 MeV, together with the results from the simulations. These data are also displayed in Figure 8.6. Data seem to slightly favor the fully relativistic results, specially around 200 MeV/c where the $1h_{11/2}$ shell, more sensitive to relativistic dynamical effects, is dominant.

p_{miss} (MeV/c)	A_{TL}(Valence States)(E_m=[6.75,10.75] MeV)		
	E06-007 DATA	Simulation DWIA Relativistic	Simulation DWIA Non-Relativistic
30	-0.286(90)	-0.190(44)	-0.196(44)
50	-0.292(60)	-0.276(23)	-0.281(23)
70	-0.098(62)	-0.105(17)	-0.097(17)
90	-0.058(52)	-0.053(13)	-0.041(12)
110	-0.278(67)	-0.282(21)	-0.268(21)
130	-0.416(71)	-0.420(16)	-0.403(15)
150	-0.38(13)	-0.306(18)	-0.279(18)
170	-0.274(40)	-0.139(15)	-0.086(14)
190	-0.363(72)	-0.279(34)	-0.224(31)
210	-0.454(37)	-0.455(18)	-0.394(17)
230	-0.703(45)	-0.688(19)	-0.642(18)
270	-0.95(14)	-0.879(55)	-0.845(54)
290	-0.48(33)	-0.480(11)	-0.317(80)

Table 8.8: A_{TL} for the aggregate of the valence states of ^{208}Pb.

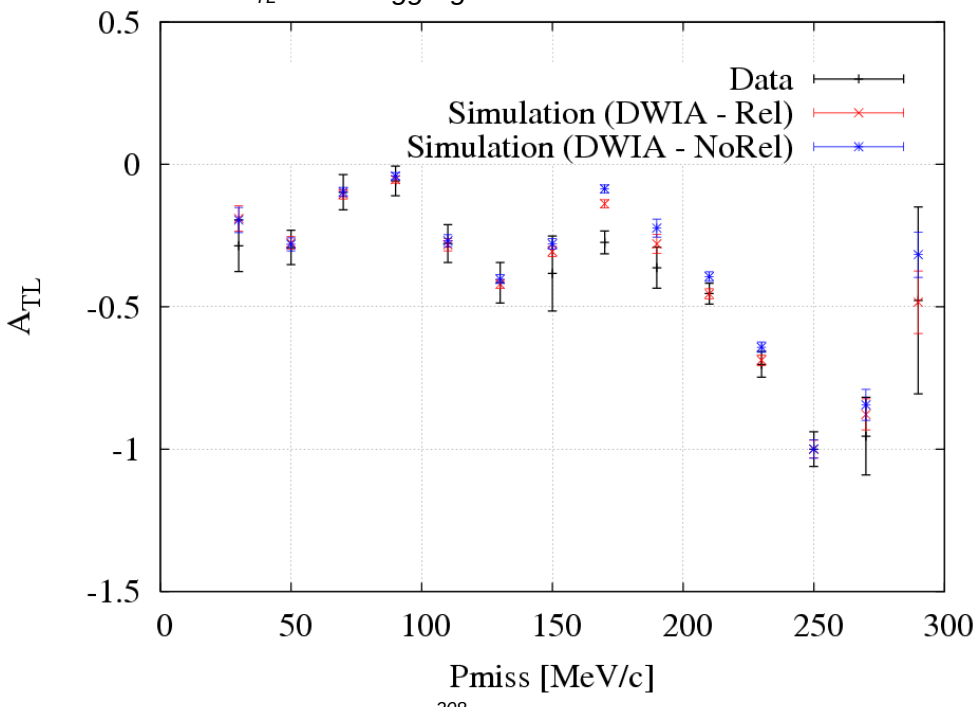

Figure 8.6: Experimental A_{TL} from ^{208}Pb(e,e'p) (black) and RDWIA simulations.

8.3.2. Comparison with Theory and Previous Experiments

Data from this experiment have been compared with MCEEP simulations based on response functions obtained with DWIA calculations with relativistic spinors and non-relativistic ones. A description of these models was given previously. Although each individual shell could not be separated in the E_{miss} spectrum, the spectroscopic factors were obtained by a fitting procedure based on 2-dimensional data E_{miss}, p_{miss}. The resulting factors are shown in Figure 8.7.

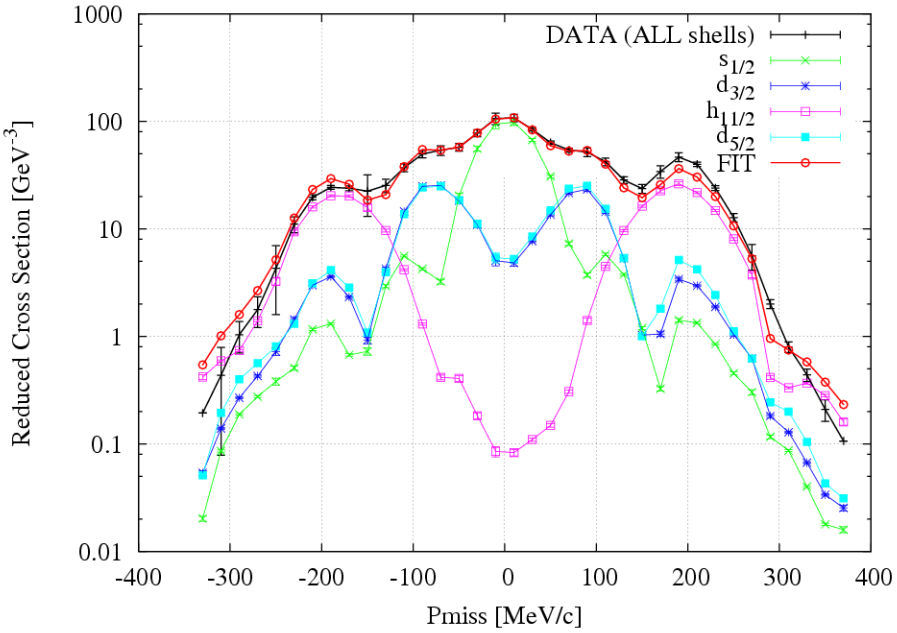

Figure 8.7: Experimental ^{208}Pb(e,e'p) reduced cross section (for the aggregate of valence states) together with the results from relativistic DWIA for the contributions from individual shells.

		JLAB E06-007	NIKHEF-K [Qui88] data, [Udi93] RDWIA	NIKHEF-K [Bat01]	SACLAY [Med99]
Q^2 (GeV/c)^2		0.82	0.1-0.4	0.26-0.49	0.70
Kinematics		Perpendic.	Parallel	Parallel	Perpendic.
Spect. Factor	$3s_{1/2}$	0.52 ± 0.06	0.70(5)	0.65 ± 0.04	0.58 ± 0.05
	$2d_{3/2}$	0.59 ± 0.06	0.73(6)	0.57 ± 0.03	0.55 ± 0.03
	$1h_{11/2}$	0.65 ± 0.06	0.60(4)	0.72 ± 0.05	0.75 ± 0.03
	$2d_{5/2}$	0.52 ± 0.06	0.63(4)	0.78 ± 0.05	0.54 ± 0.02

Table 8.9: Spectroscopic factors for the valence states in ^{208}Pb from the experiment E06-007 compared to the values obtained in previous experiments.

8.3.3. Summary and Conclusions

Cross sections and A_{TL} for the ^{208}Pb(e,e'p) reaction have been measured in the quasielastic region with Q^2 = 0.82 (GeV/c)^2 in perpendicular kinematics. Data for asymmetry favor slightly the fully relativistic calculation. With regard to the cross

section, the fitted spectroscopic factors are slightly smaller (approximately one standard deviation) than those derived from the analysis of data taken at NIKHEF-K in parallel kinematics with the same theoretical model employed here [Udi93]. They are, however, in good agreement with previous data taken at Saclay in perpendicular kinematics and with the most recent data from NIKHEF. Overall, the results of this experiment confirm the fact that spectroscopic factors for valence shells are on the order of 60% of the independent particle limit.

8.4. Spectroscopic factors as a function of Q^2

One of the goals of experiment E06-007 was to obtain spectroscopic factors at several Q^2 values. Figure 8.8 shows the spectroscopic factors obtained comparing the measured reduced cross section with the values obtained using the prescription for the DWIA simulation developed in this thesis [For83], for both ^{12}C and ^{208}Pb.

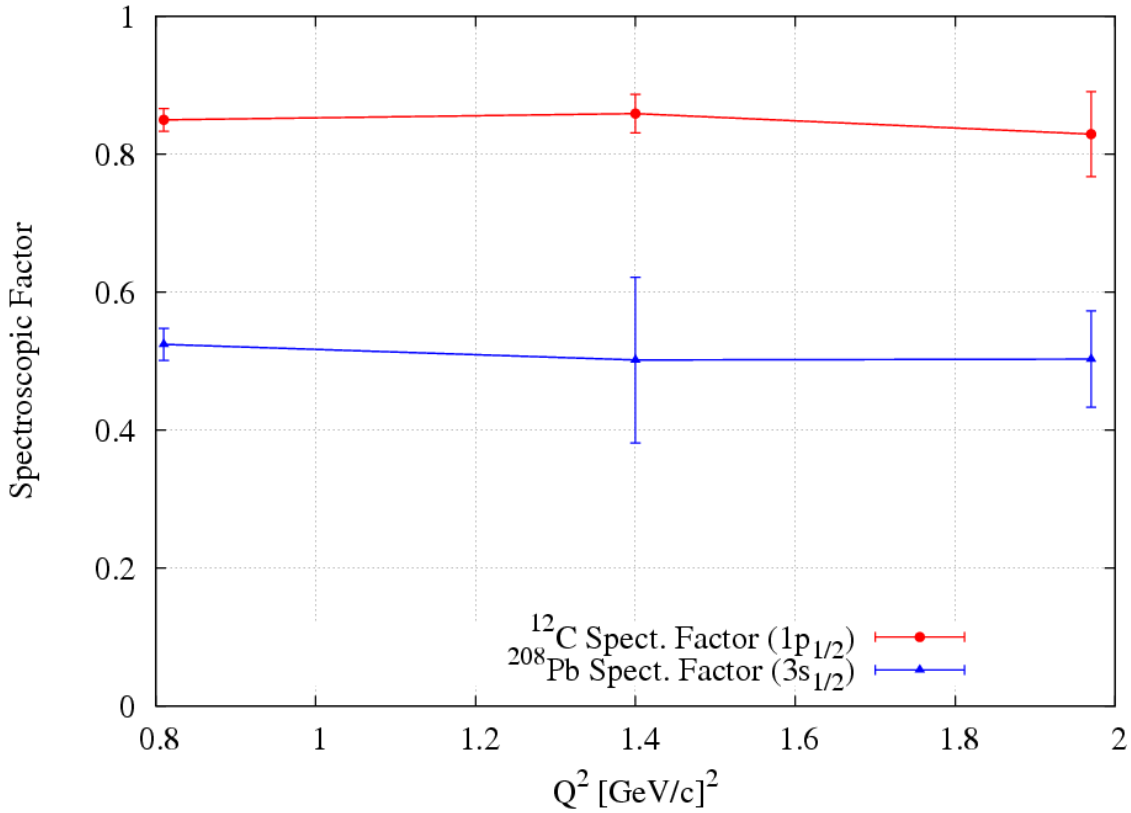

Figure 8.8: Spectroscopic factors for the $p_{3/2}$ shell of ^{12}C and the $3s_{1/2}$ state of ^{208}Pb for three different values of the four-momentum transfer Q^2.

These values were obtained by rescaling the theory to the data only in the region of low p_{miss} (between -100 MeV/c and +100 MeV/c), making identical cuts in the acceptances of the data and the simulations, so that at all values of Q^2 sampled

similar range in E_{miss} and p_{miss}. The quality of the fit to the shape of the momentum distribution for both the data and the simulations over the entire p_{miss} range shown in the figures in the previous sections makes us confident that measurements over a larger p_{miss} region would not yield a different conclusion. The spectroscopic factors needed to fit simulations to the data were constant, both in lead an carbon, to a much higher level than constrained by the statistical uncertainties. This experiment confirms the constancy of the spectroscopic factors in the range of Q^2 in between approximately 0.8 to 2 $(GeV/c)^2$ to the level of 5%.

9. Summary and Conclusions

Experimental coincidence cross section and the transverse-longitudinal asymmetry A_{TL} have been obtained for the quasielastic (e,e'p) reaction in ^{16}O, ^{12}C, and ^{208}Pb in constant *q*-*ω* kinematics. In these experiments, performed in experimental Hall A of the Thomas Jefferson National Accelerator Facility (JLAB), the beam energy and the momentum and angle of the scattered electrons were kept fixed, while the angle between the proton momentum and the momentum transfer q was varied in order to map out the p_{miss} distribution.

The first of these experiments [E00-102], performed in the fall of 2001 using a waterfall (H_20) target, measured the $^{16}O(e,e'p)$ reaction in quasielastic kinematics at Q^2=0.90 $(GeV/c)^2$ over one of the largest ranges of missing momentum ever explored with unprecedented statistical accuracy. In this work, results from proton knock-out from the $p_{1/2}$ shell of ^{16}O in the p_{miss} range [-350,350] MeV/c are shown. The experimental data obtained in this thesis are in agreement with a previous JLAB experiment (E89-003), performed at slightly lower Q^2. The measured cross sections and asymmetry A_{TL} have been compared with both Distorted Wave Impulse Approximation (DWIA) calculations with relativistic and non-relativistic spinors. Spectroscopic factors of 0.71 $\pm$ 0.05 ($p_{1/2}$ shell) were obtained for both models. A_{TL} measurements favor the relativistic DWIA calculation. There are essentially no free parameters in the theoretical calculations. The excellent agreement with the data is interpreted as a great success for the fully relativistic Impulse Approximation. Further, these data constitute compelling experimental evidence for the need to modify the structure of spinors that describe nucleons bound in nuclei to account for relativistic dynamical effects.

The second experiment [E06-007] was performed in the spring of 2007 (first run) and January 2008 (second run) using three-foil C+Pb+C and C+Bi+C targets. The goal was to study the nuclear structure of ^{208}Pb and ^{209}Bi. Additional measurements on a single carbon target foil were performed allowing for the study of the nuclear structure of ^{12}C. In this thesis, results from the knockout of protons from the $p_{3/2}$ shell of ^{12}C and the valence states of ^{208}Pb in the p_{miss} range [-350,350] MeV/c are shown.

Carbon results are in good agreement with results from previous experiments performed at JLAB [Dut03, Mon08]. The experimental cross sections and A_{TL} asymmetry have been compared with Monte Carlo simulations based on DWIA calculations with both

relativistic and non-relativistic spinor structure. The spectroscopic factor obtained for the $p_{3/2}$ shells in ^{12}C is 0.85(5) for the relativistic DWIA and 0.81(5) for the non-relativistic DWIA. The A_{TL} measurements for the $p_{3/2}$ shell in ^{12}C are in agreement with both relativistic and non-relativistic simulations. This was expected and may be interpreted as a further successful prediction of the relativistic model, as dynamical relativistic effects are less evident in the $p_{3/2}$ shell than in the $p_{1/2}$ shell [Cab95, Cab95b].

^{208}Pb(e,e'p) data were obtained at different and more complete kinematics than in previous NIKHEF-K and Saclay experiments [Qui88, Bob94, Bat01, Med99]. The A_{TL} asymmetry in ^{208}Pb was measured for the first time. The spectroscopic factors for the valence states of ^{208}Pb have been obtained from a (E_{miss}, p_{miss}) fitting procedure obtained from relativistic and non-relativistic DWIA calculations. These spectroscopic factors are one standard deviation smaller than those from similar analysis [Udi93] of NIKHEF-K data [Qui88], but in agreement with other measurements performed at Saclay [Med99] and NIKHEF-K [Bat01]. A_{TL} measurements for the aggregate of the valence states favor in the fully relativistic DWIA predictions.

Further (e,e'p) data were measured at three different Q^2 values, looking for a possible dependence of the spectroscopic factors on Q^2. The results of this analysis for both ^{12}C and ^{208}Pb have found no signs of such a dependence for $0.8 < Q^2 < 2$ $(GeV/c)^2$ to the level of 5% statistical accuracy and with reduced systematic uncertainties. This is the first time that this has been confirmed in a heavy nucleus.

To summarize, these experiments have measured the (e,e'p) reaction at the quasielastic peak (x_B =1) for several complex nuclei with good statistics and a large range of missing momentum. Spectroscopic factors of 0.6 to 0.85 have been obtained in the shells analyzed in all nuclei. Experimental cross sections in general show good agreement with RDWIA calculations. A_{TL} data, which are sensitive to dynamical relativistic effects, clearly favors the results that include relativistic dynamics. This is a clear experimental signature of the important role played by relativistic dynamics inside nuclei.

10. Resumen en Español

10.1. Introducción

La física nuclear busca respuestas a ese gran problema que constituye la estructura de la materia; de qué están hechas las cosas. El núcleo atómico proporciona un laboratorio único para estudiar las interacciones fundamentales de la naturaleza fuerte, débil y electromagnética.

Junto a todas estas motivaciones, se encuentran además las que provienen de todas aquellas ramas de la física y la ingeniería que hacen uso de los resultados sobre las propiedades del núcleo y los nucleones obtenidos por teóricos y experimentales. Dentro de este campo, se puede destacar su interés para la obtención de energía (fusión y fisión nuclear), astrofísica (modelos estelares), aplicaciones militares, industriales, médicas (radioterapia, imagen médica), o la física de partículas.

Pero, ¿por qué estudiar el núcleo mediante dispersión de electrones? La principal respuesta es que dentro de los distintos métodos existentes para el estudio de las propiedades del núcleo, y la estructura nuclear, la dispersión de electrones por núcleos se ha mostrado como uno de los más eficaces que existe hasta la actualidad.

En general, el estudio de un determinado objeto, mediante el análisis de cómo se dispersan las partículas que inciden sobre él, es uno de los métodos más populares de la física. Esto no ha de extrañarnos si tenemos en cuenta que nuestra principal fuente de información sobre el mundo exterior, la vista, está basada precisamente en este mismo principio. Observamos los objetos cuando nuestro ojo (detector) detecta el ángulo, la intensidad y el color (energía) de la luz proveniente de una fuente tras ser dispersada por un objeto. Nuestro cerebro extrae de esos datos la forma del objeto, su textura o color. Del mismo modo sucede en los experimentos de dispersión de electrones, en los que se un detector situado en un cierto ángulo respecto a la fuente de electrones, detecta la dispersión de éstos tras impactar en un determinado objeto (núcleos) en estudio. A partir de la energía, intensidad y ángulos de las partículas detectadas se pueden deducir propiedades nucleares.

Una de las principales ventajas de usar un haz de electrones como sonda para el estudio de la estructura nuclear, frente a otro tipo de partículas como por ejemplo protones, consiste en que la interacción electrón-núcleo es principalmente electromagnética, por lo que el proceso se puede estudiar haciendo uso de la Electrodinámica Cuántica (QED). Esto presenta grandes ventajas, dado que QED es la teoría física en la que los modelos teóricos presentan un mayor acuerdo con los resultados experimentales. Se evita así tener que recurrir a modelos fenomenológicos que se emplean en muchos análisis de procesos con interacción fuerte. Otra importante ventaja es que la dispersión de electrones no altera de manera significativa la estructura del núcleo en estudio, a diferencia de lo que puede suceder con otros experimentos de dispersión de hadrones.

No obstante, el uso de otro tipo de sondas y experimentos para determinar distintas propiedades nucleares y nucleónicas, como la dispersión de protones o de núcleos ligeros, colisión de iones pesados entre sí, también son interesantes, dado que ofrecen una información complementaria sobre la interacción fuerte que la dispersión de electrones no puede lograr. Por ejemplo, en nuestro modelo del proceso A(e,e'p)B, incluimos la interacción de estados finales (FSI) entre el protón extraído y el núcleo residual obtenida mediante experimentos de dispersión de protones por núcleos.

En este tipo de estudios, se puede realizar la aproximación del proceso a primer orden en teoría de perturbaciones (intercambio de un único fotón virtual) debido al pequeño valor de la constante de acoplo de la interacción electromagnética. Esto permite en general una adecuada descripción del proceso y simplifica considerablemente los cálculos pudiéndose trabajar con expresiones analíticas. Hay que hacer notar que, en determinados casos, se ha indicado la necesidad de acudir al segundo orden en este desarrollo para mejorar el acuerdo con otros resultados.

Por otro lado, la ventaja que presenta este proceso frente al uso de fotones reales como proyectiles consiste en que, en nuestro caso, el momento cinético q y la energía ω transferidos al núcleo pueden variar independientemente, sólo bajo la condición $\omega^2 - q^2 \leq 0$. Esto no sucede en el caso de los fotones reales $(\omega^2 - q^2 = 0)$. Por tanto, usando los electrones como sonda, existe la posibilidad de obtener mucha más información de la estructura nuclear.

Para finalizar, cabría resaltar uno de los principales inconvenientes del uso de los electrones frente a las sondas hadrónicas para realizar estudios de dispersión en núcleos: la sección eficaz del proceso es mucho menor en el caso de los electrones, por los que la tasa de recuento para este tipo de experimentos suele ser baja.

Figura 10.1- Fotografías del túnel del acelerador de electrones del JLAB (Newport News, USA).Se aprecian los cinco distintos recorridos que realiza el haz de electrones en función de su energía.

Dependiendo de la energía a la que se realicen los experimentos, el tipo de información que se puede obtener sobre el núcleo es muy distinta. Se pueden distinguir en general varios regímenes para la sección eficaz en función de la energía transferida por los electrones al núcleo para un valor dado del momento **q** transferido. Los experimentos de esta tesis se realizaron en el pico de la región cuasielástica. En esta región el proceso más probable es aquél en el que un nucleón es extraído del núcleo. La energía transferida por el fotón virtual es absorbida por un único nucleón, adquiriendo éste la energía suficiente para alcanzar un estado del continuo. El máximo de la sección eficaz en esta región corresponde a la situación $\omega \approx Q^2 / 2M_N$, siendo M_N la masa del nucleón y $Q^2=q^2-\omega^2$.

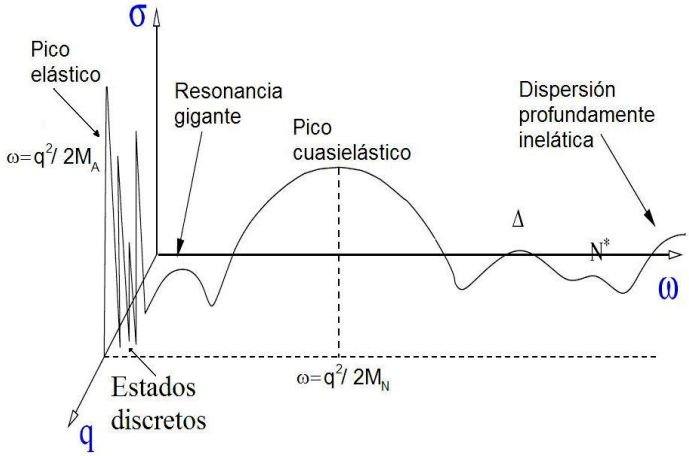

Figura 10.2: Sección eficaz de dispersión de electrones por núcleos en función de la energía y el momento transferido en el proceso.

La gran anchura de esta región es debida al hecho de que los nucleones no se encuentran en reposo dentro del núcleo; además están fuera de la capa de masas (off-shell). Esta región proporciona información sobre propiedades monoparticulares, como la distribución de momentos y energías de los nucleones dentro del núcleo.

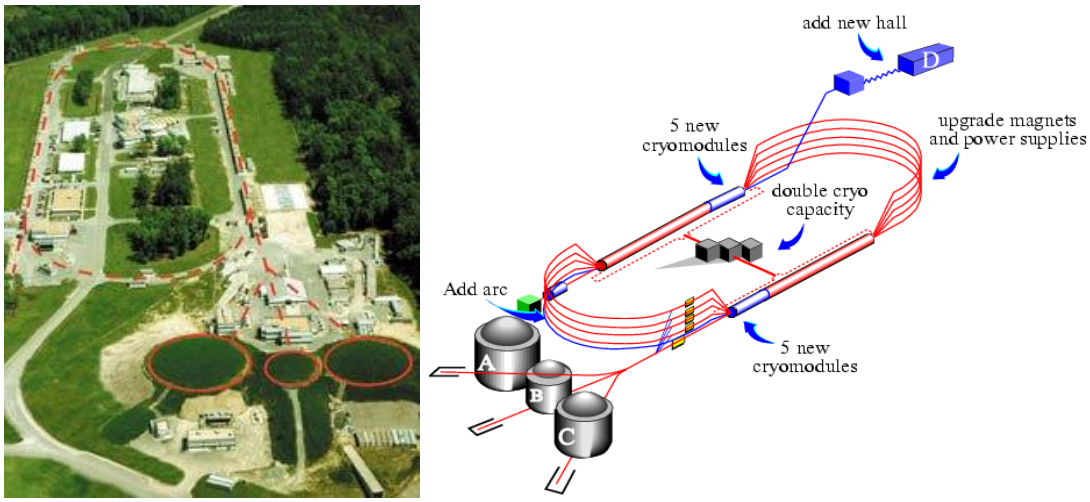

Figura 10.3: Izda: Fotografía aérea del JLAB, sobre la que se ha marcado la trayectoria del acelerador y las tres zonas de experimentos de dispersión Hall A,B y C. Dcha: Esquema de la propuesta de la futura ampliación del JLAB que podrá alcanzar así los 12 GeV e incluirá un nuevo Hall experimental.

En esta tesis se estudian dos experimentos del tipo A(e,e'p)B realizados en el pico cuasielástico. Se trata de experimentos exclusivos en los que se detecta tanto el electrón dispersado como el nucleón extraído. En este caso, se tiene un conocimiento completo de las variables del problema, como la energía del protón y su ángulo de emisión. Este tipo de estudios tienen un ritmo de conteo bajo, pero proporcionan mucha información de la estructura nuclear. La sección eficaz en este caso se obtiene a partir del número *N* de coincidencias electrón-protón medidas, dividido por las aceptancias angulares $\Delta\Omega_e\Delta\Omega_p$ y aceptancias en el momento de las partículas $\Delta\omega\Delta E_p$ que poseen los detectores, así como de la luminosidad *L* (definida como el producto del número de electrones incidentes por el número de núcleos por unidad de área presentes en el blanco)

$$\frac{d^6\sigma}{d\omega d\Omega_e d\Omega_P dE_P} = \frac{N}{L\cdot\Delta\omega\Delta\Omega_e\Delta E_p\Delta\Omega_p} \qquad (10.1)$$

En el caso de estudiar el número de protones extraídos de una determinada capa nuclear caracterizada por una cierta energía E_{miss} en un cierto rango Em_1 y Em_2, la sección eficaz diferencial dada por la ecuación (10.1) se convierte en

$$\left.\frac{d^5\sigma}{d\omega d\Omega_e d\Omega_P}\right|_{Emiss} = \int_{Em_1}^{Em_2} \frac{d^6\sigma}{d\omega d\Omega_e d\Omega_P dE_p} \cdot R \cdot dE_{miss} \qquad (10.2)$$

donde *R* representa un factor de retroceso (Jacobiano) que vale prácticamente uno en estos experimentos.

Dado que esta sección eficaz depende de manera muy importante de la energía de los electrones incidentes, con el fin de poder comparar con otros experimentos, se busca eliminar estas dependencias del resultado con la cinemática del experimento mediante el uso de secciones eficaces reducidas.

$$\sigma_{RED}\left(p_{miss}\right)\Big|_{Emiss} = \frac{1}{\left[R \cdot E_p \cdot p_p \cdot \sigma_{ep.cc1}\right]} \cdot \frac{d^5\sigma}{d\Omega_e d\Omega_p d\omega} \qquad (10.3)$$

El factor σ_{ep} representa la sección eficaz electrón-protón para protones en núcleos según la prescripción de De Forest [For83], siendo p_p y E_p el momento y la energía respectivamente del protón detectado.

Haciendo una serie de importantes aproximaciones, esta sección eficaz reducida se puede interpretar como la probabilidad de encontrar un protón con un momento p_{miss} en una determinada capa dada por una energía de ligadura E_{miss} Por tanto, a partir de estas secciones eficaces reducidas se pueden deducir propiedades monoparticulares nucleares.

En la bibliografía se pueden encontrar abundantes referencias básicas que describen este proceso (por ejemplo, [Kel96, Wal06]).

Un observable experimental muy útil a la hora de estudiar la existencia de efectos dinámicos relativistas que se deducen de la solución de la ecuación de Dirac para el proceso (e,e'p) en campo medio, es la asimetría transversal-longitudinal A_{TL}, que se deduce a partir de medidas de la sección eficaz a ambos lados de momento del fotón *q*.

10.2. Objetivos

Esta tesis presenta la descripción, análisis y resultados de dos experimentos de dispersión cuasielástica (e,e'p) de electrones en núcleos complejos realizados en el Hall A del acelerador de electrones Thomas Jefferson National Accelerator Facility (JLAB) en Virginia, EE.UU.

En estos experimentos se midió la sección eficaz del proceso cuasielástico (e,e'p) en núcleos de ^{16}O (Experimento E00-102) y ^{12}C, ^{208}Pb y ^{209}Bi (Experimento E06-007) en cinemática perpendicular.

El primero de estos experimentos [E00-102] tuvo lugar en otoño de 2001, usando

como blanco tres láminas de agua para estudiar la estructura nuclear del ^{16}O. El principal objetivo de este experimento fue el estudio de los límites del modelo nuclear de partícula independiente mediante la reacción ^{16}O(e,e'p) en el régimen cuasielástico.

El segundo de estos experimentos [E06-007] se realizó durante la primavera del 2007 (primera parte) y en enero de 2008 (segunda parte). Se usaron en este caso blancos compuestos por tres láminas de diamante-plomo-diamante y diamante-bismuto-diamante para estudiar la estructura nuclear del ^{208}Pb y el ^{206}Bi. Así mismo también se tomaron medidas en ^{12}C con un blanco de grafito, que permitió estudiar la estructura nuclear del ^{12}C.

En esta tesis se analizan los datos medidos en ^{16}O, ^{12}C y ^{208}Pb hasta un momento desaparecido (p_{miss}) de 300MeV/c. Los resultados obtenidos se comparan con simulaciones Monte Carlo basadas en distintos descripciones teóricas de la reacción (e,e'p). En concreto se analiza el factor espectroscópico necesario para ajustar los cálculos teóricos a los datos experimentales (que es del orden de 0.6 a 0.8), así como hasta qué punto la inclusión de efectos dinámicos relativistas mejora el acuerdo con los datos experimentales. En este sentido, la asimetría transversal-longitudinal A_{TL} es un buen observable que permite diferenciar entre modelos que incluyan o no estos efectos relativistas.

También se analizan datos medidos en ^{12}C y ^{208}Pb a distintos valores del cuadrumomento transferido Q^2, con el fin de estudiar una posible dependencia de los factores espectroscópicos obtenidos al comparar los datos con la teoría en ondas distorsionadas.

10.3. Estructura de la Tesis

Esta tesis está organizada de la siguiente forma. El primer tema realiza una introducción a las reacción (e,e'p) y se muestran algunos de los principales resultados obtenidos en experimentos previos en estos núcleos de ^{16}O, ^{12}C y ^{208}Pb. También se muestra una descripción general de la motivación y características de los experimentos de esta tesis. En los capítulos 2 y 3 se dan los detalles de los modelos teóricos y simulaciones empleados para comparar con los resultados experimentales obtenidos.

El cuarto capítulo ofrece una descripción detallada del montaje experimental empleado en ambos experimentos En los capítulos 5 y 6 se muestran los detalles de los pasos seguidos en el análisis de los datos, desde la calibración de los detectores, o la

corrección de eficiencias hasta cómo se han obtenido las secciones eficaces. Finalmente los últimos capítulos ofrecen los resultados de cada experimento comparándolos con simulaciones basadas en los distintos modelos teóricos. Los comentarios y conclusiones finales de este conjunto de resultados se muestra en el capítulo final.

10.4. Principales Resultados

10.4.1. Cálculos teóricos y Simulación

El programa de simulación Monte Carlo para experimentos del tipo (e,e'p) MCEEP se mejoró incorporándole funciones de respuesta nucleares para los núcleos de ^{16}O, ^{12}C y ^{208}Pb calculadas mediante un código no factorizado RDWIA. Este código ya había mostrado un buen acuerdo con anteriores experimentos [Fis04]. De esta forma se consiguió desarrollar un código de simulación que combinase los efectos experimentales (como las aceptancias de los detectores o las incertidumbres en el haz incidente) con cálculos teóricos complejos. Con el fin de comprobar la corrección del programa, se simuló inicialmente el experimento E89-003 [Gao00] (e,e'p) en ^{16}O.

La figura 10.4 muestra los resultados de la simulación de MCEEP (con puntos rojos) junto con el cálculo teórico directo (línea negra) del código RDWIA, y los resultados del experimento E89-003 [Gao00]. Además de observarse un buen acuerdo entre los datos y la simulación, se aprecia que el resultado obtenido haciendo el promedio de las aceptancias experimentales (panel superior), no es el mismo que el que se obtiene con aceptancias muy reducidas, que representa el caso ideal (panel inferior).

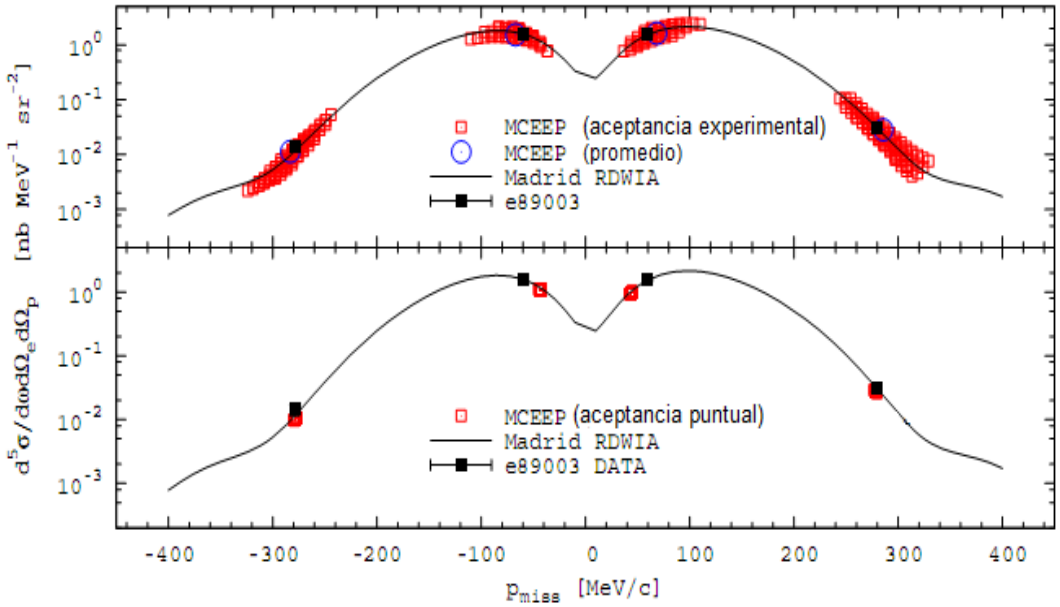

Figura 10.4:- Sección Eficaz Diferencial ^{16}O(e,e'p) de la capa $1p_{1/2}$ del experimento (E89-003)- Datos, teoría y simulaciones.

10.4.2. Análisis de Datos

Debido a las características de los experimentos de esta tesis el análisis de datos presenta algunos importantes retos:

1) La sección eficaz relativamente baja del proceso (e,e'p), especialmente a alto p_{miss}, hizo que la toma de datos se llevara a cabo durante varios meses. Esto supone que en muchos casos no bastase con realizar una única calibración de los detectores, sino que fuese necesario hacer un seguimiento de las propiedades de éstos a lo largo de los días. Esto tambien sucede con el cálculo de las eficiencias y tiempos muertos del sistema de adquisición. Además, hubo que tener un especial cuidado para no eliminar aquellos datos adquiridos en períodos en los que el haz de electrones no fue estable.

2) El conjunto de datos recogidos fue del orden de varios Terabytes. El análisis de todos estos datos ha supuesto un importante coste computacional, llevado a cabo tanto en el clúster de computación del JLAB como en el de la Facultad de Ciencias Físicas.

Se aplicó con éxito un código de optimización genético desarrollado por Udías et al. [Fer08] para la optimizar la óptica de los espectrómetros buscando alcanzar la mejor resolución posible en energía que permitiese separar estados individuales en los espectros nucleares adquiridos. La figura 10.5 muestra un espectro de energía tras haber optimizado la óptica de ambos espectrómetros. La resolución (FWHM~1MeV) obtenida está próxima a la mejor esperable en este montaje experimental.

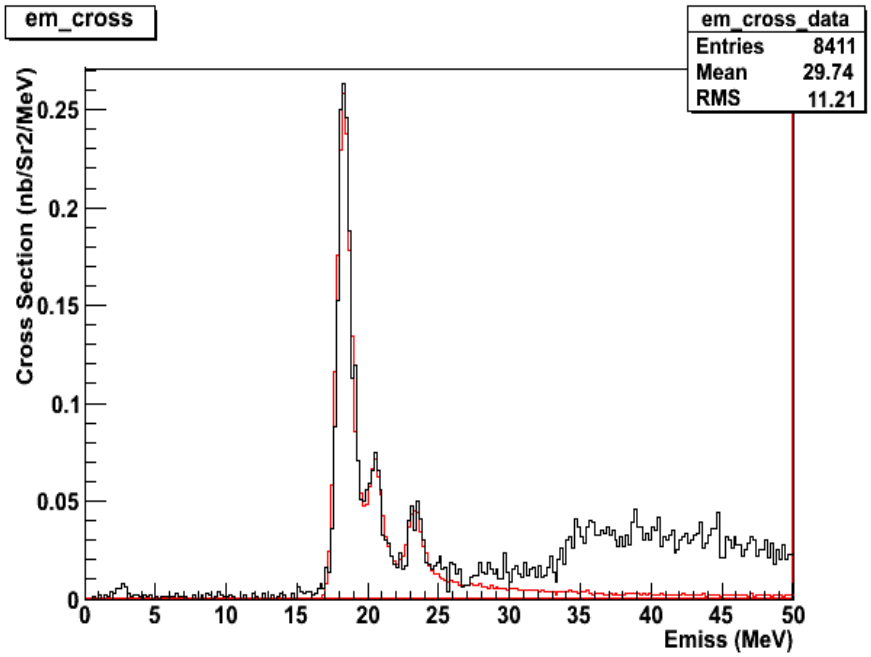

Figura 10.5: Espectro en energía del proceso $^{12}C(e,e'p)$ obtenido tras la calibración de los espectrómetros. Corresponde a un rango en p_{miss}= [-100,100] MeV/c En rojo se muestra el resultado de la simulación, en buen acuerdo con los datos (en negro).

10.4.3. Experimento E00-102: ^{16}O(e,e'p)

La figura 10.6 muestra la sección eficaz reducida obtenida de los datos de este experimento, junto a los resultados de dos simulaciones basadas en distintos cálculos teóricos. En rojo se muestra la simulación basada en funciones de respuesta completamente relativistas y en azul las obtenidas a partir de funciones de respuesta no relativistas (proyectadas). Una explicación detallada de ambos cálculos se puede encontrar en [Udi01].

La buena estadística de los datos de este experimento se refleja en la pequeña barra de error experimental. Ambas simulaciones ofrecen en general un buen acuerdo con los datos, aunque existen diferencias que se aprecian mejor en la asimetría A_{TL} (*Figura 10.7*).

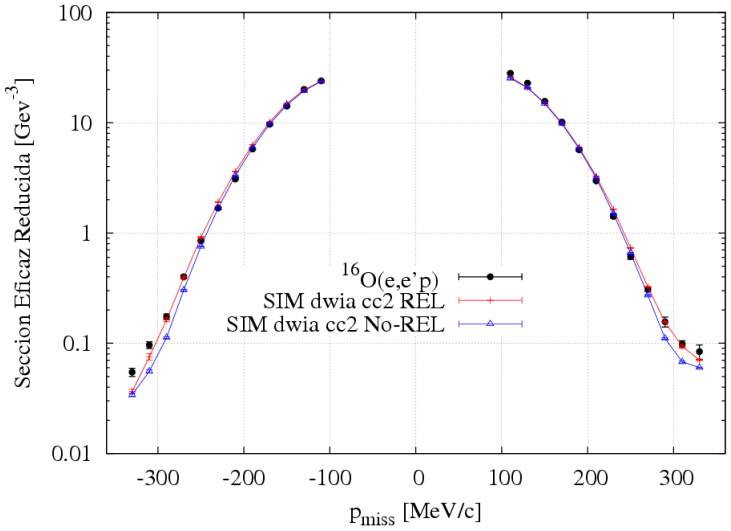

Figura 10.6 Sección eficaz reducida experimental de la capa $p_{1/2}$ del ^{16}O(e,e'p).

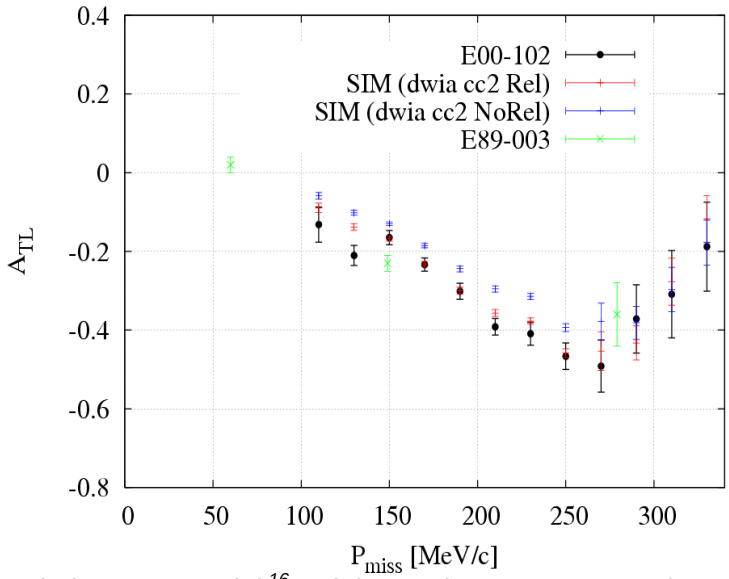

Figura 10.7: A_{TL} de la capa $p_{1/2}$ del ^{16}O del experimento E00-102, junto con los resultados de las dos simulaciones y el resultado obtenido en el experimento previo E89-003.

10.4.4. Experimento *E06-007: ^{12}C(e,e'p)*

La figura 10.8. muestra la sección eficaz reducida obtenida de los datos de este experimento, junto a los resultados de dos simulaciones basadas en distintos cálculos teóricos. En rojo se muestra la simulación basada en funciones de respuesta completamente relativistas y en azul las obtenidas a partir de funciones de respuesta no relativistas (proyectadas).

Debido a que este núcleo no era el objetivo principal del experimento E06.007, sino que estas medidas se tomaron como referencia, los datos presentan una alta barra de error a alto momento. El acuerdo entre ambas simulaciones, en este caso, es bueno, y no se aprecia una diferencia significativa entre ellos, estando en acuerdo con los datos, tanto en la sección eficaz reducida como en la asimetría A_{TL}.

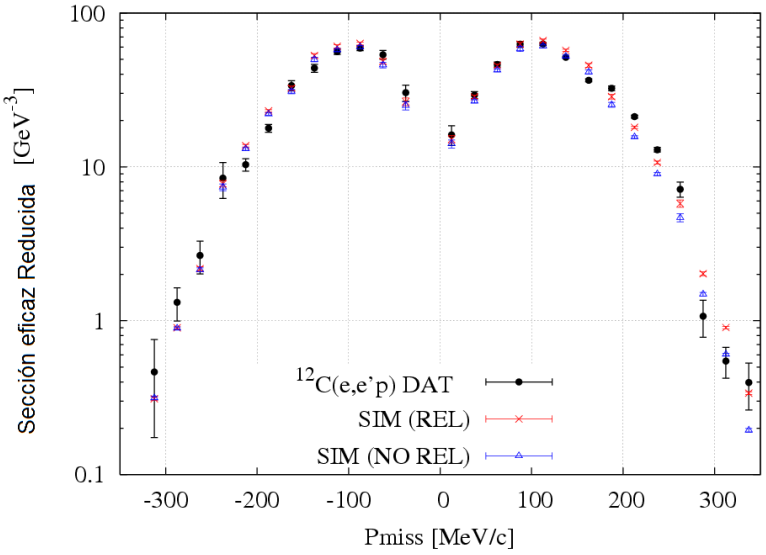

Figura 10.8: Sección eficaz reducida de la capa $p_{3/2}$ del ^{12}C(e,e'p)

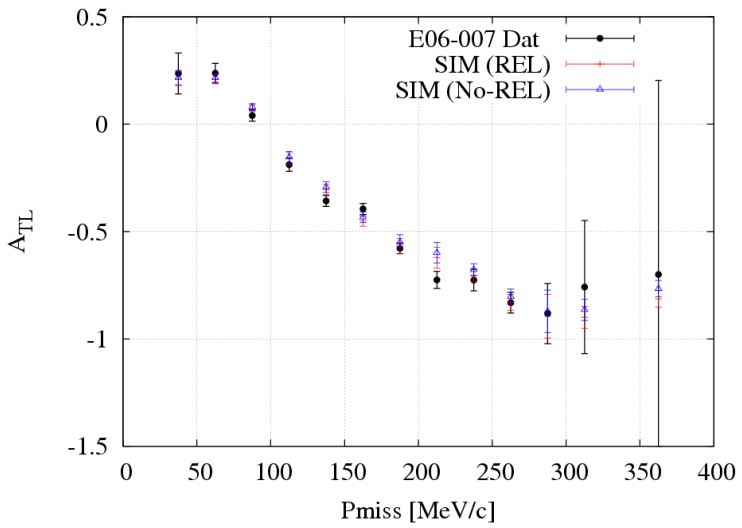

Figura 10.9: A_{TL} de la capa $p_{3/2}$ del ^{12}C del experimento E06-007, junto con los resultados de las dos simulaciones.

10.4.5. Experimento E06-007: ^{208}Pb(e,e'p)

La sección eficaz reducida ^{208}Pb(e,e'p) para los estados de valencia se muestra en la Figura 10., junto a los resultados de dos simulaciones basadas en distintos cálculos teóricos. En rojo se muestra la simulación basada en funciones de respuesta completamente relativistas y en azul las obtenidas a partir de funciones de respuesta no relativistas (proyectadas).

El acuerdo entre los datos y la simulación es bueno, apreciándose algunas diferencias significativas en la región de -300MeV/c. La A_{TL} (Figura 10.11) también muestra un excelente acuerdo con la simulación, mostrando sólo una cierta diferencia con el cálculo no relativista en la región de pmiss=200MeV/c en la que domina la capa $1h_{11/2}$, más sensible a efectos dinámicos relativistas.

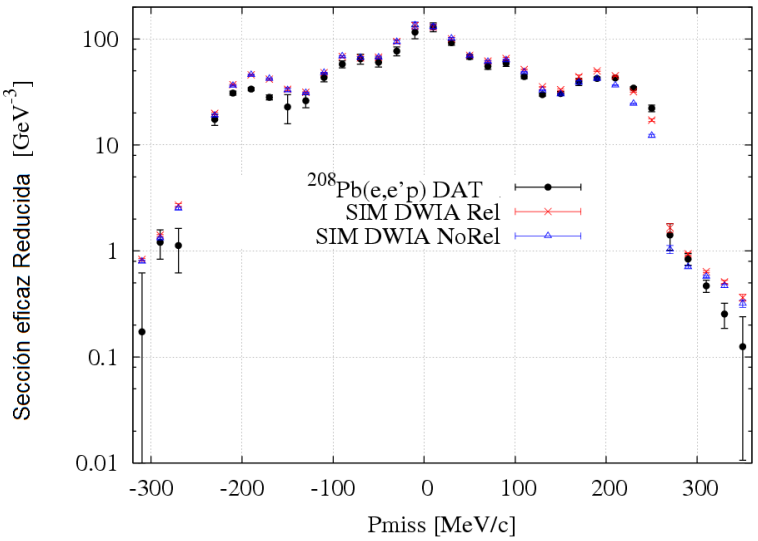

Figura 10.10: Sección eficaz reducida para los estados de valencia del ^{208}Pb(e,e'p)

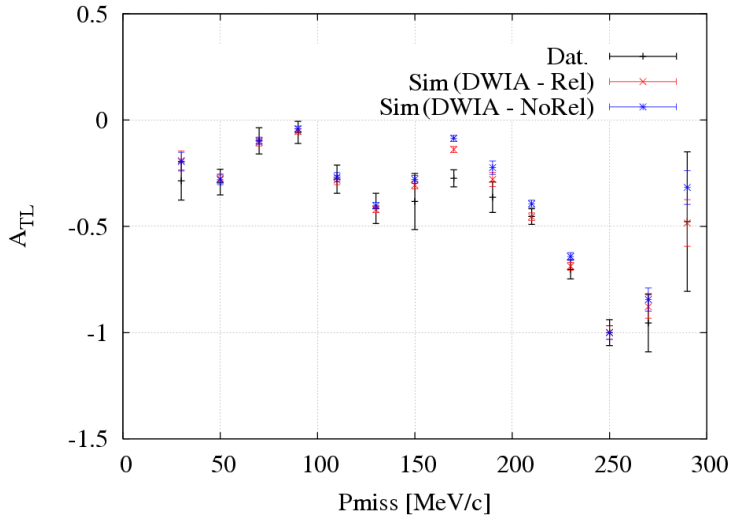

Figura 10.11: A_{TL} de los estados de valencia del ^{208}Pb(e,e'p) (en negro) y resultados de las simulaciones basadas en cálculos relativistas (rojo) y no-relativista (azul).

10.4.6. Experimento E06-007: Factores Espectroscópicos en función de Q^2

Uno de los objetivos del experimento E06-007 fue la obtención de los factores espectroscópicos (necesarios para que los cálculos teóricos reproduzcan los resultados experimentales) para distintos valores de Q^2.

La figura 10.12 muestra los factores espectroscópicos obtenidos en ^{12}C y ^{208}Pb. Es necesario indicar que estos valores se han obtenido con medidas sólo en la región de p_{miss} entre -100MeV/c y +100MeV/c. Sin embargo, dado el buen ajuste entre los datos y el modelo a lo largo de la distribución de momentos que se observa en las figuras 10.8 y 10.10 no se espera que medidas en todo el rango de p_{miss} fueran ofrecer un resultado distinto.

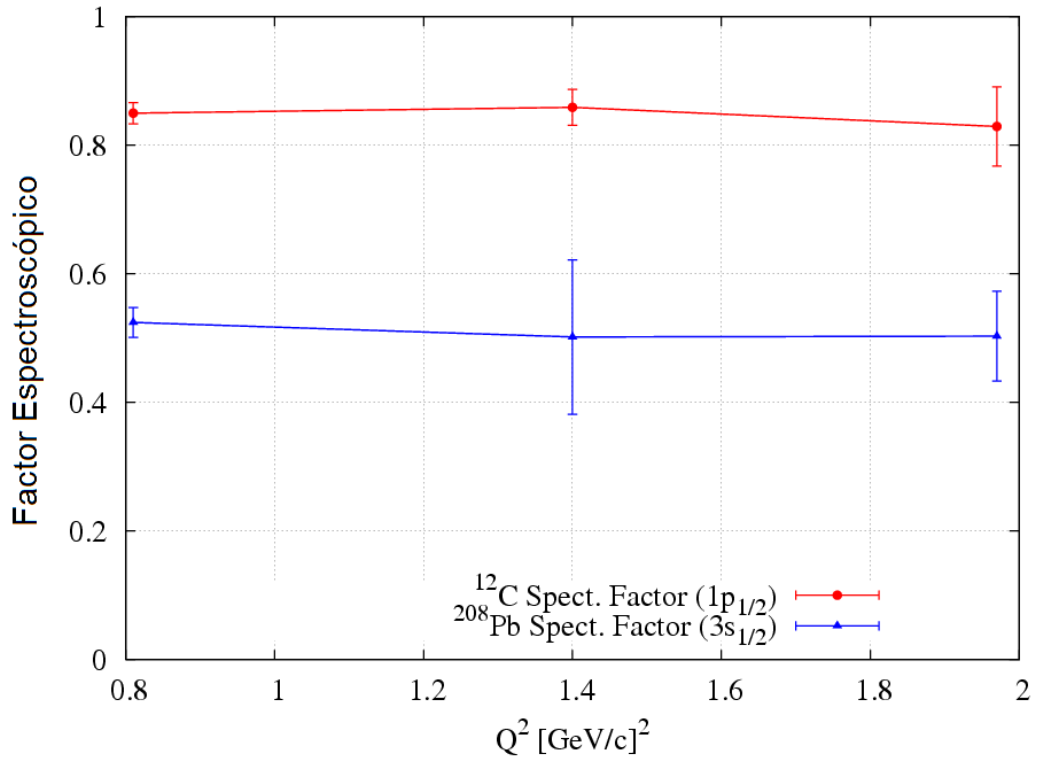

Figura 10.12: Factor espectroscópico de la capa $p_{3/2}$ del ^{12}C y de la capa $3s_{1/2}$ del ^{208}Pb para distintos valores del cuadrumomento transferido Q^2

10.5. Resumen y Conclusiones

Se ha medido la sección eficaz y la asimetría transversal-longitudinal (A_{TL}) de la reacción cuasielástica (e,e'p) en ^{16}O, ^{12}C y ^{208}Pb en cinemática con q-ω constante. En estos experimentos, realizados en el Hall A experimental del Thomas Jefferson National Accelerator Facility (JLAB, EEUU), la energía del haz y el momento y ángulo de los electrones se mantuvo fija, mientras que el ángulo entre el momento del protón y el momento transferido q se varió para medir toda la distribución del momento desaparecido.

El primero de estos experimentos [E00-102], realizado en el otoño de 2001 usando un blanco de agua, midió la reacción ^{16}O(e,e'p) en cinemática cuasielástica con una precisión estadística sin precedentes y con uno de los mayores rangos en momento desaparecido. En esta tesis se muestran los resultados de la extracción de un protón de la capa p del ^{16}O en un rango de momento desaparecido [-350,350] MeV/c. Los datos experimentales obtenidos en esta tesis están en acuerdo con los obtenidos en el experimento previo E89-003 realizado también en el Hall A del JLAB. La sección eficaz medida y la asimetría A_{TL} se han comparado con cálculos DWIA relativistas y no relativistas, y en ambos casos se obtienen factores espectroscópicos de 0.71 $\pm$ 0.05 (capa p_{12}). Sin embargo, las medidas de A_{TL} no apoyan los cálculos no relativistas, favoreciendo en cambio los relativistas.

El segundo de estos experimentos [E06-007] fue realizado en la primavera de 2007 (primera parte) y en enero de 2008 (segunda parte) usando un blanco compuesto, formado por 3 láminas finas de C+Pb+C y C+Bi+C, para el estudio de la estructura nuclear de ^{208}Pb y ^{209}Bi. Adicionalmente, se tomaron medidas en una lámina de grafito, permitiendo también el estudio de la estructura nuclear del ^{12}C. En esta tesis se estudia la extracción de protones de la capa $p_{3/2}$ del ^{12}C y de los estados de valencia del ^{208}Pb en el rango de momentos [-350,350] MeV/c.

Los resultados en ^{12}C concuerdan con los obtenidos en experimentos previos realizados en el JLAB [Dut03, Mon08]. Las secciones eficaces experimentales y la asimetría A_{TL} logrados se han comparado con simulaciones Monte Carlo basadas en cálculos DWIA relativistas y no-relativistas. Los factores espectroscópicos obtenidos para la capa $p_{3/2}$ en ^{12}C has sido de 0.85 $\pm$ 0.05 para el análisis DWIA relativista y 0.81 $\pm$ 0.05 para el no relativista. La asimetría A_{TL} medida en la capa $p_{3/2}$ en ^{12}C están en acuerdo

con ambas simulaciones. Este comportamiento era esperado, dado que los efectos dinámicos relativistas son mucho menos evidentes en la capa $p_{3/2}$ que en la $p_{1/2}$ [Cab95, Cab95b].

Se han obtenido datos del proceso ^{208}Pb(e,e'p) en cinemáticas distintas y más completas que en experimentos anteriores llevados a cabo en NIKHEF-K y Saclay [Qui88, Bob94, Bat01, Med99]. Ha sido la primera vez que se ha medido la asimetría A_{TL} en plomo. Los factores espectroscópicos para los estados de valencia del ^{208}Pb se han obtenido mediante un método de ajuste en (E_{miss},p_{miss}) de los datos con las simulaciones basadas en cálculos DWIA relativista y no-relativista. Estos factores son ligeramente menores que los obtenidos en un análisis similar [Udi93] del experimento de NIKHEF-K [Qui88] (una desviación estándar distintos) pero kkk Las medidas de A_{TL} para el conjunto de los estados de valencia parecen favorecer al modelo DWIA relativista frente al no-relativista.

La reacción (e,e'p) ha sido medida para 3 valores distintos de Q^2, con el fin de buscar una posible dependencia de los factores espectroscópicos con Q^2. Los resultados de esta tesis tanto en ^{12}C como en ^{208}Pb, no han encontrado signos de esta dependencia de los factores espectroscópicos en el rango de Q^2 entre 0.8 y 2 $(GeV/c)^2$ hasta un 5% de precisión. Esta es la primera vez que se confirma en un núcleo pesado.

En resumen, estos experimentos han medido la reacción (e,e'p) en el pico cuasielástico (x_B =1) en núcleos complejos con buena estadística y resolución. Se han obtenido factores espectroscópicos entre 0.6 y 0.85 en todas las capas analizadas de los núcleos de ^{16}O, ^{12}C y ^{208}Pb, sin que exista una dependencia de estos valores con Q^2. Las secciones eficaces experimentales muestran en general un buen acuerdo con los cálculos DWIA. Los datos para el observable A_{TL}, que tiene una importante dependencia con los efectos dinámicos relativistas, favorecen los cálculos DWIA relativistas, es decir, que incluyen la contribución de las componentes de energía negativa.

11. LIST OF FIGURES

12. LIST OF TABLES

13. Bibliography

1)[AEEXB] AEEXB Monte Carlo simulation code - From OOPS sofware at MIT-Bates - http://filburt.mit.edu/oops/Html/SW/SW.html

2)[Alc04] Alcorn J., et al. (2004). Basic Instrumentation for Hall a at Jefferson Lab. Nuclear Instruments and Methods in Physics Research Section A: Accelerators, Spectrometers, Detectors and Associated Equipment, 522, 294.

3)[Alv03] Álvarez-Rodríguez R. (2003) Dispersión de electrones en ^{3}He- Diploma de Estudios Avanzados (Unpublished).

4)[Afa08] Afanasev A. (2008). Radiative corrections for Lepton scattering. Presentation for PPD/Neutrino Department, 22 Feb 2008. Hampton University.

5)[Ama96] Amaro J. E., Caballero J. A., Donnelly T. W. and de Guerra E. M. (1996) Inclusive quasielastic scattering of polarized electrons from polarized nuclei, Nuclear Physics A, Vol. 611, Issues 2-3, Pages 163-210.

6)[Ama10] Amaro J. E., Barbaro M. B., Caballero, J. A., Donnelly T. W., Maieron, C. and Udias J. M. (2010) - Meson-exchange currents and final-state interactions in quasielastic electron scattering at high momentum transfers - Physical Review C, 81 (1), 014606.

7)[Ami97] - Amiraziminili K., Udias J.M., Muther H., Skouras L.D. and Polls A. (2007). Correlations and the cross section of exclusive (e,e'p) reactions for 16O. Nuclear Physics A, 625, 633-650.

8)[Analyzer] Hall A C++ Analyzer, http://hallaweb.JLAB.org/root/index.html

9)[Ani06] Aniol K., Saha A., Udias J.M. and Urciuoli G. (2006). Approved experiment E06-007. Jefferson National Accelerator Facility PAC29. Proposal: http://hallaweb.JLAB.org/collab/PAC/PAC29/PR-06-007-Pb-QuasiElastic.ps

10)[And05] Andersson M. (2005). E00-102: Testing the limits of the single particle model in ^{16}O(e,e'p) - Master thesis. Lund University.

11)[Arr04] Arrington J. (2004) Implications of the Discrepancy between Proton Form Factor Measurements. Physical Review C, 69, 022201.

12)[Bar90] Barry W., Heefner J. and Perry J. (1990). Electronic systems for beam position monitors at CEBAF, October 1990, Technical Report CEBAF-PR-90-023.

13)[Bat01] Van Batenburg M. (2001). Deeply-bound protons in ^{208}Pb - Ph.D. Thesis. Utrecht University.

14)[Ber82] Bernheim M., et al. (1982). The influence of bound state and optical potentials on 1p momentum distributions obtained from 12c and 16o(e,e'p) reactions. Nuclear Physics A, 375, 381.

15)[Bjo64] Bjorken J. and Drell S. (1964). Relativistic Quantum Mechanics, (McGraw-Hill, New York) - ISBN: 978-0070054943.

16)[Blo95] Blomqvist K.I., et al. (1995). High-momentum components in the 1p orbitals of ^{16}O. Physical Letters B 344-85

17)[Blok85] Blok, et al. (1985). Study of the proton optical potential with the (e,e′p) reaction in Medium Energy Nucleon and Antinucleon Scattering. Springer (Berlin)

18)[Bof92] Boffi S., Giusti C. and Pacati F.D. (1992). Private communication

19)[Bof96] Boffi S., Giusti C., Pacati F.D. and Radici M. (1996) - Electromagnetic Response of Atomic Nuclei - Oxford Studies in Nuclear Physics, 20.

20)[Bor71] Borie E. and Drechsel D. (1971) Radiative Corrections for (e,e'p) coincidence experiments. Physical Review A, 167(2), 369-375.

21)[Bra00] Brandford D., et al. (2000). Electron and photon induced proton knockout from 209Bi. Physical Review C, 63, 014310.

22)[Bob94] Bobeldijk I., et al. (1994). High-momentum protons in 208Pb. Physical Review Letters, 73, 2684.

23)[Bob95] Bobledijk I., et al. (1995) Search for nucleon-nucleon correlation in the proton spectral function of ^{208}Pb - Physics Letters B 353, 32-38.

24)[BooNE] BooNE home page http://www-boone.fnal.gov/

25)[Bro05] Brown A. (2005) Lecture Notes in Nuclear Structure Physics - http://www.nscl.msu.edu/~brown/Jina-workshop/BAB-lecture-notes.pdf

26)[Cab89] Caballero J.A. (1989) Estudio de la influencia de la deformación nuclear en el proceso de la dispersión cuasielástica de electrones por núcleos - Ph.D.Thesis - Universidad Autónoma de Madrid.

27)[Cab98] Caballero J.A., Donnelly T.W., de Guerra E.M. and Udías J.M. (1998) Relativistic current densities for bound spin-orbit partners and the longitudinal-transverse response in (e,e'p) processes. Nuclear Physics A, 643 (2), 189-204.

28)[Cab98b] Caballero J.A., Donnelly T.W., de Guerra E.M. and Udías J.M. (1998) Analysis of factorization in (e,e'p) reactions: a survey of the relativistic plane wave impulse approximation. Nuclear Physics A, 632, 323-362.

29)[Cab01] Caballero J.A., Martínez M.C., de Guerra E.M., Udías J.M., Amaro, J.E., Donnelly, T.W. (2001). Role of relativity in electron scattering: kinematical versus dynamical effects - Nuclear Physics A, 689, (1-2): 449C-452C.

30)[Cab10] Caballero J.A., Martinez M.C., **Herraiz J.L**. and Udias J.M. (2010) Superscaling analysis of the Coulomb Sum Rule in quasielastic electron-nucleus scattering. Physics Letters B (68) pp. 250-257.

31)[Cha03] Chai Z. (2003) - Study of the N to Delta Transition via $p(\vec{e},\vec{e}'\vec{p})\pi^0$ Reaction -Ph.D. Thesis. Massachusetts Institute of Technology.

32)[Chi90] Chinitz L. (1990) Ph.D. Thesis, University of Virginia.

33)[Chi91] Chinitz L., et al. (1991). Separation of the Interference Response Function R_{LT} in the ^{16}O(e,e'p)^{15}N Reaction. Physical Review Letters, 67, 568.

34[Cio05] Ciofi C. and Kaptari L. P. (2005) Calculations of the exclusive processes ^{2}H(e,e'p)n,^{3}He(e,e'p)^{2}H, and ^{3}He(e,e'p)(pn) within a generalized eikonal approximation. Physical Review C 71 (2): 024005.

35)[Cio08] Ciofi C. and Kaptari L. P. (2008) Nonfactorized Calculation of the Process ^{3}He(e,e'p)^{2}H at Medium Energies - Physical Review Letters 100, 122301.

36)[Coo93] Cooper E. D., Hama S. and Clark B. C. (1993). Global Dirac phenomenology for proton-nucleus elastic scattering. Physical Review C 47, 297-311.

37)[Die01] Dieterich S., Udias J.M. and Vignote, J.R. (2001). Polarization transfer in the ^{4}He(e,

e'p)^{3}H reaction. Physics Letters B, (1-2): 47-52.

38)[Don86] Donnelly T.W. and Raskin A.S. (1986). Considerations of Polarization in Inclusive electron Scattering from Nuclei. Annals of Physics 169:247-351

39)[Don88] Donnelly T.W., Aberico W. M., Molinari A., Kronenberg E. L. and Van Orden J. L. (1988) - Scaling In Electron Scattering from a Relativistic Fermi Gas - Phys. Rev. C38, 1801.

40)[Dub76] Dubach J., Koch J.H. and Donnelly T.W. (1976). Exchange currents in electron scattering from light nuclei - Nuclear Physics. A 271, p. 279.

41)[Dut03] Dutta D., et al. (2003). Quasielastic (e,e'p) Reaction on C12 , Fe56 , and Au197. Physical Review C, 68, 064603.

42)[Eid04] Eidelman S., et al. (2004). The Review of Particle Physics. Physics Letters, *B 592*, 1.

43) [ELISe] ELISe collaboration - Technical Proposal for the Design, Construction, Commissioning, and Operation of the ELISe setup - http://www.gsi.de/documents/DOC-2006-Mar-118-1.pdf

44) [ELISeb] ELISe collaboration (116 authors including **Herraiz J.L.**). The Electron-ion Scattering experiment ELISe at the International Facility for Antiproton and Ion Research (FAIR) - Submitted to Nuclear Instruments and Methods.

45)[Ent01] Ent B., et al. (2001). Radiative Corrections for (e,e'p) reactions at GeV Energies. Physical Review C, 64, 054610.

46)[Fer08] Fernández-Ramírez C., Moya de Guerra E., Udías A. and Udías, JM. (2008) Properties of nucleon resonances by means of a genetic algorithm. Physical Review C 77, 065212.

47)[Fis01] Fissum K.G., et al. (2001). Vertical drift chambers for the Hall A high-resolution spectrometers at Jefferson Lab. Nuclear Instruments and Methods in Physics Research Section A, 474, 108.

48)[Fis04] Fissum K.G., Udias J.M., and Vignote J.R. (2004). Dynamics of the quasielastic 16O(e,e'p) reaction at Q^2 approximate to 0.8 $(GeV/c)^2$. Physical Review C 70 (3), 034606

49)[Flo99] Florizone R. (1999)- Ph.D. Thesis - Massachusetts Institute of Technology.

50)[Foe07] Foe K. (2007). Testing the limits of the single particle model in ^{16}O(e,e'p): an update to E89-003. Old Dominion University Annual Progress Report. http://www.JLAB.org/~fissum/e00102/figsetc/odu/progress.ppt

51)[For66] de Forest T., Jr. and Walecka J. D. (1966). Electron scattering and nuclear structure. Advances in Physics, 1460-6976, Volume 15, Issue 57, Pages 1 – 109.

52)[For83] de Forest T., Jr. (1983). Off-shell electron-nucleon cross sections: the impulse approximation. Nuclear Physics A, 392, 232.

53)[Fra01] Frankfurt L., et al. (2001). Single-Particle strength restoration and nuclear transparency in high-Q^2 exclusive (e,e'p) reactions. Physics Letters B, 503, 73.

54)[Fru84] Frullani S. and Mougey J. (1984). Single particle properties of nuclei through (e,e'p) reactions. Adv. Nuclear Physics 14, 1.

55)[Gao99] Gao J. (1999). Study of quasielastic 1p-shell proton knockout in the ^{16}O(e,e'p) reaction at Q^2=0.8 $(GeV/c)^2$ - Ph.D. Thesis. Massachusetts Institute of Technology.

56)[Gao00] Gao J., et al. (2000). Dynamical relativistic effects in quasielastic 1p-shell proton

knockout from 16O. Physical Review Letters, 84, 3265.

57)[Gar92] Garibaldi F. et al., (1992). A waterfall target for electron scattering experiments. Nuclear Instruments and Methods A314 1.

58)[Gard94] Gardner S., Piekarewicz J. (1994). Relativistically generated asymmetry in the missing-momentum distribution from the (*e*,*e*'*p*) reaction. Phys. Rev. C 50, 2822–2833.

59)[Garr93] Garrido E. (1993) Dispersión electrón-núcleo y observables de polarización a energías bajas e intermedias - Ph.D.Thesis - Universidad de Salamanca.

60)[Giu88] Giusti C. and Pacati F. (1988). Nuclear Physics A, 485, 461.

61)[Her05] **Herraiz J. L.** (2005). Efectos coulombianos en la dispersión (e,e'p) - Diploma de Estudios Avanzados. Facultad Ciencias Físicas, Madrid. Universidad Complutense de Madrid.

62)[Her07] **Herraiz J. L.**, et al. (2007) Improved Rdwia Physics Models for Mceep. Jefferson Lab Technical Note – (TN 2007-068).

63)[Her09] **Herraiz J. L.**, Udías, J. M. et al. (2009). Status of the E06-007 experiment: Impulse Approximation limitations to the (e,e'p) reaction on 208Pb, 208Bi and 12C. Hall A Collaboration Meeting; 11th June 2009.

64)[Her09b] **Herraiz J. L.**, Martínez M.C., Caballero J. A. and Udías J.M. (2009) Overview of neutrino–nucleus interactions. Acta Physica Polonica B, 40(9). pages 934-937.

65)[Her09c] **Herraiz J. L.**, Martínez M.C., Caballero J. A. and Udías J.M. (2009) Overview of neutrino-nucleus quasielastic scattering. AIP Conf. Proc. 1189, pages 125-132.

66)[Hof55] Hofstadter R. and McAllister R. W. (1955). Electron Scattering from the Proton. Physical Review, 98, 217.

67)[Hor81] Horowitz C. J., Serot B. D. (1981) - Self-consistent hartree description of finite nuclei in a relativistic quantum field theory, Nuclear Physics A, Volume 368, Issue 3, 5 Pages 503-528.

68)[Hor85] Horowitz C. J. (1985) - Relativistic Love-Franey model: Covariant representation of the NN interaction for N-nucleus scattering - Physical Review C, 31, 1340–1348.

69)[Hor91] Horowitz C. J., Murdock D. P., and Serot B. D. (1991). Computational Nuclear Physics. Edited by K. Langanke, J. A. Maruhn and S. E. Koonin. Springer, Berlin.

70)[Jac62] Jacob G. and Maris T. A. J. (1962). Quasi-free electron-proton scattering. 1-Nuclear Physics, 31:139 & Quasi-free electron-proton scattering 2- Nuclear Physics, 31:152.

71)[Jes99] Jeschonnek S. and Donnelly T. W. (1999) Spin-orbit final-state interaction in the framework of Glauber theory for (*e*,*e*'*p*) reactions. Physical Review C, 59 (5) 2676-2688.

72)[Jin92] Jin Y., Onley D. S. and Wright L. E. (1992). Electron Coulomb effects in quasielastic (*e*,*e*'*p*) reactions. Physical. Review C, 45, 1311.

73)[Jin93] Jin Y., et al. (1993). (e-p) Off-shell cross section in quasielastic (e,e'p) Reactions. Physical Review C, 48, R964.

74)[JLAB] JLAB and Hall A webpages: http://www.JLAB.org, http://hallaweb.JLAB.org

75)[Jon00] Jones M. (2000). Report of electronic deadtime. www.JLAB.org/~jones/e91011/report_on_deadtime.ps

76)[Kel89] Kelly J. J., et al. (1989). Density dependence in the two-nucleon effective interaction at 135 Mev. Physical Review C, 39, 1222.

77)[Kel96] Kelly J. J. (1996). Nucleon knockout by intermediate energy electrons. Adv. Nuclear Physics, 23, 75.

78)[Kel97] Kelly J. J. (1997). Gauge ambiguities in (e,e'n) reactions. Physical Review C, 56, 2672.

79)[Kel05] Kelly J. J. (2005). Relativistic distorted-wave impulse approximation analysis of ^{12}C(e,e'p) for Q^2<2 (GeV/c)^2. Physical Review C, 71, 064610.

80)[KEK] K2K Long-baseline Neutrino Oscillation Experiment Official Homepage http://neutrino.kek.jp

81)[Ken76] Kenzo N. and Norihiko I. (1976). On the final-state interactions in (e, e'p) Reactions. Nuclear Physics A, 259, 301.

82)[Kim96] Kim K.S., Wright L.E., Jin Y. and Kosik D.W. (1996). Approximate treatment of electron Coulomb distortion in quasielastic (e,e') reactions - Physical Review. C 54, 2515.

83)[Kim97] Kim K. S. and Wright L. E. (1997). Approximate coulomb distortion effects in (e,e'p) Reactions. Physical Review C, 56, 302.

84)[Kno74] Knoll J. (1974). An analytic description of inelastic electron scattering on nuclei. Nuclear Physics A223, 462-476.

85)[Lác93] Lác J. (1993). Electron scattering: study of internal target effects and of the 209Bi(e,e'p) reaction - Ph.D. thesis. Amsterdam University.

86)[Lac06] Lachniet J. (2006). Status of the electronic deadtime measurement in E00102/E01020 - Internal report.
http://www.JLAB.org/~fissum/e00102/analysis/dt_status_report_1.pdf

87)[Lac06b] Lachniet J. (2006). Status of proton detection efficiency measurement in E00102 - Internal Report. http://www.JLAB.org/~fissum/e00102/analysis/prot_eff_status.pdf

88)[Lac07] Lachniet J. (2007). Kinematics adjustments to E00102 data. http://www.JLAB.org/~fissum/e00102/analysis/kinematics.ps

89)[Lac07b] Lachniet J. (2007). Material inventory for energy loss corrections. http://www.JLAB.org/~fissum/e00102/analysis/materials.txt

90)[Lac07c] Lachniet J. (2007).Special modules in Analyzer for the waterfall target - Private communication.

91)[Lag85] Laget J.M., (1985). Many Body Effects in Deep Inelastic Electron Scattering on He-3. Physics Letters B, 151: 325.

92)[Lap93] Lapikas L. (1993). Quasi-elastic electron scattering off nuclei. Nuclear Physics, 553, 297.

93)[Lap00] Lapikas L., et al. (2000). Transparency of ^{12}C for protons. Physical Review C, 61, 064325.

94)[Lav04] Lava P., Martínez M. C., Ryckebusch J., Caballero J. A. and Udías J. M. (2004). Nuclear transparencies in relativistic A(e,e'p) models. Physics Letters B, Volume 595, Issue 1-4, p. 177-186.

95)[Lee01] Leeman C. W., Douglas D. R. and Krafft G. A. (2001) Annual Review Nuclear and Particle Science 51, 413.

96)[LeR85] LeRose J., et. al. (1985). Direct measurement of the radiative tail in electron scattering from atomic nuclei. Physical Review C, 32 (2), 449-451.

97)[Leu94] Leuschner M. (1994). Quasielastic proton knockout from ^{16}O. Physical Review C, 49, 955.

98)[Liy99] Liyanage N. (1999). A study of the ^{16}O(e,e'p) reaction at deep missing energies - Ph.D.Thesis. Massachusetts Institute of Technology.

99)[Liy01] Liyanage N., et al. (2001). Dynamics of the ^{16}O(e,e'p): Reaction at High Missing Energies. Physical Review Letters, 86, 5670.

100)[Liy01b] Liyanage N. (2001). Spectrometer constant determination for the Hall-A High Resolution Spectrometer pair - Jefferson Lab Technical Note (JLAB-TN-01-049).

101)[Liy02] Liyanage N. (2002). Optics calibration of the Hall A high resolution spectrometer using the new optimizer - Jefferson Lab Technical Note (JLAB-TN-02-012),

102)[Lov81] Love, W. G. and Franey, M. A. (1981). Effective nucleon-nucleon interaction for scattering at intermediate energies. Physical Review C24, 3. pp 1073-1094.

103)[Ma91] Z. Y. Ma and Wambach J. (1991). Quasiparticle properties of protons in ^{208}Pb. Physics Letters B 256, 1, pp 1-5.

104)[Mah87] Mahaux C. and Sartor R. (1987). Extrapolation from positive to negative energy of the Woods-Saxon parametrization of the n-208Pb mean field. Nuclear Physics A, Vol. 468, Issue 2, Pages 193-236.

105)[Mai02] Maieron C., Donnelly T. W. and Sick I. (2002). Extended superscaling of electron scattering from nuclei. Physical Review C, 65, 025502.

106)[Mak94] Makins N. C. R., et al. (1994). Momentum transfer dependence of nuclear transparency from the quasielastic ^{12}C (e,e'p) reaction. Physical Review Letters, 72, 1986.

107)[Mal08] Malace S., Paolone M. and Strauch S. for the Jefferson Lab Hall A Collaboration (2008). Medium Modifications from ^{4}He $(\vec{e},e'\vec{p})$ ^{3}H. arXiv:0807.2252v1 [nucl-ex] 14 Jul 2008.

108)[Man93] Mandeville J. B. (1993). Measurement of the fifth structure function in quasi-elastic proton knockout from Carbon - Ph.D. Thesis. University of Illinois.

109)[Mar04] Martínez M.C., Vignote J.R., Caballero J.A., Donnelly T.W., de Guerra E.M. and Udías, J.M. (2004). Analysis of polarized ^{16}O(e,e'p) observables within the relativistic distorted wave impulse approximation. Physical Review C, 69 (3), 034604.

110)[Mar08] Martínez M. C., Caballero J. A., Donnelly T. W. and Udías J. M. (2008). Superscaling predictions for neutral current quasielastic neutrino-nucleus scattering. Physical Review Letters, 100, 052502.

111)[Max00] Maximon L.C. and Tjon J. A. (2000). Radiative corrections to electron-proton scattering. Physical Review C, 62, 054320.

112)[Meu01] Meucci A., Giusti C., and Pacati F. (2001) Relativistic corrections in (e,$e'p$) knockout reactions - Physical Review C 64, 014604.

113)[MCEEP] MCEEP simulation homepage.
http://hallaweb.JLAB.org/software/mceep/mceep.html

114)[Med99] Medaglia R. (1999). Mesure des facteurs spectroscopiques des cinq premiers niveaux en énergie du noyau de plomb 208 à l'aide de la réaction 208Pb(e,e'p)207Tl* à grande impulsion transférée - Ph.D. Thesis. Université de Paris.

115)[Mic01] Michaels R., Reitz B. and Proffitt J. (2001). Update on electronic deadtime - Jefferson Laboratory Annual Report 2001.

116)[Mic04] Michaels R. THaNormAna - Normalization class for Hall A Analyzer. http://www.JLAB.org/~rom/NormAna.tar

117)[Mic06] Michaels R., Souder P.A. and Urciuoli G.M. (2006). Jefferson National Accelerator Facility, approved experiment E06-002.

118)[Mo69] Mo L. W., and Tsai Y. S. (1969). Radiative corrections to elastic and inelastic ep and up scattering. Review Modern Physics, 41, 205.

119)[Mon08] Monaghan P. (2008). Study of the 12C(e,e'p) reaction in a correlations dominant regime with Q^2=2.0 (GeV/c)2 and x_B>1. - Ph.D. Thesis. Massachusetts Institute of Technology.

120)[Mor99] Morrison J.H., et al. (1999) Quasielastic 12C(e,e'p) reaction at high momentum transfer. Physical Review C, 59 (1): 221-232.

121)[Mou76] Mougey J., et al. (1976). Quasi-Free (e,e'p) scattering on 12C, 28Si, 40Ca and 58Ni. Nuclear Physics A, 262, 461.

122)[Mut94] Muther H. and Dickhoff W. H. (1994) Single-particle spectral function of ^{16}O - Physical Review C 49, (1): R17-R20.

123)[Mut04] Muther H. and Sick I. (2004) Correlated nucleons in configuration space - Physical Review C, 70 (4): 041301.

124)[Nik96] Nikolaev N. N., Speth J. and Zakharov B. G., (1996) Glauber theory of final-state interactions in (e,e'p) scattering. J. Exp.Theor.Phys. 82 (1996) 1046-1065.

125)[Pan84] Pandharipande V. R., Papanicolas C. N. and Wambach J. (1984) Occupation Probabilities of Shell-Model Orbits in the Lead Region - Physical Review Letters, 53, (12), pp. 1133-1136.

126)[Par09] Parcerisa D. S., **Herraiz J. L.** and Udías J. M. (2009). Correcciones radiativas en espectros de energía de la reacción cuasielástica ^{12}C(e,e'p) mediante técnicas estadístico-iterativas. XXXII Reunión Bienal de la Real Sociedad Española de Física (RSEF).

127)[PDG] http://pdg.ihep.su/sbl/pp_total.dat; http://pdg.ihep.su/sbl/pn_total.dat

128)[Pet03] Petraki M., Mavrommatis E., Benhar O., Clark J. W., Fabrocini A. and Fantoni S. (2003) Final-state interactions in the response of nuclear matter. Physical Review C 67, (1): 014605.

129)[Pic85] Picklesimer A., Van Orden J.W. and Wallace S.J. (1985). Final state interactions and relativistic effects in the $(\vec{e},e'p)$ reaction. Physical Review C, 32, (4): pp. 1312-1326.

130)[Pol06] Pollock S., Naus H. W. L. and Koch J. H. (2006). Electron-nucleon cross section in (e,ep) reactions. Physical Review C 53, 2304–2308.

131)[Qat05] Qattan I.A. (2005). Precision Rosenbluth Measurement of the Proton Elastic Electromagnetic Form Factors and Their Ratio at Q^2 = 2.64, 3.20 and 4.10 GeV2 - Ph.D. Thesis. Northwestern University

132)[Qui88] Quint E. (1988). Limitations of the mean-field description for nuclei in the Pb-region observed with the (e,e'p) reaction" - Ph.D. Thesis. University of Amsterdam

133)[Rad02] Radici M., Dickhoff W.H. and Stoddard E.R. (2002). Consistency of spectroscopic factors from (e,e'p) reactions at different momentum transfers. Physical Review C, 66, 014613.

134)[Rva03] Rvachev M.M. (2003). Study of quasielastic 3He(e,e'p) reaction at Q^2 = 1.5 $(GeV/c)^2$ up to missing momenta of 1 GeV/c. Ph.D. Thesis. Massachusetts Institute of Technology.

135)[Rei02] Reitz B. (2002). Beam position calibration for E00102 - Internal Report. http://www.JLAB.org/~fissum/e00102/analysis/br010402_rep_on_bpm.ps.gz

136)[Rei05] Reitz B., Roch, R.E., Andersson L.E.M. and Fissum K. G. (2005). E00-102 Analysis status report - Internal Report . http://www.JLAB.org/~fissum/e00102/analysis/e00102_status.pdf

137)[Rein86] Reinhard P.G. et al. (1986) Nuclear ground-state properties in a relativistic Meson-Field theory -Z. Phys. A 323, p. 13.

138)[Ryc03] Ryckebusch J., Debruyne D., Lava P., Janssen S., Van Overmeire B. and Van Cauteren T. (2003) Relativistic formulation of Glauber theory for A(e,e'p) reactions. Nuclear Physics A, 728: 226-250.

139)[Roc03] Roche R. E. (2003). Measurement of polarization observables in the electro-excitation of the proton to its first excited state -Ph.D. Thesis. Florida State University. http://www1.JLAB.org/ul/Publications/documents/thesis_2side.pdf.

140)[ROOT] ROOT project at CERN. http://root.cern.ch

141)[Sah00] Saha A. (2000). Testing the limits of the single particle model in ^{16}O(e,e'p): an update to E89-003. Jefferson Laboratory PAC 18.

142)[Sch49] Schwinger J. (1949). On radiative corrections to electron scattering. Physical Review, 75, 898.

143)[Schi02] Schiavilla R. and Pandharipande V. R. (2002) Elastic e-d scattering data and the deuteron wave function. Physical Review C 65, 6, pp 064009.

144)[Ser86] Serot B.D. and Walecka J.D. (1986). The Relativistic Many-Body Problem. Advances in Nuclear Physics Vol. 16., edited by J.W. Negele and E. Vogt (Plenum, New York).

145)[Spa92] Spaltro C. M. (1992) M.Sci. Thesis, University of Utrecht.

146)[Spa93] Spaltro C. M., et al. (1993). Separated Structure functions for the proton-knockout reaction ^{16}O(e,e'p). Physical Review C, 48, 2385.

147)[Ste88] Steenhoven G., et al. (1988) Knockout of 1p Protons from 12C Induced by the (e, e'p) Reaction. Nuclear Physics A, 480, 547.

148)[Str03] Strauch S. et al. (Udias J.M., Vignote, J.R.) (2003). Polarization transfer in the ^{4}He $(\vec{e}, e'\vec{p})$ ^{3}H reaction up to Q^2=2.6 $(GeV/c)^2$. Physical Review Letters, 91 (5), 052301.

149)[Sul06] Sulkosky, V. (2006) Jefferson Lab - E97110 Technical Note - Dec06.

150)[Tam09] Tamae T., et al. (2009) Comparison of the ^{12}C(e,e'p) cross section at low momentum transfer with a relativistic calculation. Physical Review C, 80(6), 064601.

151)[TarE00] E00-102 target information: http://www.JLAB.org/~fissum/e00102/target/

152)[TarE06] E06-007 target information:
RUN 1 - http://hallaweb.JLAB.org/experiment/E06-007/targetinfo.php
RUN 2 - http://hallaweb.JLAB.org/experiment/E06-007/run2/targetinfo.php

153)[Tem09] Templon, J. et al. (1999). Radiation tail in (e,e'p) reactions and corrections in experimental data. Physical Review C , 61, 014607.

154)[Tra01] Traini M. (2001). Coulomb distortion in quasielastic (e,e') scattering on nuclei: Effective momentum approximation and beyond. Nuclear Physics A, Volume 694, Issues 1-2, Pages 325-336.

155)[Tsa74] Tsai Y. S. (1974). Pair production and brehmstrahlung of charged leptons. Review Modern. Physics , 41, 205.

156)[Udi93] Udías J.M - (1993) Análisis Relativista del Proceso (e,e'p) en Núcleos Complejos - Ph.D.Thesis. Universidad Autónoma de Madrid.

157)[Udi93b] Udias J.M., Sarriguren P., De Guerra E.M., Garrido E. and Caballero, J.A. (1993). Spectroscopic factors in ^{40}Ca and ^{208}Pb from (e,e'p): Fully relativistic analysis. Physical Review C, 48 (6): 2731-2739

158)[Udi95] Udías J.M. (1995). Lepton-nucleus scattering in a relativistic framework: electromagnetic and neutral current case - NIKHEF-K Internal Report - NIKHEF-K 95 P12

159)[Udi96] Udias J.M., Sarriguren, P.; De Guerra, E.M. and Caballero, J.A. (1996). Relativistic analysis of the ^{208}Pb(e,e'p)^{207}Tl reaction at high momentum. Physical Review C, 53 (4): R1488-R1491.

160)[Udi99] Udías J.M., Caballero, J. A.; de Guerra, E.M.; Amaro, J. E. and Donnelly, T. W. (1999). Quasielastic Scattering from Relativistic Bound Nucleons: Transverse-Longitudinal Response. Physical Review Letters 83(26) 5451-5454.

161)[Udi01] Udías J.M., Caballero J.A., de Guerra E.M., Vignote J.R. and Escuderos A. (2001) - Relativistic mean field approximation to the analysis of ^{16}O(e,e'p)^{15}N data at $|Q^2| <= 0.4$ (GeV/c)^2. Physical Review C, 64 (2).

162)[Udi01b] Udías J.M., Vignote J. R., de Guerra E. M. and Escuderos A. (2001). Recent developments in relativistic models for exclusive A(e,e'p)B reactions -Proceedings of the 5th International Workshop on electromagnetically induced two hadron emission - Lund, June 13-16,2001. nucl-th/0109077.

163)[Udi05] Udias J.M., Sarriguren P., De Guerra E.M., Garrido E. and Caballero J.A. (1995) - Relativistic versus non-relativistic optical potentials in A(e,e'p)B reactions. Physical Review C, 51 (6): 3246-3255.

164)[Ulm87] Ulmer P.E., et al. (1987) Missing-energy dependence of the separated response functions for the 12C(e,e'p) reaction. Phys. Rev. Letters, 59 (20): 2259-2262.

165)[Ulm05] Ulmer P.E., (2005) MCEEP - Monte Carlo for Electro-Nuclear Coincidence Experiments -(V3.9) http://hallaweb.JLAB.org/software/mceep/mceep.html

166)[Urc08] Urciuoli G. M. (2008) - Hall A Collaboration meeting.

167)[Umi95] Umino Y., Udías J.M. and Mulders P.J. (1995). Exchange current corrections to neutrino-nucleus scattering. Physical Review Letters, 74 (25): 4993-4996

168)[Umi95b] Umino Y. and Udías J.M. (1995). Exchange current corrections to neutrino-nucleus scattering .1. Nuclear matter - Physical Review C, 52 (6): 3399-3415

169)[Vig04] Vignote J. R., Martínez M. C., Caballero J. A., Moya de Guerra E. and Udias J. M. (1994). A$(\vec{e},e'\vec{p})$B; responses; From bare nucleons to complex nuclei. Physical Review C, 70(4):044608.

170)[Vig04b] Vignote J.R., Álvarez-Rodríguez R., Fernández-Ramírez C., Garrido E., de Guerra E. M., Sarriguren P. and Udías J.M. (2004) - Past, Present and Future of A(e,e'p)B Experiments - Nuclear Theory 23 Rila Conference Proceedings, (Bulgary), S. Dimitrova ed. Heron Press, pp 85-98.

171)[Wal06] Walecka J. D. (2004). Electron scattering for nuclear and nucleon structure - Electron Scattering for Nuclear and Nucleon Structure. Cambridge Monographs on Particle Physics, Nuclear Physics and Cosmology.

172)[Wei90] Weinstein L. B., et al. (2008) Quasielastic reaction mechanism studied using the reaction 12C(e,e'p). Phys. Rev. Letters, 64 (14): 1646-1649.

173)[Wei08] Weinstein L. B. (2008) Private communication.

174)[Weis06] Weissbach F. (2006). Improved radiative corrections to (e, e'p) experiments and their impact on Rosenbluth measurements - Ph.D Thesis, Basel Universität.

175)[Wij99] Wijesooriya K. (1999). First $(\vec{e},\vec{e}\,'\vec{p})$ Measurement of Polarization Transfer in a Complex Nucleus: ^{16}O. William and Mary University.

176)[Yan05] Yan C., Sinkine N. and Wojcik R. - Linear beam raster for cryogenic targets. Nuclear Instruments & Methods in Physics Research, 539A:1, 2005.

177)[Yen61] Yennie D. R.; Frautschi S. C. and Suura H. (1961). The infrared divergence phenomena and high energy processes. Annals of Physics, 13 (2), 309-310.

178)[Yen65] Yennie D. R., Boos F. L. and Ravenhall D. G. (1965). Analytic Distorted-Wave Approximation for High-Energy Electron Scattering Calculations - Physics Review 137, B882.